UNIVERSITÀ DEGLI STUDI DI MILANO

DEPARTMENT OF CHEMISTRY

PH.D. COURSE IN INDUSTRIAL CHEMISTRY

XXXII CYCLE

Valorisation of biomass-derived molecules by noble metal catalysts

Tutor: Prof. Laura Prati

Cotutor: Prof. Claudia L. Bianchi

Candidate

Andrea Jouve *(R11599)*

TABLE OF CONTENTS

Abstract

Valorisation of different biomass derived molecules was successfully approached and studied in this PhD project. The focus of the thesis was addressed to the catalysts preparation, passing through an accurate catalytic designed, to be then tested in academic and industrially appealing reactions. This approach led to the synthesis of different but equally interesting catalytic systems for the valorisation of substrates derived from the first and second generation of biomass feedstock.

An extended study, at first, was conducted on the oxidation of glycerol (1st generation of biomass related), both in alkaline (needed for gold monometallic systems) and free pH (high industrial relevance) conditions. The target reaction was approached starting from the simplest Au/C catalytic systems, to finally move to more complicated and innovative materials: bimetallic once.

Initially, the Au on carbon Vulcan (with the highest graphitisation degree) SOL derived catalysts showed a remarkable initial activity (IA= 1091 h^{-1}) in comparison with the other carbonaceous supports (Norit and X40S) and the SMAD derived catalysts. This result pointed out the importance of the protecting agent (a polymer that surrounded the nanoparticles and is solely present for the SOL synthetic route) beside the importance of the support's features. Similarly, electronic effects ascribed to the interaction with the support of the nanoparticles (i.e. the strong metal support interaction (SMSI) thermally induced on Au_4Ag_1/TiO_2) showed to be the ruling factor to determine the oxidation state of the metals. This latter, subsequentially, influence the catalytic activity: an enhanced initial catalytic activity was detected for the Au_4Ag_1/TiO_2 catalyst (IA= 1616 h^{-1}), in comparison with the Au_4Ag_1/Al_2O_3 (IA= 963 h^{-1}). The SMSI have influenced also the stability of the system, avoiding the enlargement of the nanoparticles during the thermal treatments. On the other hand, the SMSI induced the presence of Ag^+ species onto the bimetallic nanoparticles titania supported, leading to a quite rapid deactivation of the catalytic system. The thermal treatments pointed out also the importance of the protecting agent (polyvinyl alcohol, PVA): on one side when it is present confers resistance to the system towards the nanoparticles aggregation, on the other when it is removed from the nanoparticles' surface (by the same thermal treatment), the catalyst acquired an enhanced initial activity. $AuPt/TiO_2$ catalytic systems were subsequentially exploited both in alkaline and free pH conditions. The gold content positively influenced the activity of the

catalytic systems in both the conditions. In particular Au_9Pt_1/TiO_2 was the most active catalyst in the alkaline condition (IA= 7389 h^{-1}), and Au_6Pt_4/TiO_2 showed the highest initial activity (IA= 301 h^{-1}) in free pH condition.

For all the bimetallic system mentioned and exploited in the valorisation of glycerol, furthermore, a synergistic effect was detected. The importance of gold as modifier to confer resistance to the catalytic system by stabilizing the oxidation state of the second metal was also established.

Subsequentially, completely different designed and synthesised catalysts were prepared for the valorisation of substrates related with the 2nd generation of biomass. Bare carbon nanofibers (CNFs) and functionalised CNFs (CNFs-P, CNFs-O and CNFs-N), for instance, were employed as supports for Ru nanoparticles (introduced by incipient wet impregnation). All the catalysts prepared showed activity in the valorisation of cellulose derived molecules. In particular, it was observed how N-containing functionalisation of the support, promoted by a strong interaction with the Ru nanoparticles, led to the highest catalytic activity among the set of catalysts tested for the levulinic acid (LA) hydrogenation (88 % of conversion after 3 h) with a full selectivity to *y*-valerolactone (GVL). On the other side, exploring the 5-hydroxymethylfurfural (HMF) valorisation, Ru/CNF-N and Ru/CNF-P showed a lower activity but also a change in selectivity. In fact, these latter two catalysts enhanced the formation of ethers due to the reaction between 2,5-dihydroxymethylfuran and/or methylfurfuryl alcohol with the solvent (2-butanol).

Similar support effects were also observed in the furfural hydrogenation over platinum nanoparticles (introduced by solvated metal atoms deposition, SMAD) supported on niobia and tailor-made modified niobia. Niobia was hydrothermally synthetized pure and doped with other two different metals (W and Ti, both 10 at.%) to tune the acidity of the system. In particular, we were able to enhance to 0.191 $mmol_{Py}/g_{CAT}$ ($W\text{-}Nb_2O_5$) and decrees to 0.014 $mmol_{Py}/g_{CAT}$ ($Ti\text{-}Nb_2O_5$) the acidity of the pure Niobia (0.078 $mmol_{Py}/g_{CAT}$). Platinum nanoparticles, showing a narrow particle size distribution (1.1-1.2 nm) for all the supports, have allowed a proper study of the acidity effect. The acidity, indeed, showed to be the ruling factor: the most acidic material showed the highest activity coupled with a selectivity addressed to the furan ether products (acid catalysed reaction's step) at the expenses of furfuryl alcohol (highest selectivity of FA showed for the lowest acid catalyst). Unfortunately, the condition and the type of acidity (Lewis

acidity) obtained were not sufficient to observe a high fraction of diols (target product, less than 10 % in selectivity), produced from the ring-opening of the substrate.

Lastly, in the benzyl alcohol oxidation (model compound for the lignin) it was highlighted how gold-based materials characterised by comparable nanoparticles dimension (Au-Pd, Au-Pt, Au-Ru and Au-Cu, all supported on carbon) could change the catalytic behaviour and the bimetallic structure just by varying the second metal. For AuPd/C and AuPt/C, for example, alloyed structures were observed. On the other hand, for the case of Ru as second metal, a core-shell structure was found. When Cu was employed, bimetallic nanoparticles with Au:Cu molar ratio lower than the nominal one were detected suggesting the presence of segregated gold nanoparticles. All the catalysts were active and highly selective towards the desired and industrial appealing product (benzaldehyde, selectivity ≥ 99 %). Only in the case of AuPd/C and AuCu/C, however, a synergistic effect was observed. In particular, the AuPd/C bimetallic sample showed the highest activity (fully conversion of the substrate after 5 min). For the interesting Au-Cu system (the only catalysts that contain a not noble metal), furthermore, the role of the Cu was clarified and the composition effect was studied. The metals were deposited on a carbonaceous support by SMAD technique in order to avoid a protecting agent influence. More in details, it was speculated how Cu, promptly oxidised at CuO (if exposed to air), is responsible of the O_2 activation, while the reaction took part at the Au-CuO interface. This reactivity is guided by a specific structure of the bimetallics particles finely characterized: Au_{core}-$CuOs_{hell}$ structure. This last evidence highlighted once more the importance of having a good knowledge and control on the catalyst synthetic routes. Furthermore, synergistic effect was observed for all the active AuCu/C bimetallic systems, even when the amount of gold was very low ($Au_{13}Cu_1$/C, IA= 329 h^{-1}). The highest initial activity, however, was reached with Au_4Cu_1/C catalysts (IA= 399 h^{-1}). All the active AuCu bimetallic catalysts showed a high selectivity towards the desired product: benzaldehyde (≥ 95%). Good stability against deactivation was also observed. For the Cu-rich sample (Au_1Cu_{17}/C) case, distinguished by the negligible activity, it was assumed how the external copper oxide shells, by entirely covering the gold atoms, have repressed any catalytic activities.

Chapter 1. Introduction

1.1. The urgency of independence from petrochemical resources

We are all aware of the urgency to switch from petrochemicals to more sustainable resources to produce materials, chemicals and fuels. Historically, the first oil crisis in 1973 started to build the bases for a consciousness about the limited availability of traditional oil and gas sources [1]. The world is witnessing a rapid population growth and vast economic developments with a consequent increase in global energy demand (estimated to double between 2000 and 2035) [2]. Fossil fuel sources, such as crude oil, coal, and natural gas, currently represent the major energy supplies. However, they are pollutant and non-renewable resource, and they predicted to have a consumption peak between early 2020s to the 2040s [3] (before decaying) depending on economics [4] and how governments will respond to global warming. The laws of economics dictate that as petroleum reserves decrease, the price of petroleum products will increase, consequentially the biofuels eventually will be cost-competitive and even cheaper than petroleum-derived fuels.

One of the major concerns of the 21st century is the increasing levels of greenhouse gas emissions (i.e. CO_2) caused by fossil fuels consumption [5, 6]. Global CO_2 emissions reached an all-time record of approximatively 40 billion tonnes in 2017, contributing to an atmospheric CO_2 concentration of approximatively 400 ppm, the highest observed since the beginning of the industrial revolution [7, 8]. If this trend will not be reversed, global average temperatures are estimated to increase drastically in the range of 2.5–5 °C by 2050 [9]. Global warming is another major threat for the humankind existence. The effects of the climatic change, indeed, can be easily observed by the increased rate and intensity of many atmospheric phenomena. Several countries, in the attempt to control this global warming, have established strict regulations to reduce the fossil fuels usage in favour of the so defined '*carbon-neutral society'*. In December 2015, the 21st Conference of the Parties to the United Nations Framework Convention on Climate Change (COP21/CMP11, Paris) led to an agreement between 195 with the major intention to reduce the CO_2 emissions. The European Union also set ecological targets: i.e. it established a target reduction of 20 % in CO_2 emissions by 2020 compared to 1990 levels [10]. Part of the European Union goal is also to expand of 20 % by 2020 the renewable energy exploiting for the total energy supply. An important study entitled '*The Roadmap for Biomass Technologies*', authored by 26 leading experts from academia, industry and

government has predicted a gradual shift back to a carbohydrate-based economy, such that by 2030 20 % of transportation fuel and 25 % of chemicals in the USA will be produced from biomass [11]. In view of these concerns and challenges, it is nowadays present a growing interest towards the use of clean and sustainable resources for the production of fuels and chemicals. Various renewable resources, such as wind, geothermal, solar and hydropower are available beside the biomass. On the other hand, biomass due to its features (abundant and natural carbon source) is considered one of the most promising renewable alternatives to fossil fuels. Furthermore, biomass can also be transformed into a wide range of value-added chemicals, clean solvents, and high-energy density fuels [2, 12, 13].

1.2. The importance of biomass valorisation

Since the beginning of industrialisation, our society was dependent on plant biomass to meet the energy demands. In the mid-1800s, for example, biomass covered more than 90 % of USA energy and fuel needs [14]. The subsequent discovery of crude oil in the 19th century gave the access to an inexpensive liquid fuel source that helped to industrialise the whole world and also to improve standards of living. For these reason in the late 1800s to early 1900s, fossil fuels became the preferred energy resource [14]. Nowadays, with the Kyoto protocol that aims to limit the environmental problems associated with the declining of the petroleum resources and an increasing demand of energy and materials, the development of economical and energetic alternative routes became imperative. In this respect, biomass has been recognised as the only real current sustainable source of organic carbon to allow such a huge change [15–19]. Biofuels production, in fact, produce significantly less pollution with respect to the corresponding fossil fuels production. Furthermore, in a near future, greenhouse gas free processes will be available for the biofuels production [20, 21]. Many developed countries have already recognised the importance of biomass valorisation using it as the major source of energy [22]. The importance of biomass in different world regions is given in Table 1-1. As we can observe from the data reported, for large portions of the rural and poorest populations (developing countries), biomass represent the only available and affordable source of energy. The biomass feedstock is exploited mainly for basic needs such as cooking and heating [14].

Table 1-1. World exploiting of the biomass.

Country	Bioderived energy consumption (%)
Uganda	94.6
Burundi	93.8
Somalia	86.5
Ethiopia	85.6
Sudan	83.7
Kenya	69.6
Africa (average)	62.0
South Asia (average)	56.3
East Asia (average)	25.1
China	23.5
Latin America (average)	18.2
Europe (average)	3.5
North America (average)	2.7
Middle East (average)	0.3

Other important and developed countries are exploiting biomass to meet a large percentage of their energy demands, such as. Sweden (≈ 17 %), Finland (≈ 20 %) and Brazil (≈ 23 %) [15]. On top of that, the urgency of the transition to renewable resource has also been recognised by many important and powerful companies including traditional oil and chemical companies such as Shell [23], UOP [24], Petrobras, Conoco-Phillips [16], Dupont and Dow [25, 26]. These companies, indeed, are investing for developing the technology and infrastructure for biofuels and biochemicals production. Many governmental leaders are also recognising the importance of these new green industries by providing tax breaks, money and mandates in order to facilitate their expansion. For example, a considerable number of EU countries (i.e. Austria, Italy, Poland, Spain, Germany, France and Sweden) has already gave a full tax exemption for biofuels. The European Union even provided a '*carbon credit*' to the farmers who grow energy crops to produce biodiesel and bioethanol [27].

Anyway, for the transition to the biomass economy to continue, it is vital to develop low-cost processing technologies. Chemists, engineers and scientists more in general, will play a key role in developing these processes.

1.3. Biomass feedstock

Biomass feedstocks are well-known for their large diversity, which makes them rather difficult to characterise. The biomass feedstock includes forest products wastes, agricultural residues, organic fractions of municipal solid wastes, paper, cardboard, food waste, green and other organic waste. Biobased materials, however, require a pre-treatment prior to be converted. The pre-treatments differ in chemical, physical or biological with all the means to open the structure of biomass and get access to the component of the biomass.

The major categories of biomass feedstock can be listed as follows:

- Food crops: grains and oil crops
- Forest products: wood, shrubs and wood residues, sawdust, bark etc.
- Bio-renewable wastes: agricultural wastes, crop residues, wood wastes, urban wastes (wood and organic)
- Energy crops: short rotation woody crops, herbaceous woody crops, grasses, starch, sugar, forage, oilseed crops.
- Aquatic plants: algae, water weed and hyacinth, reed, rushes.
- Sugar crops: sugar cane, beets, molasses, sorghum.
- Industrial organic wastes

Biomass represent the world's fourth largest energy source following coal, oil and natural gas. Biomass appears to have formidably positive environmental properties as already mentioned; in addiction biomass are more uniformed distributed in the world with respect to petrochemical resources.

Vegetable biomass, commonly referred as lignocellulose, from a chemistry and life-cycle point of views, is generated from CO_2 and H_2O using sunlight as energy source, producing O_2 as a by-product (Scheme 1-1).

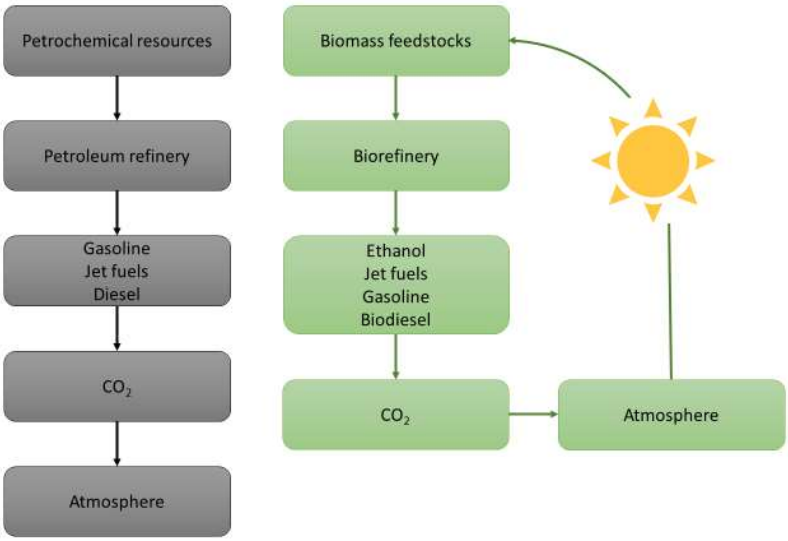

Scheme 1-1.CO_2 cycles for petrochemical and biomass feedstocks valorisation into biofuels.

The primary products that are formed are C_6 and C_5 carbohydrates (sugars) that are linked together to form cellulose (by polymerization of glucose) and hemicellulose (a polymer of glucose and xylose). The third component of lignocellulose, lignin, is a highly cross-linked aromatic polymer built of substituted phenols and gives strength to the plants (Figure 1-1). The monomers more present are: coniferyl alcohol, p-coumaryl alcohol and sinapyl alcohol [28].

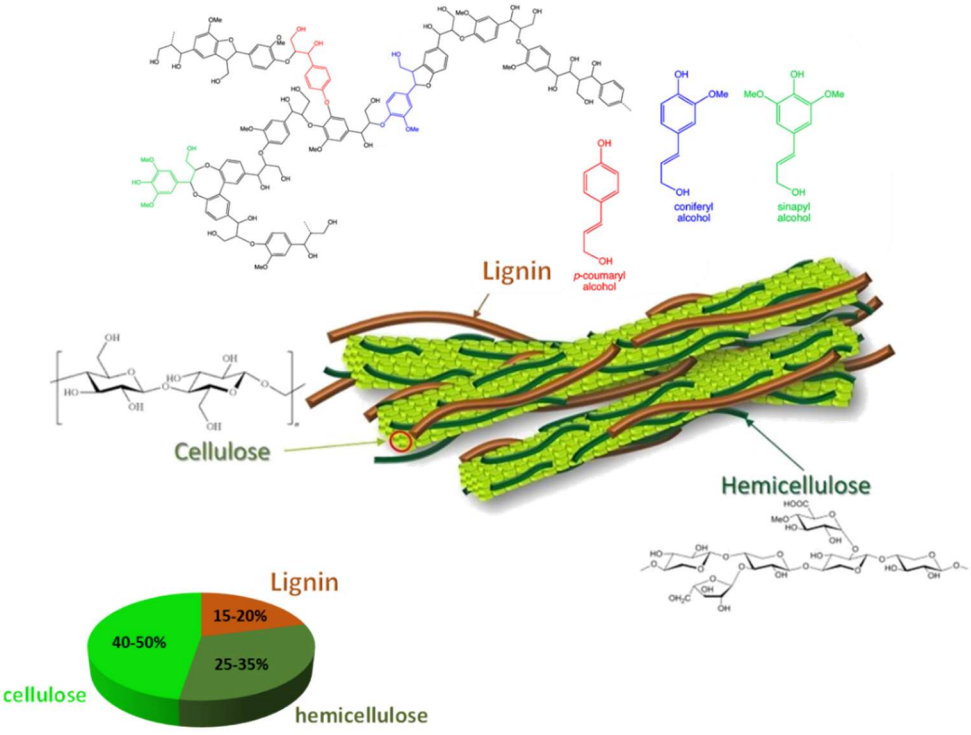

Figure 1-1. Lignocellulose composition.

Besides those major components, plants can also store energy by producing lipids, sugars and starches as well as other products relatively rich in hydrogen and carbon (i.e. terpenes). The energy content of the different biomass products sees terpenes on top of the list, followed by vegetable oils, lignin, and sugars. Since the production of terpenes is too slow, most of the world attention has focused on oils and lignocellulose [28].

Biomass can be divided, based on the type of resource from which they derive, mainly in four groups of different feedstocks as it will be discussed more in details in the following sections. The most exploited recourse for the production of renewable fuels are nowadays represented by the first and second generation of biomass feedstocks [29]: starchy feedstocks (including sugars), triglyceride feedstocks and lignocellulosic feedstocks (Scheme 1-2). Further insights will be reported during the different biomass feedstocks discussion.

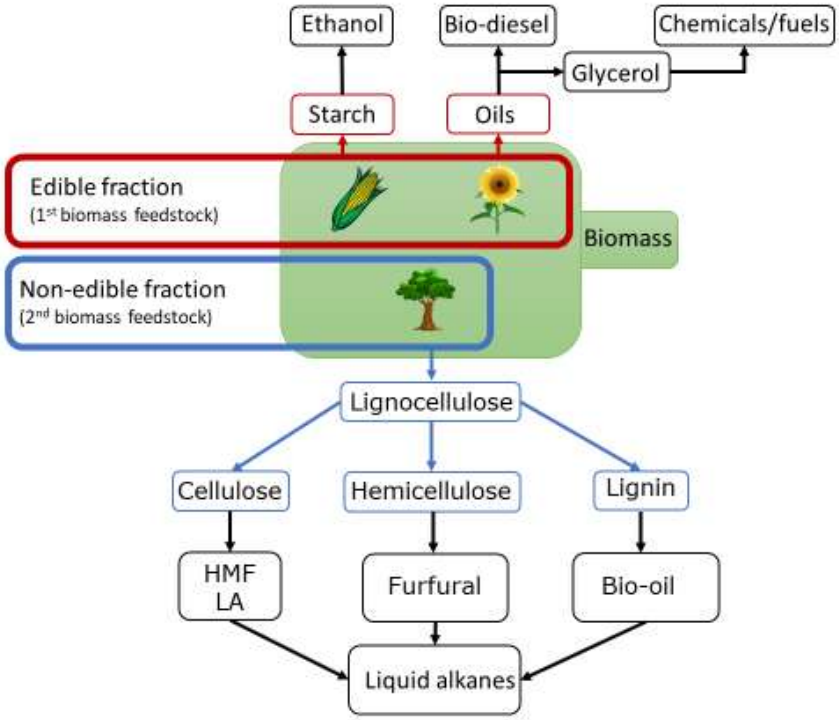

Scheme 1-2. Biomass feedstocks and platforms valorisation for conversion into biofuels.

Apart from the already mentioned uses, many other applications can be found for the biomass (i.e. production of high added-value chemicals), especially for the second generation biomass feedstock, as well as the appealing biofuels production.

However, it should be reported that in comparison with fossil fuels, for example, biomass contains much less carbon and more oxygen with a consequent low heating value. For this reason, biomass required a proper valorisation process. A general scheme

representing the main solutions to valorise the more abundant biomass feedstock is reported in Scheme 3-1. Some of the processes represented in the scheme will be discussed more in detail in the following sections [14].

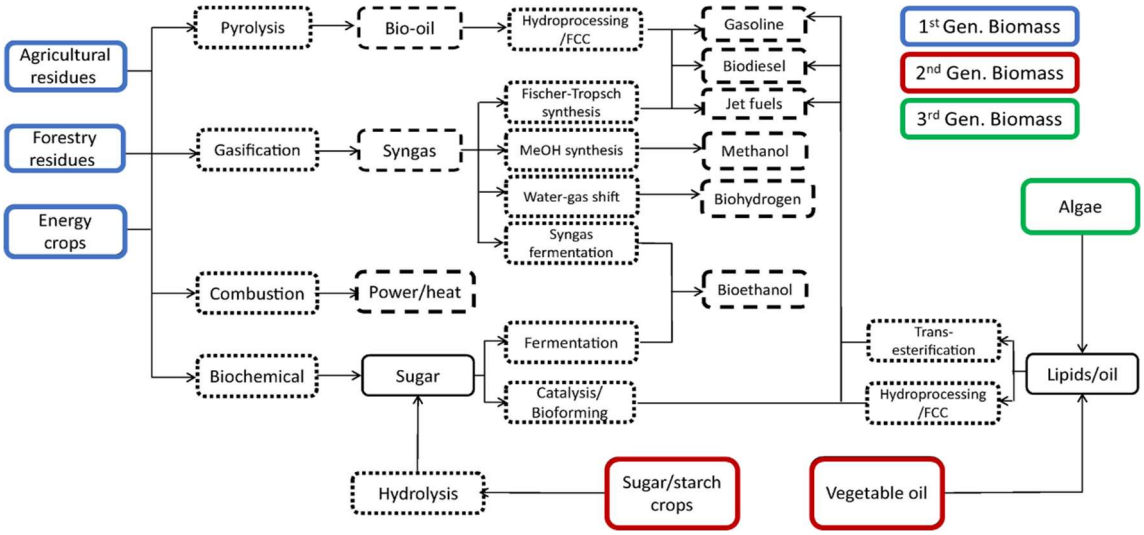

Scheme 1-3. Some different valorisation approaches available for different generation of biomass feedstocks (FCC: fluid catalytic cracking). (modified from [30]).

1.3.1. *First generation of biomass feedstock*

Biofuel production has been increasing rapidly in the last decade and currently supplies around 4 % of global road transport fuel requirements. Global biofuel production increased from 38 billion litres to 131 billion litres between 2005 and 2015 [31]. In order to supplies this production, approximatively 40 million of hectares (2.5 % of the global production) [32] are used for bioenergy crops, mainly for biofuel production (bioethanol, biodiesel and also biogas). The traditional feedstocks for first generation biofuels can be categorised as starch and sugar crops (for bioethanol), and oil seeds (for biodiesel). All these types of feedstocks derive and are grown in arable food crops. A general pathway of the different routes available to valorise the first generation of biomass is reported in Scheme 1-4.

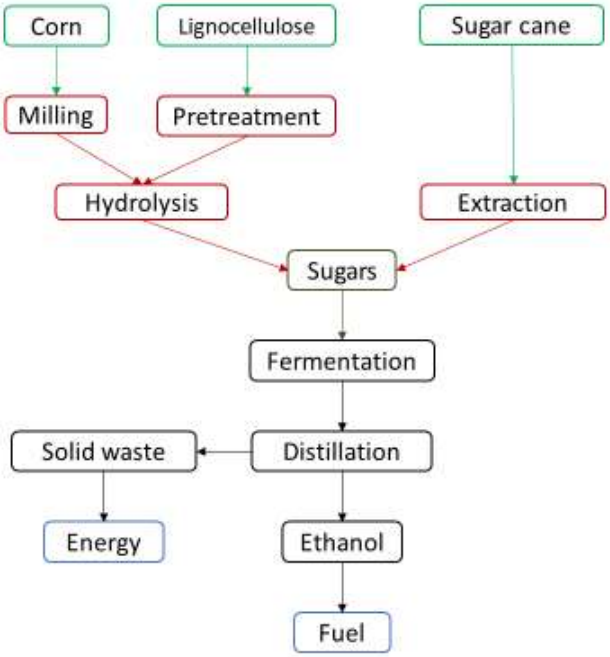

Scheme 1-4. Schematic representation of the bioethanol production.

Corn-based ethanol is leading the global market with approximatively 60 billion litres produced (with USA as the largest supplier, data of 2012), followed by sugarcane-based ethanol at 20 billion litres produced (mainly by Brazil) [33].

The process that convert sugar-based biomass to ethanol is relatively simple: it involves the fermentation of C_6 sugars (mostly glucose). For this purpose, the most used species are *Saccharomyces cerevisiae* or *Zymomonas mobilis* [34].

Valorisation of starch consists is a more complex fermentation than the one of sugars, because starch must be firstly hydrolysed to fermentable sugars. This additional step is performed by means of enzymes (α-amylase) [34]. As a result, the energy requirement for starch-based ethanol production is greater than that the corresponding sugar-based ethanol production. The ethanol produced is then purified by distillation. A litre of ethanol contains approximatively 70 % of the energy that is provided by a litre of petrol [35]. Ethanol can be burned directly or blended with petrol to improve fuel combustion in vehicles, resulting in lower CO_2 emission. In literature, it is reported how by using the E10, a commercial name for the product having 10 % ethanol blended with regular petrol, a 6 % of reduction in petroleum use, 2 % of reduction in greenhouse gas emissions and 3 % of a general reduction in fossil energy use can be achieved [35]. In addition, the by-

products of ethanol conversion processes, such as 'dried distillers' grains and solubles (so called DDGS), can be then used as feed rich in protein for animal.

Biodiesel, the second main biofuel that can be derived from the first generation of biomass feedstock, is produced by combining oil extracted from seeds and oil-rich nuts with an alcohol through a chemical process known as transesterification (Scheme 1-5) [36].

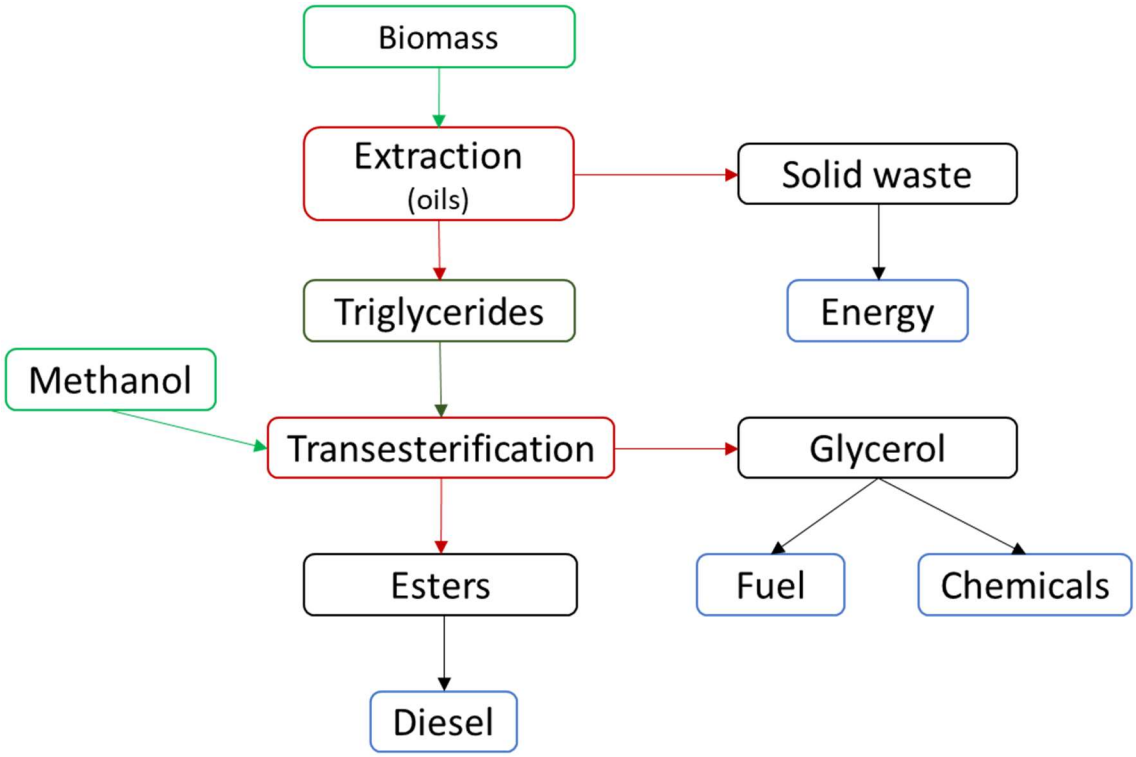

Scheme 1-5. Schematic representation of the biodiesel production.

The most common oil crops are represented by rapeseed in EU (oil content ≈ 35 %), soybean in USA and Latin America (oil content ≈ 20 %) and palm and coconut oil in tropical Asian countries (such as Malaysia and Indonesia, oil content ≈ 40 %) [36]. Moreover, beef tallow and exhausted oil (after cooking use) can also be exploited as feedstocks for biodiesel conversion. The major difference between various oil feedstocks is the types of fatty acids present, which determines the degree of saturation/unsaturation and molecular structure. All these factors can affect the production processes, quality and cost of the final biodiesel produced [37]. The transesterification of oil to biodiesel is a stepwise reaction of triacylglycerols with an alcohol (mostly methanol) to form methylesters and glycerol (approximative glycerol production: 1 Kg every 10 Kg of biodiesel produced) in the presence of a catalyst [36]. The alkali-catalysed transesterification process represents the most economical option, requiring low processing temperature and pressure and achieving a 98 % of yield [36]. On the other

hand, enzyme-catalysed processes, due to low energy consumption, reduced soap formation and high purity of glycerol, is acquiring more importance [38]. High enzyme cost and low reaction rate are two main obstacles that have to be overcome in order to commercialise this process.

Similar to bioethanol, biodiesel can be used as pure fuel or it can be blended in mixture with petroleum-based diesel. The most common fuels with a biodiesel content are the so called B2 (2 % biodiesel), B5 (5 % biodiesel) and B20 (20 % biodiesel). Biodiesel nowadays is not yet cost competitive with petroleum-based diesel. In fact, the increasing prices of the vegetable oils that represents approximatively 45–70 % of overall production cost, is slightly slowing its development. Hence, improving process efficiency and increasing use of the by-products can reduce the production cost [39].

Glycerol

Crude glycerol is a valuable by-product directly derived from biodiesel production through the already mentioned transesterification reaction. The amount of crude glycerol produced as by-product in biodiesel production is around 10wt.% [40, 41]. Refining crude glycerol into a chemically pure substance could potentially increases its value for extensive uses and applications [42–44]. Nowadays, glycerol is involved in many processes and it has extensive industrial application such as in medical, pharmaceutical, food and cosmetic industries (i.e. as additive for soaps or toothpastes, as sweetener in candies and cakes, as plasticizer or lubricant, and so on). Even more important, glycerol is also recognised as an excellent chemical building block [45]: it results suitable for the production of several types of polymers [46, 47] such as polyglycerol ethers and carbonates as well as copolymers with hydroxyacids, for instance, to produce polyether esters or polycarbonate esters [48].

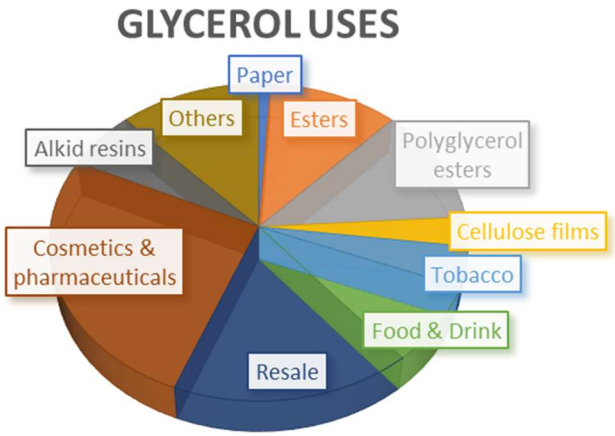

Figure 1-2. Distribution of glycerol uses (adapted from [19]).

Sustainability of the first generation feedstock

Although the first generation biofuels have been commercialised worldwide with mature technologies and markets, its sustainability has been questioned based on the competition with food crops and the effects on the environment and climate change [49]. Indeed, biofuel production leads to an increasingly consumption of the global cereal, sugar and vegetable oil production. The share of vegetable oil, to produce biodiesel, is expected to increase year by year. The outlook of Organisation for Economic Co-operation and Development (OECD) and the Food and Agriculture Organization (FAO) of the United Nations (OECD-FAO) certainly raises concerns about the impact of biofuel on food prices and food supply. Furthermore, reduction in water and soil quality due to the intensive crops feed with agrochemicals has also been linked to the increased biofuel production. This phenomena became evident in particular in Brazil (use of sugarcane for ethanol production) and in Southeast Asia (use of palm oil for biodiesel production) [49]. In addition, for countries that are facing increased risk of water scarcity, such as India, more pressure on water resources and water availability to food production is placed [50]. Although the production of first generation biofuels remains a solid reality, the interest is shifting towards less expensive and readily available biomass such as municipal waste or toward another biomass generation of feedstock such as forest resource.

1.3.2. *Second generation of biomass feedstock*

The not sufficient amount of available triglycerides together with ethical reasons (use of edible fraction of biomass), has directed the future development for large-scale production of biofuels and other added value products from food crops (first generation of biomass feedstock) toward lignocellulose (second generation of biomass feedstocks) [28]. Lignocellulosic biomass, in fact, is expected to play a major role in the transition towards a low-carbon economy. However, the lignocellulosic feedstock requires more complex steps for its valorisation compared to starch, sugars or oils; this makes the conversion processes of the second generation of biomass more complicated, more expensive coupled with a consequent need of high-efficient processes and the discover of new routes of valorisation.

The second generation of biomass feedstocks, however, is composed of non-edible lignocellulosic materials that can be divided into three main groups [51]:

(i) homogeneous, such as wood chips from energy crops with a price value of 100–120 €/ton,

(ii) quasi-homogeneous, such as agricultural and forest residues estimated at 60–80 €/ton

(iii) non-homogeneous, including low-valued municipal and industrial solid wastes between 0–60 €/ton.

In the past few years, an extensive research was conducted on new potential feedstocks and significant progresses for improving the second generation technologies have been achieved [36, 38, 52, 53]. However, several technical and economic obstacles still need to be overcome before these technologies found a widely usage.

Crops for energy

Energy crops, developed and grown specifically for energy and mostly for biofuel production, include perennial grasses (such as miscanthus, switchgrass and reed canary) and short rotation forestry (such as willows and poplar). The crops listed above can be also grown on poor and degraded soils and still provide an high yields in terms of final energy obtain. Furthermore, these type of forest crops can guarantee a steady supply stream, avoiding costly storage of large biomass volumes between harvests. The relative data on the second generation biomass feedstock valorised into biofuel, in order to give an overall idea, are reported in Table 1-2.

Table 1-2. Biomass and corresponding biofuel statistic for different energy crops.

Crop	Time establishment (years)	Biomass yield (ton/ha/year)[1]	Biofuel yield (toe/ton)[2]	References
Willow	> 3	5–11	0.7–1.8	[54]
Poplar	> 3	2–10	0.4–1.5	[54]
Eucalyptus	> 4	10–12	0.2–1.2	[55]
Miscanthus	> 3	5–43	0.8–6.9	[56]
Switchgrass	2–3	5–19	0.7–3.0	[57]
Reed canary grass	1–2	2–10	0.3–1.2	[58]
Alfalfa	1–2	1–17	0.1–1.5	[59]
Fibre sorghum	1–2	16–43	2.1–5.7	[60]

[1]tons of dry matter produced in a hectare of land in a year;
[2]toe = tons of oil equivalent.

Some fast growing trees, technically known as short rotation wood crops, have shown to be a promising feedstock for biofuel production because of their high yield, widespread geographical distribution, low costs and less work needed compared to annual crops [61]. Among all the suitable species, poplar, willow (abundant in temperate regions) and eucalyptus (mostly in tropical regions) are the most frequently mentioned and exploited. They are used in short rotation of about 3–6 years and the yield can reach up to 8–12 tons dry matter/ha/year [61]. Also perennial grasses, such as Switchgrass, which originated from North America and miscanthus, from Southeast Asia represent two good choices in terms of low input bioenergy production. These type of grass showed a marked tolerance for cold temperature, low water and nutrients presence and they are capable to grow on a broad range of land [62]. These perennial grasses, on the other hand, are also effective for carbon sequestration and soil stabilisation. These beneficial effects thus help to reduce erosion, improving the quality of water and enhance the asset of the wildlife habitat [62]. In addition, by means of crop rotation with annual food crops has shown to increase the crop yields and to improve the land efficiency [63].

Another fraction of the second generation of biomass (similar to the first generation), by producing seeds with and high oils content results suitable to be exploited in the production of biodiesel (lead again to a 10 wt.% of glycerol). Jatropha, for example, was

recognised as an ideal crop for cheap biodiesel production. It is a native plant of tropical America, a drought resistant tree that grows well even on degraded lands and can produce seeds with an high oil content (≈ 40 %) [64]. From 2010 to 2015, approximately 2 million hectare of Jatropha have been planted every year, resulted in a total of 13 million hectare of land crop distributed across India (≈ 70 %), South-East Asia (≈ 20 %) and Africa (≈ 10 %) [65].Jatropha oil can be used locally for fuel vehicles, diesel generators or even for cooking stoves (without transesterification) [64]. Some other species that can be potentially exploited for the biodiesel production include pongamia, mahua, castor and linseed. Their seed yield and consequent potential biofuel production yields are reported in Table 1-3.

Table 1-3. Seeds oils content and corresponding potential oil year [64].

Species	Oil fraction (%)	Seed yield ($\times 10^6$ tons/year)	Oil yield (tons/ha/year)[1]
Jatropha	40–60	0.20	2.0–3.0
Mahua	35–40	0.20	1.0–4.0
Pongamia	30–40	0.06	2.0–4.0
Castor	45–60	0.25	0.5–1.0
Linseed	35–45	0.1	0.5–1.0

[1] *tons of dry matter produced in a hectare of land in a year.*

While the advantages of short rotation forestry and perennial grasses over annual agricultural crops are clear, these dedicated crops for energy production are still land-based and thus not completely escaping from the food versus fuel debate. Only where food crops are not feasible would potential energy crops be the most beneficial.

Agricultural/forestry residues

Nowadays, both agricultural and forestry residues represent a promising, readily available green biomass feedstock for biofuel and bioproduct production without the need of arable land. Agricultural residues including wheat straw, corn (leaves, stalks and cobs) and sugarcane and forestry residues (including primary and secondary wood mill-processing residues) are estimated to be annually around 5.1 billion tons of agricultural residues and 501 million tons of forestry residues, respectively (global production) [66]. However, only a 10–25 % of these waste result suitable for bioenergy production. Biomass residues, in addition, are significantly different in their chemical composition. They are composed

of polysaccharides cellulose (hexose sugars, ≈ 35–50 %), hemicellulose (hexose and pentose sugars, ≈ 20–35 %) and polyaromatic compounds (lignin fraction). The corresponding data for various resources are reported in Table 1-4 [58].

Table 1-4. Composition and yield of different residues and waste [58, 65, 67, 68].

Feedstock	Residue/ crop ratio	Dry material (%)	Cell.* (%)	Hemicell.* (%)	Lig.* (%)	Heating value (GJ/ton)	Biofuel yield (L/ton)
Forest residues							
Black locust	–	–	42	18	27	19.5	390
Hybrid poplar	–	–	45	19	26	19.6	416
Eucalyptus	–	–	50	13	28	19.5	411
Spruce	–	–	43	26	29	19.5	417
Pine	–	–	45	20	29	19.6	436
Agricultural residues							
Barley straw	1.2	88.7	43	30	7	18.9	367
Corn stover	1.0	86.2	46	35	19	18.0	503
Rice straw	1.4	88.6	40	18	7	18.2	392
Sorghum straw	1.3	89.0	44	35	15	18.6	199
Wheat straw	1.3	89.1	40	28	16	19.0	410
Bagasse	0.6	26.0	33	30	29	19.4	3133
Solid waste							
Processed paper	–	–	47	25	12	16.3	–
Plastics	–	–	65	15	7.5	34	–
Food waste	–	–	45	5.3	13	18.6	–
Poultry waste	–	–	11	16	4	17.5	–
Solid cattle manure	–	–	2.7	2.3	4.5	17.1	–

**Cell. = cellulose, Hemicell. = hemicellulose and Lig. = lignin.*

Municipal and industrial wastes

To give an overall idea of the municipal solid waste (MSW) amount, it is sufficient to report that approximatively 1.3 billion tons are produced worldwide in 2012 [69]. The composition of MSW is highly variable, containing primarily putrescible, papers and plastics. The majority of the above listed wastes are biodegradable with a significant calorific (heat) value that could make it potentially suitable for energy recovery operation. It is estimated that a ton of MSW produces approximately 8–12 GJ, that correspond to one-third of the calorific value of coal [68]. In addition to the MSW, the industrial solid wastes derived from food and paper industries also counts a large number of residues and by-products that can be fruitfully exploited as biomass feedstock to produce bioenergy. These latter types of waste include, but are not limited to, peelings and other scraps from fruit and vegetables processing, meat and poultry waste, pulp and fibre from sugar and starch extraction, coffee grounds and whatnot.

Furthermore, the waste-to-energy approach adopts an eco-sustainable philosophy, closely linked to the recent waste management practices, which have moved away from disposal towards recovery, reuse, recycling and reduction. Green waste valorisation like the ones that have been reported in this section, could potentially offer many bioenergy applications replacing fossil fuels with indisputable environmental benefits such as landfill space savings and reduction in green-house gasses emission.

1.3.3. *General approaches for the lignocellulose valorisation*

Lignocellulosic biomass, even though is the most abundant and renewable resource available for human exploitation, presents a variable composition and some undesirable impurities: these features lead to some technical and economic challenges to be overcome before to see these technologies led the energy production market. Before going further into the details of the processes, a briefly introduction of the three lignocellulose components is reported.

Cellulose

Cellulose in a crystalline polymer made by glucose monomers linked together via β-glycosidic bonds. Given the rigid crystallinity nature of this component, it results impossible to perform directly an hydrolysis [70]. The biomass pre-treatments required (include milling and physical/chemical pre-treatments) are performed to selectively extract the hemicellulose (and lignin), isolating the cellulose. This step will make more

effective the subsequent already difficult hydrolysis to produce glucose monomers [22, 71]. Maximum glucose yields (≈ 90 %) can be reached by enzymatic hydrolysis [72, 73]. The hydrolysis can be also performed under harsh conditions (H_2SO_4 at high temperatures). The latter treatment, beside facing environmental issues related to the disposal of acids, could lead to appealing degradation products such as hydroxymethylfurfural (HMF) or levulinic acid (beside the insoluble humins production) [74, 75].

Hemicellulose

Hemicellulose is interwoven with the cellulose filaments and bounded to lignin. Hemicellulose is an amorphous lignocellulose polymer generally composed by five different carbohydrate monomers: D-xylose (the most abundant), L-arabinose, D-galactose, D-glucose, and D-mannose [70]. By means of pre-treatments, hemicellulose can be separated with lignin from cellulose, in order to allow an easier cellulose depolymerisation step (hydrolysis to obtain glucose). Pre-treatment routs involve a mild acidic attack (with H_2SO_4 to perform the hydrolyses) [76, 77] to produce xylose monomers with an high yield. The xylose monomers so obtained result a suitable feedstock for the bio-ethanol production by fermentation [78, 79] or for the preparation of furfural by means of dehydration steps [77].

Lignin

Lignin, as opposed to cellulose and hemicellulose, is a more complex and insoluble in water aromatic polymer. It is derived mainly from coniferyl, sinapyl and p-coumaryl alcohols as building blocks. Unlike cellulose, lignin is characterised by different linkage, and each one of those bonds need different conditions to undergo an efficient depolymerisation [80]. On the other hand, the higher carbon-content coupled with a lower oxygen content of lining compared to the plant-derived carbohydrates, makes this fraction of lignocellulose potentially a more appealing feedstock for the production of bioresources (i.e. fuels, polymers and fine chemicals). Furthermore, due to the highly-functionalisation degree accompanied by its aromatic nature, lignin could directly lead to the preparation of fine and high added-value chemicals, avoiding the full defunctionalisation to BTX (benzene, toluene and xylene) with subsequent refunctionalisation to the desired product.

Despite all the potential shown, lignin is nowadays still underutilised and often exploited as a simple low-grade fuel [80]. The USA National Renewable Energy Laboratory (NREL), for instance, suggested to exploited lignin in the biorefinery processes as heat and power sources [81]. In the future, lignin will potentially cover a key role into new routes to synthesise polymers, chemicals and fuels.

Possible routes for lignocellulosic feedstock conversion to liquid fuels

The aim of the lignocellulosic feedstock specific valorisation into hydrocarbon fuels, consists in an elimination of the high oxygen content coupled with the formation of C-C bonds. This upgrading can usually be dived in:

(i) feedstock conversion in gaseous or liquid-phase to platform molecules, involving partial removal of oxygen;
(ii) final catalytic upgrading of the so obtained platform molecules into the final product (hydrocarbon fuel). This step involves the controlled C–C coupling reactions and the elimination of the oxygen functionality remained.

This latter step in necessary to control the molecular weight of the products and the overall process should occur with the minimum consumption of hydrogen (especially if derived from petroleum steam reforming).

The upgrading could be pursued with multiple approaches; the most used solutions are briefly reported as follows. During the following sections, in fact, the gasification step will be discussed (forming CO and H_2) followed by the Fisher-Tropsch (FT) process (catalytic conversion of gaseous product in linear hydrocarbons) leading to biodiesel. Secondly, the main principles of pyrolysis will be introduced (anaerobic thermal treatment to obtain bio-oils, ≈ 80 % oxygen removal) and liquefaction steps (catalytic C-C coupling and final oxygenate groups removal, in presence of H_2) [81].

The aqueous phase reforming (APR) at first was presented for the biohydrogen production; nowadays it represent also a valid alternative to produce light alkanes [82], syngas [83] and monofunctional compounds [84]. This process takes place with a production of a solution (water media) of sugars and polyols. Successively, a mixture of appealing mono-functionalised organic compounds (i.e. alcohols, ketones, carboxylic acids, heterocyclics) are produced by C-O and C-C cleavage. As occurred for the other intermediate molecules, they are catalytically converted into hydrocarbon fuels by means

of C-C coupling with a further oxygen elimination. The whole process involves different catalysed processes such as dehydration, aromatization and alkylation (acid zeolite catalysed), aldol-condensation of alcohols and ketones (exploiting of metal and basic bifunctional catalysts) and ketonisation of carboxylic acids (basic oxides catalysed).
The electrochemical conversion of the biomass feedstocks, on the other side, is a process that could offer a solution to overcome some issues present in the other processes:

(i) replacement of the H_2 derived from petrochemical resources by protons generated in situ;
(ii) milder operating conditions (in term of temperature and pressure);
(iii) usage of a proper electrode potential to fine control the reaction rate and address the selectivity [85].

Other valid strategies, for example the upgrading by means of selective catalytic transformation of the lignocellulosic biomass into platform molecules (i.e. levulinic acid, hydroxymethylfurfural or furan), will be treated during the discussion in the next chapters. This approach could lead both to the valorisation into biofuels and to the production of high added value chemicals.

General approaches for conversion of biomass feedstock

The most adopted strategies to perform cellulose valorisation are mainly two: thermochemical and hydrolysis processes (Scheme 1-6). The thermochemical pathway includes a high temperature and high pressure treatments of the whole biomass feedstock. These processes can be gathered in three main routes: pyrolysis, gasification and liquefaction. The thermal depolymerisation leads to intermediates such as bio-oils (from pyrolysis) and synthesis gas (from gasification, syngas: CO:H_2 gas mixtures). Thermal processing is typically followed by a further chemical/catalytic process (Fischer–Tropsch (FT) synthesis, hydrodeoxygenation) to produce a broad fuel range of hydrocarbons. The hydrolysis process, on the contrary, consists in an initial separation of the sugars from the lignin, then the process goes on through either biological or chemical routes. Generally, biomass hydrolysis process involves higher costs than the thermochemical one. On the other hand, the hydrolysis route, could lead to appealing platform chemicals that can not be produced via the thermal treatment [81].

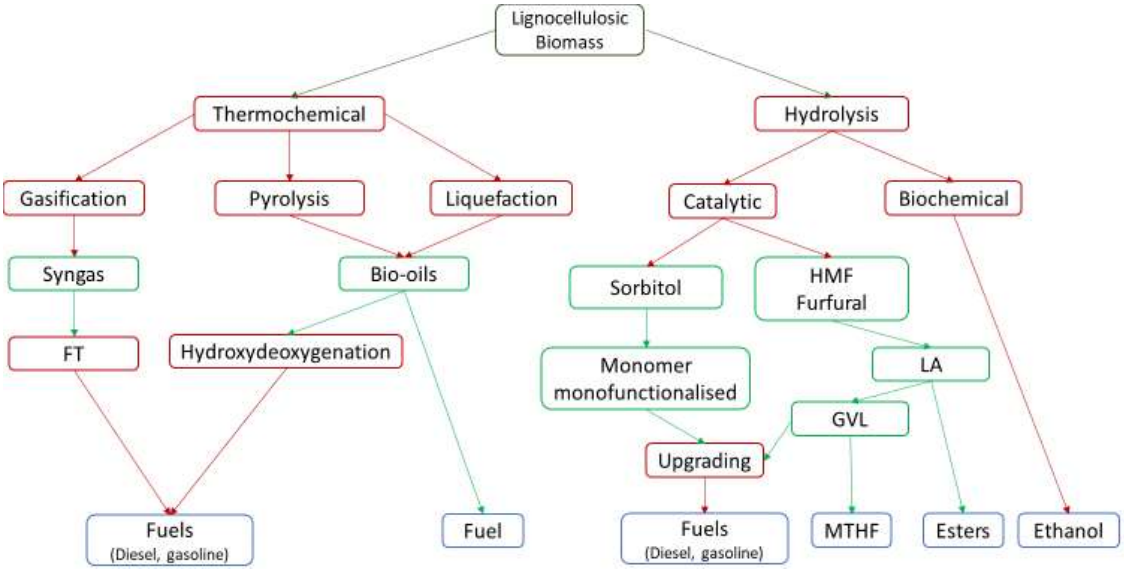

Scheme 1-6. Strategies for conversion of lignocellulosic biomass to liquid biofuels by thermochemical and hydrolysis routes (Fischer–Tropsch = FT).

Gasification

Gasification, is carried out via partial combustion of the feedstock producing syngas and also a fraction of CO_2, CH_4 and N_2 gases [22]. As already discussed, Syngas can be upgraded to liquid fuels (biodiesel and gasoline) by FT synthesis [86]. Generally, gasification is performed at temperature > 1000 K. Recently it has demonstrated how H_2 and CO could also derive from the aqueous phase reforming of the glycerol performed at lower temperature in comparison with the previous gasification (< 600 K) [83]. In these

processes, the ratio of the Syngas components can be modified by the water gas shift reaction ($CO + H_2O \rightarrow CO_2 + H_2$). The main advantage that gasification brings, unlike the other processes, is that it is not affected by the feedstock composition. However, both the amount of water [22] and eventual impurities [87] present in the feedstocks could present some problematics in the FT process, where a clean gas feed is required. At the present days, some important scaled-up implants are already present in South Africa (SASOL).

Pyrolysis

This process includes an anaerobic thermal treatment of the biomass feedstock at temperature between 650 and 800 K. With this harsh condition, the feedstock is gasified and subsequent liquefied in a mixture so called bio-oils. The bio-oils mixture is produced with a mean yield of 70 % [88] (of the initial mass) and contains usually upon 350 compounds such us alcohols, aldehydes, ketones, acids, esters, sugars and aromatic compounds. The gasification, on the basis of the exploited temperature, could lead to different products for different applications. Short residence times (seconds) lead to liquid bio-oils. For longer residence times a solid coke is produced, that is used to generate energy by combustion. Lastly, a fast catalysed pyrolysis (H-ZSM-5) have recently shown the possibility to obtain, directly from the biomass, appealing aromatic compounds with a yield of 20–30 % [89]. In conclusion, this illustrated process represent a valid and unexpansive alternative for the transformation of the lignocellulosic feedstocks without expensive pre-treatments [90, 91]. Anyway these routes are not particularly recommendable when the target product are biofuels; furthermore the direct bio-oil utilisation finds some major obstacles such as the high acids (corrosive for the equipment) and high oxygen (low energy density) content [92].

Liquefaction

This process consists in a thermal catalysed decomposition of the biomass to unstable shorter compounds that tend to re-polymerise to give again a bio-oil. For this process, the feedstock is mixed with water in presence of a basic catalyst (i.e. Na_2CO_3). The process involves harsh conditions: 525–725 K, 5–20 atm for longer residence times in respect to the pyrolysis route. The conditions adopted lead to a more expensive cost to deal with but, on the other hand, the bio-oil so obtained contains less oxygen in comparison with the one pyrolytically obtained (< 12–14 % oxygen content) [93]. A further advantage

consist in the possibility to use the obtained mixture, after just small modification, directly in engines, turbines and boilers [94]. This biofuel, however, present a major issue: an remarkable instability that makes difficult its storage [95]. Different strategies have proposed in the attempt to solve this stability problem: for instance a hydrodeoxygenation or steam reforming processes [93]. Furthermore the H_2 needed for these latter reported upgrading, could be provided by aqueous reforming of biomass [96, 97]. Alternatively the bio-oil can be used for a petroleum refineries coprocessing: hydrotreating and steam reforming are both needed in petroleum and bio-oil liquefaction derived processing [29].

Hydrolysis

This process is used when the target is a selective valorisation of biomass into target molecules, for instance for the production of platform molecules. In order to perform such transformation, the sugars need to be divided from the other components of the biomass. This isolation represents a complex and expensive process, but once the monomers are obtained, their upgrade can be performed in relatively mild conditions by means of a large typology of catalytic technologies. Wasted lignin could be employed as a feedstock to obtain phenolic resins [98] bio-oils, aromatic compounds (by means of pyrolysis or catalytic fast pyrolysis) [90] or burn to produce power [99].

Some consideration on the thermochemical and hydrolysis approaches

Both the thermochemical and the hydrolysis pathways represent valid alternatives for the sustainable production of biofuels and high added-value products. The employing of one route in favour of the other one could be dependent on the target products to be prepared and on the features of the feedstock [81]. The parallel development of both technologies, to be integrated into future biorefinery, will make this latter more adaptable than a petroleum refinery that is strictly dependent on a single feedstock.
In conclusion it has been estimated how biological, hydrolysis and thermal approaches will be all integrate in the future biorefineries to process the whole biomass feedstock with the higher yield reachable [39].

Biorefinery

With the introduction of the concept of biorefinery, lignocellulosic feedstock got the name of ‘renewable gold’ [100]. Biorefining is defined as the bio-sustainable processes to valorise the biomass feedstock into a wide range of products (food, feed, chemicals, materials) and energy (biofuels, power and/or heat) [69, 101]. The original concept of

biorefinery took inspiration from the conventional refinery, where instead of take place the production of fuels, energy and value-added products from petroleum feedstock (petrochemical derived), the same appealing derivatives can be produced from the biomass. This is exactly why lignocellulose-based biorefinery is gaining a worldwide close attention, in the attempt to replace the old and high environmental impact processes to produce key product for our society [100]. Another advantage of using the biorefinery, is represented by the possibility to enhance the value of some markets such as agriculture, forestry, chemical and energy markets by making the most from the biomass valorisation (with a remarkable yield in the production of the target products) [69]. Furthermore, the biorefinery could represent a key ally for building a future eco-sustainable closed loop (circular economy) approach where wastes can be valorised by a cascade of processes [102]. Despite the huge potential showed by these type of green-refineries, the challenge still remaining to develop efficient technologies to take advantage of the potential of lignocellulosic biomass and allow a proper development of these facilities [100]. Indeed, the new concepts of biorefineries such as Whole-Crop, Lignocellulosic Feedstock, and Thermo-Chemical-Biorefineries, are still in Research and Development stage. Nowadays, the main aim of developing these facilities is to offer a high process flexibility to reduce the risk of investment and make the realisation of these biorefinery affordable [103]. The main obstacle to overcame in order to develop this type of technology, indeed, is represented by the initial investment required and some political uncertainties [30]: for instance the investment for a commercial scale plant (≈ 500 million euros) is approximatively 2–3 times higher than the investment that have to be afforded for a corn-ethanol plant [104]. The high production cost (estimated above 0.8 euro/L of gasoline equivalent [66]) and the absence of supporting mandates are limiting the competitive market development of the second generation bio-derivates at the current stage. However, few large scale biofuel plants are currently in operation in both the USA and Europe and others have been projected and commissioned for a commercial scale-up in these last years [33].

1.3.4. *Third and fourth generation of biomass feedstock*

The third generation of biomass feedstock is represented by algae to produce mainly biofuel also called algae fuel or oilgae. The definition of fourth generation of biomass feedstock, on the other side, is referred to engineered and genetically modified crops with the key feature of consuming approximatively the same CO_2 from the atmosphere during their growth than the amount that will be produced during their combustion as a fuel [105]. With this purpose genetically modified (GM) algae are exploited with the potentially to enhance biofuel production and productivity [106]. Given that algae are photosynthetic microorganisms, they can convert light and CO_2 into a broad variety of products such as proteins, lipids, vitamins, and pigments. These chemical have already find numerous applications in chemical and pharmaceutical industries (cosmetics, food and feed supplements) [107, 108].

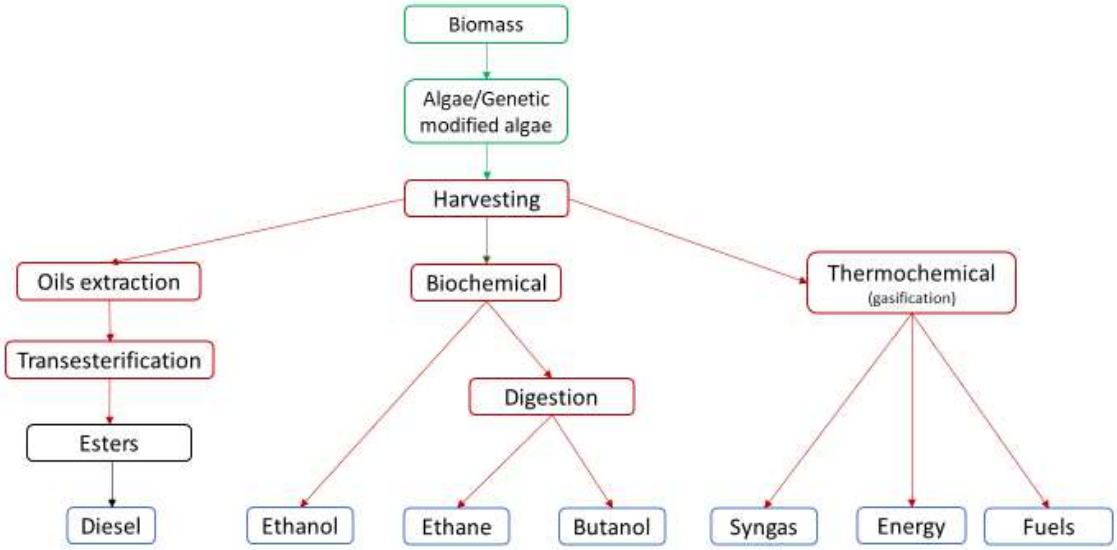

Scheme 1-7. Strategies for conversion of third and fourth generation of biomass feedstock.

Furthermore, some specific microalgae, for instance Botryococcus and Chlorella, can naturally accumulate appealing lipids (i.e. triacylglycerol) with a high content (≈ 50–80 %). These latter are suitable feedstock for the biodiesel production [107].

Other Macroalgae and cyanobacteria (i.e. Chlamydomonas, Cyanothece and Spirulina) accumulate mostly another valuable chemical: carbohydrates. These typologies of algae are suitable to be exploited as feedstock for the bioethanol production (by fermentation). Algae are organism capable of grow, with and high rate, in a large typology of water (saline, coastal sea, municipal waste water) even on land unsuitable for the agriculture and farm usage [109, 110]. In addition, these typologies of aquatic organism can double

their mass in 5 days. This could represent a tremendous advantage if compared with other biomass rate growing (1-2 years) [107].

Speaking about productivity, Pleurochrysis carterae algae, could lead to a dry biomass with a remarkable yield of ≈ 60 tons/ha/year from which 20 tons of oils can be extracted [111]. The yield just reported is 5 times higher than the corresponding yield shown by oil palm (the highest yielding among the oil crop plants) [112].

Another fundamental advantage brought by the algae is the lack of lignin and low hemicellulose content. This last reported features facilitate the hydrolysis processes enhancing its efficiency, improve the fermentation yields and reduced the general process' costs [113]. Algal biomass feedstock valorisation could also be valorised into other valuable products: i.e. hydrogen bioderived production represents an appealing application [107].

Anyway, many challenges have to be faced and overcame in order to obtain a productive algal-biofuel process: i.e. improving the algal cultivation technique and the photo-bio-reactor design will represent a fundamental step [110]. For example nowadays, with the intention of maximise the production of lipids, algae growth and its photosynthesis are often compromised, with a consequent decreasing in the whole productivity [112, 114].

Speaking of the latter issue reported, a focused investigation on genetic modifications, as already is occurring for the fourth generation of biomass feedstock growth, could represent a fruitful strategy to improve the efficiency of the entire process. Lastly, by improving the downstream, conversion and extraction processes could also enhance the general commercial viability of algal biofuels [39].

1.4. Catalysis

1.4.1. *Catalysis – a brief historical overview*

The history of catalysis started with Barzelius, Davy, Faraday, Nerst, Kirchoff and Ostwald, pioneers and founders of the modern physical-chemistry. In 1835, Jöns Jacob Berzelius introduced the concept of catalysts defining other researchers works (Sir Humphry Davy and Johann Döbereiner) [115, 116]. As a reviewer, Berzelius described what he has observed as '*catalytic powers'* of materials, that he describes as '*awaken affinities, which are asleep at a particular temperature, by their mere presence and not by their own affinity*' [116].

To complete the overall idea of catalysts, other scientists explained key concepts and experimental advances in the nineteenth century. In 1814, Kirchhoff reported an example of homogeneous catalysis: hydrolysis of starch by acids. Ostwald, soon after, described as '*substances which change the velocity of a reaction without modification of the energy factors of the reaction*' what now we know as catalysts [117].

It took several years to develop a more advanced concept on the catalysis, with Taylor in 1925, the concept of '*active sites*' and '*active centres'* was born; terms which, together with '*catalyst poisoning'* or '*deactivation'* to which they are related, are still widely used [118].

Finally, John Meurig Thomas, only in 1967, to describe catalysts in a more specific and accurate way by means of fundamental criteria: a catalyst can increase the rate of only those processes that are thermodynamically favourable but it cannot initiate reactions that are not thermodynamically feasible [115].

Lastly, catalysts are widely present in nature, in industry and in the laboratory. It has estimated that they contribute to the one-sixth of the value of all the manufactured produced by the industrialised countries [119].

1.4.2. *The Theory behind catalysis*

Following the first criteria of J. M. Thomas, the overall process has to be thermodynamically favourable in order for a reaction to occur: the Gibbs free energy must be negative ($\Delta G < 0$).

The positivity of this thermodynamic parameter is strictly related to other two chemistry-based concepts: enthalpy and entropy.

These two parameters, will be just introduced within the follow equation that correlates them:

$$\Delta G = \Delta H - T\Delta S$$

This equation takes into account the total energy of the system before the process (reactants energy) and subtracts from it the total energy of the system after the reaction (products energy). If the product of the equation gives a negative change, it indicates that the system process is spontaneous under constant temperature and pressure [120]. The thermodynamics dictate if a reaction will occur, but catalytically speaking it is more important to consider the kinetics of a reaction. In fact, catalysts do not affect the thermodynamics, but it affects the reaction kinetics as abovementioned.

The kinetic partially dictates the reaction rate and it is strictly related to the energy barrier. This latter represents, in term of energy, the obstacle that must be overcome in order to reach the transition state ($\Delta^{\ddagger}G$) before forming the products, it is also called activation energy (E_a). To overcome the energy barrier, the activation energy is at least request: the minimum energy needed by a system to trigger a chemical reaction. Efficient catalysts decrease the activation energy of the process, offering alternative reaction pathways with lower energy transition state (or states), as shown in Figure 1-3.

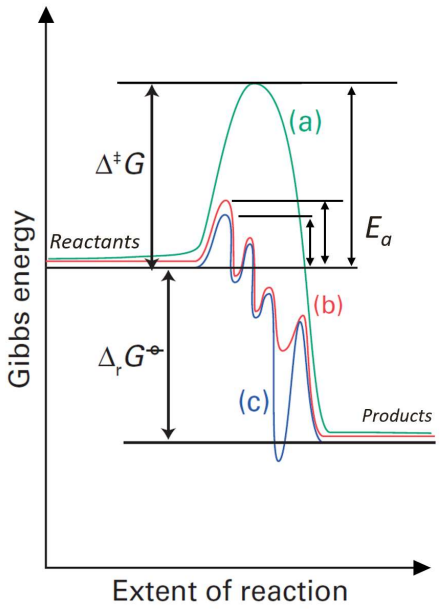

Figure 1-3. Energetics representation of a catalytic reaction. Marked with (a) is depicted the non-catalysed reaction, with (b) the multistep-catalysed reaction. The Gibbs energy of the overall reaction is reported as $\Delta_r G^{\ominus}$ and the activation energies as E_a. The curve (c) shows the profile for a reaction mechanism with a more stable intermediate than the product [121].

1.4.3. *Heterogeneous and homogeneous catalysis*

Catalysis field is divided into two big branches, dividing them for the catalysts physical state compared to the reactant one: homogeneous and heterogeneous catalysts.

Homogeneous catalyst is a type of catalysis in which the catalyst operates in the same phase as the reactants usually dissolved in a solvent. Furthermore, mechanistic studies of homogeneous catalysts are generally easier than those of heterogeneous catalysts [122]. Homogeneous catalysts are usually coordination complexes composed by a metal centre bonded to organic ligands through a coordinate covalent bond. The nature and the oxidation state of the metal and the electronic properties of the ligands dominate the chemistry of such complexes. Homogeneous catalysts are generally liquid that act in the same media phase system. These type of catalysts are not often economically viable at large scale mainly because of recycling/separation problems and as a result, they represent only 20 % of the total catalytic industrial processes [123]. Hydroformylation of olefins [124], acetic acid synthesis [125] and coupling reactions [126] are examples of industrial reactions that make use of homogeneous catalysts.

Heterogeneous catalysts, on the other side, are in a different phase from the reactants and products. Heterogeneous catalysts are more frequently solid materials, as bulk metals or supported nanoparticles, that take part in reactions in liquid, solid or gas phase [127]. Furthermore, heterogeneous catalysts can be more easily recycled as opposed to homogeneous one and often show a higher thermal stability, although their characterisation and optimisation can result more difficult. Due to the beneficial features reported, more than 90 % of chemicals factoring in all over the world rely at some production point on a heterogeneous catalyst: from food to drugs, plastics, fuels and fertilising and many other commodity chemicals [128].

Science and its technological instruments fulfil a key role in the world catalysts development. What is changing nowadays, is the evolution methods and the novel approach toward this world. Until recent years, the majority of catalysts and processes involving a catalytic process were discovered and developed in an empirical way. Within the last decades, the humankind has the possibility to properly design certain catalysts and chemical processes. Academically speaking, the interest is also grown up, trying to understand in which way and witch features could influence the catalytic behaviour [129].

1.4.4. *Metal nanoparticles as active catalysts*

Nowadays the term nanoparticles is mostly used to define spherical particles with a diameter in the range of 1-100 nm. With the terms cluster or nanocluster, on the other side, are usually defined particles with a diameter < 4 nm [130]. Colloidal nanoparticles, to clarify the two terms, are nanometre-sized particles that are stable in a solution. The capability to be dispersed are usually conferred by surfactant present at their surface [131]. In the previous century, on the contrary, the term nanoparticles and colloids were not clearly distinguished. Faraday, for instance, in the 1857 defined a colloidal metal solution a solution with finely dispersed metal inside [130]. Anyway, since the medieval period, the nanoparticles were already well-known for their proprieties, and in particular noble metal nanoparticles. Gold nanoparticles, for instance, used to be dispersed in a glassy matrix to obtain the so called '*ruby glasses'*. Faraday proposed that gold, in that particular form, was the responsible of the intense red colour of the material. Some years later, this hypothesis was confirmed by the Mie's studies, that by resolving the Maxwell's equation for the absorption and scattering of electromagnetic radiation of spherical metal particles, elaborated a theory on the light adsorption by metal nanoparticles [132]. When the dimension of a noble metal particle goes below the electron-free path (distance travelled by the electron between an impact with the lattice centres and the successive one), the nanoparticle shows an absorbance in the UV-Vis light. This absorbance is to be ascribed to a coherent oscillation of the free electrons on the surface of the nanoparticle. This phenomenon takes the name of surface plasmon absorption, and it represents one of the physical principle behind the UV-Vis characterisation technique on nanomaterials [133].

In a material of the dimension in the order of the nanometres, thus, both physical and chemical properties can be significantly altered in comparison with the corresponding bulk material [134].

The surface area is the most important feature that is deeply altered when a material is in the nanometric range. The catalyst's surface area, indeed, is a critical parameter since it determines the availability and population of catalytic sites: one of the main rate determining step of the catalytic reactions, is often represented by the adsorption of reactants and subsequent desorption of the products due to the low availability of active sites as above mentioned. The nanoparticles, due to their high surface area, favour the interaction between the reactants and the surface. This feature was previously associated

to homogeneous catalysts; the nanoparticles, however, are considered the bridge between homogeneous and heterogeneous catalysis, by combining the advantages of both the approaches [135–137]. What is further associated to this high superficial area, is the lack of coordination of the superficial atoms of the nanoparticle: the smaller the nanoparticle, the higher is the superficial area and thus the coordinative instaurations enhance. For instance, a cluster of 13 atoms offers 12 atoms to its surface with just one in the inner part; if the cluster counts 55 atoms, the internal atoms will be 13 compared with the 42 that constitute the surface of the nanoparticle. In general, the n^{th} shell includes $10n^2 + 2$ atoms [134]. The superficial atoms, however, can interact only with atoms inside the particle, leaving valences outside. This is another key aspect to take in consideration: the highly presence of instaurations leaves the atom instable and more prone to interact with the environment in the attempt to saturate its valences conferring catalytic activity to the nanomaterial. Furthermore, by offering the maximum possible number of atoms to the surface, the metal loading can be reduced, thus leading to a higher catalytic efficiency [138, 139]. The high-vacuum surface science and electrochemistry fields have investigated and reported different catalytic efficiencies for different metallic surfaces [140]. For instance, for atoms that belong to different types of nanoparticles facets, different electronic structures can be assigned. It is well-know how by exposing selectively a distinct atomic arrangements at the surface, it will lead to a different chemisorption features with a consequent difference in activity and/or selectivity [141].

Another phenomenon that occur when a metal particle is in the nanometric scale, is the alteration of the distribution of the electron in the electronic band and the subsequent drastic change in the electronic properties. When the particle size decreases and the band gap (energy gap between the valence and conduction band) became higher, the metal could pass from an electrical conductor to a semiconductor or, how it was demonstrated in the case of the 3 atoms cluster, even reach the insulating status. This quantum size effects can drastically change the overall catalytic features of the nanoparticles [142].

As the catalytic performance and physicochemical properties can be tuned by the size and shape of the particle, the precise control of these parameters became a key synthesis point and gained importance in the last decades [143–145]. For all the reasons listed above, an extraordinary interest in the investigation (and application) on noble metal nanoparticles in catalysis is still ongoing nowadays. At present day, an already wide exploiting of noble metal nanoparticles-based materials is in place for important reactions investigation.

1.4.5. *Catalysis by gold*

Gold represents a unique metal and it has been used, since early civilisation, for jewellery, coins, precious decoration and other form of art. Even at present days, 50 % of the overall world demand for gold is for the jewellery sector; the other 50 % is split between investments and industrial applications [146]. Some important features of gold, such as resistance to corrosion, good thermal and electrical conductivity, malleability, ductility and biocompatibility have contribute to the expansion of the gold uses [146, 147]. A peculiar and appealing use of gold is surely catalysis. Even if gold in bulk form does not present any catalytic activity [148], when it is finely dispersed (i.e. nanoparticles) gold presents unique catalytic properties. However, the first investigations about the use of gold as catalyst had not reported any encouraging results: gold showed to be not superior to the other catalysts [149]. The remarkable step forward was made by Bond at al. when, in 1973, they discovered the remarkable activity of gold supported catalysts for the hydrogenations of olefins [150]. A decade later, also Haruta and Hutchings prognosticated and subsequently demonstrated gold to be an active catalyst. Haruta, for instance, was the first able to obtain by means of a Deposition Precipitation (DP) synthesis a novel ultra-fine gold particles (dispersed on oxide) that showed their superiority in performance for the low-temperature oxidation of CO [151] and for the hydrochlorination of ethyne to vinyl chloride [148], both heterogeneous catalysed reactions. From those discoveries, the research into gold as catalyst increased constantly, as demonstrated by the numerous reviews on the topic [152–154].

Other landmarks for this metal use was again by Haruta, who showed that gold supported on titanium dioxide could be exploited in the oxidation of propene to propene oxide: one of the top targets in industrial chemistry [155]. Prati on the other side, was the first capable to successfully prepare and support, by sol-immobilisation synthesis, small nanoparticles highly dispersed on carbon [156]; Prati with co-workers, indeed, demonstrated the importance of gold (supported on carbon) for the high activity and selectivity shown in both ethylene glycol and 1,2-propandiol oxidations [156, 157]. In 2002 Hutchings and co-workers showed gold to be effective for the direct and selective synthesis of hydrogen peroxide [158]. At present days, other uses of gold are investigated for instance in hydrogenation of alkenes [159] and α,β-unsaturated aldehydes [160], oxidation of benzyl alcohol and glycerol [161], water gas shift reaction [162], acetylene hydrochlorination [163] and the already above mentioned CO oxidation [164].

Ultimately, gold finds also an extensive use when it is coupled with a second noble or non-noble metal with the intent to combine the proprieties of both the metals resulted with an enhanced activity, selectivity and stability [165, 166]. Some examples are palladium [167], platinum [168], ruthenium[147] silver [148] and copper [169].

1.4.6. *Gold in bimetallic systems*

The lifetime of a catalysts, especially for large scale application, is a vital parameter. The time-limited durability, indeed, represents the main reason of a restricted industrial application of metal-supported catalysts, especially for liquid oxidation with pure oxygen or air as oxidant agents [170]. Gold has shown promising features, especially in resistance and in some cases even in selectivity, compared to other very active noble metals (i.e. Pd and Pt) [170]. On the other side, gold suffers from a sever drawback that actually is limiting its industrial exploitation: the apparent needs of a base (glycerol oxidation) [171, 172]. Bimetallic systems, however, showed the potential to overcome the mentioned limitations. Usually, the two metals can be fruitfully combined together to produce a new material with unique properties derived from the combination of the features of the two components [173]. In most of the cases, indeed, a marked enhancement of physic and chemical features can be observed; the reaction's kinetic, selectivity towards the desired product and stability of the catalysts have shown to improve in comparison with the use of corresponding monometallic species. Furthermore, where gold was used as modifier, it improved the performances of the other metals (that usually shows better catalytic activity) and, even more important, conferred resistance to the systems (i.e. combined with Pd, Pt and Ru) [161, 174]. The importance of dealing with a bimetallic systems become evident for different chemical reactions such as CO oxidation [175, 176], oxidation of alcohols to aldehydes [161, 174, 177, 178], direct synthesis of hydrogen peroxide [179], oxidation of primary C–H bonds [180] and for the valorisation of biomass [165, 181].

The effects responsible of the synergetic phenomena are mainly two: ligand and ensemble effect [182]. The former, also known as electronic effect, takes in consideration the electronic interaction between the two metals: for instance, the charge redistribution and changes of the *d*-band electron structure. The latter, called also geometric effect, reports the change in catalytic activity and features based on the surface effective composition [183]. The two effects participate simultaneously to the final result and for this reason it results very difficult to discriminate the two different contributes. Thus, the nature of the

synergistic effect most of the time easily observable from an experimental point of view, is not always completely understood from the surface science, though much effort has been put on this aim [173, 184]. One of the main reasons responsible of this absence of understanding lies in the wide possible combination of reactants, composition of bimetallic systems and, more in general, of experimental conditions. Many experimental data have been reported without a proper characterisation of the systems leading to doubts about the real composition and morphology (i.e. alloy, core–shell, decoration) of the bimetallic systems. This lack in information was subsequentially translated into a marked limitation in the vital correlation between bimetallic features and their corresponding catalytic properties.

In order to mention the possible arrangements of the two metals within a bimetallic particle, a list of the main possible structures is here below reported:

- Core-shell structure: one metal encapsulates the second one.
- Segregated structure: the two metals are isolated, but still sharing a common surface.
- Mixed structure: in this structure the metals are either ordered or in solid solution. The latter is better known as random alloys.
- Multi-shelled structure: similar structure to the core-shell, but with the presence of more than one shell.

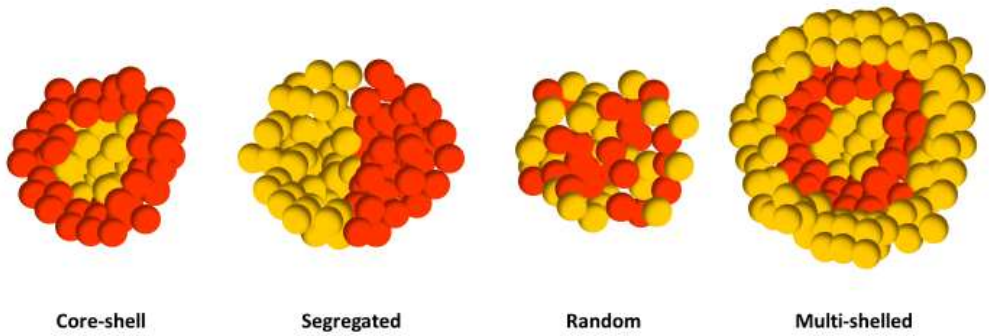

Figure 1-4. Schematic representation of some possible bimetallic structures.

1.4.7. *Ru and Pt - "Active role in biomass valorisation"*

Ruthenium is a noble metal, and it finds application in many fields beside catalysis. Ruthenium containing-complexes, for instance, are well known for medical and biological application. Some example of its wide application can be listed as cellular imaging tools, radiopharmaceutical imaging tools, drugs for fighting several diseases such as cancer, malaria, Leishmania to name a few [185]. Other applications see ruthenium, since the previous century, as effective catalyst for organic synthesis [185],

oxidations [186], hydrogenation [187] and hydrogen transfer reactions [188]. Ruthenium, furthermore, covers a key role in the development of green strategies to arrest the world dependence from the fossil fuels. Several ruthenium-containing complexes are fundamental (i.e. dyes for solar cells) in the conversion of solar energy into chemical and electrical energy. Another interesting application is the use of ruthenium to replace more expensive materials (i.e. palladium, rhodium [189]) to produce electrode suitable to for the precious hydrogen production by means of water splitting catalyse process [190–192]. Another fundamental role covered by ruthenium nanoparticles is in the valorisation of biomass (with lignocellulose as feedstock in particular). Some examples are the conversion of cellulose into sorbitol [193, 194] and also the subsequentially conversion of sorbitol into sugar alcohols [195], 5-hydroxymethyl-2-furfural (HMF) into 2, 5-diformylfuran (DFF) [196, 197], levulinic acid (LA) into valerate esters [198], xylitol into glycols [199], γ-valerolactone (GVL) into alcohols [200], furfural into cyclopentanone [201], lignin derived molecules into toluene [202] or other more recent and demanding process such as one-pot transformation of biomass directly into gasoline [203], Fischer–Tropsch reactions (syngas transformation into liquid alkanes) [204] or even in fast pyrolysis to produce bio-oils [205]. Some of these valorisations have already been presented in the previous section and other specific ones will be reported in the lignocellulose's section (Chapter 3).

Platinum, on the other hand, is one of the most expensive noble metal. It finds multiple uses in biomedical and electrolytical applications like ruthenium and, in some occasions, given the similar behaviour of the two materials and the marked difference of prize, platinum can be replaced with ruthenium [185].

Platinum was exploited since the 19th century; this precious metal was used to catalyse the ignition of hydrogen and the hydrogenation of oils [127]. To the present day, platinum is employed in many catalytic routes such as vehicles' converters to complete the oxidation of the unburned fuels (into CO_2 and oxygen). Platinum also finds application in the fossil fuel industry, in processes of separation and in particular, in the catalytic reforming of naphtha into higher-octane gasoline [206]. Platinum is also well-known for being an efficient catalyst in the hydrogen peroxide decomposition into water and oxygen [206] and for its use in fuel cells [207–209].

Other well-known applications of platinum are in catalysis for the valorisation of the biomass. For instance, platinum can be fruitfully exploited in hydrogenation processes

and in hydrogen evolution (both from electrolytical and aqueous phase reforming routes) [210–212], in the direct conversion of biomass into sugar alcohols [213, 214] or alkanes (hydrocracking) [215], in the production of syngas from glycerol [214] or from other biomass feedstocks or even catalyse the combustion of biomass to produce energy [216, 217]. In addition, platinum-based materials can also exploited be in more fine valorisations such as the selective conversion of HMF to FDCA (for a subsequentially plastic production) [218] or of LA into GVL [219] and for the upgrading of bio-oils [220–222]. More details regarding the reactions treated in this thesis' work will be given in section 3.2.

1.5. Crucial role of the support

According to IUPAC, '*the active catalytic material is often present as the minor component dispersed upon a support sometimes called a carrier'*. The finely dispersed and supported metals typically suffer, due to its high surface energy, from agglomeration in the attempt to reduce the area and reach a more stable status. For this reason, the support covers a key role in the heterogeneous catalysis: it often does not act like a mere carrier. The support, in fact, may be catalytically active as well, for example by providing acidic/base sites or by forming strong metal-support interactions [223]. The former catalytic systems, by presenting two type of catalytic sites (bifunctional catalysts), are also capable to catalyse two different types of reactions or two steps of the same reaction. A unique advantage which distinguishes these types of catalysts is the potential to convert also the highly reactive intermediates that usually lead to carbonaceous deposits and cause a loss of activity [224, 225]. Furthermore, by use of acidic or basic functionalities (replacing thus liquid acids by solid acids), less waste and by-product will be formed: i.e. in the reforming of naphtha, in selective hydrogenations, in petrochemical processes as well as Fisher-Tropsch and ammonia processes. The other contribute that a support could provide is represented by the so called strong metal–support interaction (SMSI). Tis definition was introduced in 1978 by Tauster describing the changes observed in the chemisorption features of 8 noble metals on a reducible oxides (i.e. Pt/TiO_2) before and after a thermal treatment (i.e. high temperature in presence of hydrogen) [226, 227]. Afterwards, the definition of SMSI was extended to including the interaction between the active metal and the support with comparable features with the phenomena observed by Tauster [228]. More details on these phenomena and the properties through which

supports usually exert their own function, will be dealt with separately hereinafter, in proper paragraphs. Finally, according to Bond classification, noble metals could establish other typologies of metal-support interaction: *weak metal-support interactions* (WMSI) could be shown with irreducible oxides (i.e. SiO_2, Al_2O_3, MgO, etc.) and carbonaceous materials (activated carbon, graphite) as supports or *medium metal-support interactions* (MMSI) could evolve in presence of zeolite as supports.

Any bulk material could be potentially exploited to play the support role. In a practical way, however, the support should satisfy some important requirements in terms of physical (i.e. mechanical resistance, thermal stability) and chemical (i.e. stability) properties. A support characterised by a high surface area is also preferred. The wide variety of the materials usable as supports are classified and listed in Table 1-5.

Table 1-5. General support classification.

INORGANIC BINARY OXIDES	
2nd group metal oxides	CaO, MgO, BaO
Transition metal oxides	TiO2, NiO, ZrO_2
Silicas	Amorphous silica, SiO_2, Mesoporous Silica
Aluminas	Al_2O_3 of different phases (e.g. γ, δ, θ, etc.)
COMPLEX MULTICOMPONENT OXIDES	Aluminum silicates, Zeolites, Aluminum phosphates, Hydrotalcites, Clays, Vanadium phosphates, Bismuth molybdates, Antimonites, Scheelites, Perovskite, Hydroxylapatites, Heteropolyanions, etc.
CARBIDES	SiC
CARBON BASED MATERIALS	
Carbon	Charcoal, Activated Carbon (AC)
Graphitized Materials	Graphite
Carbon nanostructures	Carbon nanotubes (CNTs), Carbon nanofibers (CNFs), Graphene
POLYMER AND RESINS	Ion Exchangers, Sulfonic resins, Nafion

In the next section, the attention will be focused on two of the main important and exoloited branch of supports:

- Inorganic binary oxides: including binary metal oxides (MgO, TiO_2, NiO, ZrO_2), aluminas and silicas.
- Carbon based materials: including activated carbons and graphitic materials.

1.5.1. *Metal oxides supports* [229]

Metal oxides, generally solid, are compounds were the oxygen atom is the more electronegative component. Metal oxides, due to their multi-functionality properties such as acid-base, electron transfer and transport, hydrocarbon chemisorption by σ and π-bonding, H-abstraction, O-insertion, represent a wide class of materials that clan play an active role in catalysis both when used alone (i.e. methanol oxidation) [230] or when used as supports. More in detail, the use of these type of materials have to be correlate to three main features: the composition and the type of bonding, the coordination environment at the surface (mainly determined by the faces exposed at the surface of the oxide) and by the presences of impurities an defects. The redox and acid-base features of the oxides, on the other side, are ruled out by the electronic structures and the oxidation states of the metal bounded to oxygen. The bulk structure of the most exploited oxides, to the present day, are well-know and deeply investigated (fully characterised).

Generally, due to the bigger ionic radium, in close packing structure the O^{2-} anions are close-packed while the metal ions characterised by smaller ionic radium and are positioned in the octahedral or tetrahedral holes. The more significant crystallographic structures are the face-centred cubic (fcc), the body-centred cubic (bcc) and the hexagonal close-packed (hcp).

A key aspect that should be taken into consideration in the choice of the proper oxide support, is its affinity with water. The oxide dissolution tendency, in fact, have to be carefully evaluated since oxides can be exploited in synthesis occurring in water media and can be sequentially exposed to aqueous reaction mixture. For the reasons just mentioned, it is important to deal with insoluble support to facilitate both the preparation of the catalysts and the recovery of this latter at the end of the reaction.

The tendency to be dissolute of a material is strongly related with the surface features (acid – base properties) and also with the functionalisation groups present at the surface. Generally, the acidic oxides (i.e. SiO_2 or zeolites) together with transition metal oxides in their highest oxidation state (i.e. V_2O_5 or CrO_3) could potentially be dissolved in water with the subsequent formation of acids or anions. On the other side, basic oxides (i.e. MgO, lanthanide oxides) could form hydroxides or can be dissolved with the formation of bases or cations. Alternatively, amphoteric oxides (i.e. Al_2O_3, ZnO) could lead to cations in acidic media and anions in basic media.

1.5.2. *Carbonaceous materials* [231–233]

Carbonaceous materials, on the basis of its atomic orbital hybridisation level, are peculiar material that could combine its atoms in several allotropes (polymorph), thus, with identical chemical composition but with different physical structure. For instance, graphite, diamond and lonsdaleite (also called hexagonal diamond) are three different allotropic solid carbon forms.

Since 1980s with the discovery of fullerene, the investigation on carbonaceous materials covered an important role in the scientific field: many new classes of synthetic allotropic carbons have been discovered since then and culminated with the isolation of graphene (2004).

Among the all synthetized material, it could be reported the family of the so called low-dimensional carbon allotrope: from nanostructured carbon (<100 nm with dimensions ranging from the zero-dimensional - 0-D, fullerenes) to one-dimensional (1-D, carbon nanotubes) and two-dimensional (2-D, graphene).

Table 1-6. Main advantages and disadvantages of the use of carbonaceous material as support in catalysis.

Advantages	Disadvantages
Large surface area and tuneable surface chemistry	Easy gasification inhibits their use in high temperature hydrogenation and oxidation processes
Easy reduction and recovery of supported metals	Poor reproducibility in synthesis: different batches of the same material can contain varying ash amounts
High resistance to acids and bases	
High thermal stability (even above 750 °C under inert atmosphere)	
Plasticity, allowing to prepare porous carbon in different physical forms (granules, cloth, fibers, pellets)	
Lower cost compared to metal oxides	

Carbons materials, due to their unique both physical and chemical features reported in Table 1-6, represent an outstanding material suitable to be exploited as support for heterogeneous catalytic purpose, even in many industrial relevant processes.

On this latter purpose, activated carbon (AC) and carbon black (CB, partially graphitised) are the most employed materials: characterised by a remarkable surface area and pore volume that facilitate the anchoring of the nanoparticles. This latter aspect helps to have

a homogenously dispersed nanoparticles-based material and reduces the sintering allow even important metal loading. Within the class of activate carbons (AC) it could be found a wide variety of amorphous materials with a high content of carbon (85-95 %) and high internal surface area (inter-particulate- normally between 800-1500 m^2/g) and a high pore volume (0.2-1 cm^3/g). They also have the capability of trap gases and liquids due to their adsorbing features. Carbon black (CB), on the other hand, consists in an aggregate of small spherical crystallites connected via polycyclic aromatic hydrocarbon in a random branching structure and represent the carbon most exploited, after only the activated carbon.

The two typologies of carbons presented above, are often not well defined. Despite this, the two materials present evident differences: AC is characterised by a more intricate porosity and an higher mean particle size (at least three order of magnitude larger) in comparison with the carbon black (0.01-1 mm vs. 0.01-1 μm). Furthermore, the surface chemistry and the pore size distribution of these two carbons can be opportunely tuned to meet the needs of the target reaction or to improve the dispersion of the active phase (i.e. nanoparticles) for example by increasing the hydrophilicity of the carbon's surface (i.e. with an oxidative treatment). In addition to the most exploited type of carbons presented so far, also the low-dimensional graphitised allotropes (carbon nanofibers (CNFs), carbon nanotubes (CNTs) and graphene) have shown to be suitable employed as supports. This class of materials is characterised by remarkable features such as high surface area, high resistance to abrasion, thermal stability and peculiar adsorption properties.

Theoretically speaking, the graphene (two-dimensional carbon allotrope), could represent the ideal support with its highest surface area (≈ 3000 m^2/g) coupled with other unique physical, electronic, chemical and mechanical features. Unfortunately, from a practical point of view, some unsolved issue (i.e. difficult to be synthetised and tendency to agglomerate) are hindering its use. On the contrary, CNTs and CNFs have exhibited, beside a remarkable surface area, a high stability and allow a controlled and relatively easy functionalisation. Anyway, despite they present many similarities (synthesis procedure and the nanometric sizes), CNTs and CNFs strongly differ from a morphological point of view: the anisotropic growth direction, in the case of nanofibers, occur in the absence of the central cavity [234]. Furthermore, the CNFs are distinguished by a higher length in comparison with CNTs (50-200 nm).

1.5.3. *Strategies for surface tuning*

Surface tuning induces radical modifications in term of composition, acidity, geometric and electronic structures. As aforementioned, the surface of a material and subsequentially its relative modification covers a key role in determining the nature and the amount of the active sites. Beside the typical introduction of acid or base sites to tune the catalytic range of activities, the functionalisation could be also performed to tune the hydrophilic or hydrophobic behaviour of the material. In the case of supported noble metal nanoparticles, for instance, the modification of the support's surface alters the support-metal interaction affecting the stabilisation and dispersion of the nanoparticles and, consequently, the activity and selectivity of the overall system [235].

Continuing in the description, a general distinction can be made to differentiate between functionalisation and doping strategies [236]. The former consists in the addition of new functionalities, chemically knows as functional groups, and it involves the formation of localised covalent bonds, thus modifying the surface morphology. The latter refers to the physisorption or chemisorption of foreign species with the aim to modify just the electronic structure thus preserving the crystal lattice, or alternatively, as happen for the semiconductor doping, it could be successfully introduce an impurities (foreign atoms) replacing an atom belong to the target structure. However, in most of the cases the difference between the doping and functionalisation results too subtle to be well defined. For this reason, the functionalisation can be also distinguishing on the base of the interactions involved: physical or chemical. The former refers to the formation of non-covalent interactions between molecules and surface. Some example of physical functionalisation could be the wrapping of polymers around a nanostructure or the encapsulation of chemical species inside the pore of the material. As suggested by the name of this type of functionalisation, it involves weak interactions leading to a mild modification of the surface's properties.

On the other side, in the case of chemical functionalisations, the introduction of functional groups (or foreign atoms) occurs by chemical reactions (or substitution). For instance, in the case of oxides, chemical functionalization provides by condensation reaction or oxidative addition are for example grafting between the functionalities of the foreign molecule and the hydroxyl groups of the oxide [237]; similarly, nucleophilic or electrophilic addition to coordinatively unsaturated centres (randomly distributed) such as defects, can be fruitfully used to functionalise the surface of the support, even if this

strategy leads to a not homogeneous functionalisation due to the distribution of the defects. Different strategies, on the other hand, can to be adopted for the insertion of a dopant inside the structure of the target materials. For instance, to dope a metal oxide such as Nb_2O_5 or TiO_2, several approaches can be employed in order to obtain the so-called mixed or doped oxides: i.e. hydrothermal synthesis, sol-gel and co-precipitation techniques [238–244]. These latter synthesis methods, lead to new materials with a modified surface.

Lastly, also a wide number of functionalisation can be employed to tune the surface's properties of carbonaceous materials. For instance, by means of a relatively simple treatments, oxygen and nitrogen-containing groups can be successfully introduced at the surface of the activated carbon. These strategies involved a hot treatments with strong and inorganic acid (i.e. nitric, phosphoric or hypochlorous acids) or ammonia and amines [245]. Also the surface modification of CNTs is well studied: it can be carried out either by sidewall functionalisation (fluorination and derivate reactions, hydrogenation, cycloaddition, and radical attachment) or defect functionalisation (amidation, esterification, thiolation, silanization, and polymer grafting) [246].

1.6. Different synthesis approaches and techniques

One of the reasons for which heterogeneous catalysts are generally less active than the corresponding homogeneous counterpart, is to ascribe to the less exposed surfaces offered by supported nanoparticles in comparison with isolated active sites of the former [247]. Moreover, as already reported in the previous section, the activity of a heterogeneous catalyst can be correlated with many factors or, in the most of the cases, of a combination of them. Some of the aforementioned phenomena are represented by the quantum confinement [248, 249], oxygen or hydrogen spill-over [250, 251], the strong metal-support interaction [252], the metal oxidation state [253, 254] and its coordination number [255, 256].

In reference to what is reported, the preparation of a catalyst covers a delicate role since it affects all the crucial parameters reported so far and therefore the performance of the overall catalytic system. Here below, some of the most diffuse synthesis routes, that was also exploited for the catalyst preparation of the present work, will be briefly reported.

1.6.1. *Impregnation*

The impregnation method is the technique used to synthesise the very first supported gold nanoparticles by Bond et al. in 1973 [257]. Furthermore, due to its simplicity and good metal dispersions showed for many noble metals (however gold is not included), this technique is perhaps the most commonly used technique from an industrial point of view [258]. For this method, a solution containing the metal precursor is prepared to be subsequentially mixed with the support (powder). The impregnation technique can be performed with two variants: wet of dry. For the dry-impregnation (also known as incipient-wetness), the proper amount of metal precursor is dissolved in a well-defined volume of solution: this latter corresponds to the pore volume (previously calculated) of the support that has to impregnated. The solution fills the pore of the support driven by capillary force [259]. This strategy allows to avoid an excess use of water (out of the pores), allowing a good particle distribution. However, when the metal precursor solubility is low, high metal loading are difficult to obtain. For the wet-impregnation (also called diffusional-impregnation), on the contrary, the support is firstly dispersed into the solvent and then mixed with the precursor solution. In this latter case the precursor diffuses into the support driven by the concentration gradient. For both cases, a drying step to eliminate the solvent is necessary before submitting the catalysts to the activation process. The metal precursor, after the solvent removal, remains stuck to the supports' surface by means of weak interactions such as hydrogen bonds, van der Waals forces, dipole-dipole interactions and London dispersion forces. However, the control over the particle size could be affected (for both the routes) during the activation step exploited to produce the nanoparticles which typically involves thermal treatments.

1.6.2. *Sol-immobilization* [260, 261]

In the sol-immobilisation synthesis technique, the active phase (metal nanoparticles) is formed in a solution (often aqueous) and subsequently deposited onto the support [262]. This method was firstly successfully adopted, in parallel in 1999 by Grunwaldt and Prati with the corresponding co-authors, to synthetise gold colloids supported on oxides (TiO_2 and ZrO_2) and carbon, respectively [156, 263].

The formation of the metal nanoparticles usually is induced by the reduction of metal salts or organometallic complex (metal precursors). The reduction can occur both by thermal, chemical or photochemical decomposition. The metal colloid shows a remarkable resistance towards agglomeration by van der Waals forces, due to the presence of the protecting agent. The stabilisation induced could be ascribed to two different contributes: an electrostatic or steric effect depending on the nature of the protective agent.

The electrostatic stabilisation is bases on the repulsive Coulomb forces dictated by the high charge density forces present when ionic species are adsorbed on the metal nanoparticles' surface. On the other side, when a long chain polymer is employed as protective agent, it wraps the nanoparticles leading to the formation of an isolating layer that reduces the van der Waals attraction forces.

This synthesis strategy offers a great control over the nanoparticles size, size distribution and shape. Another important feature of this techniques is that normally it can be applied with almost every support. The immobilisation step, indeed, depends only on the sol stabiliser and the iso-electric point (IEP) of the support. Surface depositions can be induced by charge modifications of the support's surface to lead to an interaction with the nanoparticles. The nanoparticles show in fact a surface potential (i.e. negative for gold nanoparticles) which induces the presence of the Helmontz plane. The driving force of this phenomena is electrostatic in nature. In functionalised supports or for functionalisation present on the surface of the material (i.e. carbon contain many -OH groups on its surface) or induced in presence of water (i.e. oxides cases), the charge of the support's surface can be properly tuned by the control of the pH of the solution. If the induced charge at the support's surface is opposite in sign with the one of the nanoparticles, these latter can be successfully anchored to the surface. Other possibilities consist in the use of materials such as hydrotalcites or montmorillonites: they exhibit in fact a layered structure in which big positive cations are present and if the process is

thermodynamically favoured, they can exchange and replace their cations with other positively charged groups. For these reasons, the choice of protective agent and the choice of a correct pH are vital to promote the interaction and subsequent adsorption of the nanoparticles onto the support for this synthesis. Lastly, with most of the other synthesis methods (i.e. with deposition-precipitation or impregnation) where the precursor of the active phase is deposited before nanoparticles formation, a sequential activation step is required. This activation step, however, could lead to undesirable changes in surface morphology, particle size and metal dispersion. This latter reason represents a further advantage brings from use of the SOL-immobilisation technique.

1.6.3. *Deposition-Precipitation*

Haruta, as already above mentioned, was the first to adopt successfully this technique to obtain gold nanoparticles [155]; subsequently Louis's group, by means of a new more efficient variant of the technique (in presence of a delay base, urea), showed that small nanoparticles (≈ 3 nm) with an high gold content (> 3 wt.%) could be achieved, even on an oxide of rather low surface area (i.e. 50 m^2/g) [264].

The deposition-precipitation (DP) foresees the deposition of the active phase (generally in hydroxide or a hydrated oxide forms) directly on the surface of the support that is finely dispersed in the synthesis mixture [265]. The metal precursor is dissolved into a large volume of solvent in presence of a precipitating agent and the support. At specific synthesis conditions the nucleation of nanoparticles starts directly onto the support's surface. This growth can be induced by the pH modulation (a rise of a pH could change the valency of the dissolved active precursor) or increasing the concentration of a low soluble metal precursor. In any case, the concentration of the metal precursor should never exceed the limit of supersolubility in the solution: only at the support-solution interface, due to the strong support-precursor interactions that decrease the nucleation barrier, is allowed a growth of the particles. In the former case, on the other hand, the gradual increase of the pH can be induced by the addition of bases (i.e. NaOH,$NaCO_3$ or KOH), or can be easily performed thanks to the use of urea ($CO(NH_2)_2$, delay base) coupled with heating (also called DPU technique) [264]. Metal loading higher than the corresponding achievable with the impregnation methods can be reached due to the larger volume of the stock solution adopted. However, the need of a rapid transport of the precursor from the stock solution to the support requires a relatively high surface area support to achieve a good dispersion of the active phase.

1.6.4. *Metal Vapour Synthesis*

The most popular metal vapour synthesis from an academic point of view is the chemical vapour deposition (CVD), where a solid metal precursor is vaporised by heating in vacuum and then it is deposited directly onto a solid support from the gas phase [266]. The vaporised precursor forms a metal film by the decomposition of chemicals on the surface of the target substrate. Most frequently the process is thermally driven and the deposition of the film is controlled by a chemical reaction [267]. Based on the method used to vaporise the precursor, the CVD can be categorised as: plasma CVD, thermal laser CVD, photolytic CVD, fluidised-bed CVD and microwave plasma CVD. The chemical vapour deposition is also widely used at industrial scale due to its potential to deposit both metal and non-metal onto supports of almost any size and shape [268]. On the other hand, chemical precursors with high vapour pressure are required (usually toxic and hazardous) and additionally, the products derived from their decomposition are also often toxic and corrosive. Therefore, the special precautions that have to be taken coupled with a required neutralization step increases the costs of the entire process.

An interesting variant of this class of synthesis is represented by the solvated metal atom (SMA) route. With this technique, the bulk metal (powder or pellets) is heated in an alumina holder (by Joule effect) under high vacuum. Metal vapours are co-condensed in presence of weakly organic ligand that act as stabiliser (i.e. acetone, acetonitrile or benzene). This latter condensation is promoted on the wall of the reactor that it totally immersed in liquid nitrogen (-196 °C). Subsequentially to a gradual worming, is reached the melting of the frozen matrix, starting thus the nucleation and growth on the metal nanoparticles. Lastly, the immobilisation step occurs simply by the insertion of the target support. A final evaporation of the solvent is then required. The advantage of this techniques is to synthetised directly the nanoparticles in metal oxidation state, avoiding post-synthesis activation steps that could induce undesirable modification on the catalytic system (similarly to what has reported for sol-immobilisation technique). Another features that characterise this variant, it the use of the bulk metal as precursor avoiding the employing of the often toxic and/or corrosive metal precursors (used in the CVD) [260].

1.6.5. *Catalysts activation step*

Most of the synthetic routes presented so far, foresees the deposition of a metal precursor on the surface of the target support. A subsequentially step, in order to degrade the precursor into the final active phase (i.e. nanoparticles), is therefore strictly required. This procedure is so called activation step (or process) and generally it occurs by n heat treatment in inert, oxidising (i.e. oxygen or air) or reducing (i.e. hydrogen) atmosphere.
This last step, as well as leading to the active phase, can deeply modify the features of the catalytic systems therefore it has to be carefully designed. The heat treatment, indeed, could potentially affect the dispersion degree of the metal nanoparticles (by induce sintering phenomena) and also change the interactions between precursor and support (i.e. strong metal-support interactions, SMSI), as well as alter the surface structure of the final catalytic system (i.e. surface area and porosity) [250, 251].

1.7. Catalyst characterization: an overview [269]

The characterisation of a catalytic system is not just one step that belong to the catalyst design, it represents a key and vital validation tool that allows the monitoring of the overall catalytic process. Furthermore, just by means of a full and deep characterisation of the catalysts' features, it can be disclosed a correlation between the features of the studied system with its catalytic behaviours. At the present day, a wide range of characterisation techniques are available to investigate both model and real solid catalysts for different levels (i.e. nanoscopic, microscopic or macroscopic) and for all the steps of synthesis (i.e. during the preparation, after a thermal treatment or functionalisation, during and after the catalytic tests). Thus, the real task of a characterisation is not just to merely observe the catalyst but is to provide vital and precise information about its structure such as morphology, porosity, chemical composition, acidity and other precious chemical-physical information. In addition, some specific characterisations have the potential to investigate even the surface reactivity allowing a prediction of the catalytic behaviour and/or identify the specific features of the active sites responsible of the reactivity. According to the literature, a general guideline can be proposed to describe the principles on which the characterisation techniques are based. Almost all the characterisation strategies, indeed, share the same approach: a probe system (i.e. photons, electrons, ions, electric, magnetic or thermal fields) scan the sample by interact with it

and give back an emitted signal (i.e. photons, electrons, ions, electric, magnetic or thermal fields) that is collected and elaborate.
The characterisation techniques can be classified in many different ways, for instance based on the nature of the probe's nature or on the information gained (even if the two aspects are strictly correlated).
Here as follow a briefly classification will be presented dividing the characterisation in two main different classes: physical and chemical.

1.7.1. *Physical characterisation*

The physical characterisations allow to investigate different aspect of a catalytic system:

- Morphology, particle size and dispersion of the active phase

X-ray powder diffraction is a widely use technique for the identification of crystalline phases of the exanimated samples by means of a comparison with databases. A useful aspect, catalytically speaking, is the possibility, by means of the Sherrer equation, to estimate the average crystallite size (or estimate the nanoparticles mean dimension).
The vibrational spectroscopy (i.e. Fourier-transform infrared spectroscopy FT-IR, Diffuse Reflectance Infrared Fourier Transform Spectroscopy DRIFT, Attenuated Total Reflection Infrared Spectroscopy ATR-FTIR and Raman Spectroscopy) is valuable to investigate for instance the material's phase, changes in compositions of bulk catalyst materials, crystallinity and surface functional groups. Another technique, especially sensible to light elements (i.e. H or D) and useful to acquire structural and in defects determination, is the characterisation by neutron scattering. This latter usually provides information complementary to the ones gained by XRD.
By using the electron microscopies (Scanning Electron Microscope SEM, Transmission Electron Microscopy TEM, High-resolution Transmission Electron Microscopy HR-TEM, Scanning Transmission Electron Microscopy STEM), the size and shape of both the support and of the active phase can be investigated. In addition, particle shape and size of the support and active phase, their size distribution and also lattice spacing can be determined.

- Porosity and surface area

Physisorption of probe gas molecules allows, taking advantage of the Brunauer– Emmett – Teller (BET) method, to measure the pore volume and pore dimension, surface area and

pore-size distributions. In the range of mesopores the calculations are possible by the Kelvin equation (cylindrical shaped pores approximation) and in the range of micropores by theoretical (Dubinin – Radushkevich and the Dubinin – Stoeckli theories) and empirical (t-method and α_s-method) methods. Alternatively, in the case of both meso and macropores, the pore size distribution can be calculated by mercury porosimetry**.**

On the other side, by means of temperature programmed desorption (TPD), the behaviour of the catalysts under a thermal treatment can be followed (i.e. calcination or activation processes) or if the desorption technique is coupled with CO as probe molecule also the reactivity can be investigated. In addition, for the case of metal oxides, the interaction of probe molecules such as ammonia or pyridines, an evaluation of the acidic sites of the system can also be performed.

1.7.2. *Chemical characterisation*

With the so defined chemical characterisation, other important aspect of the catalytic system can be evaluated. Some examples are reported as follows:

- Bulk composition

In order to investigate the overall elemental composition of a material, the inductively coupled plasma atomic emission spectroscopy (ICP-AES) is a widely used technique. This instrument results particularly useful to evaluate the metal loading of the prepared catalysts and also to check for eventual metal leaching analysing the final reaction mixture (liquid samples). On the other side, for solid samples and to detect elements with a high atomic number (Z>11), energy-dispersive X-ray spectroscopy (EDX) can be employed. This detector is often coupled with the electron microscopy instruments. Alternatively and particularly useful to evaluate light elements (Z < 11), electron energy loss spectroscopy (EELS) can be exploited.

Another useful spectroscopy technique, is the already mentioned Raman characterisation. It takes the name from its inventor C. V. Raman. This technique is normally exploited to determine the vibrational modes of molecules (also rotational and other low-frequency modes can be detected) to provide a structural fingerprint by which molecules can be identified. The technique is based on inelastic scattering of photons phenomena, known as Raman scattering. The electromagnetic radiation is usually provided from a laser source (in the range of visible, near infrared, near ultraviolet light or even x-ray). The shift in energy of the probe laser light after the interaction with the sample gives useful

information about the material. The technique, for instance, results particularly useful to determine the graphitisation degree of carbon or to investigate modification induced on a material (i.e. by evaluate the metal-oxygen bonds).

- Surface analysis

o Surface composition, valency and oxidation states

By means of Electron Spectroscopy for Chemical Analysis (ESCA, better known as X-ray Photoelectron Spectroscopy, XPS), after the exposure to X-ray radiation, the emitted photoelectrons coming from the surface (≈ 2 nm) of the sample are collected and elaborate (according to their kinetic energy) to determine the value of the binding energy. The latter parameter, as a function of the electron configuration, allows to identify the element and also its valence state. This particular technique results of vital importance to evaluate the condition of the catalysts' surface (oxidation states of the metals and/or presence of functionalisation groups). Moreover, if the instrument is equipped with a pre-treatment chamber, a useful *in-situ* simulated activation step before the characterisation can be performed. This possibility allows to study the same sample in two different states avoiding any possible modification or contamination after the treatment, allowing also an easier comparison.

Another spectroscopic technique based on a similar principle to the one just described, is the Auger Electron Spectroscopy (AES, also evaluated within an XPS characterisation): surface is irradiated by high-energy electrons (≈ 1–5 keV) causing an emission of photoelectrons and X-ray fluorescence (also called Auger electrons, valence shell's electrons derived from relaxation phenom). Measuring the kinetic energy of Auger electrons is possible to determine their bonding energy and it results particularly efficient in the determination of oxidative state of particular elements (i.e. of silver). Another advantage brings from this technique is the possibility to obtain a concentration profile by moving the electron beam across the surface.

Another surface investigation technique is represented by the Scattering Spectroscopy (ISS): the composition and structure (of outer layers) are evaluated by ion bombardment. Elaborating the energy of the probe ray after and before the interaction with the sample, indeed, is possible to identify the superficial elements. The same principle unites also the Secondary Ion Mass Spectrometry (SIMS), where charged fragments (both positive and

negative ions or clusters) derived from the surface of the examined material, are analysed and identified by mass spectrometry.

By taking advantage of the spectrophotometry, such as the Fourier-transform infrared spectroscopy (FTIR), that can simultaneously collect high spectral resolution data over a wide spectral range, it can be investigated the molecules and particles present at the surface of the catalyst (i.e. functional groups and oxidation state of the nanoparticles). This is powerful method gains important information about the examined solid, as for the structure, the concentration, the strength (usually determine for basicity and acidity), the reactivity, and the distribution of the surface sites. In addition, the IR spectroscopy of probe molecules, CO especially, is one of the most useful techniques to deeply characterise nanostructured catalysts. Carbon monoxide adsorption can be non-reactive (carbonyls species are formed) and reactive (this is the case in which CO undergoes chemical transformations on the catalyst surface). Additionally, CO is also a reactant itself, thus in CO oxidation and in the water-gas shift (WGS) reactions, the reactivity of carbon monoxide can be followed directly by *in-situ* analysis.

- Surface acidity/basicity

By means of vibrational spectroscopy, for example with the aforementioned Fourier-transform infrared spectroscopy (FTIR), the adsorption of selected probe molecule can be also evaluated. In the case that the probe is a basic molecule (i.e. pyridine), the detection and discrimination between Brønsted and Lewis acid sites, and even evaluate the strength of the sites, results possible. Similar acidity evaluation can be also performed by means of the microcalorimetry (measure of differential heats of adsorption of probe molecules) or by titration methods.

- Redox Properties

By exploiting the temperature-programmed reaction methods, (Temperature-Programmed Reduction, TPR and Temperature-Programmed Oxidation, TPO), a chemical reaction can be monitored (increasing the temperature). These types of experiments and their cyclic application offer a useful tool to investigate the redox behaviour of catalytic materials.

- Surface coordination

To evaluate the nature and the coordination of a species present in the catalytic material, the X-ray Absorption Spectroscopy (XAS) is often used. Depending on the range of incident energy evaluation, this technique can be divided in X-ray Absorption Near-Edge Structure (XANES) and Extended X-ray Absorption Fine Structure (EXAFS).

This characterisation technique induces, by bomb with X-ray photon, the ejection of a photoelectron by a central atom (exited by specific wavelength). The outgoing photoelectron wave can be subsequentially backscattered by neighbouring atoms. In EXAFS characterisation, the analysis of the interference between a primary photoelectron wave and a backscattered one provides information on the nature and coordination of the central atom. On the other side, the X-ray Absorption Near-Edge Structure (XANES), results useful to evaluate the oxidation states and from it can be extracted information about the dimension of the analysed particles.

References

1. A. Wittstock, M. Bäumer (2014) Catalysis by Unsupported Skeletal Gold Catalysts. Acc Chem Res 47(3):731–739.
2. L.T. Mika, E. Cséfalvay, Á. Németh (2018) Catalytic Conversion of Carbohydrates to Initial Platform Chemicals: Chemistry and Sustainability. Chem Rev 118(2):505–613.
3. Oil demand to peak in three years, says energy adviser DNV GL - Reuters. https://www.reuters.com/article/us-oil-demand-dnv-gl-idUSKCN1VV2UQ. Accessed 30 Oct 2019
4. Wells, Wires, and Wheels - EROCI and the Tough Road Ahead for Oil - Investors' Corner. https://investors-corner.bnpparibas-am.com/investment-themes/sri/petrol-eroci-petroleum-age/. Accessed 30 Oct 2019
5. W. Schutyser, T. Renders, S. Van den Bosch, S.-F. Koelewijn, G.T. Beckham, B.F. Sels (2018) Chemicals from lignin: an interplay of lignocellulose fractionation, depolymerisation, and upgrading. Chem Soc Rev 47(3):852–908.
6. B. Mallesham, P. Sudarsanam, G. Raju, B.M. Reddy (2013) Design of highly efficient Mo and W-promoted SnO_2 solid acids for heterogeneous catalysis: acetalization of bio-glycerol. Green Chem 15(2):478–489.
7. G.P. Peters, C. Le Quéré, R.M. Andrew, J.G. Canadell, P. Friedlingstein, T. Ilyina, R.B. Jackson, F. Joos, J.I. Korsbakken, G.A. McKinley, S. Sitch, P. Tans (2017) Towards real-time verification of CO2 emissions. Nat Clim Chang 7(12):848–850.
8. K. Sordakis, C. Tang, L.K. Vogt, H. Junge, P.J. Dyson, M. Beller, G. Laurenczy (2018) Homogeneous Catalysis for Sustainable Hydrogen Storage in Formic Acid and Alcohols. Chem Rev 118(2):372–433.
9. A. Halilu, T.H. Ali, A.Y. Atta, P. Sudarsanam, S.K. Bhargava, S.B. Abd Hamid (2016) Highly Selective Hydrogenation of Biomass-Derived Furfural into Furfuryl Alcohol Using a Novel Magnetic Nanoparticles Catalyst. Energy & Fuels 30(3):2216–2226.
10. Paris Agreement | Climate Action - European Commission. https://https//ec.europa.eu/clima/policies/international/negotiations/paris_en.
11. J.C. Colmenares, R. Luque, J.M. Campelo, F. Colmenares, Z. Karpiński, A.A. Romero (2009) Nanostructured Photocatalysts and Their Applications in the Photocatalytic Transformation of Lignocellulosic Biomass: An Overview. Materials (Basel) 2(4):2228–2258.
12. S. Santoro, F. Ferlin, L. Luciani, L. Ackermann, L. Vaccaro (2017) Biomass-derived solvents as effective media for cross-coupling reactions and C–H functionalization processes. Green Chem 19(7):1601–1612.
13. M. Dusselier, M. Mascal, B.F. Sels (2014) Top Chemical Opportunities from Carbohydrate Biomass: A Chemist's View of the Biorefinery. Springer, Cham, pp 1–40
14. A. Demirbas (2009) Chapter 2: Biomass Feedstocks. In: Biofuels - Secur. Planet's Futur. Energy Needs. Springer London, London, pp 45–85
15. D.L. Klass (2004) Biomass for renewable energy and fuels. Encyclopedia of energy. Elsevier 1:193–212.
16. G.W. Huber, J.W. Shabaker, J.A. Dumesic, J.A. Dumesic (2003) Raney Ni-Sn Catalyst for H2 Production from Biomass-Derived Hydrocarbons. Science 300(5628):2075–2077.
17. L. Petrus, M.A. Noordermeer (2006) Biomass to biofuels, a chemical perspective. Green Chem 8(10):861.
18. G.W. Huber, J.N. Chheda, C.J. Barrett, J.A. Dumesic, J. Cairney, C.A. Eckert, W.J. Frederick, J.P. Hallett, D.J. Leak, C.L. Liotta, J.R. Mielenz, R. Murphy, R. Templer, T. Tschaplinski (2005) Production of Liquid Alkanes by Aqueous-Phase Processing of Biomass-Derived Carbohydrates. Science 308(5727):1446–1450.
19. S. Dumitriu (2005) Polysaccharides: Structural Diversity and Functional Versatility, Second Edition.
20. C.E. Wyman (1994) Alternative fuels from biomass and their impact on carbon dioxide accumulation. Appl Biochem Biotechnol 45–46(1):897–915.

21. A.G. Russell, D. St. Pierre, J.B. Milford, C.E. WYMAN (1990) Ozone Control and Methanol Fuel Use. Science 247(4939):201–205.
22. G.W. Huber, S. Iborra, A. Corma (2006) Synthesis of Transportation Fuels from Biomass: Chemistry, Catalysts, and Engineering. Chem Rev 106(9):4044–4098.
23. M. Barrio, B. Gøbel, H. Risnes, U. Henriksen, J.E. Hustad, L.H. Sørensen (2000) Progress in thermochemical biomass conversion. Tyrol, Austria
24. J. Homgren (2006) American Chemical Society Annual Meeting.
25. R. Datta, S.-P. Tsai, P. Bonsignore, S.-H. Moon, J.R. Frank (1995) Technological and economic potential of poly(lactic acid) and lactic acid derivatives. FEMS Microbiol Rev 16(2–3):221–231.
26. K. Buchta (1983) Lactic acid. Biotechnology 3:409–417.
27. K. Bendz (2005) EU-25 Oilseeds and Products Biofuels Situation in the European Union 2005.
28. A. Corma, S. Iborra, A. Velty, A. Corma Canos, S. Iborra, A. Velty (2007) Chemical routes for the transformation of biomass into chemicals. Chem Rev 107(6):2411–2502.
29. G.W. Huber, A. Corma (2007) Synergies between Bio- and Oil Refineries for the Production of Fuels from Biomass. Angew Chemie Int Ed 46(38):7184–7201.
30. D. Yue, F. You, S.W. Snyder (2014) Biomass-to-bioenergy and biofuel supply chain optimization: Overview, key issues and challenges. Comput Chem Eng 66:36–56.
31. R.L. Naylor, M.M. Higgins (2018) The rise in global biodiesel production: Implications for food security. Glob Food Sec 16:75–84.
32. F.N. Tubiello, M. Salvatore, S. Rossi, A. Ferrara, N. Fitton, P. Smith (2013) The FAOSTAT database of greenhouse gas emissions from agriculture. Environ Res Lett 8(1):15009.
33. J.L. Sawin (2013) Renewables 2013: Global status report. REN21
34. Y. Lin, S. Tanaka (2006) Ethanol fermentation from biomass resources: current state and prospects. Appl Microbiol Biotechnol 69(6):627–642.
35. M. Wang, C. Saricks, D.J. Santini (1999) Effects of fuel ethanol use on fuel-cycle energy and greenhouse gas emissions.
36. M. Balat, H. Balat (2010) Progress in biodiesel processing. Appl Energy 87(6):1815–1835.
37. M.J. Ramos, C.M. Fernández, A. Casas, L. Rodríguez, Á. Pérez (2009) Influence of fatty acid composition of raw materials on biodiesel properties. Bioresour Technol 100(1):261–268.
38. L.P. Christopher, Hemanathan Kumar, V.P. Zambare (2014) Enzymatic biodiesel: Challenges and opportunities. Appl Energy 119:497–520.
39. D.P. Ho, H.H. Ngo, W. Guo (2014) A mini review on renewable sources for biofuel. Bioresour Technol 169:742–749.
40. S. Kongjao, S. Damronglerd, M. Hunsom (2010) Purification of crude glycerol derived from waste used-oil methyl ester plant. Korean J Chem Eng 27(3):944–949.
41. F. Sun, H. Chen (2008) Organosolv pretreatment by crude glycerol from oleochemicals industry for enzymatic hydrolysis of wheat straw. Bioresour Technol 99(13):5474–5479.
42. M.M. Nobrega, J.B. Olivato, A.P. Bilck, M.V.E. Grossmann, F. Yamashita (2012) Glycerol with different purity grades derived from biodiesel: Effect on the mechanical and viscoelastic properties of biodegradable strands and films. Mater Sci Eng C 32(8):2220–2222.
43. R.W.M. Pott, C.J. Howe, J.S. Dennis (2014) The purification of crude glycerol derived from biodiesel manufacture and its use as a substrate by Rhodopseudomonas palustris to produce hydrogen. Bioresour Technol 152:464–470.
44. M. Hunsom, C. Autthanit (2013) Adsorptive purification of crude glycerol by sewage sludge-derived activated carbon prepared by chemical activation with H3PO4, K2CO3 and KOH. Chem Eng J 229:334–343.
45. J.A. Kenar (2007) Glycerol as a platform chemical: Sweet opportunities on the horizon? Lipid Technol 19(11):249–253.
46. A. Behr, J. Eilting, K. Irawadi, J. Leschinski, F. Lindner (2008) Improved utilisation of renewable resources: New important derivatives of glycerol. Green Chem 10(1):13–30.
47. A. Singhabhandhu, T. Tezuka (2010) A perspective on incorporation of glycerin purification process in biodiesel plants using waste cooking oil as feedstock. Energy 35(6):2493–2504.

48. Now near 100 million bpd, when will oil demand peak? | Sustainability. https://blogs.thomsonreuters.com/sustainability/2018/10/02/now-near-100-million-bpd-when-will-oil-demand-peak/. Accessed 30 Oct 2019
49. A. Gasparatos, P. Stromberg, K. Takeuchi (2013) Sustainability impacts of first-generation biofuels. Anim Front 3(2):12–26.
50. O. Publishing (2011) OECD-FAO agricultural outlook 2011-2020. Organisation for Economic Co-operation and Development
51. R.A. Lee, J.-M. Lavoie (2013) From first- to third-generation biofuels: Challenges of producing a commodity from a biomass of increasing complexity. Anim Front 3(2):6–11.
52. R.E.H. Sims, W. Mabee, J.N. Saddler, M. Taylor (2010) An overview of second generation biofuel technologies. Bioresour Technol 101(6):1570–1580.
53. R. Potumarthi, A. O'Donovan, G.D. Sharma (2014) Bioenergy Research: An Overview on Technological Developments and Bioresources. Bioenergy Res Adv Appl :23–47.
54. M.J. Aylott, E. Casella, I. Tubby, N.R. Street, P. Smith, G. Taylor (2008) Yield and spatial supply of bioenergy poplar and willow short-rotation coppice in the UK. New Phytol 178(2):358–370.
55. T.L. Romanelli, M. Milan, R.C. Tieppo (2012) Energy-Based Evaluations on Eucalyptus Biomass Production. Int J For Res :1–13.
56. S. Cadoux, A.B. Riche, N.E. Yates, J.M. Machet (2012) Nutrient requirements of Miscanthus x giganteus: Conclusions from a review of published studies. Biomass and Bioenergy 38:14–22.
57. E. Heaton, T. Voigt, S.P. Long (2004) A quantitative review comparing the yields of two candidate C4 perennial biomass crops in relation to nitrogen, temperature and water. Biomass and Bioenergy 27(1):21–30.
58. A. Singh, D. Pant, N.E. Korres, A.-S. Nizami, S. Prasad, J.D. Murphy (2010) Key issues in life cycle assessment of ethanol production from lignocellulosic biomass: Challenges and perspectives. Bioresour Technol 101(13):5003–5012.
59. A. Gallego, A. Hospido, M.T. Moreira, G. Feijoo (2011) Environmental assessment of dehydrated alfalfa production in Spain. Resour Conserv Recycl 55(11):1005–1012.
60. L. Barbanti, S. Grandi, A. Vecchi, G. Venturi (2006) Sweet and fibre sorghum (Sorghum bicolor (L.) Moench), energy crops in the frame of environmental protection from excessive nitrogen loads. Eur J Agron 25(1):30–39.
61. S. Hauk, T. Knoke, S. Wittkopf (2014) Economic evaluation of short rotation coppice systems for energy from biomass—A review. Renew Sustain Energy Rev 29:435–448.
62. I. Lewandowski, J.M.O. Scurlock, E. Lindvall, M. Christou (2003) The development and current status of perennial rhizomatous grasses as energy crops in the US and Europe. Biomass and Bioenergy 25(4):335–361.
63. G. Zhang, Z. Yang, S. Dong (2011) Interspecific competitiveness affects the total biomass yield in an alfalfa and corn intercropping system. F Crop Res 124(1):66–73.
64. M.Y. Koh, T.I. Mohd. Ghazi (2011) A review of biodiesel production from Jatropha curcas L. oil. Renew Sustain Energy Rev 15(5):2240–2251.
65. M.A. Carriquiry, X. Du, G.R. Timilsina (2011) Second generation biofuels: Economics and policies. Energy Policy 39(7):4222–4234.
66. A. Eisentraut (2010) Sustainable production of second-generation biofuels.
67. H.L. Choi, S.I.A. Sudiarto, A. Renggaman (2014) Prediction of livestock manure and mixture higher heating value based on fundamental analysis. Fuel 116:772–780.
68. N.-B. Chang, Y.-H. Chang, W.C. Chen (1997) Evaluation of heat value and its prediction for refuse-derived fuel. Sci Total Environ 197(1–3):139–148.
69. I.E.A. Bioenergy (2013) Biofuel-driven biorefineries: a selection of the most promising biorefinery concepts to produce large volumes of road transportation biofuels by 2025. IEA Bioenergy, Netherlands
70. L.R. Lynd, J.H. Cushman, R.J. Nichols, C.E. Wyman (1991) Fuel etanol from cellulosic biomass. Science 251(4999):1318–1323.
71. N. Mosier, C. Wyman, B. Dale, R. Elander, Y.Y. Lee, M. Holtzapple, M. Ladisch (2005) Features

of promising technologies for pretreatment of lignocellulosic biomass. Bioresour Technol 96(6):673–686.
72. T.A. Lloyd, C.E. Wyman (2005) Combined sugar yields for dilute sulfuric acid pretreatment of corn stover followed by enzymatic hydrolysis of the remaining solids. Bioresour Technol 96(18):1967–1977.
73. C.E. Wyman, B.E. Dale, R.T. Elander, M. Holtzapple, M.R. Ladisch, Y.Y. Lee (2005) Comparative sugar recovery data from laboratory scale application of leading pretreatment technologies to corn stover. Bioresour Technol 96(18):2026–2032.
74. C. Wyman, S. Decker, M. Himmel, J. Brady, C. Skopec, L. Viikari (2005) Hydrolysis of Cellulose and Hemicellulose, Polysaccharides: structural diversity and functional versatility, CRC Press, NW, Suite. In: 2nd Ed. CRC Press, pp 1023–1062
75. R. Rinaldi, F. Schüth (2009) Acid hydrolysis of cellulose as the entry point into biorefinery schemes. ChemSusChem 2(12):1096–107.
76. F. Isakov Yu., E.A. Stepanov, A.F. Dronov, N.D. Shumov, O.I. Blinnikov, A. Archibong (1990) Diagnosis and treatment of adhesive intestinal obstruction in children. Khirurgiya 66(8):3–7.
77. A.S. Mamman, J.-M. Lee, Y.-C. Kim, I.T. Hwang, N.-J. Park, Y.K. Hwang, J.-S. Chang, J.-S. Hwang (2008) Furfural: Hemicellulose/xylosederived biochemical. Biofuels, Bioprod Biorefining 2(5):438–454.
78. J. Zaldivar, J. Nielsen, L. Olsson (2001) Fuel ethanol production from lignocellulose: a challenge for metabolic engineering and process integration. Appl Microbiol Biotechnol 56(1–2):17–34.
79. B.C. Saha (2003) Hemicellulose bioconversion. J Ind Microbiol Biotechnol 30(5):279–291.
80. R. Rinaldi, R. Jastrzebski, M.T. Clough, J. Ralph, M. Kennema, P.C.A. Bruijnincx, B.M. Weckhuysen (2016) Paving the Way for Lignin Valorisation: Recent Advances in Bioengineering, Biorefining and Catalysis. Angew Chemie Int Ed 55(29):8164–8215.
81. D.M. Alonso, J.Q. Bond, J.A. Dumesic (2010) Catalytic conversion of biomass to biofuels. Green Chem 12(9):1493.
82. G.W. Huber, R.D. Cortright, J.A. Dumesic (2004) Renewable Alkanes by Aqueous-Phase Reforming of Biomass-Derived Oxygenates. Angew Chemie Int Ed 43(12):1549–1551.
83. R.R. Soares, D.A. Simonetti, J.A. Dumesic (2006) Glycerol as a Source for Fuels and Chemicals by Low-Temperature Catalytic Processing. Angew Chemie Int Ed 45(24):3982–3985.
84. E.L. Kunkes, D.A. Simonetti, R.M. West, J.C. Serrano-Ruiz, C.A. Gartner, J.A. Dumesic (2008) Catalytic conversion of biomass to monofunctional hydrocarbons and targeted liquid-fuel classes. Science 322(5900):417–421.
85. J. Carneiro, E. Nikolla (2019) Electrochemical Conversion of Biomass-Based Oxygenated Compounds. Annu Rev Chem Biomol Eng 10(1):85–104.
86. M.E. Dry (2002) The Fischer–Tropsch process: 1950–2000. Catal Today 71(3–4):227–241.
87. H. Heinemann, J.J. Carberry (1974) Catalysis reviews: science and engineering. M. Dekker
88. D.J. Hayes (2009) An examination of biorefining processes, catalysts and challenges. Catal Today 145(1–2):138–151.
89. T.R. Carlson, G.A. Tompsett, W.C. Conner, G.W. Huber (2009) Aromatic Production from Catalytic Fast Pyrolysis of Biomass-Derived Feedstocks. Top Catal 52(3):241–252.
90. J. Jae, G.A. Tompsett, Y.-C. Lin, T.R. Carlson, J. Shen, T. Zhang, B. Yang, C.E. Wyman, W.C. Conner, G.W. Huber (2010) Depolymerization of lignocellulosic biomass to fuel precursors: maximizing carbon efficiency by combining hydrolysis with pyrolysis. Energy Environ Sci 3(3):358.
91. R.J. Evans, T.A. Milne, M.N. Soltys (1986) Direct mass-spectrometric studies of the pyrolysis of carbonaceous fuels. III. Primary pyrolysis of lignin. J Anal Appl Pyrolysis 9(3):207–236.
92. B. the C. and E.B. to L. Biofuels, G.W. Huber (2008) Breaking the chemical and engineering barriers to lignocellulosic biofuels: next generation hydrocarbon biorefineries. Citeseer
93. D.C. Elliott (2007) Historical developments in hydroprocessing bio-oils. Energy and Fuels 21(3):1792–1815.
94. S. Czernik, A. V. Bridgwater (2004) Overview of applications of biomass fast pyrolysis oil. Energy

and Fuels 18(2):590–598.
95. J.P. Diebold (2000) A Review of the Chemical and Physical Mechanisms of the Storage Stability of Fast Pyrolysis Bio-Oils. Nrel/Sr-570-27613 (January):59.
96. R.R. Davda, J.A. Dumesic (2004) Renewable hydrogen by aqueous-phase reforming of glucose. Chem Commun 10(1):36–37.
97. R.D. Cortright, R.R. Davda, J.A. Dumesic (2002) Hydrogen from catalytic reforming of biomass-derived hydrocarbons in liquid water. Nature 418(6901):964–967.
98. R.J.A. Gosselink, E. De Jong, B. Guran, A. Abächerli (2004) Co-ordination network for lignin - Standardisation, production and applications adapted to market requirements (EUROLIGNIN). In: Ind. Crops Prod. Elsevier, pp 121–129
99. R. Wooley, M. Ruth, J. Sheehan, H. Majdeski, A. Galvez (1999) Lignocellulosic Biomass to Ethanol Process Design and Economics Utilizing Co-Current Dilute Acid Prehydrolysis and Enzymatic Hydrolysis Current and Futuristic Scenarios Lignocellulosic Biomass to Ethanol Process Design and Economics Utilizing Co-Current D. Contract (July):132.
100. S. Kumar, R.K. Sani (2017) Biorefining of biomass to biofuels : opportunities and perception.
101. E. de Jong, G. Jungmeier (2015) Biorefinery Concepts in Comparison to Petrochemical Refineries. In: Ind. Biorefineries White Biotechnol. Elsevier, pp 3–33
102. S. Venkata Mohan, G.N. Nikhil, P. Chiranjeevi, C. Nagendranatha Reddy, M. V. Rohit, A.N. Kumar, O. Sarkar (2016) Waste biorefinery models towards sustainable circular bioeconomy: Critical review and future perspectives. Bioresour Technol 215:2–12.
103. E. Gnansounou, A. Dauriat (2011) Technoeconomic analysis of lignocellulosic ethanol. In: Biofuels. Academic Press, pp 123–148
104. J. Popp, Z. Lakner, M. Harangi-Rákos, M. Fári (2014) The effect of bioenergy expansion: Food, energy, and environment. Renew Sustain Energy Rev 32:559–578.
105. M.F. Demirbas (2011) Biofuels from algae for sustainable development. Appl Energy 88(10):3473–3480.
106. B. Abdullah, S.A.F. Syed Muhammad, Z. Shokravi, S. Ismail, K.A. Kassim, A.N. Mahmood, M.M.A. Aziz (2019) Fourth generation biofuel: A review on risks and mitigation strategies. Renew Sustain Energy Rev 107:37–50.
107. J.A.V. Costa, M.G. de Morais (2011) The role of biochemical engineering in the production of biofuels from microalgae. Bioresour Technol 102(1):2–9.
108. C.U. Ugwu, H. Aoyagi, H. Uchiyama (2008) Photobioreactors for mass cultivation of algae. Bioresour Technol 99(10):4021–4028.
109. J.K. Pittman, A.P. Dean, O. Osundeko (2011) The potential of sustainable algal biofuel production using wastewater resources. Bioresour Technol 102(1):17–25.
110. C.-Y. Chen, K.-L. Yeh, R. Aisyah, D.-J. Lee, J.-S. Chang (2011) Cultivation, photobioreactor design and harvesting of microalgae for biodiesel production: A critical review. Bioresour Technol 102(1):71–81.
111. N.R. Moheimani, M.A. Borowitzka (2006) The long-term culture of the coccolithophore Pleurochrysis carterae (Haptophyta) in outdoor raceway ponds. J Appl Phycol 18(6):703–712.
112. J.G. Day, S.P. Slocombe, M.S. Stanley (2012) Overcoming biological constraints to enable the exploitation of microalgae for biofuels. Bioresour Technol 109:245–251.
113. K. Li, S. Liu, X. Liu (2014) An overview of algae bioethanol production. Int J Energy Res 38(8):965–977.
114. R.P. John, G.S. Anisha, K.M. Nampoothiri (2011) Micro and macroalgal biomass: A renewable source for bioethanol. Bioresour Technol 102(1):186–193.
115. J.M. Thomas, W.J. Thomas, H.W. Salzberg (1967) Introduction to the Principles of Heterogeneous Catalysis. J Electrochem Soc 114(11):279.
116. M.W. Roberts (2000) Birth of the catalytic concept (1800-1900). Catal Letters 67(1):1–4.
117. F. Trifirò, F. Trifirò (2009) A history of chemistry. In: Fundam. Chem. - Vol. I. Eolss Publisher Co. Ltd., pp 27–70
118. H.S. Taylor (1925) A Theory of the Catalytic Surface. The Royal Society

119. P.W. Atkins, T. Overton, J. Rourke, M. Weller, F. Armstrong, M. Hagerman (2010) Shriver & Atkins' inorganic chemistry. Oxford University Press
120. P. Atkins and J. Paula (2009) Elements of physical chemistry, Fifth Edit. Oxford University Press
121. P. Atkins, T. Overton, J. Rourke, M. Weller, F. Armstrong (2006) Inorganic chemistry, Fourth Edi. Oxford University Press
122. Nature Heterogeneous catalysis. https://www.nature.com/subjects/heterogeneous-catalysis.
123. P.C.H. Mitchell (2007) Industrial catalysis: a practical approach. John Wiley & Sons, Ltd
124. E. Karsten, H. Erhard, R. Roland, H. Hartmut (2005) Amines, Aliphatic in Ullmann's Encyclopedia of Industrial Chemistry.
125. H. Cheung, R.S. Tanke (2005) et GP Torrence, Acetic acid.
126. V. L. Budarin, P. S. Shuttleworth, J. H. Clark, R. Luque (2010) Industrial Applications of C-C Coupling Reactions. Curr Org Synth 7(6):614–627.
127. R.I. Masel (2002) Chemical kinetics and catalysis. Focus Catal (7):8.
128. P. Schlexer (2017) Computational Modeling in Heterogeneous Catalysis. Ref. Modul. Chem. Mol. Sci. Chem. Eng.
129. G.A. Somorjai, Y. Li (2010) Introduction to surface chemistry and catalysis. John Wiley & Sons
130. M. Faraday (1857) The Bakerian Lecture : Experimental Relations of Gold (and Other Metals) to Light. Philos Trans R Soc London 147(1857):145–181.
131. Y. Yin, A.P. Alivisatos (2005) Colloidal nanocrystal synthesis and the organic-inorganic interface. Nature 437(7059):664–70.
132. G. Mie (1908) Articles on the optical characteristics of turbid tubes, especially colloidal metal solutions. Ann Phys 25(3):377–445.
133. V. Amendola, R. Pilot, M. Frasconi, O.M. Maragò, M.A. Iatì (2017) Surface plasmon resonance in gold nanoparticles: a review. J Phys Condens Matter 29(20):203002.
134. Y. Tan, Y. Li, D. Zhu (2004) Noble metal nanoparticles. In: Encycl. Nanosci. Nanotechnol. American Scientific Publishers, pp 9–40
135. D.J. Cole-Hamilton (2003) Homogeneous Catalysis--New Approaches to Catalyst Separation, Recovery, and Recycling. Science 299(5613):1702–1706.
136. R.M. Mohamed, D.L. McKinney, W.M. Sigmund (2012) Enhanced nanocatalysts. Mater Sci Eng R Reports 73(1):1–13.
137. A. Corma (2016) Heterogeneous catalysis: Understanding for designing, and designing for applications. Angew Chemie - Int Ed 55(21):6112–6113.
138. F. Grieser, R. Hobson, J. Sostaric, P. Mulvaney (1996) Sonochemical reduction processes in aqueous colloidal systems. Ultrasonics 34(2–5):547–550.
139. K.S. Suslick, M. Fang, T. Hyeon (1996) Sonochemical synthesis of iron colloids. J Am Chem Soc 118(47):11960–11961.
140. M.A. El-Sayed (2001) Some interesting properties of metals confined in time and nanometer space of different shapes. Acc Chem Res 34(4):257–264.
141. B. Roldan Cuenya, F. Behafarid (2015) Nanocatalysis: Size- and shape-dependent chemisorption and catalytic reactivity. Surf Sci Rep 70(2):135–187.
142. Y. Wang, N. Herron (1991) Nanometer-sized semiconductor clusters: Materials synthesis, quantum size effects, and photophysical properties. J Phys Chem 95(2):525–532.
143. F. Mafuné, J.Y. Kohno, Y. Takeda, T. Kondow (2002) Full physical preparation of size-selected gold nanoparticles in solution: Laser ablation and laser-induced size control. J Phys Chem B 106(31):7575–7577.
144. F. Mafuné, J.Y. Kohno, Y. Takeda, T. Kondow, H. Sawabe (2001) Formation of gold nanoparticles by laser ablation in aqueous solution of surfactant. J Phys Chem B 105(22):5114–5120.
145. F. Mafuné, J.Y. Kohno, Y. Takeda, T. Kondow, H. Sawabe (2000) Formation and size control of silver nanoparticles by laser ablation in aqueous solution. J Phys Chem B 104(39):9111–9117.
146. Gold Demand Sectors | [Gold Demand | Sectors or Demand | World Gold Council]. https://www.gold.org/about-gold/gold-demand/sectors-of-demand. Accessed 20 Oct 2019
147. A. Villa, C.E. Chan-Thaw, S. Campisi, C.L. Bianchi, D. Wang, P.G. Kotula, C. Kübel, L. Prati

(2015) AuRu/AC as an effective catalyst for hydrogenation reactions. Phys Chem Chem Phys 17(42):28171–28176.
148. F. Boccuzzi, A. Chiorino, M. Manzoli, D. Andreeva, T. Tabakova, L. Ilieva, V. Iadakiev (2002) Gold, silver and copper catalysts supported on TiO 2 for pure hydrogen production. Catal Today 75(1–4):169–175.
149. A. Stephen, K. Hashmi (2004) Homogeneous catalysis by gold. Gold Bull 37(1–2):51–65.
150. G.C. Bond, P.A. Sermon, G. Webb, D.A. Buchanan, P.B. Wells (1973) Hydrogenation over supported gold catalysts. J Chem Soc Chem Commun (13):444.
151. M. Haruta, T. Kobayashi, H. Sano, N. Yamada (1987) Novel Gold Catalysts for the Oxidation of Carbon Monoxide at a Temperature far Below 0 °C. Chem Lett 16(2):405–408.
152. A.M. Echavarren, A.S.K. Hashmi, F.D. Toste (2016) Gold Catalysis - Steadily Increasing in Importance. Adv Synth Catal 358(9):1347–1347.
153. C. Della Pina, E. Falletta, M. Rossi (2012) Update on selective oxidation using gold. Chem Soc Rev 41(1):350–369.
154. A. Corma, H. Garcia (2008) Supported gold nanoparticles as catalysts for organic reactions. Chem Soc Rev 37(9):2096–2126.
155. T. Hayashi, L.B. Han, S. Tsubota, M. Haruta (1995) Formation of Propylene Oxide by the Gas-Phase Reaction of Propane and Propene Mixture with Oxygen. Ind Eng Chem Res 34(7):2298–2304.
156. L. Prati, G. Martra (1999) New gold catalysts for liquid phase oxidation. Gold Bull 32(3):96–101.
157. L. Prati, M. Rossi (1998) Gold on carbon as a new catalyst for selective liquid phase oxidation of diols. J Catal 176(2):552–560.
158. P. Landon, P.J. Collier, A.J. Papworth, C.J. Kiely, G.J. Hutchings (2002) Direct formation of hydrogen peroxide from H2/O2 using a gold catalyst. Chem Commun 18:2058–2059.
159. Geoffrey C. Bond (2006) Chemisorption and Reactions of Hydrogen. In: Met. React. Hydrocarb. Springer US, pp 93–152
160. C. Milone, C. Crisafulli, R. Ingoglia, L. Schipilliti, S. Galvagno (2007) A comparative study on the selective hydrogenation of α,β unsaturated aldehyde and ketone to unsaturated alcohols on Au supported catalysts. Catal Today 122(3–4):341–351.
161. S.E. Davis, M.S. Ide, R.J. Davis (2013) Selective oxidation of alcohols and aldehydes over supported metal nanoparticles. Green Chem 15(1):17–45.
162. J.A. Rodriguez (2011) Gold-based catalysts for the water-gas shift reaction: Active sites and reaction mechanism. Catal Today 160(1):3–10.
163. P. Johnston, N. Carthey, G.J. Hutchings (2015) Discovery, Development, and Commercialization of Gold Catalysts for Acetylene Hydrochlorination. J Am Chem Soc 137(46):14548–14557.
164. N. Russo, D. Fino, G. Saracco, V. Specchia (2006) Supported gold catalysts for CO oxidation. Catal Today 117(1–3):214–219.
165. D.M. Alonso, S.G. Wettstein, J.A. Dumesic (2012) Bimetallic catalysts for upgrading of biomass to fuels and chemicals. Chem Soc Rev 41(24):8075–8098.
166. M. Sankar, N. Dimitratos, P.J. Miedziak, P.P. Wells, C.J. Kiely, G.J. Hutchings (2012) Designing bimetallic catalysts for a green and sustainable future. Chem Soc Rev 41(24):8099–8139.
167. W. Hou, N.A. Dehm, R.W.J. Scott (2008) Alcohol oxidations in aqueous solutions using Au, Pd, and bimetallic AuPd nanoparticle catalysts. J Catal 253(1):22–27.
168. D. Mott, J. Luo, P.N. Njoki, Y. Lin, L. Wang, C.J. Zhong (2007) Synergistic activity of gold-platinum alloy nanoparticle catalysts. Catal Today 122(3–4):378–385.
169. C.L. Bracey, P.R. Ellis, G.J. Hutchings (2009) Application of copper–gold alloys in catalysis: current status and future perspectives. Chem Soc Rev 38(8):2231.
170. T. Mallat, A. Baiker (2004) Oxidation of alcohols with molecular oxygen on solid catalysts. Chem Rev 104(6):3037–3058.
171. F. Porta, L. Prati (2004) Selective oxidation of glycerol to sodium glycerate with gold-on-carbon catalyst: an insight into reaction selectivity. J Catal 224(2):397–403.
172. S. Carrettin, P. McMorn, P. Johnston, K. Griffin, C.J. Kiely, G.J. Hutchings (2003) Oxidation of

glycerol using supported Pt, Pd and Au catalysts. Phys Chem Chem Phys 5(6):1329–1336.
173. A.K. Singh, Q. Xu (2013) Synergistic Catalysis over Bimetallic Alloy Nanoparticles. ChemCatChem 5(3):652–676.
174. N. Dimitratos, J.A. Lopez-Sanchez, G.J. Hutchings (2012) Selective liquid phase oxidation with supported metal nanoparticles. Chem Sci 3(1):20–44.
175. J. Xu, T. White, P. Li, C. He, J. Yu, W. Yuan, Y.F. Han (2010) Biphasic Pd-Au alloy catalyst for low-temperature CO oxidation. J Am Chem Soc 132(30):10398–10406.
176. C. George, A. Genovese, A. Casu, M. Prato, M. Povia, L. Manna, T. Montanari (2013) CO oxidation on colloidal Au0.80Pd0.20-Fe xOy dumbbell nanocrystals. Nano Lett 13(2):752–757.
177. D.I. Enache, J.K. Edwards, P. Landon, B. Solsona-Espriu, A.F. Carley, A.A. Herzing, M. Watanabe, C.J. Kiely, D.W. Knight, G.J. Hutchings (2006) Solvent-free oxidation of primary alcohols to aldehydes using Au-Pd/TiO2 catalysts. Science 311(5759):362–265.
178. N. Dimitratos, A. Villa, D. Wang, F. Porta, D. Su, L. Prati (2006) Pd and Pt catalysts modified by alloying with Au in the selective oxidation of alcohols. J Catal 244(1):113–121.
179. J.K. Edwards, S.J. Freakley, A.F. Carley, C.J. Kiely, G.J. Hutchings (2014) Strategies for designing supported gold-palladium bimetallic catalysts for the direct synthesis of hydrogen peroxide. Acc Chem Res 47(3):845–854.
180. L. Kesavan, R. Tiruvalam, M.H.A. Rahim, M.I. bin Saiman, D.I. Enache, R.L. Jenkins, N. Dimitratos, J.A. Lopez-Sanchez, S.H. Taylor, D.W. Knight, C.J. Kiely, G.J. Hutchings (2011) Solvent-Free Oxidation of Primary Carbon-Hydrogen Bonds in Toluene Using Au-Pd Alloy Nanoparticles. Science 331(6014):195–199.
181. H. Zhang, N. Toshima (2013) Glucoseoxidation using Au-containing bimetallic and trimetallic nanoparticles. Catal Sci Technol 3(2):268–278.
182. P. Liu, J.K. Nørskov (2001) Ligand and ensemble effects in adsorption on alloy surfaces. Phys Chem Chem Phys 3(17):3814–3818.
183. M. Chen, D. Kumar, C.W. Yi, D.W. Goodman (2005) Chemistry: The promotional effect of gold in catalysis by palladium-gold. Science 310(5746):291–293.
184. A. Wang, X.Y. Liu, C.Y. Mou, T. Zhang (2013) Understanding the synergistic effects of gold bimetallic catalysts. J Catal 308:258–271.
185. G.P. Keeler (2014) Ruthenium: Synthesis, physicochemical properties and applications. Nova Science Pub Inc
186. T. Shioiri, T. Aoyama (1995) In Encyclopedia of Reagents for Organic Synthesis, Paquette LA, Ed. John Wiley & Sons, Chichester, p 4415
187. J.S. Albert, A.D. Hamilton (1995) In Encyclopedia of Reagents for Organic Synthesis, Paquette, LA, Ed. Wiley: Chichester, p 4410
188. M.A. Bennett, M.I. Bruce, T.W. Matheson (1982) Comprehensive Organometallic Chemistry. by G. Wilkinson, FGA Stone, EW Abel, Pergamon Press. Oxford 4:
189. J.L. Dempsey, A.J. Esswein, D.R. Manke, J. Rosenthal, J.D. Soper, D.G. Nocera (2005) Molecular chemistry of consequence to renewable energy. Inorg Chem 44(20):6879–6892.
190. M.A. Gordon, W. Zhang, H.J. Lenz (2006) Pharmacogenomics of 5-fluorouracil/oxaliplatin in colorectal cancer. Curr Pharmacogenomics 4(4):277–283.
191. A.J. Esswein, D.G. Nocera (2007) Hydrogen production by molecular photocatalysis. Chem Rev 107(10):4022–4047.
192. P. Du, K. Knowles, R. Eisenberg (2008) A homogeneous system for the photogeneration of hydrogen from water based on a platinum(II) terpyridyl acetylide chromophore and a molecular cobalt catalyst. J Am Chem Soc 130(38):12576–12577.
193. W. Deng, X. Tan, W. Fang, Q. Zhang, Y. Wang (2009) Conversion of cellulose into sorbitol over carbon nanotube-supported ruthenium catalyst. Catal Letters 133(1–2):167–174.
194. A. Romero, E. Alonso, Á. Sastre, A. Nieto-Márquez (2016) Conversion of biomass into sorbitol: Cellulose hydrolysis on MCM-48 and d-Glucose hydrogenation on Ru/MCM-48. Microporous Mesoporous Mater 224:1–8.
195. H. Kobayashi, H. Matsuhashi, T. Komanoya, K. Hara, A. Fukuoka (2011) Transfer hydrogenation

of cellulose to sugar alcohols over supported ruthenium catalysts. Chem Commun 47(8):2366–2368.
196. K. Ghosh, R.A. Molla, M.A. Iqubal, S.S. Islam, S.M. Islam (2016) Ruthenium nanoparticles supported on N-containing mesoporous polymer catalyzed aerobic oxidation of biomass-derived 5-hydroxymethylfurfural (HMF) to 2,5-diformylfuran (DFF). Appl Catal A Gen 520:44–52.
197. A.S. Nagpure, A.K. Venugopal, N. Lucas, M. Manikandan, R. Thirumalaiswamy, S. Chilukuri (2015) Renewable fuels from biomass-derived compounds: Ru-containing hydrotalcites as catalysts for conversion of HMF to 2,5-dimethylfuran. Catal Sci Technol 5(3):1463–1472.
198. T. Pan, J. Deng, Q. Xu, Y. Xu, Q.X. Guo, Y. Fu (2013) Catalytic conversion of biomass-derived levulinic acid to valerate esters as oxygenated fuels using supported ruthenium catalysts. Green Chem 15(10):2967–2974.
199. J. Sun, H. Liu (2011) Selective hydrogenolysis of biomass-derived xylitol to ethylene glycol and propylene glycol on supported Ru catalysts. Green Chem 13(1):135–142.
200. M.G. Al-Shaal, W.R.H. Wright, R. Palkovits (2012) Exploring the ruthenium catalysed synthesis of γ-valerolactone in alcohols and utilisation of mild solvent-free reaction conditions. Green Chem 14(5):1260.
201. R. Fang, H. Liu, R. Luque, Y. Li (2015) Efficient and selective hydrogenation of biomass-derived furfural to cyclopentanone using Ru catalysts. Green Chem 17(8):4183–4188.
202. S.J. Yoon, Y.K. Kim, J.G. Lee (2011) Catalytic oxidation of biomass tar over platinum and ruthenium catalysts. Ind Eng Chem Res 50(4):2445–2451.
203. Y. Liu, L. Chen, T. Wang, Q. Zhang, C. Wang, J. Yan, L. Ma (2015) One-Pot Catalytic Conversion of Raw Lignocellulosic Biomass into Gasoline Alkanes and Chemicals over LiTaMoO6 and Ru/C in Aqueous Phosphoric Acid. ACS Sustain Chem Eng 3(8):1745–1755.
204. K. Okabe, K. Murata, M. Nakanishi, T. Ogi, M. Nurunnabi, Y. Liu (2009) Fischer-tropsch synthesis over Ru catalysts by using syngas derived from woody biomass. Catal Letters 128(1–2):171–176.
205. Y. Xu, T. Wang, L. Ma, G. Chen (2012) Upgrading of fast pyrolysis liquid fuel from biomass over Ru/γ-Al 2O 3 catalyst. Energy Convers Manag 55:172–177.
206. M.R. Rahimpour, M. Jafari, D. Iranshahi (2013) Progress in catalytic naphtha reforming process: A review. Appl Energy 109:79–93.
207. R.J. Lim, M. Xie, M.A. Sk, J.M. Lee, A. Fisher, X. Wang, K.H. Lim (2014) A review on the electrochemical reduction of CO2 in fuel cells, metal electrodes and molecular catalysts. Catal Today 233:169–180.
208. N.A. Hampson, M.J. Willars, B.D. McNicol (1979) The methanol-air fuel cell: A selective review of methanol oxidation mechanisms at platinum electrodes in acid electrolytes. J Power Sources 4(3):191–201.
209. S. Zhang, X.Z. Yuan, J.N.C. Hin, H. Wang, K.A. Friedrich, M. Schulze (2009) A review of platinum-based catalyst layer degradation in proton exchange membrane fuel cells. J Power Sources 194(2):588–600.
210. W. Liu, Y. Cui, X. Du, Z. Zhang, Z. Chao, Y. Deng (2016) High efficiency hydrogen evolution from native biomass electrolysis. Energy Environ Sci 9(2):467–472.
211. W.F. Chen, S. Iyer, S. Iyer, K. Sasaki, C.H. Wang, Y. Zhu, J.T. Muckerman, E. Fujita (2013) Biomass-derived electrocatalytic composites for hydrogen evolution. Energy Environ Sci 6(6):1818–1826.
212. B. Meryemoglu, S. Irmak, A. Hasanoglu, O. Erbatur, B. Kaya (2014) Influence of particle size of support on reforming activity and selectivity of activated carbon supported platinum catalyst in APR. Fuel 134:354–357.
213. H. Kobayashi, Y. Yamakoshi, Y. Hosaka, M. Yabushita, A. Fukuoka (2014) Production of sugar alcohols from real biomass by supported platinum catalyst. Catal Today 226:204–209.
214. A. Yamaguchi, O. Sato, N. Mimura, Y. Hirosaki, H. Kobayashi, A. Fukuoka, M. Shirai (2014) Direct production of sugar alcohols from wood chips using supported platinum catalysts in water. Catal Commun 54:22–26.
215. K. Murata, Y. Liu, M. Inaba, I. Takahara (2010) Hydrocracking of biomass-derived materials into

alkanes in the presence of platinum-based catalyst and hydrogen. Catal Letters 140(1–2):8–13.
216. Y.C. Chao, G.B. Chen, H.W. Hsu, J.R. Hsu (2004) Catalytic combustion of gasified biomass in a platinum monolith honeycomb reactor. Appl Catal A Gen 261(1):99–107.
217. D.C. Elliott (2008) Catalytic hydrothermal gasification of biomass. Biofuels, Bioprod Biorefining 2(3):254–265.
218. C. Zhou, W. Deng, X. Wan, Q. Zhang, Y. Yang, Y. Wang (2015) Functionalized Carbon Nanotubes for Biomass Conversion: The Base-Free Aerobic Oxidation of 5-Hydroxymethylfurfural to 2,5-Furandicarboxylic Acid over Platinum Supported on a Carbon Nanotube Catalyst. ChemCatChem 7(18):2853–2863.
219. J.J. Bozell (2010) Connecting biomass and petroleum processing with a chemical bridge. Science 329(5991):522–523.
220. C.A. Fisk, T. Morgan, Y. Ji, M. Crocker, C. Crofcheck, S.A. Lewis (2009) Bio-oil upgrading over platinum catalysts using in situ generated hydrogen. Appl Catal A Gen 358(2):150–156.
221. T. Nimmanwudipong, R.C. Runnebaum, D.E. Block, B.C. Gates (2011) Catalytic conversion of guaiacol catalyzed by platinum supported on alumina: Reaction network including hydrodeoxygenation reactions. Energy and Fuels 25(8):3417–3427.
222. R.C. Runnebaum, R.J. Lobo-Lapidus, T. Nimmanwudipong, D.E. Block, B.C. Gates (2011) Conversion of anisole catalyzed by platinum supported on alumina: The reaction network. Energy and Fuels 25(10):4776–4785.
223. A. McNaught, A. McNaught (1997) Compendium of chemical terminology (Vol. 1669). Oxford: Blackwell Science
224. Y.J. Pagán-Torres, J. Lu, E. Nikolla, A.C. Alba-Rubio (2017) Well-Defined Nanostructures for Catalysis by Atomic Layer Deposition. In: Stud. Surf. Sci. Catal. Elsevier Inc., pp 643–676
225. B.J. Oneill, D.H.K. Jackson, J. Lee, C. Canlas, P.C. Stair, C.L. Marshall, J.W. Elam, T.F. Kuech, J.A. Dumesic, G.W. Huber (2015) Catalyst design with atomic layer deposition. ACS Catal 5(3):1804–1825.
226. S.J. Tauster (1987) Strong metal-support interactions. Acc Chem Res 20(11):389–394.
227. S.J. Tauster, S.C. Fung, R.L. Garten (1978) Strong Metal-Support Interactions. Group 8 Noble Metals Supported on TiO2. J Am Chem Soc 100(1):170–175.
228. G.L. Haller, D.E. Resasco (1989) Metal–Support Interaction: Group VIII Metals and Reducible Oxides. Adv Catal 36(C):173–235.
229. A. West (2014) Solid state chemistry and its applications. John Wiley & Sons
230. I.E. Wachs (2005) Recent conceptual advances in the catalysis science of mixed metal oxide catalytic materials. Catal Today 100(1–2):79–94.
231. F. Rodríguez-Reinoso (1998) The role of carbon materials in heterogeneous catalysis. Carbon N Y 36(3):159–175.
232. V.A. Likholobov, V.F. Surovikin, G. V. Plaksin, M.S. Tsekhanovich, Y. V. Surovikin, O.N. Baklanova (2009) Nanostructured carbon materials for catalysis and adsorption. Catal Ind 1(1):11–16.
233. P. Serp, J.L. Figueiredo (2008) Carbon Materials for Catalysis. John Wiley & Sons, Inc.
234. K.P. De Jong, J.W. Geus (2000) Carbon Nanofibers: Catalytic Synthesis and Applications. Catal Rev - Sci Eng 42(4):481–510.
235. C.E. Chan-Thaw, A. Villa, G.M. Veith, L. Prati (2015) Identifying the Role of N-Heteroatom Location in the Activity of Metal Catalysts for Alcohol Oxidation. ChemCatChem 7(8):1338–1346.
236. M.J. Schulz, V.N. Shanov, Z. Yin (2013) Nanotube superfiber materials: changing engineering design. William Andrew
237. X. Sheng, J. Gao, L. Han, Y. Jia, W. Sheng (2011) One-pot synthesis of tryptophols with mesoporous MCM-41 silica catalyst functionalized with sulfonic acid groups. Microporous Mesoporous Mater 143(1):73–77.
238. K. Omata, S. Izumi, T. Murayama, W. Ueda (2013) Hydrothermal synthesis of W–Nb complex metal oxides and their application to catalytic dehydration of glycerol to acrolein. Catal Today 201:7–11.

239. C. García-Sancho, J.A. Cecilia, A. Moreno-Ruiz, J.M. Mérida-Robles, J. Santamaría-González, R. Moreno-Tost, P. Maireles-Torres (2015) Influence of the niobium supported species on the catalytic dehydration of glycerol to acrolein. Appl Catal B Environ 179:139–149.
240. Â. Silva, K. Wilson, A.F. Lee, V.C. dos Santos, A.C. Cons Bacilla, K.M. Mantovani, S. Nakagaki (2017) Nb2O5/SBA-15 catalyzed propanoic acid esterification. Appl Catal B Environ 205:498–504.
241. F.B. Noronha, D.A.G. Aranda, A.P. Ordine, M. Schmal (2000) The promoting effect of Nb2 addition to Pd/Al2O3 catalysts on propane oxidation. Catal Today 57(3–4):275–282.
242. M.J.C. Molina, M.L. Granados, A. Gervasini, P. Carniti (2015) Exploitment of niobium oxide effective acidity for xylose dehydration to furfural. Catal Today 254:90–98.
243. D. Stošić, S. Bennici, V. Rakić, A. Auroux (2012) CeO 2 -Nb 2 O 5 mixed oxide catalysts: Preparation, characterization and catalytic activity in fructose dehydration reaction. Catal Today 192(1):160–168.
244. A. Zaleska (2008) Doped-TiO_2 : A Review. Recent Patents Eng 2008, 2, 157-164 (1):157–164.
245. C. Moreno-Castilla, M.A. Ferro-Garcia, J.P. Joly, I. Bautista-Toledo, F. Carrasco-Marin, J. Rivera-Utrilla (1995) Activated Carbon Surface Modifications by Nitric Acid, Hydrogen Peroxide, and Ammonium Peroxydisulfate Treatments. Langmuir 11(11):4386–4392.
246. A. Hirsch (2002) Functionalization of single-walled carbon nanotubes. Angew Chemie - Int Ed 41(11):1853–1859.
247. D.J. Cole-Hamilton, R.P. Tooze (2006) Homogeneous Catalysis — Advantages and Problems. pp 1–8
248. Z. Yang, R. Wu, D.W. Goodman (2000) Structural and electronic properties of Au on TiO2 (110). Phys Rev B 61(20):14066–14071.
249. M. Chen, Y. Cai, Z. Yan, D.W. Goodman (2006) On the origin of the unique properties of supported Au nanoparticles. J Am Chem Soc 128(19):6341–6346.
250. C.W.B. Bezerra, L. Zhang, H. Liu, K. Lee, A.L.B. Marques, E.P. Marques, H. Wang, J. Zhang (2007) A review of heat-treatment effects on activity and stability of PEM fuel cell catalysts for oxygen reduction reaction. J Power Sources 173(2 SPEC. ISS.):891–908.
251. J.K. Edwards, J. Pritchard, M. Piccinini, G. Shaw, Q. He, A.F. Carley, C.J. Kiely, G.J. Hutchings (2012) The effect of heat treatment on the performance and structure of carbon-supported Au-Pd catalysts for the direct synthesis of hydrogen peroxide. J Catal 292:227–238.
252. L. Prati, A. Villa, L. Prati, A. Villa (2011) The Art of Manufacturing Gold Catalysts. Catalysts 2(1):24–37.
253. P. Haider, J.D. Grunwaldt, R. Seidel, A. Baiker (2007) Gold supported on Cu-Mg-Al and Cu-Ce mixed oxides: An in situ XANES study on the state of Au during aerobic alcohol oxidation. J Catal 250(2):313–323.
254. G.J. Hutchings, M.S. Hall, A.F. Carley, P. Landon, B.E. Solsona, C.J. Kiely, A. Herzing, M. Makkee, J.A. Moulijn, A. Overweg, J.C. Fierro-Gonzalez, J. Guzman, B.C. Gates (2006) Role of gold cations in the oxidation of carbon monoxide catalyzed by iron oxide-supported gold. J Catal 242(1):71–81.
255. S. Carrettin, P. Concepción, A. Corma, J.M. López Nieto, V.F. Puntes (2004) Nanocrystalline CeO2increases the activity of Au for CO oxidation by two orders of magnitude. Angew Chemie - Int Ed 43(19):2538–2540.
256. N. Lopez, T.V.W. Janssens, B.S. Clausen, Y. Xu, M. Mavrikakis, T. Bligaard, J.K. Nørskov (2004) On the origin of the catalytic activity of gold nanoparticles for low-temperature CO oxidation. J Catal 223(1):232–235.
257. G.C. Bond, P.A. Sermon (1973) Gold catalysts for olefin hydrogenation - Transmutation of catalytic properties. Gold Bull 6(4):102–105.
258. A.J. Van Dillen, R.J.A.M. Terörde, D.J. Lensveld, J.W. Geus, K.P. De Jong (2003) Synthesis of supported catalysts by impregnation and drying using aqueous chelated metal complexes. In: J. Catal. Academic Press Inc., pp 257–264
259. E. Marceau, X. Carrier, M. Che, O. Clause, C. Marcilly (2008) Ion Exchange and Impregnation.

Handb. Heterog. Catal.
260. L. Prati, A. Villa (2016) Gold catalysis : preparation, characterization, and applications. CRC Press
261. A. Villa, D. Wang, G.M. Veith, F. Vindigni, L. Prati (2013) Sol immobilization technique: a delicate balance between activity, selectivity and stability of gold catalysts. Catal Sci Technol 3(11):3036.
262. P. Zhao, N. Li, D. Astruc (2013) State of the art in gold nanoparticle synthesis. Coord Chem Rev 257(3–4):638–665.
263. J.D. Grunwaldt, C. Kiener, C. Wögerbauer, A. Baiker (1999) Preparation of supported gold catalysts for low-temperature CO oxidation via "size-controlled" gold colloids. J Catal 181(2):223–232.
264. R. Zanella, S. Giorgio, C.R. Henry, C. Louis (2002) Alternative methods for the preparation of gold nanoparticles supported on TiO2. J Phys Chem B 106(31):7634–7642.
265. F. Schüth, K. Unger (2008) Precipitation and Coprecipitation. In: Prep. Solid Catal. Wiley-VCH Verlag GmbH & Co. KGaA, Weinheim, Germany, pp 60–84
266. Y. Iwasawa (2008) Model Systems: Supported Catalysts From Chemical Vapor Deposition and Related Techniques. In: Handb. Heterog. Catal. Wiley-VCH Verlag GmbH & Co. KGaA, pp 853–873
267. A.S.H. Makhlouf (2011) Current and advanced coating technologies for industrial applications. In: Nanocoatings Ultra-Thin Film. Elsevier, pp 3–23
268. K.L. Choy (2003) Chemical vapour deposition of coatings. Prog Mater Sci 48(2):57–170.
269. M. Che, J. Védrine (2012) Characterization of solid materials and heterogeneous catalysts: From structure to surface reactivity.

Chapter 2. Catalytic oxidation of Glycerol (1st generation biomass)

2.1. State of the art - key role of gold

2.1.1. *Glycerol oxidation over mono-metallic gold-based catalysts*

As already discussed in the introduction section (Chapter 1), biomass represents a renewable source for new chemical platforms. Nowadays, great part of the chemical processes depends on petrochemical sources for the production of fine and commodity chemicals, polymers and fuels.

Moreover, it is well-know that the transformation of fossil resources is one of the main causes of air pollution, greenhouse effect and global warming. It is therefore of primary importance a change in trend, from the use of non-renewable and pollutant fossil resources to much greener renewable resources such as biomass. In particular, among the biomass-derived molecules, glycerol has been recognized as one of the most relevant chemical platforms for products of industrial relevance. Glycerol, in fact, is the main by-product in the production of biodiesel, with a mass yield of roughly 10 % [1, 2]. The growing production of biodiesel represent the largest production source of raw glycerol [3]. In 2016 more than 30.8 million m^3 (Mm^3) were produced, 7.5 % more than in 2015. The main producing countries in 2016 were the United States (5.5 Mm^3), Brazil (3.8 Mm^3), Germany (3.0 Mm^3), Indonesia (3.0 Mm^3) and Argentina (3.0 Mm^3). The countries of the European Union produced 10.7 Mm^3, i.e. the equivalent of 34.7 % of global biodiesel production, in 2016 [4]. It is estimated that in the future, biodiesel production will grow by around 4.5 % annually, reaching 41 Mm^3 in 2022 [5]. The valorisation of this important green feedstock is therefore of primary importance and new alternative ways must be developed to satisfy both the energy needs and the environmentally friendly production of chemicals and fuels [6].

The glycerol conversion process has been tackled from both an academia and industrial point of view from the past two decades; since then, many processes, such as dehydration, esterification, etherification and oxidation, have been explored and demonstrated the possibility to selectively transform glycerol into different chemicals of industrial relevance [7]. Among all the mentioned reactions, oxidation is a well-used means of glycerol conversion for the synthesis of several chemical intermediates. Glycerol is a three-carbon molecule containing three hydroxyl groups in its structure that can be oxidized. The selective oxidation of these groups leads to a wide range of different

products: C3 products such as glyceric acid (GA), dihydroxyacetone (DHA) and tartronic acid (TA), and C2 products such as glycolic acid (GlyA), oxalic acid (OxA) and formic acid (FA), as reported in the general scheme here below (Scheme 2-1) [8].

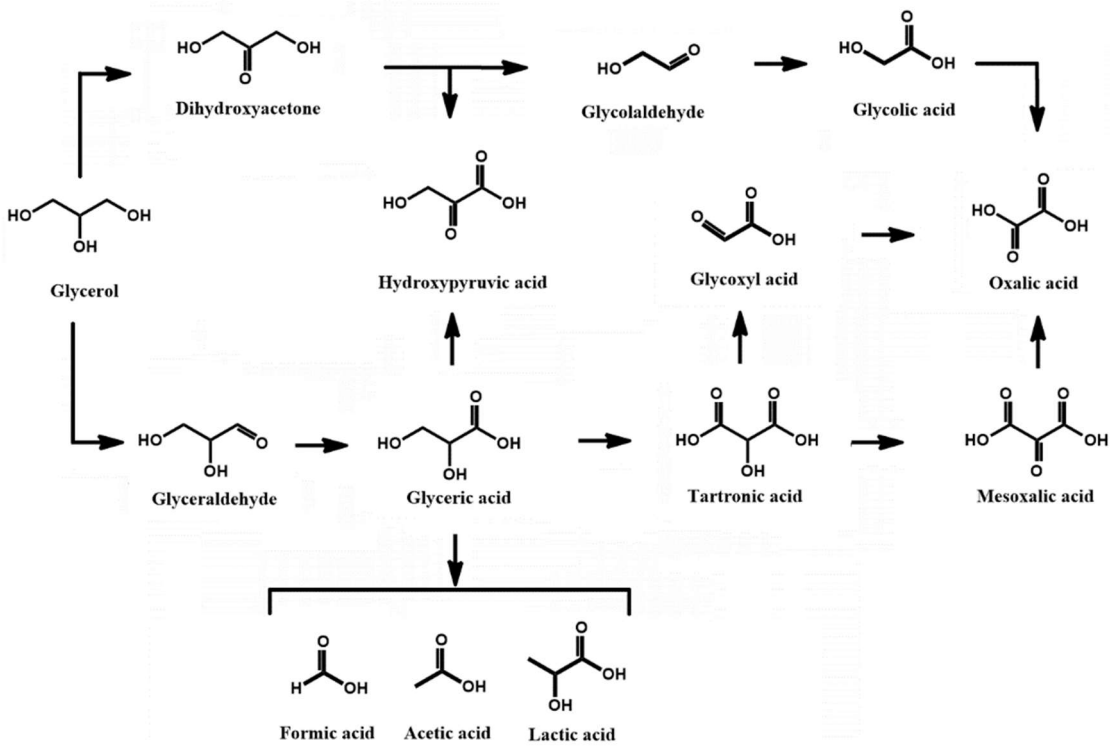

Scheme 2-1. General pathway of the main products derived from the glycerol oxidation.

These added-value products are a useful resource and find used in different fields. Glyceric acid for example, usually the main product of glycerol oxidation, can be used for skin disorders treatments, as building block of bio-based polyesters and in its ester as biodegradable fabric softener [9]. Dihydroxyacetone, on the other hand, is commonly used as a tanning agent in the cosmetics industry, while DHA constitutes a building block for several chemical compounds: i.e. methotrexate (used in chemotherapeutical treatment) [10]. Tartronic acid finds application as pharmaceutical and anti-corrosive protective agent, as well as for the biopolymers production [11]. Glycolic acid is used in a wide range of chemical processes, in cosmetic industry, as a precursor for biopolymers and in food processing as a flavouring agent and as a preservative [12]. Oxalic acid, finds some applications as bioleaching, in food preservatives and it is also used as a cleaning agent [13]. Formic acid (FA) is a commodity chemical that is widely used in the chemical, agricultural, textile, leather, pharmaceutical, and rubber industries. More recently, FA has been proposed as a suitable hydrogen storage compound since it can be easily and

selectively decompose to hydrogen and CO_2 through metal catalysed processes under very mild conditions [14].

The crucial points in glycerol oxidation are the activity and selectivity of the catalyst. Both features are governed by the physical and chemical properties of the catalyst as well as reaction conditions and oxidant source. Thus all these variables play a key role in the valorisation of glycerol [1, 15, 16].

Generally, carbon-supported metal nanoparticles combined with oxygen as oxidant under basic conditions and moderate temperature are the most investigated systems for glycerol oxidation [17–20]. Alkaline conditions are required to improve the oxidation kinetics and reduce the poisoning from (by)products irreversibly adsorbed on the surface of the active sites [21]; in addition, the primary alcoholic groups were preferentially oxidised to glyceric acid (main product) under alkaline conditions, thus, the presence of a base also influence the reaction pathway [22].

This system represents also the first study conducted on these type of reactions, in particular starting with palladium and platinum nanoparticles supported on activated carbon [21, 23]. However, a drawback was immediately raised: metal oxidation and irreversible adsorption of products and intermediates led to a rapid deactivation of most of the noble metal-based systems [19, 22]. Indeed, supported Pt and Pd based catalysts are very effective for the oxidation of polyols, although their susceptibility to deactivation (due to overoxidation in presence of oxygen) phenomena associated with the challenge to properly address the selectivity limit their industrial applications [24, 25]. In order to overcome the deactivation problem a strategy based on the use of gold as active metal, less prone to suffer of overoxidation, was employed. In fact, one of the main advantage in using gold is its stability under liquid-phase oxidation conditions with oxygen as oxidant [20, 26, 27]. In addition, gold based catalysts showed higher selectivity toward glyceric acid, among all the other metals [17, 27, 28]. Glyceric acid represents one of the main target products of the glycerol valorisation. These reasons are responsible for extended studies towards gold. One of the most accurate preliminary comparison was performed by Carrettin et al. between Pd, Pt and Au as active metal nanoparticles. The results showed that gold on both graphite and activated carbon could achieve, at relatively low conversion (≈ 55 %) a selectivity toward glyceric acid > 99 %, despite its lack of activity in the absence of a base (NaOH) [17, 27]. Since the first studies, it was clear how alkaline conditions play a crucial role in this reaction. DFT calculations for the

deprotonation of a model alcohol (ethanol to form an adsorbed alkoxide on Au in water solvent at high pH) coupled with isotopic-labelling experiments (glycerol oxidation) suggested how the presence of co-adsorbed hydroxides on the gold surface acts as a Brønsted base to facilitate O-H bond activation (by significantly lowers the activation barrier) via proton transfer (in much the same way as it can occurs in solution) [29, 30]. The presence of adsorbed hydroxide considerably lowers also the barrier for the subsequent activation of the C-H bond of the ensuing alkoxide intermediate to form the aldehyde over Au nanoparticles. On the other hand, it has demonstrated how in the absence of a base, the initial dehydrogenation step is totally inhibited for Au/C catalysts, while the reaction occurs for Pd/C and Pt/C catalysts, although with a much slower rate compared to the rate in the presence of a base [17, 31]. Hence, it has been proposed that the glycerol oxidation process proceeds via an initial deprotonation pathway in presence of a base on Au-based catalysts. In this sense, different bases have been tested by Carrettin et al., while the other reaction parameters have been maintained constant, and it was established how NaOH represents the best option in term of both activity and selectivity towards glyceric acid [17]. A full reaction pathway was later proposed by Porta and Prati in 2004 and here reported in Scheme 2-2 [20]. In blue the preferred pathway under alkaline is highlighted conditions; according to the proposed mechanism, the intermediates dihydroxyacetone and glyceraldehyde can interconvert, although the further oxidation of glyceraldehyde into glyceric acid is very fast and dictates the reaction pathway.

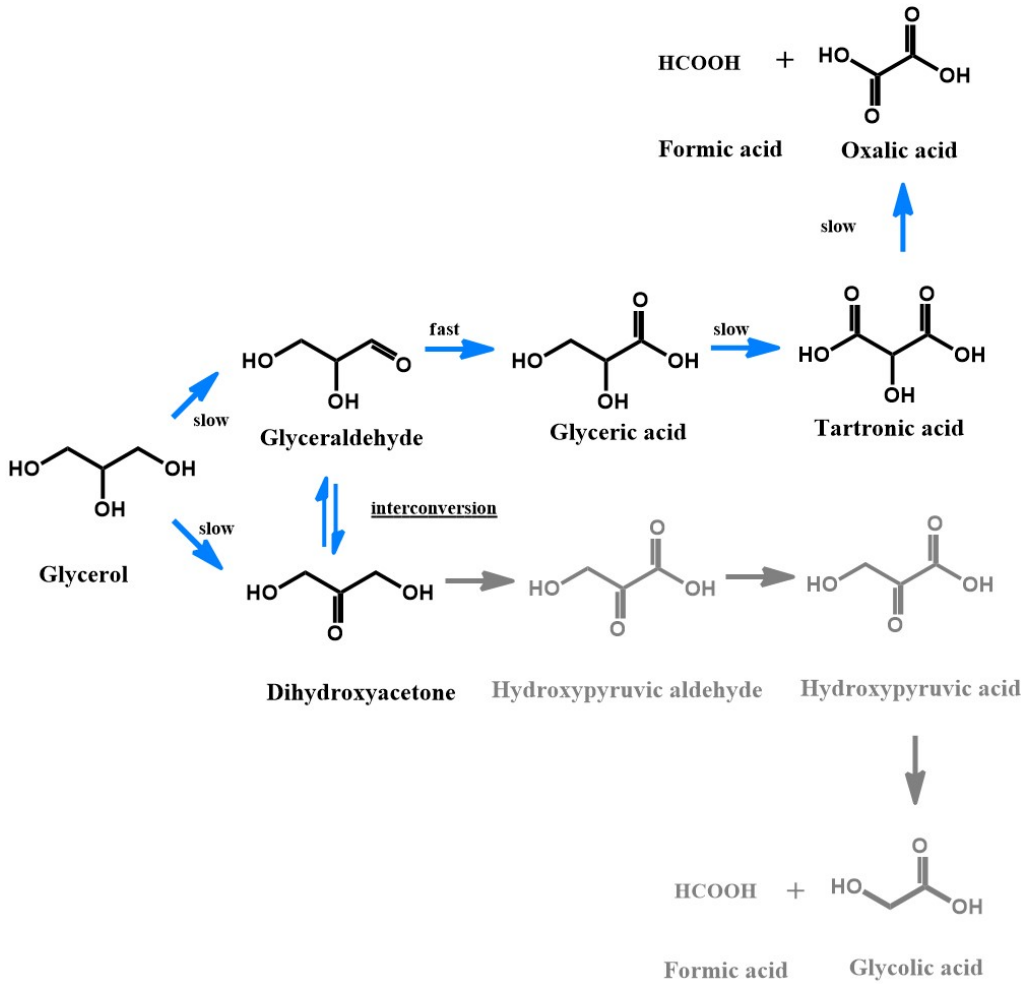

Scheme 2-2. General reaction pathway of the glycerol oxidation process. Highlighted in blue is the preferred pathway under alkaline conditions.

The role of the base on the selective oxidation of glycerol by Au-based catalysts has been deeply investigated in the past years. For instance, Ketchie and colleagues observed that increasing the NaOH concentration, the initial glycolate concentration increased with a consequent increase of the initial reaction rate. The formation of glycerolate species in the first step is also in line with the proposed reaction mechanism previously discussed [32]. However, glyceraldehyde and dihydroxyacetone were not detected as they are highly reactive intermediates. In addition, the general scarce amount of lactic acid observed during glycerol oxidation reactions, suggests that the glyceraldehyde intermediate must be readily oxidised on Au rather than degrade in the alkaline solution [20]. The formation of lactic acid, acetic acid and formic acid, in fact, has been associated with the base-catalysed degradation of the aldehyde or ketone [33]. Further experiments conducted on glyceraldehyde or dihydroxyacetone as substrates and in absence of a base, led to unconverted reaction mixture, thus highlighting the importance of the addition of a base in the conversion of glycerol over gold-based catalysts.

It is therefore clear that, in water media and oxygen as oxidant, the presence of a basic environment promotes the first reaction step, making the OH group active leading to the formation of sodium salt of glyceric acid as main product [34]. However, increasing the NaOH:GLY molar ratio, it has been observed a decreased tartronic acid formation in favour of glyceric acid [17]. On the other hand, glycolic acid is not formed by the base catalysed process: the C-C cleavage derives from another reaction path (Scheme 2-2–path below). Concerning this, it has been proved how H_2O_2 is formed during glycerol oxidation at basic pH [32]. In particular, the concentration of H_2O_2 decreased as the reaction proceeded; lower reaction temperatures resulted in detection of greater H_2O_2 concentrations, which led to higher selectivity toward glycolic acid. By using directly H_2O_2 as oxidising agent at free pH (over Au-based catalysts), it results a low selectivity towards glycolic acid with an evident decreased rate in respect with the oxidation (H_2O_2 as oxidant) occurred in presence of a base. Thus, hydroxyl ions enhance the reaction rate and affect also the selectivity, even in presence of H_2O_2 as oxidant. In this regard, Zope and co-workers investigated the oxidation mechanism by $^{18}O_2$ and $H_2{}^{18}O$ labelling experiments [30]. The authors demonstrated that oxygen atoms from the hydroxide are incorporated into glycerol during the oxidation step. The theory was backed up by DFT calculations showing that molecular oxygen did not dissociate but rather participated in the catalytic cycle: they are responsible of regeneration of the hydroxide ions formed via catalytic decomposition of peroxide intermediates. The hydrogen peroxide, indeed, is formed through oxygen reduction by metal hydride (Au-H); the presence of this latter intermediate was studied and demonstrated by Conte and co-workers [35].

Wang et al. studied the effect of the Au particle structure on the selectivity in the liquid-phase oxidation of glycerol, proving that the exposed facets of the Au nanoparticles were a key factor. In addition, the authors claimed that Au (111) facets promoted the C-C bond cleavage and enhanced the selectivity to glycolate and formate; Au (111) surfaces, in fact, are the most active for H_2O_2 direct synthesis [36]. The selectivity in the glycerol oxidation, thus, can be influenced by a preferential orientated growth of Au nanoparticle's facet.

The activity of the catalyst, beside to be proportional to the number of active sites, is inversely proportional to Au particle size; catalysts with smaller size lead to more active systems [20, 27, 28, 37]. Au particle size also affects the selectivity, in fact big Au particles (≥ 20 nm) showed more selectivity towards glyceric acid than smaller ones (ca.

4 nm). The reduced particle size normally leads to an increase of the number of edges and corners, which are the active centres for oxygen activation and promote the formation of more hydrogen peroxide favouring the C-C cleavage and thus the formation of oxidised compounds (glycolate and formate) [37, 38]. In a later study, Dimitratos and co-workers studied the effect of particle size on both mono and bimetallic Au and Pd nanoparticles on carbon systems: the results showed a lower catalytic activity but a higher selectivity to sodium glycerate as the particle size increased [39]. Another interesting study has been recently carried out by Rogers et al., where the authors highlighted the crucial role of ultra-small Au clusters in the promotion of the reaction [40]. Another valuable contribution on the size effect has been given by Veith and colleagues by comparing carbon-supported Au catalysts prepared with two different techniques, namely sol-immobilisation and magnetron sputtering, in order to obtain consistent differences in mean nanoparticles diameters [41]. Small nanoparticles, obtained by magnetron sputtering, (average diameter 1.7 nm) were reported to be more active but less selective towards glycerate than Au particles prepared by sol-immobilisation (average diameter 6.9 nm). A similar study was carried out by Demirel and colleagues, reporting that Au/AC and prepared by sol-immobilisation method are more active compared to the ones prepared by deposition-precipitation due to different particle size [42]. Dimitratos et al. demonstrated, the same particle size trend by using different reduction methods during the catalyst synthesis (calcination versus chemical reduction). The authors highlighted how a calcination step could result in a significant growth of gold particles (ranging from 5 to 25 nm), while on the other hand the chemical reduction resulted in the formation of gold particles in the range of 2–5 nm [34]. The confinement effect of Au nanoparticles was further investigated by supporting the nanoparticles on either the surface or the inner walls of carbon nanofibers (CNFs) [43]. The authors were able to deposit Au nanoparticles selectively on the external surface of CNFs by sol-immobilisation technique, while by incipient wetness impregnation method the nanoparticles were deposited almost quantitatively inside the pores. Enhanced activity and higher selectivity to tartronic acid were reported for the catalyst with Au particles confined inside the CNFs channels. The authors ascribed this change in selectivity to a higher number of collisions, different electron densities and modified desorption rate of the primary product. The same authors, in a later study, deeply investigate the role of the capping agent used during the synthesis of the Au nanoparticles. Different capping agents (PVA, THPC and citrate)

were used to synthesise Au-based catalysts [44]. The authors observed that the nature of the protective agent affected the catalytic activity guiding the particle size. In particular, higher catalytic activity (lowest nanoparticles dimension) was obtained when PVA was used. Furthermore, PVA-stabilised Au nanoparticles supported on TiO_2 showed remarkable and increased catalyst stability upon recycling [45]**.** A further significant step forward in understanding the influence of the protecting agent came again from Villa's workgroup. The direct interaction between PVA and glycerol was demonstrated using Au/TiO_2 catalysts prepared with different amount of PVA [33]. The presence of PVA lowered the activity of the catalysts but increased their stability upon recycling, prolonging considerably the catalyst life. Moreover, this effect depended on the amount of the protective agent: small amounts of PVA (Au/PVA 1:0.125 molar ratio) enhanced the activity of the catalyst. A possible electron transfer from the PVA to the Au particles was excluded by XPS analysis, thus it was hypothesised how PVA could take an active role in the reaction mechanisms. IR adsorption studies evidenced a direct interaction between PVA and glycerol. It was suggested that PVA could orient the glycerol molecules toward the catalytic active surface [45]. Thus, not only the nature of the capping agent plays a crucial role, but also the amount of it. Bigger particles were also obtained by either increasing the concentration of Au precursor or decreasing the amount of PVA used. A low Au/PVA ratio led to partial aggregation and coalescence of Au.

Villa et al. also investigated the effect of the support in the selective oxidation of glycerol, comparing different monometallic gold clusters deposited on activated carbon, TiO_2, $MgAl_2O_4$, and acidic H-mordenite prepared by a sol-immobilisation technique [21].

The authors observed that the acidic H-mordenite support significantly reduced the carbon-carbon cleavage, with consequent drop in C_1 products in favour of C_3 products, compared with the other systems tested. Further studies compared the catalytic activity of Au nanoparticles supported on different carbonaceous (carbon black, activated carbon and graphite) and metal oxides (TiO_2, MgO and Al_2O_3) supports [38]. They were able to efficiently isolate the support influence using the same reaction conditions and comparable Au particle size for all the catalysts synthesised.

Demirel-Gulen et al. also investigated the liquid phase oxidation of glycerol over gold supported on different carbons. The results showed that the support strongly influenced the catalyst properties; indeed, the activity was higher for carbon black support than active carbon or graphite [38]. Moreover, studies on the specific interaction between Au and

graphite showed that defects on graphitic layers change structure and stability of Au clusters [46]. Rodrigues et al. [47] studied the influences of surface chemical characteristics of activated carbon on the activity of gold-supported catalysts in the glycerol oxidation: changing the support properties, gold particles with similar average sizes resulted in different performances.

Support effects were further investigated and observed by Prati et al. with Au nanoparticles supported on different functionalised carbon nanotubes and nanofibers [48]. The authors reported an increase in activity with the increased basicity of the functionalised support in accordance with the phenomenon observed in the presence of a base. On the other hand, the selectivity appeared to be mostly related with the type of surface group present on the support: basic and hydrophobic functional groups enhanced the selectivity to C_3 products, whereas hydrophilic surfaces increased the C−C bond cleavage products. In Table 2-1 are reported some significant catalytic results obtained by using Au as catalyst for glycerol oxidation.

Table 2-1. Activity, selectivity and reaction conditions for glycerol oxidation over selected monometallic Au-based catalysts.

Catalyst	Reaction conditions				Catalytic data			Sel.	Ref.
	T	P O_2 (bar)	Me/GLY	Base	Initial Activity	Conv.	Time		
	(°C)		(mol/mol)		(h-1)	(%)	(h)	(%)	
1% Au/AC	60	3	1:500	NaOH	n.a.	56	3	100 GA	[27]
1% Au/graphite	60	3	1:500	NaOH	n.a.	54	3	100 GA	[27]
1% Au/graphite	60	6	1:500	NaOH	n.a.	91	3	92 GA	[17]
0.5% Au/graphite	60	3	1:500	NaOH	n.a.	26	3	61 GA	[28]
1% Au/TiO_2 THPC	50	3	1:500	NaOH	367	n.a.	-	52 GA 28 TA 15 GLYCA	[34]
1% Au/TiO_2 PVA	50	3	1:500	NaOH	178	n.a.	-	69 GA 17 GLYCO 10 TA	[34]
1.6% Au/TiO_2	60	10	1:8000	NaOH	n.a.	83	2	61 GA 34 GLYCA	[49]
1% Au/$MgAl_2O_4$	100	3	1:500	-	n.a.	6	2	35 GA 41 C1 products	[21]
1% Au/TiO_2	100	3	1:500	-	n.a.	8	2	38 GA 32 C1 products	[21]
1% Au/AC	100	3	1:500	-	n.a.	3	2	39 GA 10 TA 51 C1 products	[21]
1% Au/CNTs	50	3	1:1000	NaOH	648	n.a.	-	26 GA 53 OXA 14 GLYCA	[48]
1% Au/CNF	50	3	1:1000	NaOH	182	n.a.	-	55 GA 27 GLYCA	[48]

2.1.2. *Glycerol oxidation over multi-metallic Au-based catalysts*

In recent years, in order to increase the catalytic performance of Au catalysts and combine their resistance to deactivation, different metals were combined in bimetallic systems. Indeed, bimetallic catalysts are interesting because they can often improve both reactivity and stability for a broad range of catalytic processes compared to their monometallic counterparts [50, 51]. These bimetallic systems, in many cases, show high activity and resistance derived by the combination of the features of the two metals, enhanced by the synergetic effects often observed.

Most syntheses provide a mixture of monometallic and bimetallic particles and in addition, alloyed phases obtained by calcination, presented a low metal dispersion. Furthermore, the presence of metal segregation or multi-phases made the correlation between active species and catalytic performance very difficult or even speculative. Prati and colleagues were one of the pioneers to successfully synthetised, by sol-immobilisation, a single-phase bimetallic system (AuPd) [52]. Once again the first comparative approach was carried out on noble bimetallic nanoparticles (Au-Pt and Au-Pd) supported on carbon by sol-immobilisation and compared also with the respective monometallic counterparts in presence of a base [53]. By exploiting supported Au-Pd nanoparticles, the selectivity was addressed towards tartronic acid; Au-Pt favoured instead the formation of glycolic acid. Moreover, the resistance to deactivation, by means of Au alloying process, proved to be enhanced. Furthermore, both the bimetallic systems showed an enhanced activity in comparison with the correspondent monometallics.

The addition of a second active metal, however, further complicates the study of correlations between activity/selectivity and catalyst features. For instance, the nature of Pt precursor and the reducing agent used in the preparation of bimetallic catalysts significantly affected the process of reduction and particle growth. Dimitratos et al. compared different reducing agents, namely $NaBH_4$, N_2H_4 and H_2, highlighting how different reductants lead to different catalysts in terms of nanoparticles dimension and thus, of activity [54]. The order of addition of the two metals can affect the final catalyst as well; supported nanoparticles of the first reduced metal (Au/C) act as nucleation centres for the second metal (Pd) modulating the nanoparticles features and avoiding the segregation of the latter [52]. Prati's group, for examples, synthesised Au-Pd nanoparticles on activated carbon by first deposition of Au and then reduction of Pd by H_2 (slower reductive agent). The alloyed phase was much more active than segregated

palladium and it was responsible for the synergistic effect and conferred resistance and stability to recycling avoiding poisoning of the system. In this case, the catalyst was active and stable even after 11 recycles [55]. Another key parameter in bimetallic catalysts is the ratio between the two metals [37]. For instance, bimetallic Au–Pd nanoparticles supported on activated carbon were prepared with different Au:Pd molar ratios and compared in the oxidation of glycerol with oxygen as oxidant. The synergistic effect was evident and maximised for Au-rich systems, which showed both increased durability and activity [37].

For bimetallic Au-based systems, the immobilisation of Au is the key point to control particle features. Ketchie et al. reported AuPd carbon-supported catalysts synthesised by two different methods. The first one consisted in the deposition of Au on already supported Pd nanoparticles, while the second one, consisted in the deposition of a preformed and stabilised AuPd sol [56]. The characterisation of the systems revealed how Au was preferentially located on the surface on the nanoparticles; with these preparation methods none of the catalyst prepared showed activity greater than the monometallic Au catalyst. However, the bimetallic catalysts addressed the selectivity towards glyceric acid, thus Pd is able to catalyse the H_2O_2 decomposition and thus, decrease the C-C cleavage promoted by the peroxide presence. Different preparation methods have been explored also for bimetallic systems as was investigated for the monometallic case. Impregnation and sol-immobilisation were compared by Dimitratos et al. [57] for AuPd nanoparticles deposited on both TiO_2 and carbon. The alloyed nanoparticles showed enhanced catalytic activity in both cases; in particular, the sol-immobilisation preparation method showed the highest performance in terms of activity. Sol-immobilisation confirmed the characteristic to lead to homogeneous alloys with narrow particle size distribution, whereas impregnation resulted in larger particle with Pd enrichment on the nanoparticles surface. The importance of the bimetallic systems was also highlighted by Purushothaman et al., reporting the one-pot conversion of glycerol to lactic acid performed at high temperature (100 °C). Au was combined with Pt and supported on CeO_2; a synergistic effect between the two noble metals was observed [58]. Bimetallic Au-based catalysts, showed their potential also for the industrially appealing base-free glycerol oxidation.

As discussed in the previous section, the basic environment is strictly necessary to observe any activity in glycerol oxidation for the Au-based systems. Because of using basic conditions, salts of acids are obtained instead of free carboxylic acids, as it is

desired. From an industrial point of view, this condition represents a restriction, whereas working under a neutral/acidic regime could lead directly to the desired products. Since this condition became evident, many efforts and experiments have been carried out trying to overcome this limitation. Supported bimetallic nanoparticles have been explored with this purpose. Villa et al. reported for the first time active AuPt catalysts in the base-free oxidation of glycerol [21]. The same authors also demonstrated how the support can strongly influence activity and selectivity of the AuPt system in glycerol oxidation. For example, it has shown how at 80 °C basic supports (MgO, NiO) promoted the activity but also increased C-C bond cleavage reactions. On the contrary, acidic supports (MCM41, SiO_2, H-mordenite and sulfated-ZrO_2) showed a higher selectivity (>80 %) to C_3 oxidation products, (glyceric acid and glyceraldehyde) resulted from the negligible formation of H_2O_2, in contrast to AuPt nanoparticles supported on activated carbon [21]. Moreover, few studies investigated into the effect of Au-Pt atomic ratio in base free glycerol oxidation, showing that Pt-rich systems are more active than Au-rich ones [59–62]. Most of these systems, however, seem to suffer from deactivation after prolonged reuses, probably due to leaching into the solution of the active phase or irreversible adsorption of the diacid products. On the other hand, the same workgroup has shown how titania (TiO_2 P25) exploit as AuPt nanoparticles support lead to active and durable systems for oxidation (and hydrogenolysis) of polyols [63, 64]. Furthermore, they were able to tune the selectivity of AuPt catalysts towards glyceraldehyde, an important intermediate, playing with different supports. The acid/base properties, and especially the acid site density, were one of the key factors in tuning the selectivity [65]. Finally, Brett et al. were able to address the selectivity towards C_3 products by comparing AuPt and AuPd nanoparticles on $Mg(OH)_2$, a basic support [66]. Thus, the support plays a crucial role also for modulating the selectivity and activity even in base-free conditions. Once again, the complexity and the multifactorial dependence of the catalytic performances of this type of systems is a relevant aspect to face. From the discovery of the peculiarity of Au as catalytic material, since its confirmation as a key role player for the liquid phase oxidation of glycerol, this type of process have been differently viewed [33].

2.2. Aims and objectives of the chapter

The aim of this section is to investigate the behaviour of the catalysts synthesised specifically for the oxidation of glycerol. The final goal will be correlate the features investigated by means of characterization techniques (HRTEM, XPS, UV-Vis, DRIFT) with the catalytic results.

The focus will be initially addressed to study the effects of different features of a family of supports (carbonaceous supports), for monometallic gold-based systems, and the impact of different synthesis method adopted. In most of the case, indeed, a comparison between different preparation techniques is provided, the Sol-immobilization will be compared with others (SMAD and DPU) that do not include the use of the protecting agent, and thus lead directly to "naked" nanoparticles.

These comparisons will result useful to study and understand also how the protecting agent could influences the results, in terms of catalysts' features and thus, in catalytic behaviours.

The focus of the discussion will pass then to the synthesis and study of the bimetallic systems, always Au-based. The main aim of this section's work is to reveal the bimetallic effect and the real structure of bimetallic AuAg and AuPt particles and its impact on their catalytic efficiency.

Furthermore, in the case of Au-Ag bimetallic systems, we investigate the influence play by the different supports (alumina and titania). We will further evaluate the different thermal treatment effects on the nanoparticles and on the metal oxidation states evolution and then, on the activity and selectivity of the target reaction. Finally, in the last section Pt- and Au-rich catalysts was investigated and tested at two different pH conditions, keeping in mind the importance to find an efficient system to perform the target oxidation in absence of a base, with the related advantages already mentioned in the previous section. The stability of the catalysts was also investigated in most of the cases in order to clarify the durability of the systems and the reasons of the deactivation phenomena.

2.3. Gold on different carbons

Carbon is a stable support in both acidic and basic environments; carbon-based supports have a wide range of tuneable properties that can improve the catalytic performance according to the specific application [67]. The quantity of the different type of carbons combined with the easiness of tuning its features, makes it an appealing support. Furthermore, carbon brings the advantage, especially useful at industrial level, that the precious supported metal can be easily recovered by burning off the carbon. As already widely discussed, Au-based catalysts showed activity and selectivity particle size-dependent and they can be modulated also by the support. The support, in turn, can modulate also the tendency of the system to passivate. It has been also observed that metal exposure and chemical surface groups of carbon have an important role in determining the activity in liquid phase oxidations [68]. All these considerations pushed our curiosity to synthesise, characterise and test Au nanoparticles supported on three on different carbons. In this section, the support influence has been explored. A comparison between two different synthesis techniques will be also provided: sol immobilization (SOL) and solvated metal atom deposition (SMAD). For these purposes, two series of Au catalysts on different carbon supports have been synthesised: the carbons employed were commercial Vulcan-XC72R, X40S and Norit GSX, all three with different features.

The carbon Vulcan is a graphitised carbon black from Cabot (surface area of SA= 218 $m^2\ g^{-1}$; pore volume of PV= 0.4 mL g^{-1}), it has a fluffy form and is a well-known conductive carbon black. Then two different commercial activated (partially graphitised) carbons were used: Norit GSX (SA= 933 $m^2\ g^{-1}$; PV= 1.9 mL g^{-1}) and Camel X40S (SA= 900–1100 $m^2\ g^{-1}$; PV= 1.5 mL g^{-1}). This type of carbon is used in liquid and vapour-phase applications (purification, decolorization, separation, catalyst and deodorization).

In order to be able to identify and correlate the features of the supports and the catalytic results, a deep characterization was performed beside catalytic test.

2.3.1. *Catalysts characterisation*

TEM characterization

The morphological features of both the SMAD and SOL-derived catalysts were investigated by high-resolution transmission electron microscopy (HRTEM, Figure 2-2) and scanning transmission electron microscopy (STEM, Figure 2-1). As expected, the micrographs of the carbon-supported catalysts show that the nature of the carbon exerts a great influence on the resulting supported Au nanoparticles size and distribution. The best result obtained for the SMAD technique set of catalysts is the Au/C_{Vulcan} SMAD sample; this catalyst exhibited a very narrow particle size distribution over the 1.0 - 4.0 nm range associated with an average diameter of 2.5 nm. Furthermore, also the dispersion of Au on this support appeared highly homogeneous. On the other hand, the catalysts supported on carbon Norit and carbon X40S, loaded with the same metal percentage (1 wt.%) showed a notably wider Au nanoparticles size distribution: 1.0 - 12.0 nm range (d_m = 3.9 nm) in Au/C_{Norit} SMAD and 4.0 - 20 nm range (d_m = 7.1 nm) in Au/C_{X40S}SMAD. Moreover, in the latter sample a fraction of polycrystalline particles larger than 15 nm in size was detected (see STEM micrographs reported in Figure 2-1- C). The homogeneous dispersion coupled with a narrow particle size distribution guarantees an optimum sample to be studied: fewer differences allow an easier correlation of the nanoparticles features with the catalytic behaviours. The results obtain by HRTEM images are in line also with what was observed during the synthesis processes; the deposition rate of Au nanoparticles varies a lot depending on the carbon used, indicating possible different metal-support interactions. In the case of carbon Vulcan supports, a deposition of the Au nanoparticles was observed leading to a completely clear water (or acetone for SMAD method) solution within 2 hours. On the other hand, the complete deposition of the Au nanoparticles onto the carbon Norit and especially onto carbon X40S supports occurred at longer times (approx. 3 hours), suggesting that in these latter cases the aggregation phenomena of the Au nanoparticles in solution can effectively compete with their immobilization onto the supports. We address this difference, at least as regards the carbon X40S, to its low adsorption capacity already reported in literature [69]. This phenomenon was more marked in the SMAD synthesis cases.

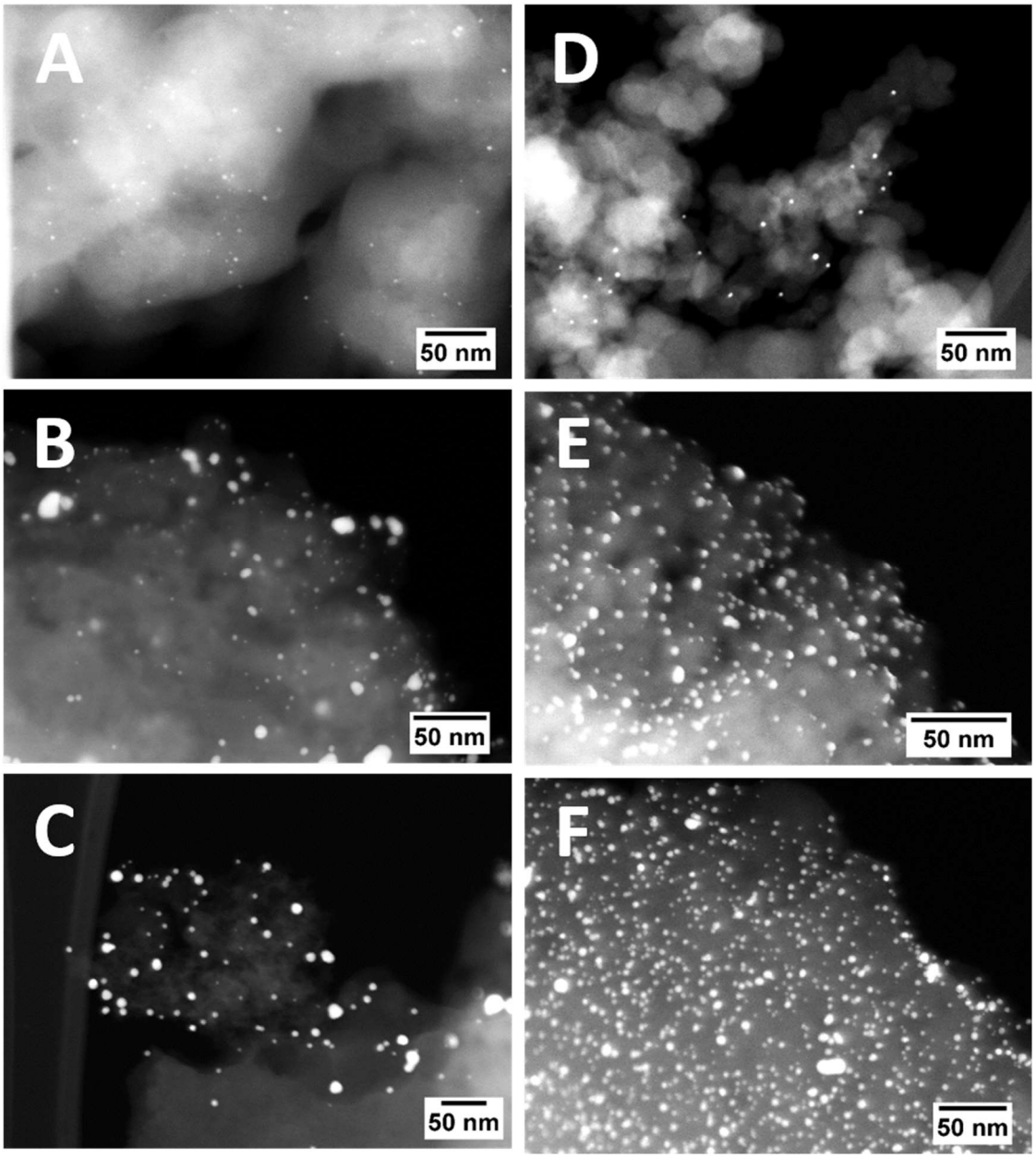

Figure 2-1. Representative HAADF-STEM micrograph of Au@C_{Vulcan} SMAD (A); Au@C_{Norit} SMAD (B); Au@C_{X40S} SMAD (C); Au@C_{Vulcan} SOL (D); Au@C_{Norit} SOL (E); Au@C_{X40S} SOL (F).

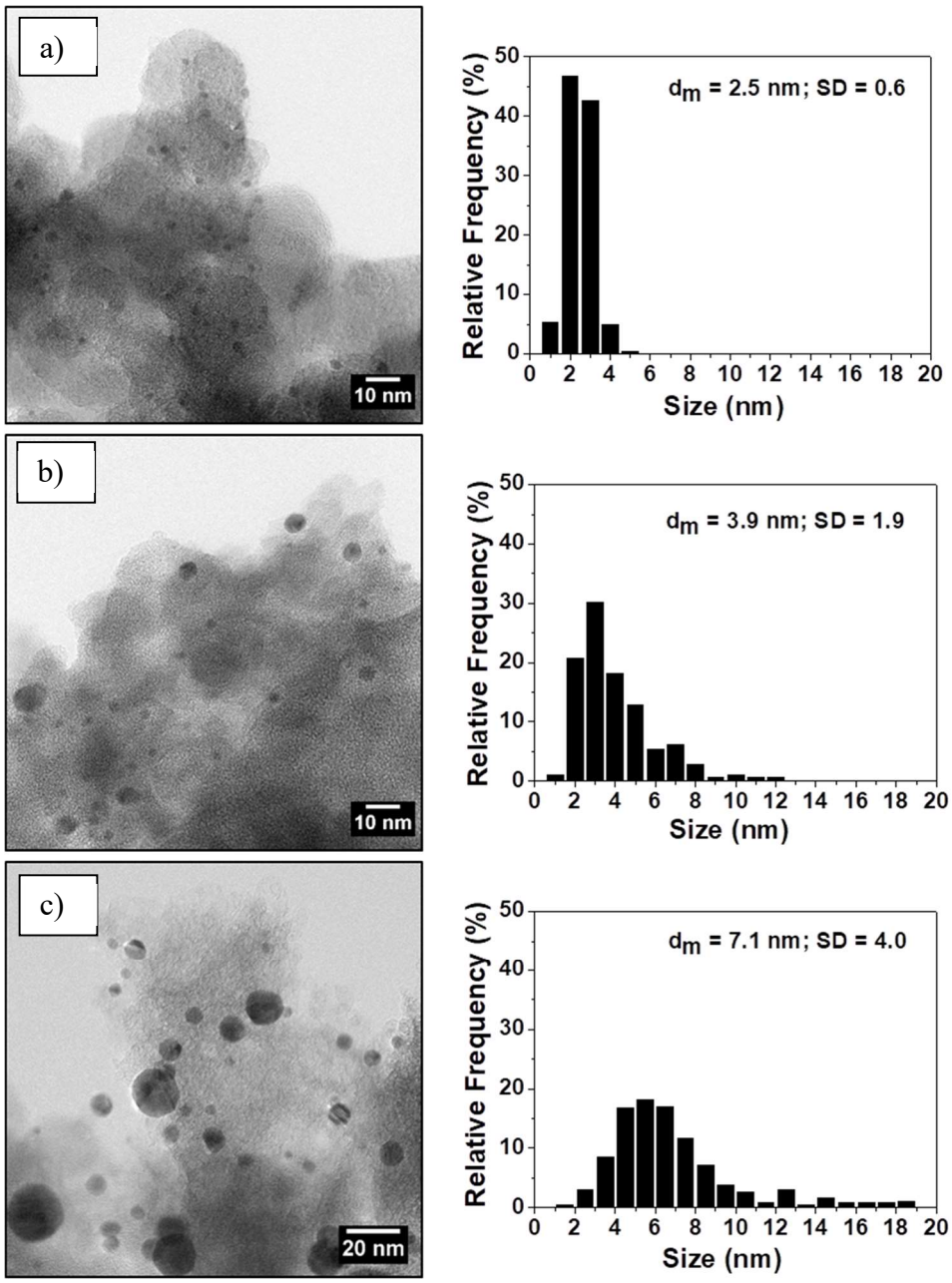

Figure 2-2. Representative HRTEM micrograph (left side) and histogram of particle size distribution (right side) of SMAD derived Au/C_{Vulcan} (a); Au/C_{Norit} (b); Au@C_{X40S} (c).

The HRTEM analysis comparison of the Au/C_{Vulcan} synthesised by Sol method (Figure 2-2-a) revealed the presence of Au nanoparticles of slightly larger sizes (size distribution 1.0 – 6.0 nm, d_m = 2.9 nm) respect to those observed in the corresponding SMAD-derived sample. Analogously to the results of the HRTEM analyses on the SMAD-derived samples (although in minor extent), SOL-derived Au Nanoparticles deposited on carbon Norit and carbon X40S showed larger sizes than those observed on the corresponding Au/C_{Vulcan} sample (d_m = 3.5 nm for carbon Norit and d_m = 3.0 nm for carbon X40S). In particular, the carbon X40S-supported sample showed the presence of a higher amount of larger particles (range 6 - 11 nm).

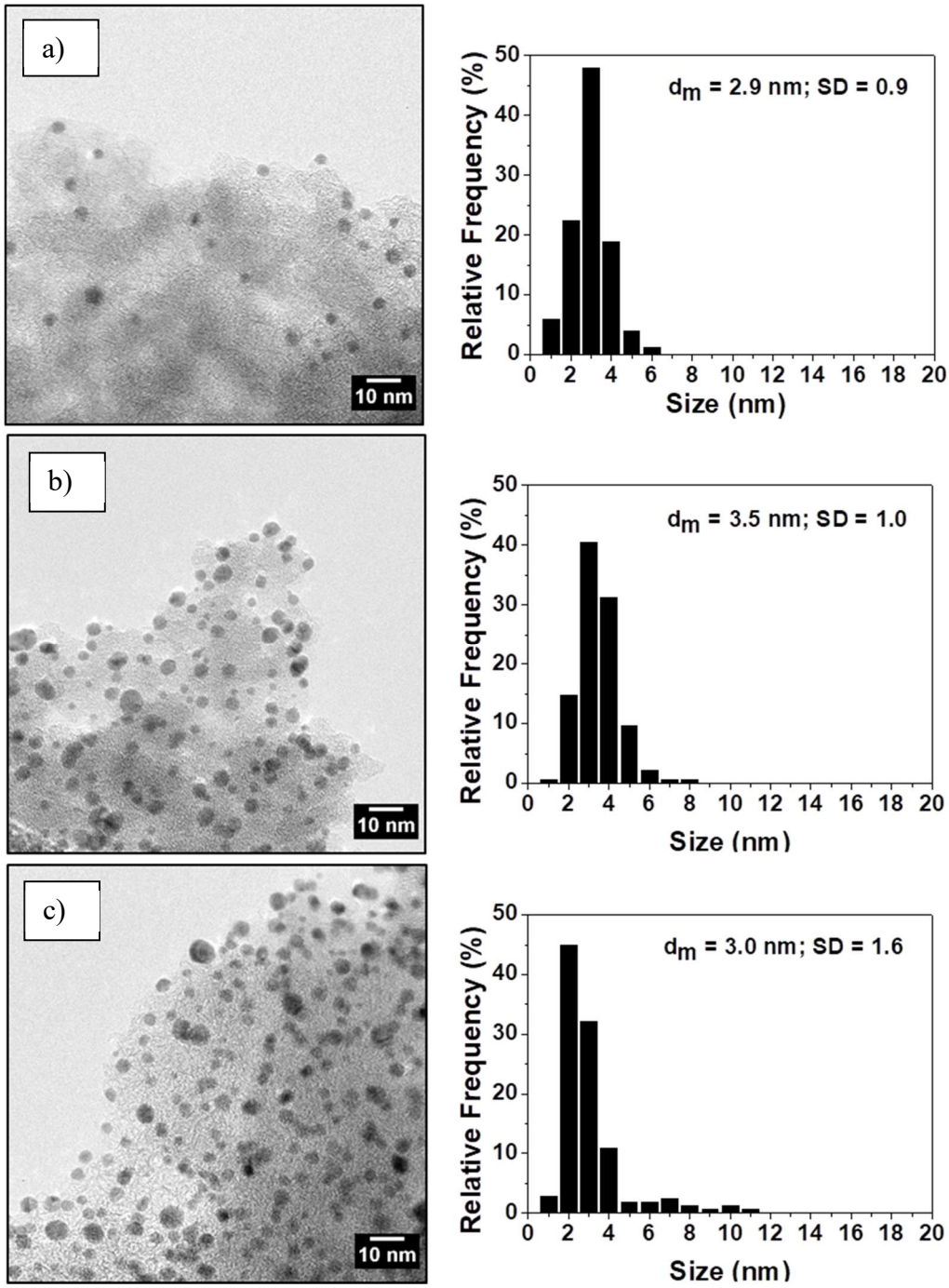

Figure 2-3. Representative HRTEM micrograph (left side) and histogram of particle size distribution (right side) of SOL derived Au/C_{Vulcan} (a); Au/C_{Norit} (b); Au@C_{X40S} (c).

These differences observed between the two different synthetic approaches (SMAD and SOL) can be explained by the presence of the PVA ligand in SOL preparation that can effectively limit in some extent the further Au nanoparticle growth in solution, also for long deposition times (active carbons). Also in the case where the carbon is less prone to give samples with less homogeneous nanoparticles, the capping agent is able to limit these phenomena, leading to more similar and comparable systems.

XPS characterization

X-ray photoelectron spectroscopy (XPS) of the different Au catalysts was performed in order to investigate the surface chemistry of the different carbons, the oxidation state and the exposure of Au at the surface. The chemical species present on the surface and their relative amount are summarised in Table 2-2 and the spectra are reported in Figure 2-4.

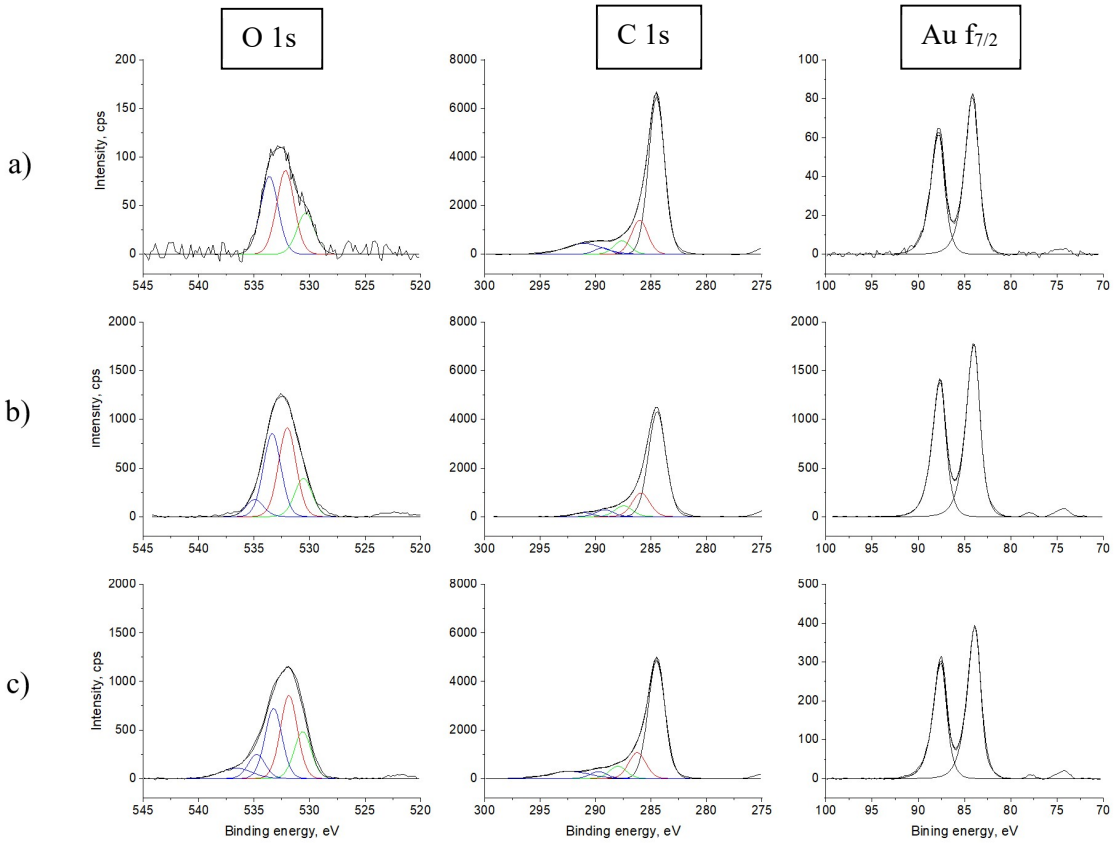

Figure 2-4. XPS O 1s, C 1s and Au $4f_{7/2}$ XPS spectra for (a) Au/C_{Vulcan}, (b) Au@C_{Norit}, and (c) Au@C_{X40S} synthetised by SMAD method.

Table 2-2. XPS analysis of Au carbon-supported Nanoparticles synthetised nanoparticles by SMAD and SOL method.

Catalyst		O 1s					C 1s				Surface Ratio		
		C=O	C-O-C	C-O-H	O-C=O	Ads. H_2O	C-C C-H	C-O	C=O	O-C=O	Au $4f_{7/2}$	Au/C	O/C
Vulcan	BE (eV)	531.7	-	533.1	534.2	–		285.7	287.1	288.8	-	-	0.009
	Rel. am. %	27.8	-	35.9	24.7	0.0	70.5	17.7	8.0	3.8	-	-	
Norit	BE (eV)	531.2	-	532.6	533.9	537.5		286.0	287.5	289.0	-	-	0.128
	Rel. am. %	12.9	-	30.9	15.9	3.3	69.7	17.1	8.0	5.2	-	-	
X40S	BE (eV)	531.3	-	532.6	534.0	537.2		285.7	287.2	288.8	-	-	0.101
	Rel. am. %	22.0	-	29.3	27.5	11.7	70.6	14.9	9.2	5.3	-	-	
SMAD Vulcan	BE (eV)	530.3	532.2	533.6	-	-	284.5	286.0	287.6	289.4	84.0	0.0007	0.008
	Rel. am. %	20.4	41.2	38.4	-	-	74.2	16.3	6.5	3.0	100		
SMAD Vulcan (used)	BE (eV)	530.7	532.3	533.6	-	-	284.5	286.1	287.5	289.0	84.1	0.0005	0.023
	Rel. am. %	17.2	38.3	44.6	-	-	75.9	15.9	5.9	2.2	100		
SMAD Norit	BE (eV)	530.6	532.0	533.2	535.1	-	284.5	285.9	287.5	289.2	83.9	0.0235	0.137
	Rel. am. %	16.8	39.2	36.6	7.4		71.7	16.2	7.4	4.7	100		
SMAD X40S	BE (eV)	530.6	531.8	533.2	534.7	536.3	284.5	286.3	288.0	289.8	83.9	0.0044	0.125
	Rel. am. %	19.3	34.1	28.8	9.9	7.9	72.0	16.0	7.6	4.3	100		
SOL Vulcan	BE (eV)	530.8	532.4	533.7	-	-	284.5	286.1	287.9	289.9	84.0	0.0008	0.010
	Rel. am. %	20.5	55.2	24.3			74.4	15.5	6.4	3.7	100		
SOL Vulcan (used)	BE (eV)	530.6	532.2	533.4	534.9	-	284.5	286.0	287.5	289.2	84.1	0.0010	0.019
	Rel. am. %	14.5	39.2	38.7	7.6		72.6	17.7	6.9	2.7	100		
SOL Norit	BE (eV)	530.5	532.1	533.2	534.8	-	284.5	285.9	287.0	288.6	83.9	0.0517	0.183
	Rel. am. %	11.4	42.1	37.4	9.1		68.5	18.3	8.2	5.0	100		
SOL X40S	BE (eV)	530.7	532.1	533.4	535.2	-	284.5	286.1	287.8	289.3	84.0	0.0393	0.157
	Rel. am. %	16.7	48.4	28.3	6.6		67.9	19.5	8.2	4.4	100		

[1] Reaction conditions: Glycerol 0.3M, free pH, Gly/metals= 2000 mol/mol, pO_2 = 3atm, T= 50 °C.
[2] initial activity calculated as: moles converted/moles of metal x h (0,25 h).
[3] Selectivity calculated at 30 % of conversion.

The data show a different oxygen content in the three carbonaceous supports, which remains unchanged after the nanoparticles deposition as highlighted by the comparison between SMAD samples. Norit shows the highest O/C ratio value (0.137), which is superior to the X40S (0.125) and one order of magnitude higher than Vulcan (0.008). The trend is also maintained in the SOL series, although the presence of PVA could alter the real values. We speculate that this trend may suggest a higher graphitisation degree in the case of Vulcan compared to Norit and X40S. The higher is the graphitisation degree and the lower is the space available for the carbon to coordinate with other heteroatoms, forming functionalisation groups. The oxygen species are dominated by the presence of C-O groups as indicated by the large signal present at binding energy (BE) of 285.9-286.1 eV for C 1s species and the two signals at BE at 531.8-532.4 and 533.2-533.7 eV corresponding to C-O-C and C-O-H, respectively for the O1s species (Table 2-2). A contribution at BE of 530.3-530.8 eV for O 1s species assigned to C=O evidenced also the presence of carbonyl groups. An additional contribution at BE of 534.8-536.3 eV corresponding to COOH groups was observed for Norit and X40S based catalysts. These signals confirm the highly functionalisation of the two Norit and X40S carbons. The Au XPS spectra collected for the catalysts show Au $4f_{7/2}$ BE at 83.9-84.0 eV (Table 2-2, see Figure 2-4, third column), which is consistent with the presence of metallic Au nanoparticles. No positively or partially-positive charged Au was detected; this can be ascribed also to the reducing nature of the carbonaceous supports. However, significant differences were observed in the relative amount of Au at the surface, which depends on the carbon used as support and the preparation method. Considering the support, Au exposure follows a similar trend as observed for oxygen species: the higher the O content the higher the Au exposure. It should be pointed out that BE shifts can also be slightly affected by differences in particle size. Vulcan catalysts characterised by smaller particle size, showed in fact a lower Au/C ratio than X40S and Norit (Table 2-2); Au/C ratio should increase by decreasing the particle size (given an equal metal loading) [68].

In general, a higher concentration of Au on the surface for Sol prepared catalysts compared to SMAD ones is observed. This behaviour could find an elegant explanation taking in consideration the PVA-protected Au nanoparticles. On one hand, these nanoparticles could be less prone to enter inside the carbon pores than SMAD prepared ones due to the presence of the capping agent which increases the hydrodynamic radius [43]. On the other hand, however, it could be related to the functional group of PVA: its

-OH groups could more efficiently interact with the carbon surface group retain the particle at the surface and therefore less prone to enter inside the carbon pores [36].

2.3.2. *Catalytic tests*

As mentioned in the Experimental Section (Chapter 4), the reactions were carried out in a glass reactor (30 mL capacity) at 50 °C and 3 bar of pure oxygen (the high stirring speed guarantees to work in kinetic regime and to avoid diffusion limitations). All the reaction parameters were optimised for this reaction and they were kept uniform for all the experiments performed in order to allow comparisons. The catalytic results are reported here below in Table 2-3.

Table 2-3. Au particle size and related catalytic results[1].

Catalyst	**Au particle size (nm)**	**Activity[2] (h^{-1})**	**Selectivity [3] (%)**				
			Glyceric acid	Tartronic acid	Glycolic acid	Oxalic acid	Formic acid
1%Au@C_{Vulcan} SMAD	2.5	952	48	10	15	-	8
1%Au@C_{Vulcan} SOL	2.9	1091	54	18	11	2	7
1%Au@C_{Norit} SMAD	3.9	154	52	2	16	-	9
1%Au@C_{Norit} SOL	3.5	519	61	11	4	1	7
1%Au@C_{X40S} SMAD	7.1	76	46	1	7	-	5
1%Au@C_{X40S} SOL	3.0	413	49	6	11	0.5	7

[1] Reaction conditions: Glycerol 0.3M, free pH, Gly/metals= 2000 mol/mol, pO_2 = 3atm, T= 50 °C.
[2] initial activity calculated as: moles converted/moles of metal x h (0,25 h).
[3] Selectivity calculated at 90 % of conversion for catalyst reaching complete glycerol oxidation, or at maximum conversion value for uncompleted glycerol oxidation.

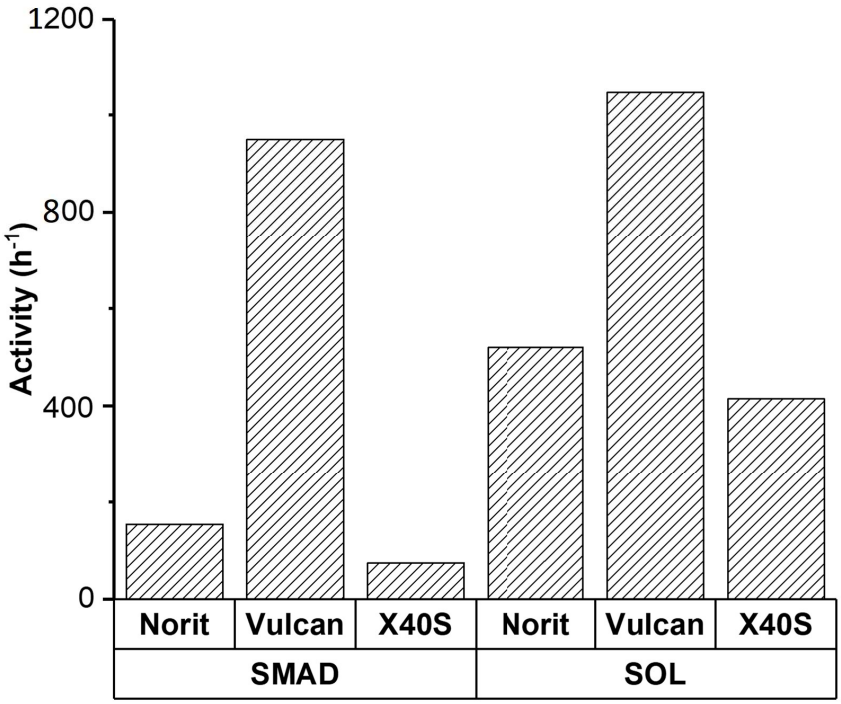

Figure 2-5. Comparison of the initial activities for Norit, Vulcan and X40S carbon synthesised by SOL and SMAD method.

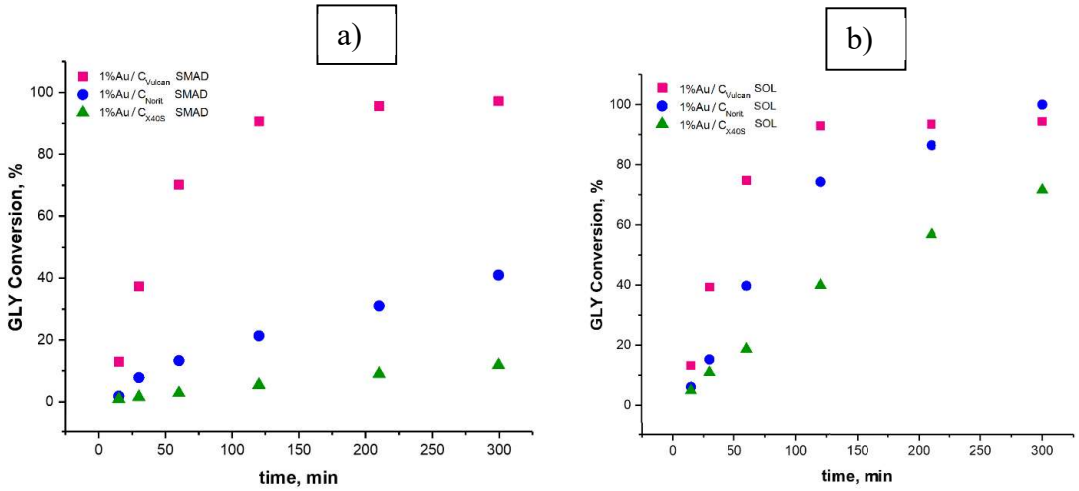

Figure 2-6. Glycerol oxidation conversion profile over Au Nanoparticles supported on Vulcan (□), Norit (○) and X40S (Δ) carbon synthesised by SMAD (a) or SOL (b) method.

From Figure 2-5 it is clear how Vulcan carbon supported catalysts showed the highest initial activity compared to Norit and X40S regardless the preparation method (952 and 1091 h^{-1}, for Au/C_{Vulcan} SMAD and Au/C_{Vulcan} SOL, respectively reported in Table 2-3). In the case of SMAD preparation, the different activity Au/C_{Vulcan} SMAD (952 h^{-1}) > Au/C_{Norit} SMAD (154 h^{-1}) > Au/C_{X40S} SMAD (76 h^{-1}), can be correlated with the different particle size. As reported in the introduction section, the activity of a catalyst is inversely proportional to its average nanoparticles dimension. Indeed, Au/C_{Vulcan} SMAD presents the smallest particle size (2.5 nm) and a narrow particle distribution, whereas

Au/C_{Norit}SMAD and Au/C_{X40S} SMAD samples showed larger particles (3.9 and 7.1, respectively) and a wider nanoparticles distribution (Figure 2-2 and Table 2-3).

The same catalytic trend was observed for SOL prepared catalysts: Au/C_{Vulcan} SOL (1091 h^{-1}) > Au/C_{Norit} SOL (519 h^{-1}) > Au/C_{X40S} SOL (413 h^{-1}) (Table 2-3). With the SOL catalysts set, however, the differences in terms of mean size are minimised: 2.9, 3.5 and 3.0 nm, for Au/C_{Vulcan} SOL, Au/C_{Norit} SOL, Au/C_{X40S} SOL respectively (Figure 2-3). In fact, it can be envisaged how PVA protected nanoparticles could maintain similar size even when supported on carbons with different morphology and surface properties, as already observed in the case of carbon nanofibers [36]. The capping agent can therefore influence the synthesis and it affects also the dimension of the nanoparticles, minimising the support influence. Thus, in this case, we were able to exclude an effect of the particle size on the different activity.

The higher Au exposure observed when Norit was used as support (Au/C ratio of 0.0517 and 0.0393 for Au/C_{Norit} SOL and Au/C_{X40S} SOL, respectively) can be the reason of the higher activity observed (519 and 413 h^{-1} for Au/C_{Norit} SOL and Au/C_{X40S} SOL, respectively – Table 2-3). However, this parameter cannot justify the highest activity of Au/C_{Vulcan} SOL, which present an Au/C ratio (0.008) of almost two orders of magnitude lower than the other two catalysts (Table 2-2). In this case, the catalytic results can be explained taking into account the nature of the different carbonaceous supports, and the lower content of oxygen and therefore of defects in Au/C_{Vulacn} SOL compared to Au/C_{Norit} SOL and Au/C_{X40S} SOL (O/C ratio of 0.010, 0.183 and 0.157, respectively, Table 2-2). In fact, Gil et al. have reported that carbonaceous supports with higher graphitisation degree and lower oxygen content promote the activity of Au based catalysts in glycerol oxidation. A lower number of structural defects led to Au particles strongly anchored to the orderly exposed graphite edges [70]. Overall, the carbon supports showed a comparable trend in terms of catalytic activity, that was X40S < Norit < Vulcan. The reason of this trend, however, can be found not only in different particle size or metal exposure but also in the different surface chemistry of carbons. Generally, the SOL method resulted in a series of catalysts more active than those prepared by SMAD.

All the catalysts showed glyceric acid as the major product (selectivity of 46 - 61%, Table 2-3), with tartronic acid (especially high for Vulcan SOL sample), produced by the successive oxidation of glyceric acid, and glycolic acid deriving from C-C cleavage, as by-products. We ascribe the notable conversion of the glyceric acid into tartronic acid to

the aforementioned high activity shown by Vulcan SOL sample. This consumption of the glycerate leads to the characteristic trend for an intermediate product transformation. This consecutive reaction became evident when the substrate is almost totally converted.

2.3.3. *Recyclability tests*

To test the resistance against deactivation, the catalysts that have shown the highest activity (Vulcan supported) were employed in multiple consecutive reactions. Recycling test were carried out by simply filtering the catalyst and re-using it without any further treatment. As reported in Figure 2-7, SMAD sample on Vulcan suffered of a rapid deactivation. In fact, after only 3 runs, the activity is reduced by ca. 60 %. On the contrary, the SOL derived sample showed a better stability (over 5 runs); the small decrease in activity observed can be attributed to an unavoidable loss of catalyst during the work-up of the reaction. This behaviour has to be addressed to the tendency of the carbon to remain stuck onto the filter surface. On the contrary, the small increase in activity between the first and the second run can be attributed to the loss of part of the protective agent as reported in a previous study [71]. Thus, the surface of the active sites is more available to actively participate to the glycerol transformation.

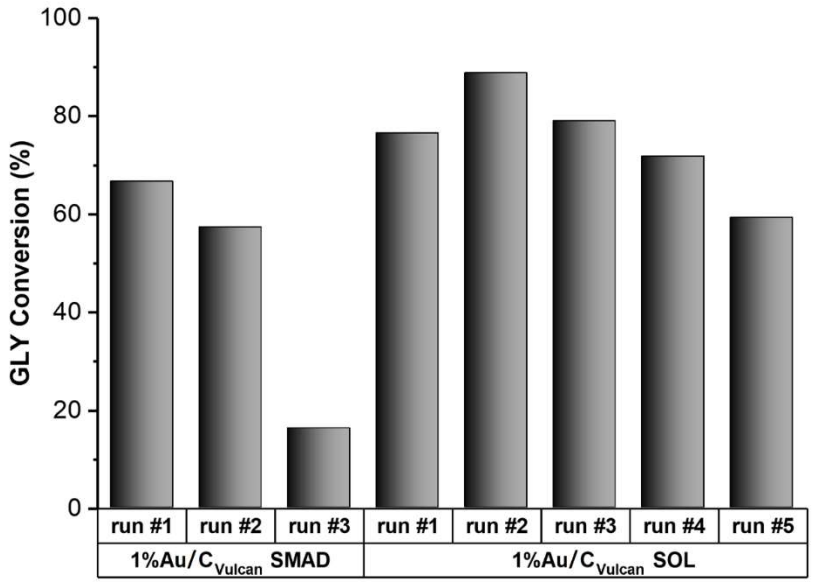

Figure 2-7. Reusability tests on Au/C$_{Vulcan}$ prepared by SMAD (left side) and SOL method (right side).

In order to better investigate the deactivation phenomena, further TEM analyses of the used catalysts were performed. In the samples analysed, the micrographs revealed only a slight increase of the Au Nanoparticles dimensions in respect to the corresponding freshly

prepared samples (d_m = 3.0 nm vs. 2.5 nm for the SMAD-derived catalyst and d_m = 3.6 nm vs. 2.9 nm for the SOL-derived one, Figure 2-8). Thus, the sintering of the nanoparticles with the consequent loss of activity has to be excluded. No leaching of noble metal was detected in the reaction solution; the analysis of the reaction mixture was carried out by means of ICP-OES analysis. In conclusion, decrease in glycerol conversion observed cannot be ascribed to the growth of the Au nanoparticles but, probably, to the irreversible adsorption of glycerol oxidation products which can partially block the active sites. Indeed, a higher content of oxygen on the surface of the catalyst after reaction was observed (Table 2-3). Further investigation, i.e. by means of IR spectroscopy resulted difficult to be performed, due to the carbonaceous origin of the substrates (complete absorption of the inquirer light).

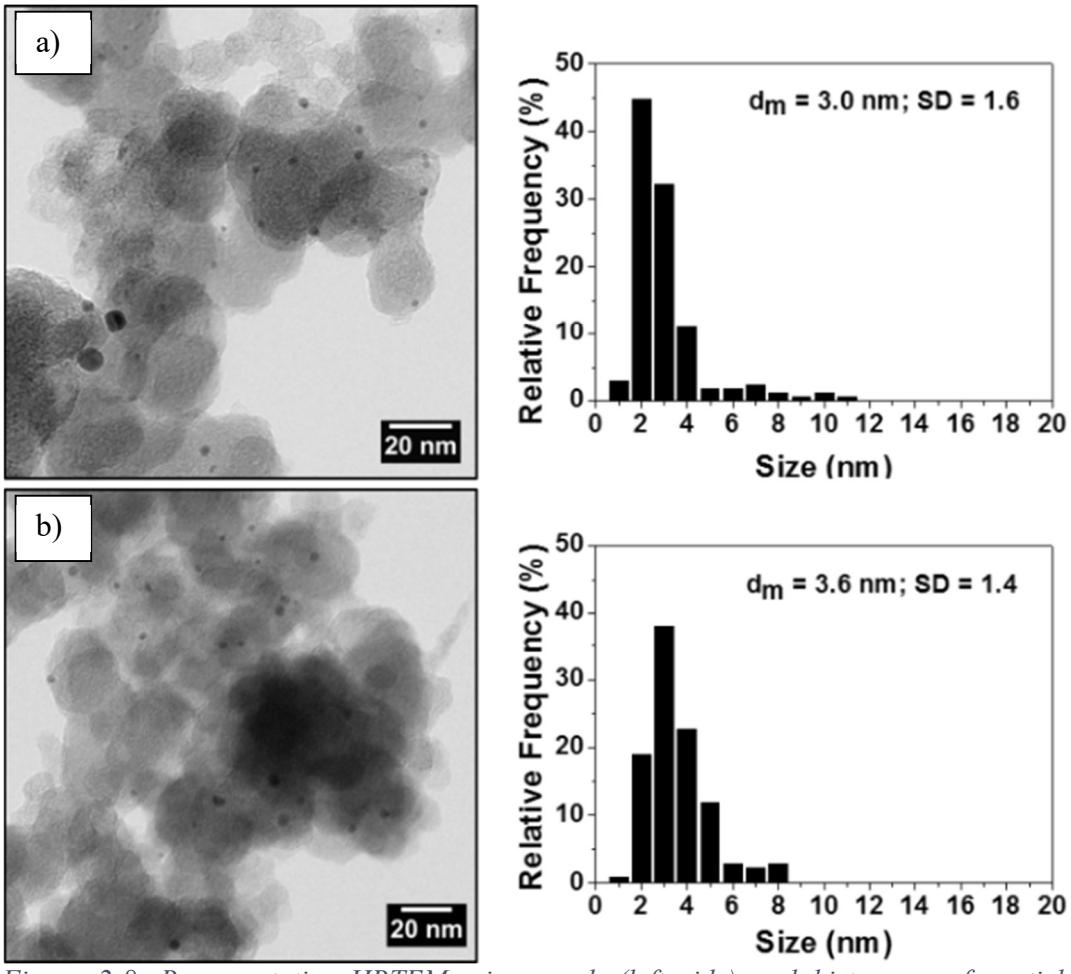

Figure 2-8. Representative HRTEM micrograph (left side) and histogram of particle size distribution (right side) of Au/C_{Vulcan} SMAD after the 3rd catalytic cycle (a) and Au/C_{Vulcan} SOL after the 5th catalytic cycle (b).

2.3.4. *Conclusions*

Two different methodologies (SOL and SMAD) were applied for preparing different set of Au catalysts on three types of carbonaceous supports: Vulcan, Norit and X40S. HRTEM and XPS analyses were carried out on all the catalysts in order to determine the main features of the catalysts in terms of particle size, particle distribution, metal surface exposure and functionalities of the supports. We observed by XPS analysis how both the synthetic techniques led to Au nanoparticles completely reduced, with no charged or partially-charged Au contribute. In particular, on Vulcan, Au nanoparticles showed narrow size and good dispersion, whereas on Norit and X40S a notably wider size distribution has been revealed. Overall, the carbon supports showed a comparable trend in term of catalytic activity. The order is X40S < Norit < Vulcan. The reasons of this trend however can be found not only in different particle size or metal exposure, but also in the different surface chemistry of the carbons. We observed that the higher O-containing functionalities of the support determined a higher exposure of Au nanoparticles at the surface but also an increased particle size. These two findings have an opposite effect on the catalytic activity of the samples. A lower particle size should correspond to a higher activity, while to a lower metal exposition should correspond a lower activity. The highest activity has been shown by SOL derived Au nanoparticles on Vulcan, samples that showed the lowest exposure of Au but the smallest particle size of the SOL samples. This sample was the only catalysts able to show a remarkable conversion of the glyceric acid into tartronic acid. Comparing SMAD and SOL samples supported on Vulcan, we observed a remarkable higher activity shown by SOL samples, despite the comparable nanoparticle's dimensions, and also differences between the selectivities. This difference can be addressed to the presence of the capping agent. Furthermore, SOL prepared samples have more comparable and similar nanoparticles, in term of particle size and size distribution: these has represented a key factor to better identify the support contribute. Finally, SOL sample on Vulcan showed a good stability upon recycling, while the SMAD sample underwent strong deactivation. Further TEM analyses showed that not significant changes in Au particle size is observed supporting the conclusion that deactivation is mainly due to irreversible adsorption of products on the surface of the nanoparticles.

2.4. Au-Ag bimetallic systems

Ag is one of the most employed catalyst in oxidation reactions [72–75]; Ag based catalysts are in fact used in gas phase oxidations due to their activity and peculiar selectivity towards the desired products [76] avoiding over oxidation or by-products formation [77]. Several are the examples of the utilisation of Ag catalysts in oxidation reaction, including ethylene [78] or methanol oxidation [79], but also in liquid media [77, 80–83]. However, its tendency to suffer from deactivation phenomena represent a severe drawback that is currently limiting its employment [84]. A possible solution to overcome this limitation is to combine Ag with a second metal, in particular Au. Au has been shown to be an excellent modifier in presence of other precious metals such as Pt and Pd [21, 85]. Au is able to confer resistance to deactivation and improve both activity and selectivity in alcohol oxidation [37, 86, 87].

AuAg bimetallic systems have been studied in CO oxidation, and also in the aerobic oxidation of glucose and alcohols showing a synergistic effect which depends on Au/Ag ratio and particle morphology [88–90]. Especially in selective oxidations, the Au-rich alloy and Au nanoparticles largely exceeded the activity of monometallic Ag nanoparticles. Furthermore, what makes more appealing this combination of metals is that Au-Ag bimetallic systems were rarely studied in glycerol oxidation and just few examples are present in literature [91, 92]. In this work, monometallic Au and Ag and bimetallic AuAg nanoparticles have been supported on two metal oxides, namely alumina (Al_2O_3) and titania (TiO_2). These two oxides, covered a remarkable role in Ag-based and metal-based systems, leading to active and durable catalysts [72, 75, 93–96].

Glycerol oxidation has been chosen as reaction, due to the importance of glycerol as a platform molecule [7, 97] but also because of the complex reaction pathway which allows to disclose a correlation between structure and activity/selectivity (Scheme 2-2).

2.4.1. *AuAg/Alumina*

For this AuAg/Al_2O_3 bimetallic system the target ratio will be in 4:1. These exceed in Au was exploit in order to limit as much as possible the deactivation phenomena, the worst drawback that Ag suffers. Our intention was revealing synergetic effects between the two metals and study the eventual influence of this combination also on selectivity. In order to follow our aim, we had to reveal the real structure of bimetallic AuAg particles and its impact on their catalytic efficiency, and even before that, be able to synthesise proper bimetallic nanoparticles. In order to pursuit our purpose we exploited two different synthetic techniques: sol-immobilisation (SOL) and solvated metal atom deposition (SMAD). In this way we were able to compare the effect of the synthesis methods on the features of the nanoparticles and then on their activity. For the two sets of catalysts prepared, the thermal treatment effect was further investigated through a calcination step in static air. This treatment helped to understand the effect of the protecting agent that surrounds the metal nanoparticles in the SOL prepared catalysts in comparison with "naked" nanoparticles obtained by SMAD. Monometallics for both techniques were prepared as a benchmark.

Electron microscopy characterization

The particle size distribution and dispersion of both mono- and bi-metallic catalysts were investigated by transmission electron microscopy techniques (TEM, HAADF STEM, and HAADF-STEM/EDS). A summary of particle size and size distribution for all the catalysts synthesised is presented in Table 2-4, along with the experimental metal loading measured by inductively coupled plasma - atomic emission spectroscopy (ICP-AES).

Table 2-4. Metal loading calculated by ICP-AES and mean particle size with the standard deviation, calculated by TEM.

Catalyst	Metal loading (%wt.) (target loading)		Mean diameter (nm)	Mean diameter (nm)
	Au	Ag	As prepared	Calcined*
Au/Al_2O_3 SOL	1.8 (1.8)	-	2.2 ± 0.7	1.9 ± 0.5
Au/Al_2O_3 SMAD	1.8 (2.0)	-	4.0 ± 1.0	7.2 ± 3.0
Ag/Al_2O_3 SOL	-	1.9 (2.0)	7.5 ± 5.1	11.2 ± 7.7
Ag/Al_2O_3 SMAD	-	1.0 (1.0)	4.0 ± 5.0	15.0 ± 5.0
$AuAg/Al_2O_3$ SOL	2.90 (2.8)	0.49 (0.4)	2.4 ± 0.7	2.8 ± 0.6
$AuAg/Al_2O_3$ SMAD	2.80 (2.8)	0.40 (0.4)	4.7 ± 1.7	7.8 ± 2.7

** 400 °C for 30 min in static air.*

In both Au monometallic samples, a high dispersion and distribution of the metal phase onto the alumina grains was observed, as can be observed by both HRTEM and STEM analysis (Figure 2-9 and Figure 2-10). In particular, a narrow particle size distribution was detected in the Au/Al_2O_3 SOL catalyst, within the 1.0 – 5.0 nm range (dm = 2.2 nm; Sd = 0.7 nm, Figure 2-9). However, as evidenced by the poor symmetry of particle distribution, the presence of not detectable particles below 1.0 nm cannot be excluded. Indeed, for the electronic microscope used, the cut-off size is ca. 1.0 nm. Previous studies already highlighted the presence of clusters (dozens of atoms) on the catalyst surface that are not characterisable with conventional HRTEM [98].

On the other hand, the Au/Al_2O_3 catalyst prepared by SMAD exhibited a size distribution between 2.0 and 7.0 nm (dm = 4.0; Sd = 1.0 nm, Figure 2-10), in agreement with previous reports on similar SMAD-derived Au catalysts on different supports [87, 99]. In the monometallic case the sol-immobilization techniques can thus lead to smaller Au nanoparticles, that we aspect to be more active in glycerol oxidation. In addition, HRTEM analysis highlights the crystalline nature of the alumina; in the micrographs (i.e. Figure 2-11), crystalline domains are easily detectable.

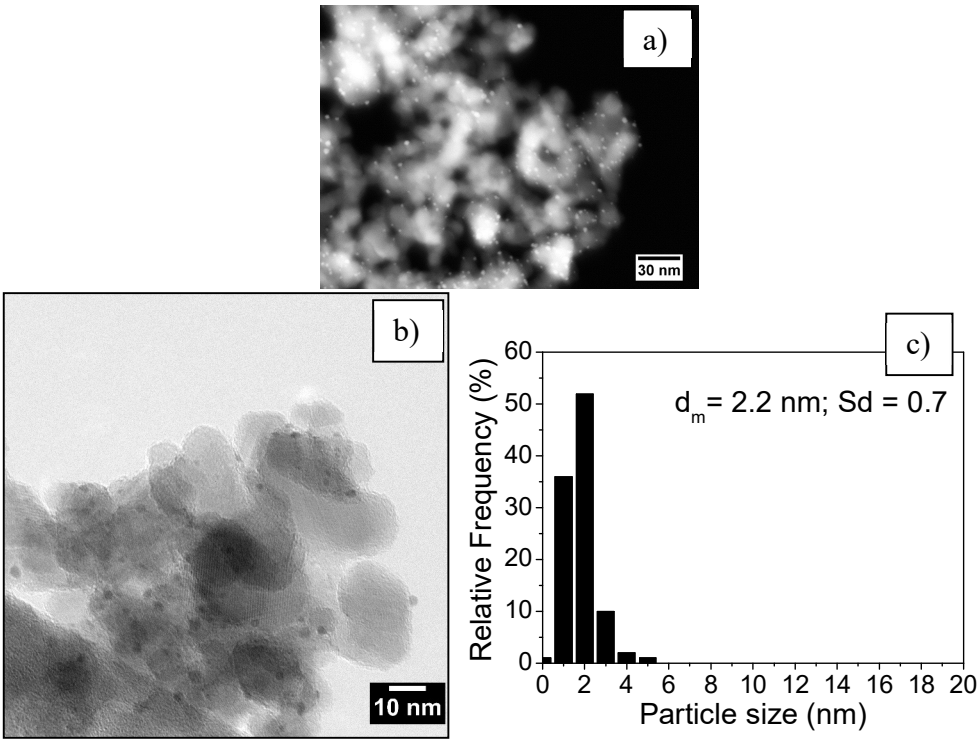

Figure 2-9. Representative (a) HAADF-STEM micrograph, (b) HRTEM micrograph and (c) histogram of particle size distribution of the Au/Al_2O_3 SOL catalyst as prepared.

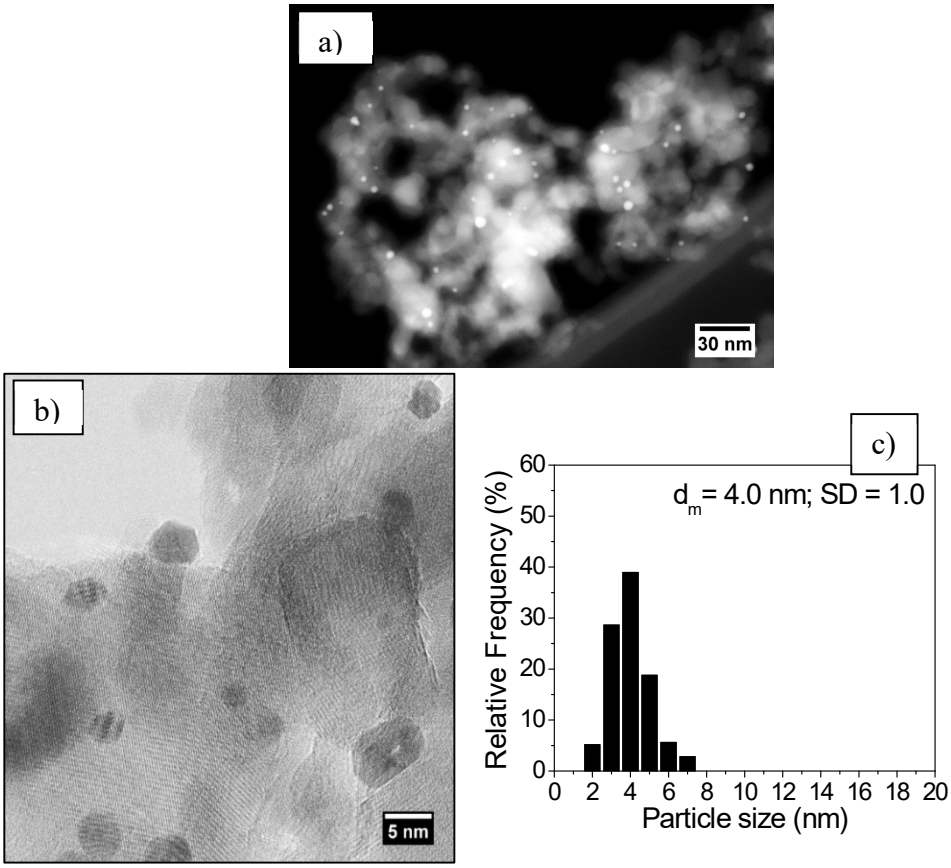

Figure 2-10. As prepared Au/Al_2O_3 SMAD: representative HAADF-STEM micrograph of catalyst grain (a), high resolution TEM micrograph (b) and histogram (c) of particle size distribution.

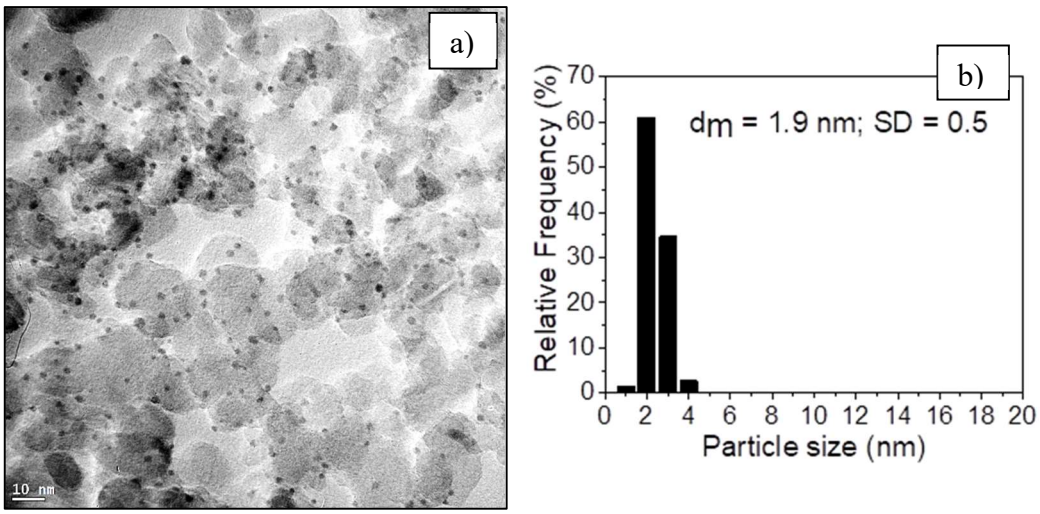

Figure 2-11. High resolution TEM micrograph (a) and histogram of particle size distribution (b) of calcined Au/Al_2O_3 SOL catalyst.

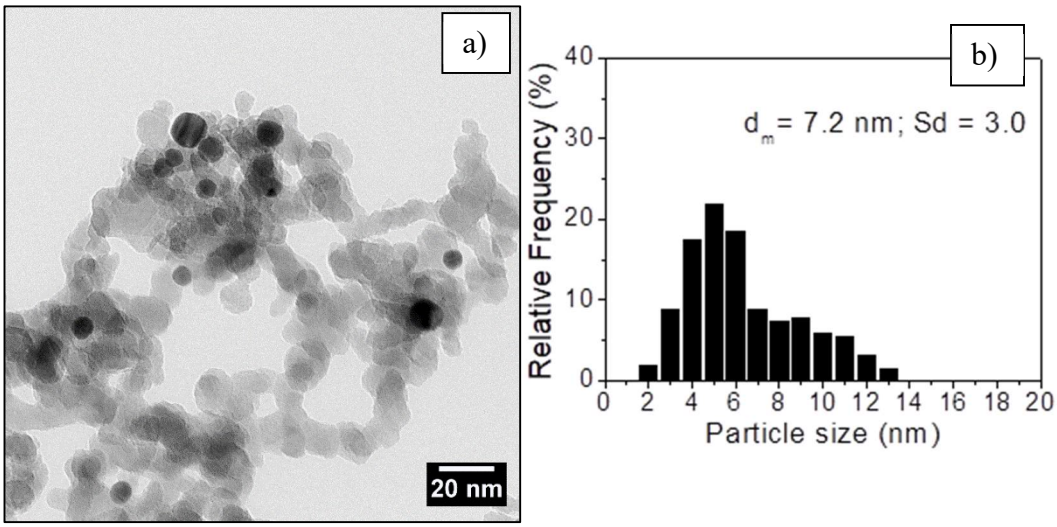

Figure 2-12. High resolution TEM micrograph (a) and histogram of particle size distribution (b) of calcined Au/Al_2O_3 SMAD catalyst.

Ag monometallic samples prepared by both methods presented wider particle size distribution compared to the Au-containing samples. (Table 2-4, Figure 2-13, Figure 2-14). Moreover, contrary to what observed for the Au monometallic samples, the SMAD synthesised samples possess smaller particles.

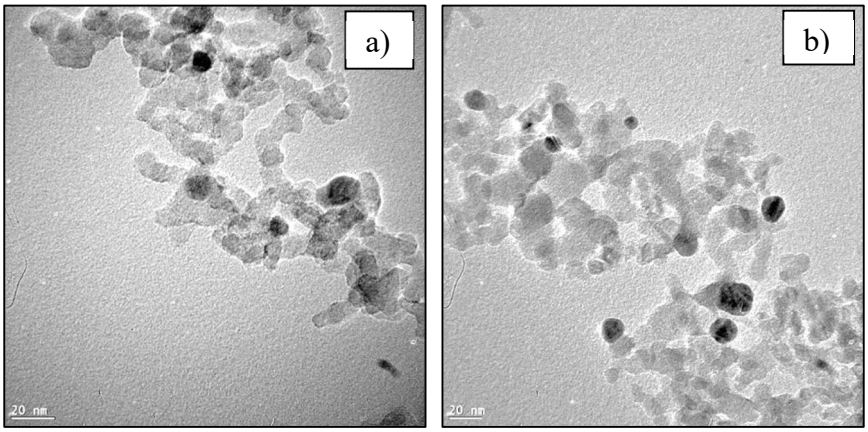

Figure 2-13. TEM micrograph of Ag/Al_2O_3 SOL in as prepared (a) and calcined state (b).

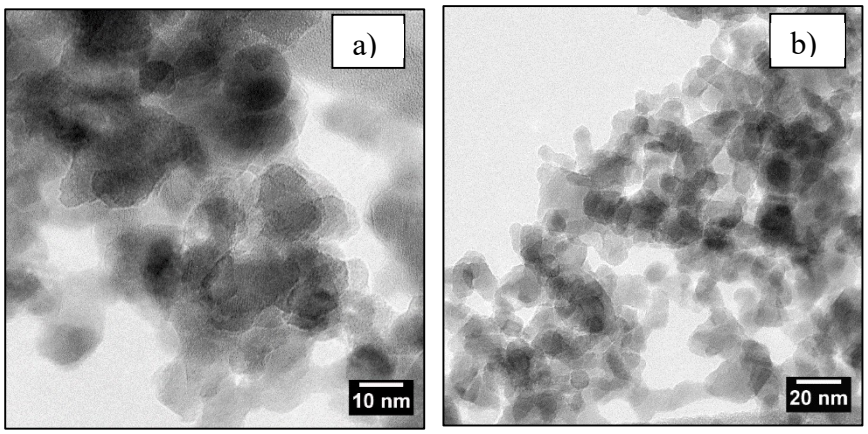

Figure 2-14. TEM micrograph of Ag/Al_2O_3 SMAD in as prepared (a) and calcined state (b).

Regarding the two bimetallic catalysts, in both $AuAg/Al_2O_3$ SOL (Figure 2-15) and $AuAg/Al_2O_3$ SMAD (Figure 2-16) samples, the support appeared densely populated by nanometric metal particles. By observing the size distributions, we can observe how the presence of Ag did not significantly affect the size of the metal nanoparticles with respect to Au monometallic ones. However, in SOL derived catalysts the mean particle size of the bimetallic sample (dm = 2.4; S_d = 0.7 nm) appeared very similar to that observed for the corresponding monometallic Au one whereas in the SMAD-derived sample a slightly broader particle size distribution was found (dm = 4.7 nm; S_d = 1.7 nm). It is important to highlight how comparable nanoparticles dimension allows to rule out any particle size effect during the discussion of the catalytic behaviours.

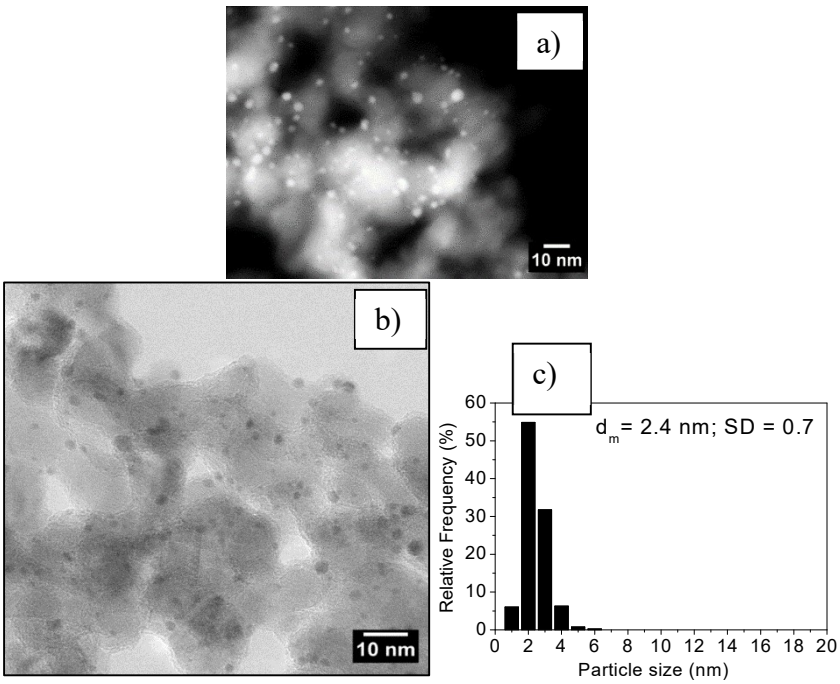

Figure 2-15. As prepared $AuAg/Al_2O_3$ SOL catalyst: representative HAADF-STEM micrograph (a), high resolution TEM micrograph (b) and histogram of particle size distribution (c).

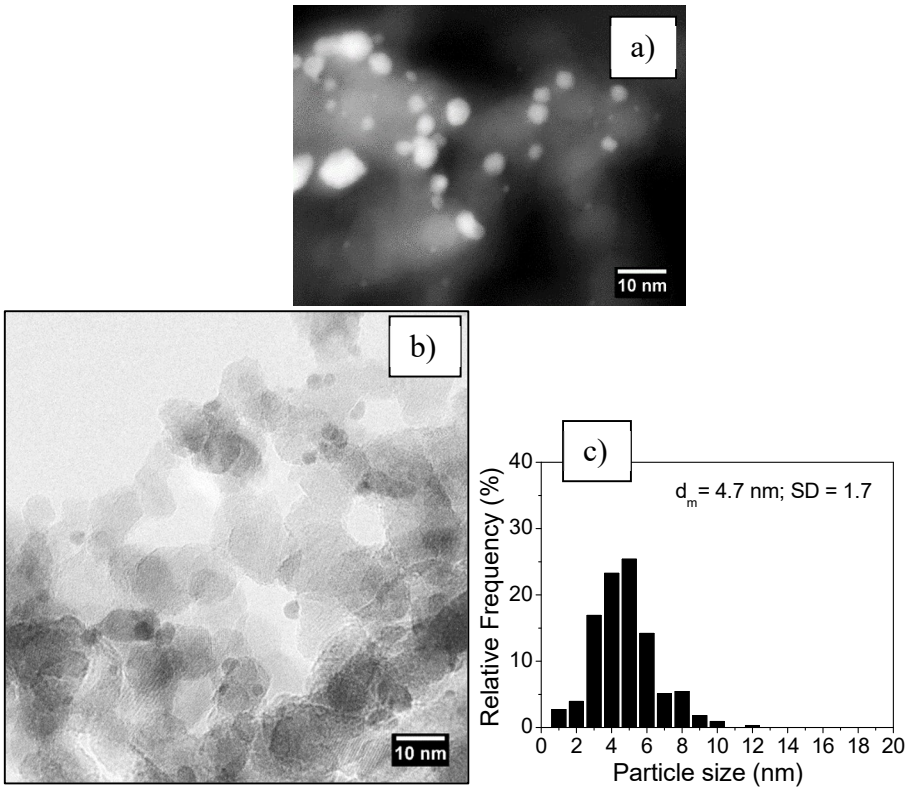

Figure 2-16. As prepared $AuAg/Al_2O_3$ SMAD catalyst: representative HAADF-STEM micrograph (a), high resolution TEM micrograph (b) and histogram of particle size distribution (c).

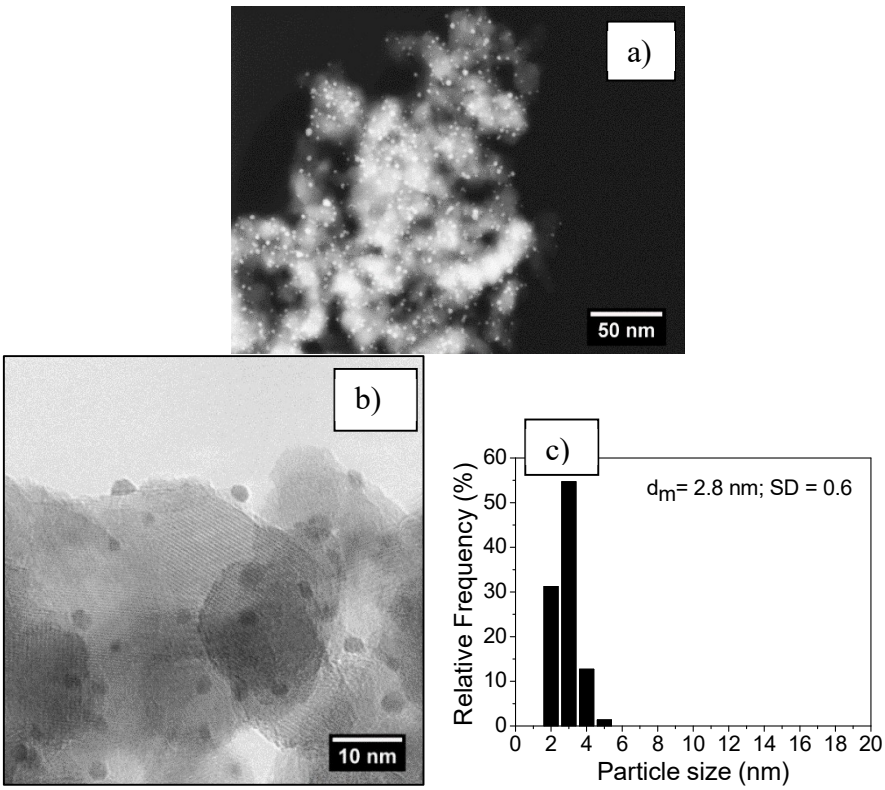

Figure 2-17. Calcined AuAg/Al_2O_3 SOL catalyst: representative HAADF-STEM micrograph (a) and Au (and Ag) atomic % measured on single metal particles by EDS analysis (b). High resolution TEM micrograph (c) and histogram of particle size distribution (d).

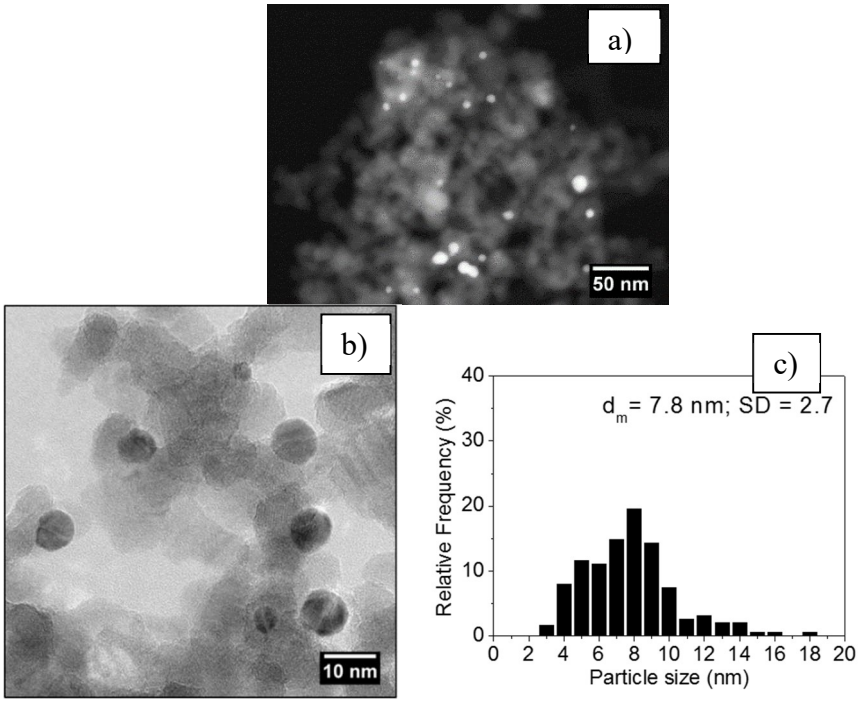

Figure 2-18. Calcined AuAg/Al_2O_3 SMAD catalyst: representative HAADF-STEM micrograph (a), high resolution TEM micrograph (b) and histogram of particle size distribution (c).

As discussed before, the metal composition of single nanoparticles is a crucial parameter in catalysis. For this reason, it is extremely important to be able to analyse the composition of the bimetallic nanoparticles. In order to deeply investigate the composition of the bimetallic particles, we have performed HAADF-STEM imaging coupled with X-ray energy dispersive spectroscopy (EDS) analysis.

For each sample, about fifteen particles were analysed in different locations well separated from their nearest neighbours and having particle size close to their mean diameter (i.e. 2–3 nm and 3–5 nm for AuAg SOL and SMAD, respectively). The results confirmed the coexistence of both metals, Au and Ag, in every single nanoparticles analysed (X-ray peaks at 2.12 and 2.98 KeV for Au atoms (M_α) and Ag atoms (L_α), respectively) for both bimetallic samples (Figure 2-19). Moreover, all the particles examined showed an average Au/Ag atomic ratio in good agreement with ICP-OES measurements: 83/17 for AuAg/Al_2O_3 SOL and 81/19 for AuAg/Al_2O_3 SMAD. This further confirms the successful preparation of bimetallic AuAg nanoparticles with a Au/Ag molar ratio of 4:1 with both sol-immobilisation and SMAD techniques.

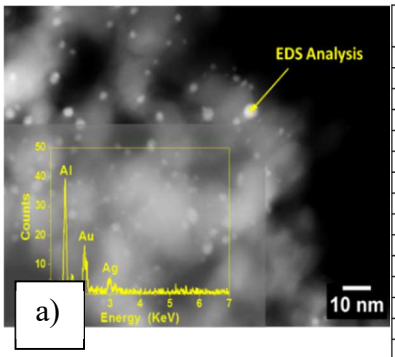

Particle	Au atomic %	Ag Atomic %
1	85	15
2	87	13
3	88	12
4	86	14
5	81	19
6	84	16
7	85	15
8	91	19
9	79	21
10	90	10
11	72	18
12	92	8
13	85	15
14	69	31
15	74	26
Average	83	17

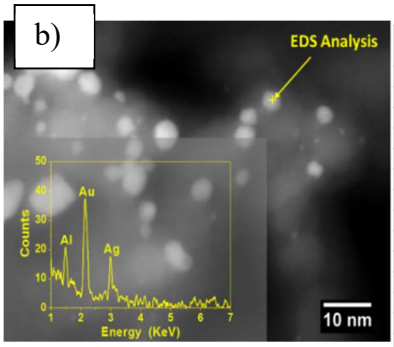

Particle	Au atomic %	Ag Atomic %
1	87	13
2	86	14
3	90	10
4	87	13
5	76	24
6	89	11
7	75	25
8	79	21
9	80	20
10	92	8
11	88	12
12	68	32
13	67	33
14	75	25
15	84	16
Average	81	19

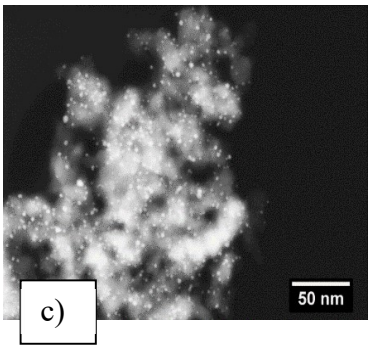

Particle	Au atomic %	Ag Atomic %
1	88	12
2	79	21
3	93	7
4	89	11
5	86	14
6	76	24
7	73	27
8	46	54
9	69	31
10	87	13
11	80	20
12	68	32
13	91	8
14	57	63
15	77	23
Average	77	23

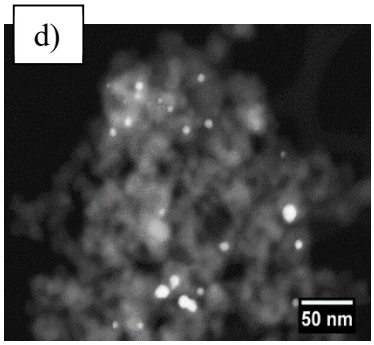

Particle	Au atomic %	Ag Atomic %
1	89	11
2	94	6
3	93	7
4	84	16
5	86	14
6	92	8
7	81	19
8	80	20
9	95	5
10	72	28
Average	87	13

Figure 2-19. Representative HAADF-STEM micrograph of (a) as prep. $AuAg/Al_2O_3$ SOL, (b) as prep. $AuAg/Al_2O_3$ SMAD (with relative EDX spectrum of the selected particle as example (yellow inset)), (c) Calcined $AuAg/Al_2O_3$ SOL and (d) Calcined $AuAg/Al_2O_3$ SMAD with corresponding Au (and Ag) atomic % measured on single metal particles by EDS analysis (right column).

In order to test the different thermal stability of the materials prepared by different synthetic approaches, and consequently the differences in terms of catalytic activity, we performed a calcination step for 30 minutes at 400 °C in static air. In addition, at these conditions, the protective agent used during the sol-immobilisation synthesis (PVA) decomposes. With this thermal treatment we were able to study the effect of the protective agent in term of resistance against sintering and the evolution of the bimetallic composition at the surface of the nanoparticles. Furthermore, performing the calcination also for the SMAD synthesised catalysts, a comparison can be made. A first investigation was performed by electron microscopy in order to evaluate the dimension of the nanoparticles. Regarding the SOL calcined samples, a high stability towards aggregation was observed. In fact, as summarised in Table 2-4, only a slight increase of the mean particle size was observed for both Au monometallic and bimetallic AuAg samples in respect to the analogous samples before the thermal treatment. On the other hand, the Ag

catalyst suffers of marked enlargement (from dm= 7.5 to 11.2 nm). The tendency of the Ag nanoparticles to spread onto the surface more than Au is due to its lower melting point. With the SMAD-derived samples, a more marked growth of the metal particles was observed (Au: dm= 4.0 nm as prepared vs. 7.2 nm calcined; AuAg: dm = 4.7 nm as prepared vs. 7.8 nm calcined, see Table 2-4). This trend could be associated with the lack of protecting agent. Once again, Ag nanoparticles underwent major sintering, with a mean particle size shifting from 4.0 nm to 15.0 nm.

XPS characterisation

XPS measurements were carried out in order to get information about the surface composition and the oxidation state of the elements. The analyses were carried out both before and after calcination. It is already established that the Au in monometallic samples, for both the synthesis techniques, is present in its zerovalent form [100]. In this case, the calcination step was conducted *in situ* in a pre-treatment chamber connected directly to the XPS spectrometer. The treatment was performed after recording the spectra of the as prepared catalysts.

Table 2-5. XPS results of catalysts.

	Ag $3d_{5/2}$[a]	Ag/Al[b]	Au $4f_{7/2}$	Au/Al[c]	Au/Ag[c]	AP[c]
Ag/Al_2O_3 SOL						
As prepared	368.6	0.013	-	-	-	718.6
Calcined	368.7	0.029	-	-	-	717.1
$AuAg/Al_2O_3$ SOL						
As prepared	368.0	0.005	83.9	0.011	2.25	719.6
Calcined	368.0	0.005	83.6	0.009	1.92	719.9
$AuAg/Al_2O_3$ SMAD						
As prepared	367.6	0.006	83.3	0.005	0.81	720.3
Calcined	368.1	0.007	83.3	0.003	0.52	719.3

[a] *binding energies (eV) of the corresponding photoelectron peaks.*
[b] *metal to metal ratios calculated from the peak area of the corresponding XP peaks (Al 2p, Ag 3d, Au 4f).*
[c] *Auger parameter of Ag. The sum of the binding energy of Ag $3d_{5/2}$ and the kinetic energy of Ag MNN Auger peak.*

Figure 2-20 shows the XPS spectra and the corresponding Ag MNN Auger peaks of Ag/Al_2O_3 SOL catalyst. The binding energy (B.E.) of Ag $3d_{5/2}$ peak did not changed significantly after calcination (Table 2-5) and it was slightly higher than reference metallic Ag (368.3 eV) [101]. In this particular case, it is possible to take advantage of Auger parameter to extract more information about the Ag oxidation state. Auger spectra have unique peak shapes and positions and they are useful for both the elemental identification and chemical state analyses. The Auger parameter (normally indicated as AP) is a calculated value from both photoelectron and Auger peak positions (AP = binding energy (Ag $3d_{5/2}$ eV) + Kinetic Energy (Ag MNN)). This parameter is particularly useful for chemical state analysis and can be used without interference of surface charging. In fact, it was essential in this case in order to determine the oxidation state of Ag after calcination. It has been previously reported that the Auger parameters determined for metallic Ag, AgO and Ag_2O, are 720.5, 718.4 and 717.8 eV, respectively [102]. In our case, the Auger parameter of the as prepared Ag SOL catalyst (718.6 eV) decreases after calcination (717.1 eV), so it can be concluded that the as prepared catalyst has metallic and ionic Ag on its surface, while after calcination only ionic Ag is present. The slightly increased Ag 3d peak intensity and so the higher Ag/Al ratio detected after calcination also refers to the oxidation of Ag. In fact, since Ag oxide has lower surface free energy than metallic Ag, it can spread on the alumina surface easier.

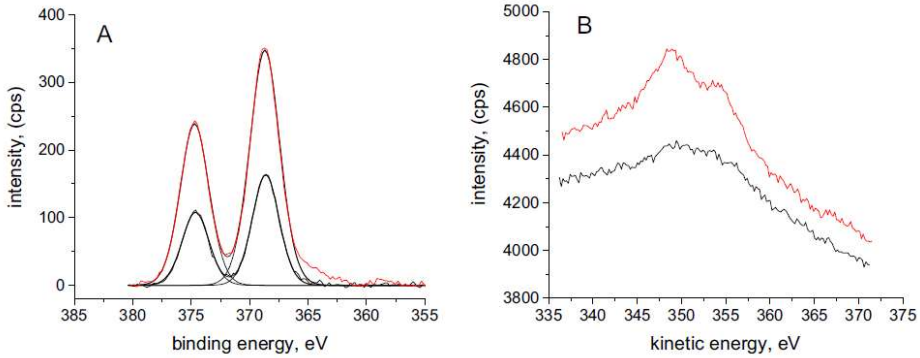

Figure 2-20. (A) Ag 3d region of Ag/Al_2O_3 SOL catalyst as prepared (black) and calcined (red - calcination at 400 °C); (B) Ag MNN region of the Ag/Al_2O_3 SOL catalyst as prepared (lack) and calcined (red).

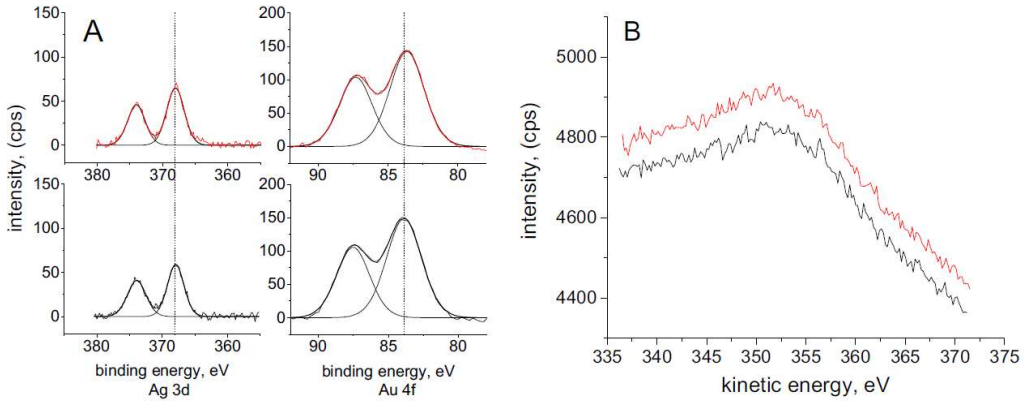

Figure 2-21. (A) XPS spectra of Ag 3d and Au 4f region for as prepared AuAg/Al_2O_3 SMAD catalyst as prepared (black) and calcined (red). (B) Ag MNN region of the catalyst as prepared (black) and calcined (red).

Similarly to the Ag/Al_2O_3 SOL catalyst, that presents similar binding energies of Ag 3d peaks (368.6 eV for the as prepared and 368.7 eV for the calcined), the as prepared and calcined AuAg/A_2O_3 SOL are identical in this case (368.0 eV). The values are 0.6–0.7 eV lower than in case of the monometallic catalyst. Furthermore, the calcination had no effect on the peak intensity (Figure 2-21-A). The Ag MNN Auger peaks (AP) of the bimetallic SOL catalyst were almost identical before and after calcination, the calculated AP is very close to that of the bulk metallic (Ag 720.5 eV) in both cases (719.6 and 719.9 eV respectively - Table 2-5) indicating the presence of only Ag^0. This means that the Ag is less prone to oxidation in the presence of Au, which suggests the presence of interaction between the two metals. The Au shows its tendency to confers resistance to passivation to the bimetallic particles as expected.

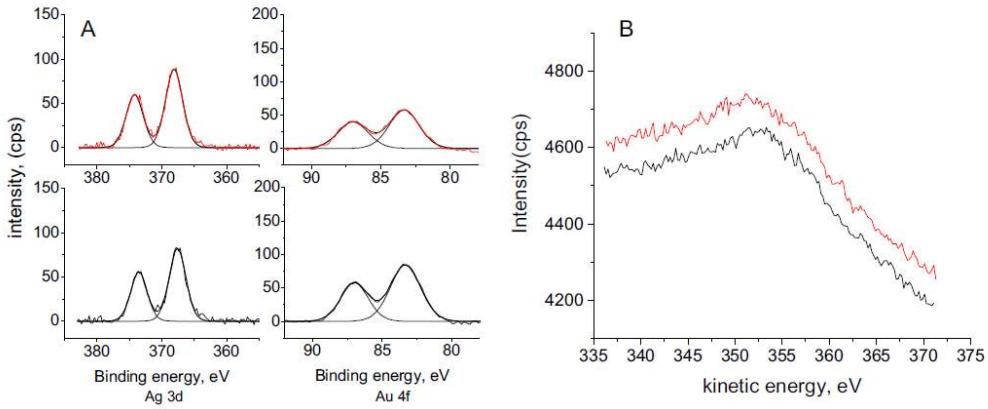

Figure 2-22. (A) XPS spectra of Ag 3d and Au 4f region of AuAg/Al_2O_3 SMAD catalyst (B) Ag MNN region of the catalyst as prepared (black) and calcined (red).

The binding energy of the Ag $3d_{5/2}$ peak of $AuAg/Al_2O_3$ SMAD catalyst slightly increased (Figure 2-22), while the calculated Auger parameter decreased from 720.3 to 719.3 eV after calcination, a stronger shift respect of what observed in the case of SOL. Thus, it is reasonable to deduce that in the case of bimetallic SMAD catalysts, Ag present a fraction of oxidised metal with respect to the case of SOL. Therefore, the effect of Au on the stability of Ag was weaker in this case. We ascribed this difference to the lower Au concentration on the surface: the initial Au/Ag ratio was 0.81 of the $AuAg/Al_2O_3$ SMAD catalyst compared to 2.25 calculated on the AuAg/ Al_2O_3 SOL sample. Generally, the metal with more tendency to be oxidised has the tendency to segregate to the surface of bimetallic nanoparticles [103].

Synchrotron light characterization

X-ray absorption fine structure (XAFS) spectroscopy was used in order study the nanostructure of the monometallic and bimetallic AuAg catalysts. Since Au and Ag have both face centred cubic (FCC) structures and very similar lattice parameters (Au_a = 4.08 Å and Ag_a = 4.09 Å) [104], a structural characterisation using techniques like X-Ray Diffraction (XRD) cannot be performed: being able to distinguish between Au and Ag is a difficult challenge to overcome. In this sense, XAFS spectroscopy, being element sensitive, allows probing separately the Au and Ag sites. Au and Ag, in fact, have different backscattering functions [105] and by means of XAFS analysis these atomic elements can be distinguished even when they are present as alloy. In order to extract the information needed, the X-ray absorption near edge region (XANES) spectra information on the electronic structure (oxidation state) of the monometallic and bimetallic catalysts was exploited. Analogously, using the extended x-ray absorption fine structure (EXAFS) spectra, information on the coordination shells around the Au and Ag central absorbing elements was determined. All the analyses were performed in the Grenoble's synchrotron and elaborated with the help of an expert (Doc. Antonella Balerna – affiliated to the Frascati National Laboratories (INFN) – Rome, Italy).

*Table 2-6. Distances (**R**), coordination numbers (**N**), distances and Debye Waller factors (σ^2) achieved for the Au foil sample and for the as prepared monometallic Au/Al_2O_3 and bimetallic $AuAg/Al_2O_3$ catalysts ($FT(k^3\chi(k))$ – (2.5-15)$Å^{-1}$ SOL samples) ($FT(k^3\chi(k))$ – (2.5-18)$Å^{-1}$ SMAD samples).*

	Coordination Shell	N	R (Å)	$\sigma^2(Å^2)$
Au Foil	Au-Au (I)	12 (fixed)	2.871(6)	0.0031(6)
(R-factor = 0.007)	Au-Au (II)	6 (fixed)	4.066(8)	0.0044(9)
Au/Al_2O_3 SOL	Au-Au (I)	7.6	2.828	0.007
(R-factor = 0.007)				
$AuAg/Al_2O_3$ SOL	Au-Au (I)	8.2	2.844	0.006
(R-factor = 0.006)	Au-Ag(I)	0.8	2.845	0.008
	Au-Au (II)	4.0	4.030	0.011
Au/Al_2O_3 SMAD	Au-Au (I)	10.8	2.863	0.0047
(R-factor = 0.008)	Au-Au (II)	5.4	4.057	0.0075
$AuAg/Al_2O_3$ SMAD	Au-Au (I)	9.1	2.862	0.0045
(R-factor = 0.009)	Au-Ag(I)	1.7	2.862	0.0055
	Au-Au (II)	4.4	4.056	0.0079
Ag Foil	Ag-Ag (I)	12 (fixed)	2.874(6)	0.0032(6)
(R-factor = 0.009)	Ag-Ag (II)	6 (fixed)	4.070(7)	0.0058(8)
Ag_2O	Ag-O (I)	2(fixed)	2.053	0.0034
(R-factor = 0.007)				
$AuAg/Al_2O_3$ SOL	Ag-O (I)	0.9	2.3	0.0067
(R-factor = 0.007)	Ag-Ag(I)	1.3	2.867	0.0049
	Ag-Au(I)	2.3	2.845	0.0082
$AuAg/Al_2O_3$ SMAD	Ag-Ag (I)	3.7	2.870	0.0048
(R-factor = 0.004)	Ag-Au(I)	3.2	2.862	0.0055

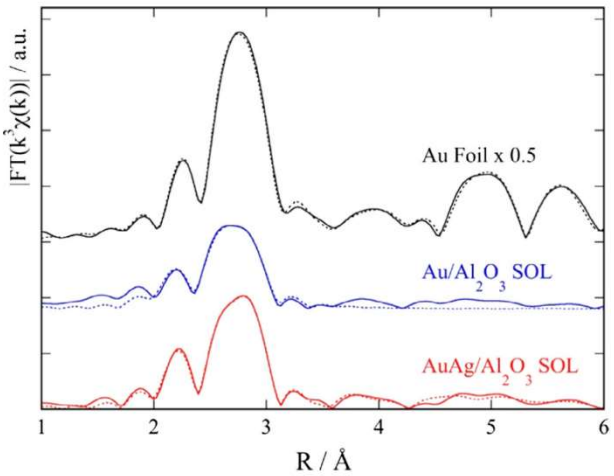

Figure 2-23. Fourier transforms of the experimental (full lines) and theoretical (dashed lines) EXAFS spectra of the as prepared Au and AuAg samples prepared by SOL procedure compared to the ones of the Au reference sample.

The EXAFS data analysis of the as prepared monometallic Au/Al_2O_3 SOL sample confirmed the presence of very small Au nanoparticles already observed by HRTEM. As clearly visible in Figure 2-23 and Table 2-6 the fitting procedure was limited to the first coordination shell. The results achieved show the presence of a relevant contraction of the first shell Au-Au distance and also a low coordination number. The coordination number found is smaller than the one theoretically predicted [106] for nanoparticles having a mean dimension of about 22 Å as found by the TEM data analysis (Table 2-4). While TEM identifies individual particles, EXAFS gives average coordination numbers of all absorbing atoms in the x-ray paths. The reason of the discrepancy in the particle size determination between EXAFS and TEM can be attributed to the fact that TEM is able to detect only particles above a specific cut-off size, whereas particles of all sizes contribute to the EXAFS signal. This could also justify the detected apparent decreasing of the mean diameter of Au SOL samples after calcination process (2.2 nm as prep. – 1.9 nm calc.). The aforementioned Au cluster not detectable by TEM could in fact, due to the restricted dimension, suffer of a liquefaction or partial liquefaction as consequence of the thermal treatment. This phenomenon could lead to an agglomeration of the clusters in small nanoparticles, at this point detectable with HRTEM: if the number of these small nanoparticles becomes influential, following a recount of the mean diameter, it could lead to an apparent decrease of the latter. It is well known that the estimation of the mean nanoparticle size using the first shell EXAFS coordination number, especially in the presence of very small dimensions, is strictly related to the atom packing and geometric arrangement used in the calculation [107] but in this case the result achieved using a

spherical model seems compatible with the other structural values found and with the XANES features as it will be shown. The distances (R) and the coordination numbers (N) found (Table 2-6) determine the presence of small Au nanoparticles having a mean dimension between 11 Å and 15 Å, therefore containing about 55 atoms, [108, 109] seems to confirm the hypothesis assumed about the discrepancy between the TEM and EXAFS results. This means that the surface (potentially catalytically active) atoms represent average more than the 70 % of the total number of atoms [110].

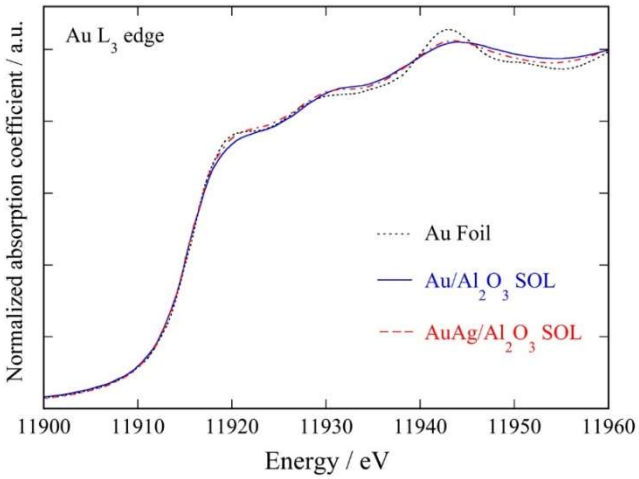

Figure 2-24. XANES spectra of the Au and AuAg samples prepared by SOL procedure compared to the ones of the Au reference sample

The small nanoparticles size is also clearly visible in the XANES spectra reported in Figure 2-24 where the feature at about 11920 eV (Au white-line) has a lower intensity and the other features are shifted to higher energy values compared to the ones of the Au foil. This shift is normally attributed to smaller interatomic distances [108] while the intensity of the white-line is related to the presence of unoccupied 5d states or d-holes [87]. In Au bulk the presence of this white line is related to the s-p-d atomic level hybridization that gives a partial depletion of the filled $5d^{10}$ orbitals (the higher the number of d-holes, the higher the intensity of the white line). In the presence of small Au nanoparticles, the reduced number of Au-Au bonds reduces this hybridisation, resulting in an increase of the 5d level occupancy and hence in a decrease of the intensity of this feature.

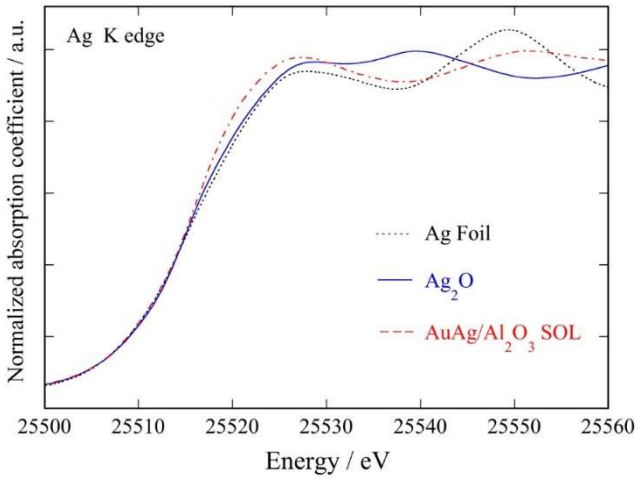

Figure 2-25. XANES spectra of the AuAg sample prepared by SOL procedure compared to the ones of the Ag and Ag_2O reference samples

Moving from the monometallic to the bimetallic $AuAg/Al_2O_3$ SOL sample and taking into account the XANES spectra, an increase of intensity of the white line and also a lower energy shift of the other features is clearly observable (Figure 2-25). As shown in Table 2-6 there is an evident increase of the first shell Au-Au coordination number and interatomic distance, meaning that the presence of Ag has an effect on the size of the Au nanoparticles (as observed also by TEM analysis). The fitting procedure of this sample was also extended to the second FCC Au-Au coordination shell. In order to fit the first coordination shell, a small (N= 0.8) Au-Ag contribution had to be included.

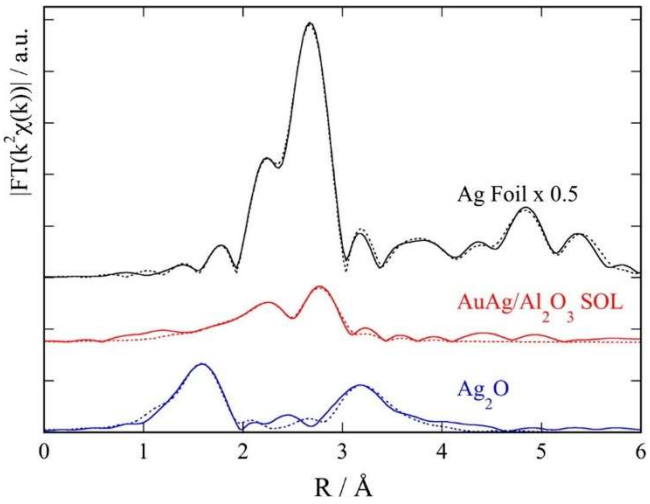

Figure 2-26. Fourier transforms of the experimental (full lines) and theoretical (dashed lines) EXAFS spectra of the AuAg sample prepared by SOL procedure compared to the ones of the Ag and Ag_2O reference samples.

On this sample, measurements were performed also at the Ag K edge to test the Ag site. The fitting procedure of the bimetallic sample was limited to the first coordination shell (Figure 2-26).

As reported in Table 2-6 three contributions had to be included: Ag-O, Ag-Ag and Ag-Au. From the EXAFS data analysis of the first coordination shell of this bimetallic sample, at the Au and Ag edges, we achieved four partial coordination numbers: N_{Au-Au}, N_{Au-Ag}, N_{Ag-Au} and N_{Ag-Ag}. The total coordination numbers at the two edges are respectively $N_{AuM} = N_{Au-Au} + N_{Au-Ag} \approx 9$ and $N_{AgM} = N_{Ag-Au} + N_{Ag-Ag} \approx 3.6$. Since $N_{AgM} < N_{AuM}$, this means that Ag atoms are segregated to the surface (surface atoms have fewer neighbours) while Au atoms are mostly confined to the core [111]. These results are in line with what extracted from XPS analysis. Considering the values of the coordination numbers found at both edges we can determine that the atoms of the Ag shell are not uniformly distributed on the Au core being the metallic Ag amount (N_{Ag-Ag}) very small. On the other hand, the N_{Ag-Au}, R_{Ag-Au} and N_{Au-Ag}, R_{Ag-Au} values suggest some mixing between Ag atoms with Au probably at the surface of the Au-rich cores [112, 113]. The Ag-O contribution found in the analysis of the data around the Ag site, whose presence is also visible in the XANES spectra reported in Figure 2-25, can be related to a surface oxidation or an interaction with the Al_2O_3 substrate (Ag dispersion on Al_2O_3) or with the oxygen containing group of PVA.

As clearly visible in Figure 2-26 and Table 2-6 the Ag-O distance in the Ag_2O reference sample (2.05 Å) is much shorter than the one found in the bimetallic SOL sample (2.3 Å). The large Ag-O distance found is in agreement with the values obtained for Ag/Al_2O_3 samples containing ionic species of Ag [114]. This means that the strength of the chemical bond between Ag and O in this bimetallic sample is weaker than that of Ag_2O. Therefore, this Ag-O contribution could be ascribed to the interaction between Ag and the oxygen containing group of PVA and/or Al_2O_3.

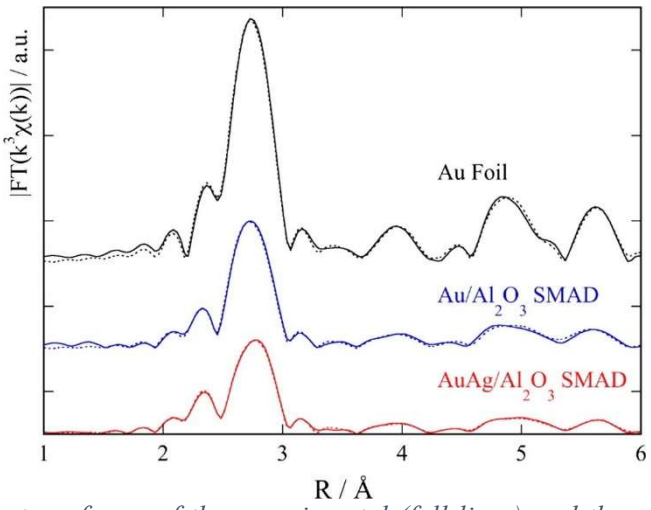

Figure 2-27. Fourier transforms of the experimental (full lines) and theoretical (dashed lines) EXAFS spectra of the Au and AuAg samples prepared by SMAD procedure compared to the ones of the Au reference sample.

The structural characterisation of the monometallic Au and bimetallic AuAg samples, prepared using the SMAD procedure, revealed big differences if compared to the one of the SOL samples. As shown in Figure 2-27 both SMAD samples show an FCC structure up the higher coordination shells: in Table 2-6 results achieved for the first and second coordination shells are reported. The coordination number of the first shell of the monometallic Au sample, given by the fitting procedure is very close to the one theoretically predicted for nanoparticles having a mean dimension of about 40 Å as found by the TEM data analysis (N = 10.8) [106].

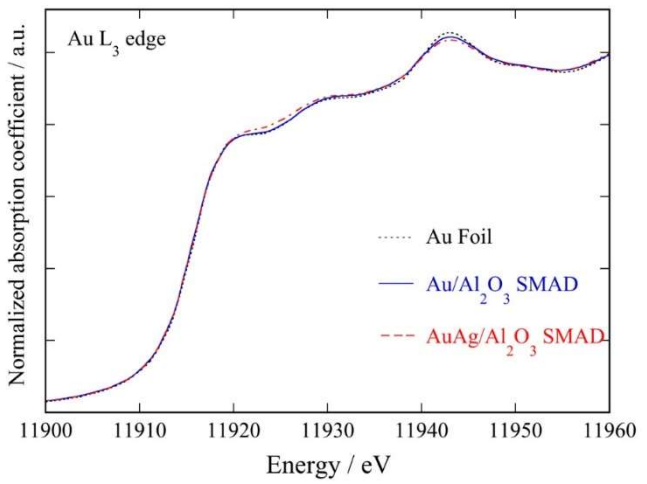

Figure 2-28. XANES spectra of the Au and AuAg samples prepared by SMAD procedure compared to the ones of the Au reference sample.

The mean size of the monometallic SMAD nanoparticles is larger than the SOL ones and this is evidenced by the presence of the Au higher coordination shells (Figure 2-27) but also by the XANES features shown in Figure 2-28 that are very similar to the ones of the

Au reference sample. In the fitting procedure of the bimetallic AuAg SMAD sample, an Au-Ag contribution had to be included only for the analysis of the first coordination shell. As shown in Figure 2-28, for this sample there is an increase of the XANES feature at 11920 eV that is related to changes in the electronic structure of Au that gives a d-charge reduction (or increase of d-holes) [87]. In the case of the bimetallic AuAg SOL samples the effect observed in the XANES region could be related to the increase of the nanoparticle mean dimension; on the other hand, in the case of the AuAg SMAD sample this effect is due to the presence of Ag. The XANES sensitivity can probe changes in the Au 5d charge redistribution given by small charge transfer from Au to Ag [115]. The presence of Ag in this bimetallic sample is higher than in the SOL sample. This is given by the coordination numbers found in the analysis of the EXAFS data at the Au and Ag sites (Table 2-6). The total coordination numbers at the two edges in this case are respectively $N_{AuM} = N_{Au-Au} + N_{Au-Ag} = 10.8$ and $N_{AgM} = N_{Ag-Au} + N_{Ag-Ag} = 6.9$. Being $N_{AgM} < N_{AuM}$, this means that also in the bimetallic SMAD sample Ag atoms are segregated to the surface while Au atoms are mostly confined to the core [111]. Taking into account the values of the coordination numbers found at both edges we can now determine a higher presence of Ag atoms on the Au core surface being now the metallic Ag amount $N_{Ag-Ag} = 3.7$ and N_{AgM} (SMAD) > N_{AgM} (SOL; $N_{Ag-Ag} = 1.7$).

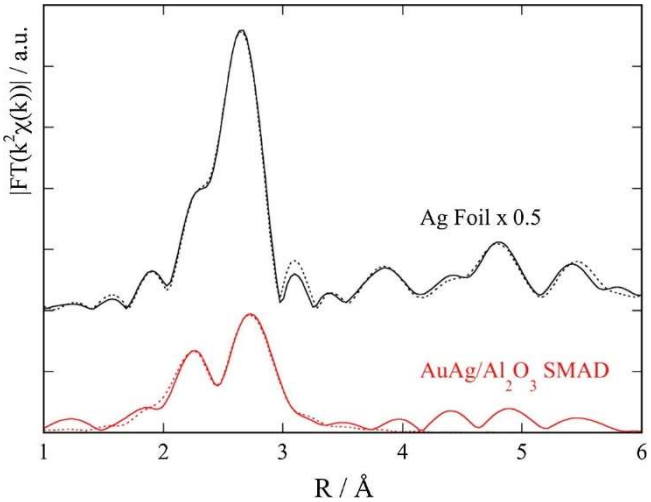

Figure 2-29. Fourier transforms of the experimental (full lines) and theoretical (dashed lines) EXAFS spectra of the AuAg sample prepared by SMAD procedure compared to the one of the Ag foil reference sample.

Probably due to the bigger dimension of the bimetallic nanoparticles of the SMAD sample in the EXAFS, analysis of the Ag site data showed no Ag-O contribution (Figure 2-29). XPS and EXAFS analyses stated that in both bimetallic samples there are bimetallic

particles with Au-rich core and an Ag-rich shell, but the surface Au/Ag ratio is higher in the SOL prepared sample. Based on the XPS results the electronic structure is also different, being the Ag in the SOL prepared catalyst more resistant to oxidation. We thus expect a different behaviour in the catalytic test carried out under oxidative conditions.

Catalytic tests

The catalysts prepared and characterised were finally tested in the oxidation of glycerol. The results are reported in Figure 2-30 (as prepared catalysts) and in Table 2-7. As mentioned in the Experimental section (Chapter 4), the reactions were carried out in a glass reactor (30 mL capacity) at 50 °C, 3 bar of pure oxygen and a stirring speed of 1250 rpm (the high stirring speed guarantees to work in kinetic regime and to avoid diffusion limitations, while the other parameters were optimised for this type of reaction and kept uniform for all the experiments in order to allow comparisons).

Table 2-7. Catalytic results.

Catalyst	Thermal Treatment	Initial activity	Conversion (2h)	Selectivity (%)*				
		(h^{-1})	(%)	GA	GlyA	TA	FA	OxA
Au/Al_2O_3 SOL	-	247	65.9	52.5	11.2	9.1	6.8	1.0
Au/Al_2O_3 SOL	Calc.	810	93.3	37.6	6.6	20.4	3.5	3.4
Au/Al_2O_3 SMAD	-	144	9.8	43.7	28.9	0.0	20.2	0.0
Au/Al_2O_3 SMAD	Calc.	372	37.2	49.0	19.1	1.9	13.4	0.9
Ag/Al_2O_3 SOL	-	< 1	0	-	-	-	-	-
Ag/Al_2O_3 SOL	Calc.	< 1	0	-	-	-	-	-
Ag/Al_2O_3 SMAD	-	< 1	0	-	-	-	-	-
Ag/Al_2O_3 SMAD	Calc.	< 1	0	-	-	-	-	-
$AuAg/Al_2O_3$ SOL	-	771	82.1	33.8	14.3	23.0	8.5	5.9
$AuAg/Al_2O_3$ SOL	Calc.	936	> 99	28.4	10.1	26.5	5.4	5.6
$AuAg/Al_2O_3$ SMAD	-	853	43.6	51.2	10.4	10.1	7.4	2.3
$AuAg/Al_2O_3$ SMAD	Calc.	194	23.2	53.1	22.1	5.7	12.6	2.0

**values calculated at 90 % of conversion; where the target conversion is not reached the values were taken at the maximum conversion. Reaction conditions: Glycerol 0.3M, Gly/NaOH = 1/4 mol/mol, Gly/metals= 2000 mol/mol, pO_2 = 3atm, T= 50 °C.*

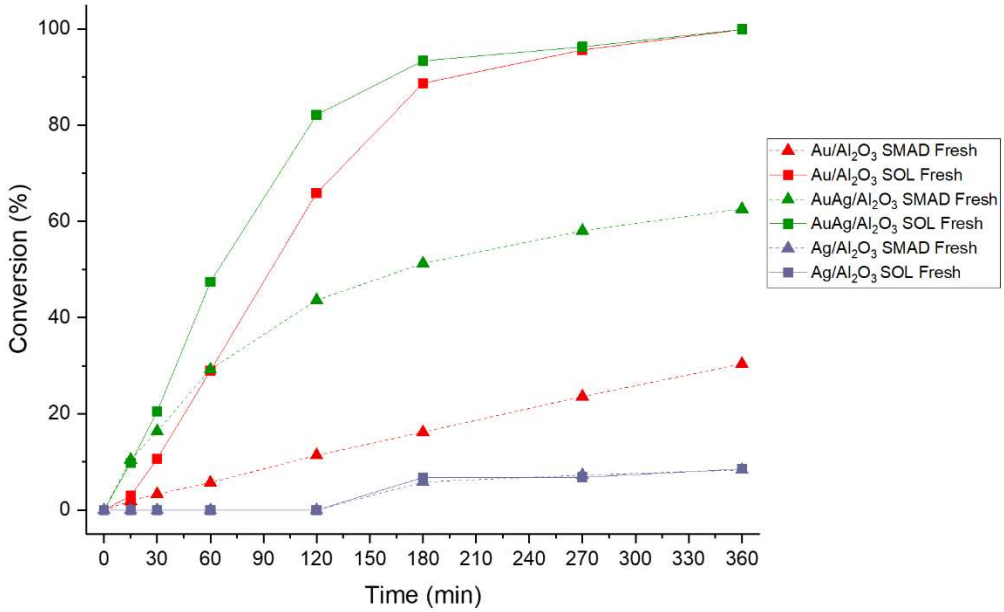

Figure 2-30.Glycerol oxidation profiles for as prepared samples. Reaction conditions: Glycerol 0.3M, Gly/NaOH = 1/4 mol/mol, Gly/metals= 2000 mol/mol, pO_2 = 3atm, T= 50 °C.

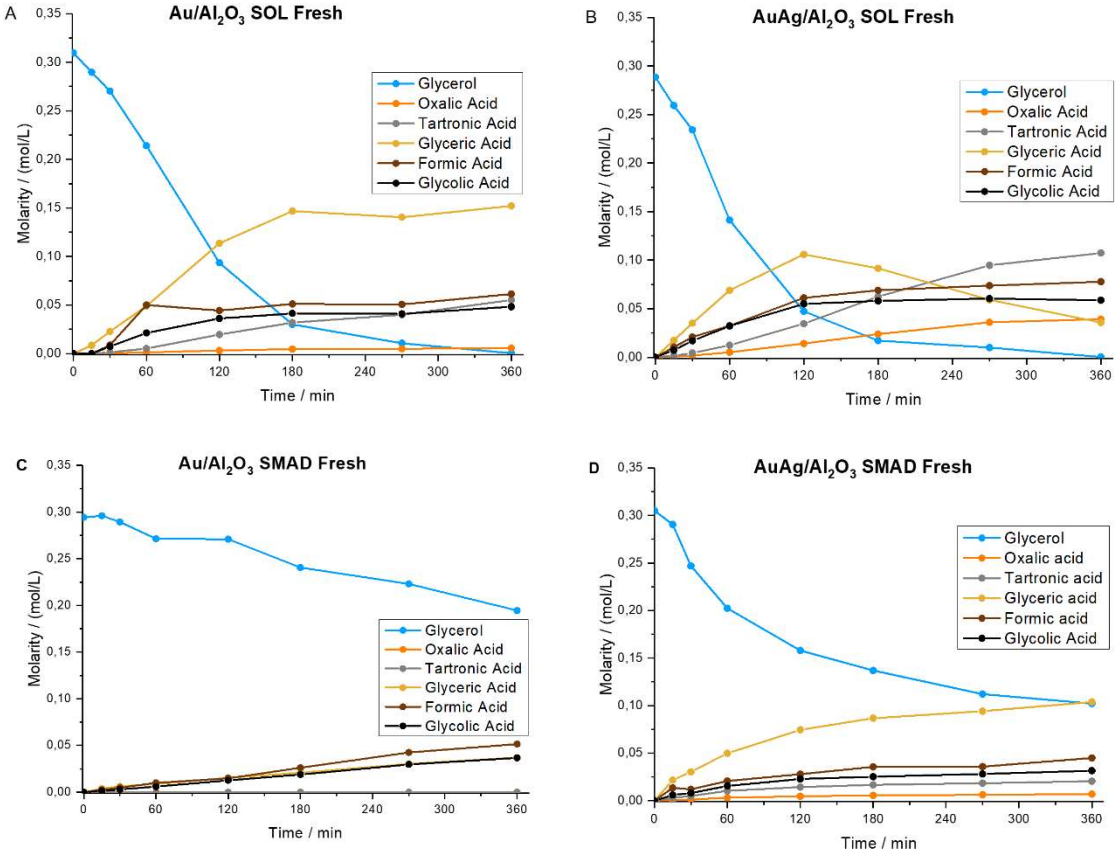

Figure 2-31. Product distributions in glycerol oxidation of as prepared samples with (A) Au/Al_2O_3 SOL fresh, (B) $AuAg/Al_2O_3$ SOL fresh, (C) Au/Al_2O_3 SMAD fresh (D) $AuAg/Al_2O_3$ SMAD fresh catalysts. Reaction conditions: Glycerol 0.3M, Gly/NaOH = 1/4 mol/mol, Gly/metals= 2000 mol/mol, pO_2 = 3atm, T= 50 °C.

From these data we can observe a correlation between the two preparation techniques, the features of the nanoparticles and the combination of the two metals with the catalytic activity. In general, the SOL prepared catalysts lead to a more active catalysts compared with the prepared by SMAD. This is a first result that proves how the preparation method can influence the final catalytic activity of the catalyst.

Taking in consideration the as prepared samples, in the case of monometallic Au catalysts, the activity of SOL and SMAD catalysts were very different, being the SOL much more active than the SMAD (247 h^{-1} compared to 144 h^{-1} respectively). The difference in the initial activity seems to find a plausible response in the average particle size. In fact, the nanoparticles obtained by SOL preparation appear to be much smaller than the SMAD ones (dm= 2.2 and 4.0 nm, respectively). Furthermore, the EXAFS characterisation estimated the presence of smaller nanoparticles of about 1.1–1.5 nm mean diameter in the SOL sample. These truly small particles could be responsible for very active catalytic sites and conferring to the material this high activity observed. Also in the bimetallic catalysts, the SOL prepared sample (771 h^{-1} with a conversion at 2h of 82.1 % - 2.4 nm), compared to the SMAD one (853 h^{-1} with a conversion at 2h of 43.6 %), apart from the slightly smaller initial activity value, show an evident higher activity (2 h conv.%) that could be partially ascribed to the smaller particle size, given the large difference observed between the two catalysts. In fact, a fundamental role can also be played by the different surface Au/Ag ratio and the oxidation states of Ag. Ag is less prone to be oxidised in the SOL case, as put in evidence by the XPS characterisation. This could find a confirm in the comparable initial activity, but with a prompt deactivation of the SMAD sample, probably due to the Ag oxidation and/or easier absorption of by-products on the surface. This highest activity of the bimetallic system confirms the presence of a synergistic effect between the two metals. This synergic effect is noticeable for both SOL and SMAD catalysts, although it is more pronounced for the SMAD sample.

The catalytic activity for both the Ag monometallic catalysts, however, was negligible (Figure 2-30, blue lines). This behaviour can be explained by the bigger dimension of the nanoparticles for the catalyst prepared by sol-immobilisation (Table 2-4, 2.2 nm versus 11.2 nm of the SOL and SMAD catalysts respectively), although deactivation phenomena cannot be ruled out at this stage.

Furthermore we can hypothesise that the Ag not play an active role for this type or reaction or at this conditions.

From a selectivity point of view, the Au as prepared SOL prepared, show common and expected values for this type of reaction (Table 2-7); regarding the SMAD sample, the C-C cleavage became evident with a selectivity toward glycolic acid of 28.9 % (11.2 % - SOL) and formic acid of 20.2 % (6.8 % - SOL sample) to the expense of glyceric acid 43.7 % (52.5 % - SOL sample) and tartronic acid 0 % (9.1 % - SOL sample). This unusual behaviour, showed only by Au SMAD could be addressed to the low rate conversion (conv. <10 % at 2 h, unique case) and the consequent lowest conversion value where the selectivity was calculated: it was confirmed how H_2O_2 concentration decreased as the reaction proceeded [116], indeed, for lower conversion values should correspond higher C-C cleavage products.

Regarding the bimetallic systems, the SMAD samples showed a selectivity for this type of reaction comparable with the Au-based SOL samples. The SOL sample showed a peculiar selectivity, with a remarkable higher selectivity toward the tartronate, show its capability to oxidise the primary alcohol of the glycerate (normally the main product). This change in selectivity was ascribed to the presence of Ag. In fact, the particle size was comparable for the bimetallic sample and the corresponding Au monometallic catalyst (dm = 2.2 and 2.4 nm respectively).

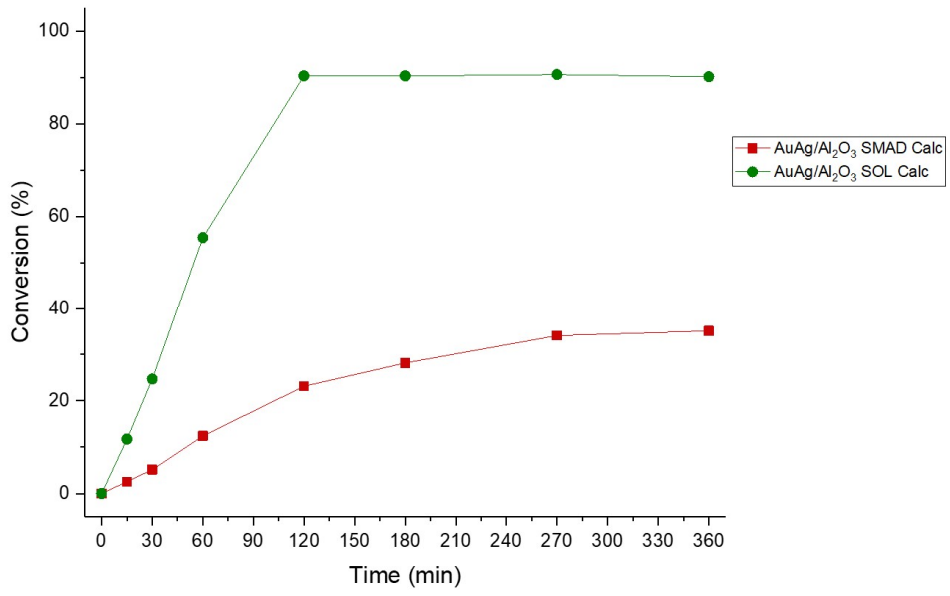

Figure 2-32. Glycerol oxidation profiles for bimetallic calcined samples. Reaction conditions: Glycerol 0.3M, Gly/NaOH = 1/4 mol/mol, Gly/metals= 2000 mol/mol, pO_2 = 3atm, T= 50 °C.

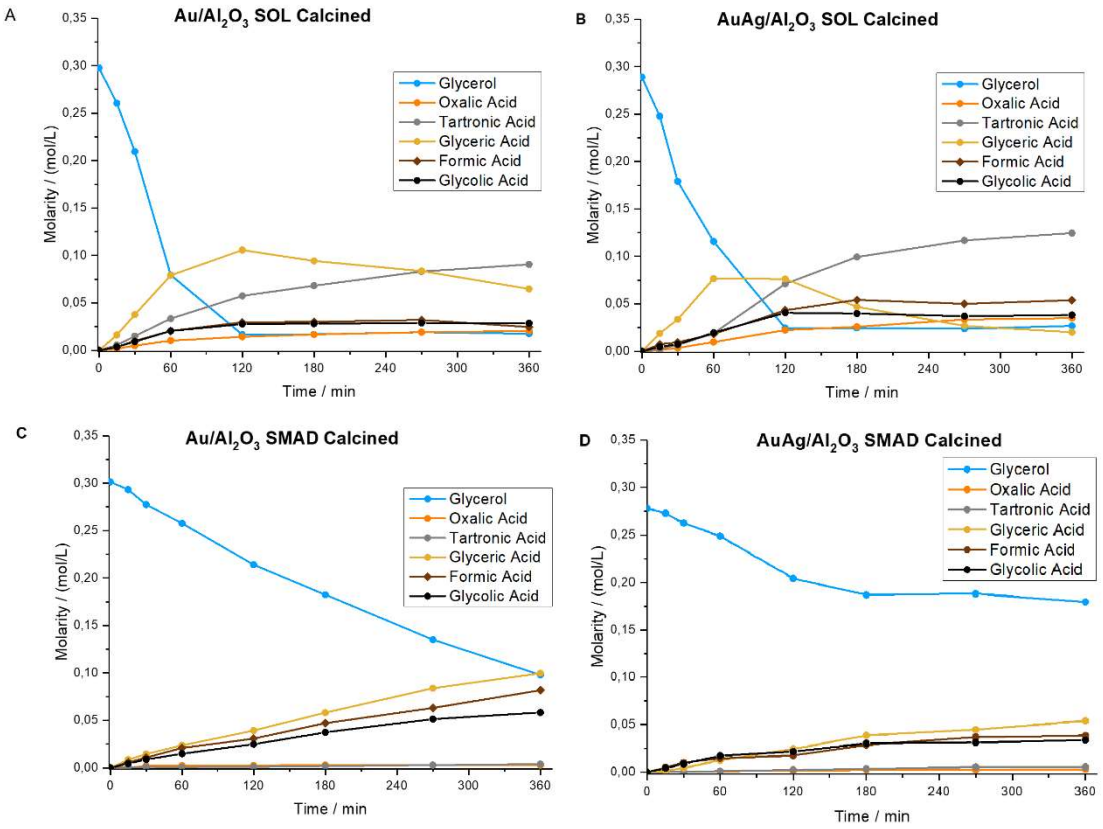

Figure 2-33. Product distributions in glycerol oxidation of calcined samples with (A) Au/Al_2O_3 SOL calc., (B) $AuAg/Al_2O_3$ SOL calc., (C) Au/Al_2O_3 SMAD calc. (D) $AuAg/Al_2O_3$ SMAD calc. catalysts. Reaction conditions: Glycerol 0.3M, Gly/NaOH = 1/4 mol/mol, Gly/metals= 2000 mol/mol, pO_2 = 3atm, T= 50 °C.

After the evaluation of the as prepared samples, the calcined catalysts were tested with the same reaction conditions. The calcination was carried out in static air at 400 °C, and it was therefore able to provide a removal of the capping agent, leaving "naked" nanoparticles at the surface. The SMAD samples underwent the same thermal treatment for comparison. The SOL monometallic Au-based sample is more active (810 h^{-1} with 93.3 % of conv. at 2 h; 1.9 nm) than the SMAD (372 h^{-1} with 37.2 % at 2 h; 7.2 nm); this difference was addressed to the particle size effect, in fact the SMAD sample suffers a severe enlargement (from 4.0 to 7.2 nm) that did not occur in the SOL sample, as discussed in the previous TEM section. This different behaviour was attributed to the presence of PVA that can block the coalescence of the nanoparticles.

The monometallic Ag remains inactive in both the samples, SMAD and SOL. In fact, the surface of the nanoparticles completely oxidises as shown by XPS analysis (Table 2-5) and the particle size increases in both cases, although it occurred more for the SMAD sample (from 4.0 to 15.0 nm for SMAD and from 7.5 to 11.2 nm for SOL). Also in this

case, even if the capping agent was not able to block the tendency of Ag to undergo sintering, was able to limit this phenomenon in SOL sample showing its valuable effect.
For the AuAg catalysts, the sintering phenomena occurred during the calcination is marked for the SMAD sample (from 4.7 to 7.8 nm, Table 2-4); in the SOL sample, however, the increase of particle size during calcination is limited (dm = 2.4 to 2.8 nm). This difference in mean particle size could be addressed again to the beneficial presence of the protective agent. This discrepancy lead to an effect also, as for the other cases, in terms of activity: AuAg SOL calcined samples showed an initial activity of 936 h^{-1} coupled with a complete conversion of the substrate at 2h (conv. > 99 %), unlike the AuAg SMAD sample that showed an initial activity of 194 h^{-1} and a conversion of 23.2 % at 2 h.
Others plausible and complementary explanations for these differences in activity derive from XPS characterisation. In fact a predominant Ag surface content was detected on the SMAD sample (Au/Ag 0.52, AP=719.3 eV), unlike the corresponding sample prepared via SOL (Au/Ag= 1.92) which showed an amount of superficial Au 4 times higher. Furthermore, the bimetallic SMAD sample, suffered from deactivation after calcination due to the marked enlargement of the particle size (from 4.7 to 7.8 nm) caused by sintering phenomena.
In addition, all the SOL catalysts benefit from the thermal treatment (Table 2-7) in comparison to the respective as prepared samples. The thermal treatment conditions and duration exploited, in fact, allow the slow removal of the polymer at the surface of the nanoparticles, but is not sufficient to induce sintering. The temperature of PVA pyrolysis, in fact, occur at around 400 °C [117]. Thus, the calcination process adopted leads to "naked" nanoparticles for SOL samples freeing their surface from the protecting agent and, consequentially, offers more active surface for the reaction to take part.
After calcination, the Au/Al_2O_3 SMAD became more active compared to the as prepared catalyst. This trend does not find an easy explanation since the particle size increased after the thermal treatment, but it could be addressed to a not successfully complete reduction of all the Au present at the surface for the as prepared samples.
From a selectivity point of view, the already highlighted trend of bimetallic SOL (remarkable higher selectivity toward the tartronate), became even more significant after the calcination process (Table 2-7, Figure 2-31-B and Figure 2-33-B). Since a similar effect was noticed with the Au/Al_2O_3 SOL catalyst (Table 2-7, Figure 2-31-A and Figure

2-33-A), we speculate that the PVA removal can contribute to a change in selectivity. It should be pointed out that the lower production of glycolate and formate of the AuAg SOL calcined samples compared to the as prepared samples, is in line with the selectivity shown by larger particles. In fact, larger particles lead to a less C-C cleavage products, due to the lower production of H_2O_2 [118].

Considering SMAD catalysts, we can observe how the Au and bimetallic samples show a comparable selectivities; this trend could be associated to the similar particle size (7.2 nm Au SMAD calc. – 7.8 nm AuAg SMAD calc.). Furthermore, both of them produced glycerate and formate in higher amount with respect to the Au SOL as prepared samples. We speculate, as for the SMAD as prepare sample, that the low conversion reached leads to more hydrogen peroxide concentration in the solution, incrementing the C-C cleavage.

Conclusions

AuAg catalysts on Al_2O_3 have been prepared following two different methodologies, namely sol-immobilisation and SMAD. The particle sizes in the bimetallic samples were slightly larger than the corresponding monometallic Au, but smaller than the corresponding monometallic Ag particles. Thus, the presence of Ag could lead to bigger nanoparticles. Generally, SMAD techniques is more efficient to synthesise nanoparticles with similar average size and size distribution then the SOL one. In particular, the SOL procedure can lead to a smaller Au and bimetallic nanoparticles but it is not able to avoid aggregation phenomena in the monometallic Ag samples. On the other hand, the stabilising agent (PVA) offers a precious protective layer on the nanoparticles, which is noticeable especially during the calcination step where it prevents nanoparticles sintering. This shows how the phenomena of nanoparticle enlargement, dictate by heat treatment, is strictly dependent on the metal and to the synthetic method adopted. In addition, the calcination allows also the decomposition of PVA, cleaning up the surface of the SOL prepared nanoparticles and thus enhancing the catalytic activity. The Ag catalysts had negligible activity compared to the Au containing ones, and both the SOL and SMAD bimetallic systems showed a synergistic effect by the alloying of the two metals, with a consequent boost in activity. The presence of bimetallic nanoparticles was revealed in both cases by TEM, XPS and EXAFS analysis. In particular, the nanoparticles showed a Au-rich core and a Ag-rich shell. XAS showed that in SOL preparation Ag only partially covers Au whereas in the case of SMAD the Ag enrichment on the surface is much larger

than in the SOL case. This was ascribed to the different electronic interaction revealed by Auger spectrum in the two cases. As consequence, Ag resulted more resistant to oxidation in the SOL sample than in the SMAD one. Apart from differences due to particle size, strong differences can be revealed in the catalytic oxidation of glycerol in terms of activity and selectivity. The AuAg SOL catalyst is more active than AuAg SMAD one and, most interestingly, the SOL sample showed a different product distribution compared to the monometallic one being glycerate further oxidised to tartronate. The calcined sample showed a higher selectivity toward tartronate and a lower to C-C cleavage product probably due to the enlargement of the metal particle size.

2.4.2. *AuAg/Titania*

Titania had already shown to be a valid support for noble metal nanoparticles leading to active systems exploited in alcohol oxidations [96, 119–124]. It has already been demonstrated how nanoparticles composition and their structure such as disordered/ordered, segregated or core-shell play a role modulating the catalytic activity [125]. Although it is clear that the extent of these features, the catalytic activity and selectivity and the understanding the origin of this effect is still lacking [126]. Theoretical studies [127] investigated the segregation of Ag that could occur in AuAg nanoparticles based systems and discovered that it is strongly affected by the composition, size and temperature. In agreement with this, Slater et al. [128] studied AuAg nanoparticles with controlled composition and structures through the combination of STEM imaging coupled with EDX spectroscopy, showing that nanoparticle surface segregation inverts from Au-rich to Ag-rich as Au content increases [128]. On the other hand, segregation in bimetallic particles can be also influenced by the synthetic route and by post-treatments. Zanella et al. [125], for instance, studied AuAg bimetallic catalysts supported on TiO_2 by sequential deposition–precipitation method, with 4 wt.% Au loading and various amounts of Ag proving the synergistic effect between Au and Ag, also detecting Ag segregation. It was already reported in the previous section the different behaviour in glycerol oxidation of AuAg catalysts supported on alumina, synthesised by SOL immobilization and SMAD (Solvated Metal Atom Dispersion) method. Both preparations showed synergistic effect between the two metals; a different metal distribution was revealed depending on the preparation method and post treatments, which rebounded on different catalytic activity. Based on these facts and considering the already proven efficiency of AuAg bimetallic catalysts in glycerol oxidation, here we compared the catalytic activity

and selectivity of differently synthesised and post-treated $AuAg/TiO_2$ catalysts. We decided, thus, to evaluate the effect of a different support (by choosing titania instead of alumina), and of one different synthetic route (by choosing deposition precipitation - DPU - instead of SMAD) to be compared with sol-immobilisation technique.

For this study, two sets of catalysts were prepared: the first one by sol-immobilisation (SOL) and the second one by deposition precipitation with urea (DPU). Analogously to the previous study, monometallic samples have been prepared as comparison. In addition, we decide also to test the influence of an enhanced presence of Ag, by preparing catalysts with a Au/Ag molar ratio of 1/1 in addition to the Au/Ag molar ratio 4/1 samples. In this section, unlike the previous study conducted on the AuAg nanoparticles supported on alumina, we focus on the evolution of bimetallic species. The reaction conditions were kept the same in order to be able to compare the results with the previous sets of experiments. For all the DPU catalysts, an additional thermal treatment was added (550 °C under H_2 flux for 1 hour) following the optimised activation procedure adopted for this system [129]. In addition, the calcination was performed at 300 °C in static air for 1 hour, instead of 400 °C for 30 minutes. We decide to decrease the calcination temperature to 300 °C in order to limit the eventual enlargement of the naked nanoparticles (DPU synthesised), based on the experience maturated with the SMAD samples.

Characterisation of $1\%Au_1Ag_1/TiO_2$

HRTEM

The particle size distribution and the composition of the bimetallic particles (for the as prepared samples only) was investigated by transmission electron microscopy (TEM and HAADF-STEM/EDS – reported in Table 2-8). As evidenced by HAADF-STEM/EDS analysis, the SOL preparation provided bimetallic particles already in the as prepared catalyst (Figure 2-34). The average composition of the particles resulted very close to the nominal value (Au atomic % = 48.5 ± 5). The mean diameters of the nanoparticles measured by TEM is 2.7 nm for the as prepared sample and 5.3 nm for the calcinated one. The capping agent in this case was not able to block the enlargement of the nanoparticles. Regarding the DPU bimetallic samples, on the contrary, we were able to evaluate only the mean dimension of the thermal threated (TT) sample, that correspond to 2.6 nm. The as prepared samples, on the contrary, did not show any nanoparticles formed. We speculate that the dimension of particles for the as prepared Ag sample is sub nanometric

and thus not observable with the resolution of the microscope [129]; on the contrary, for Au and AuAg as prepared samples, the metals are present as amorphous compound and the nanoparticles are not jet formed [130].

The DPU sample after the thermal treatment is characterised by smaller particle size compared to the SOL ones (dm = 2.6 nm vs 5.3 nm). We speculate that the support plays a crucial role mediated by the presence of PVA. We assume that the strong interaction between the support and the nanoparticles is responsible to the limited sintering phenomena for the DPU derived samples. On the other hand, the PVA presence, that as expected leads to small nanoparticles, could interfere with this interaction lading to bigger nanoparticles during the calcination step.

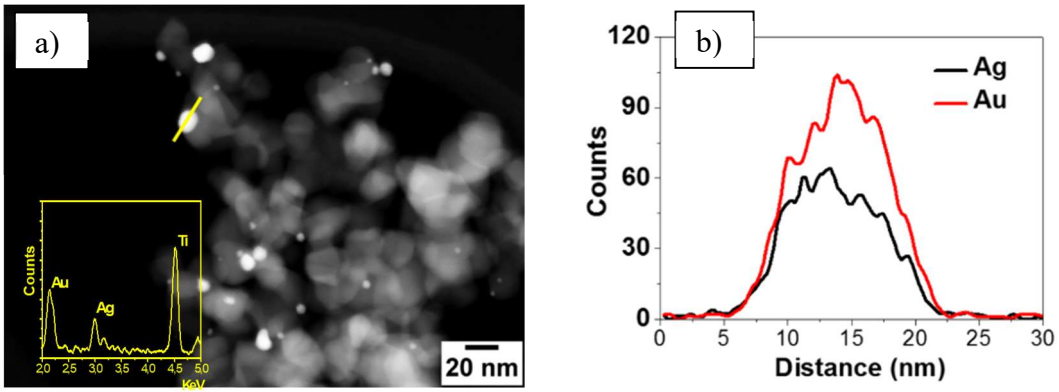

Figure 2-34. Representative HAADF-STEM micrograph (a - with relative EDX spectrum, yellow inset) with relative EDS particle profile of the selected NP of as prepared SOL Au_1Ag_1/TiO_2 sample.

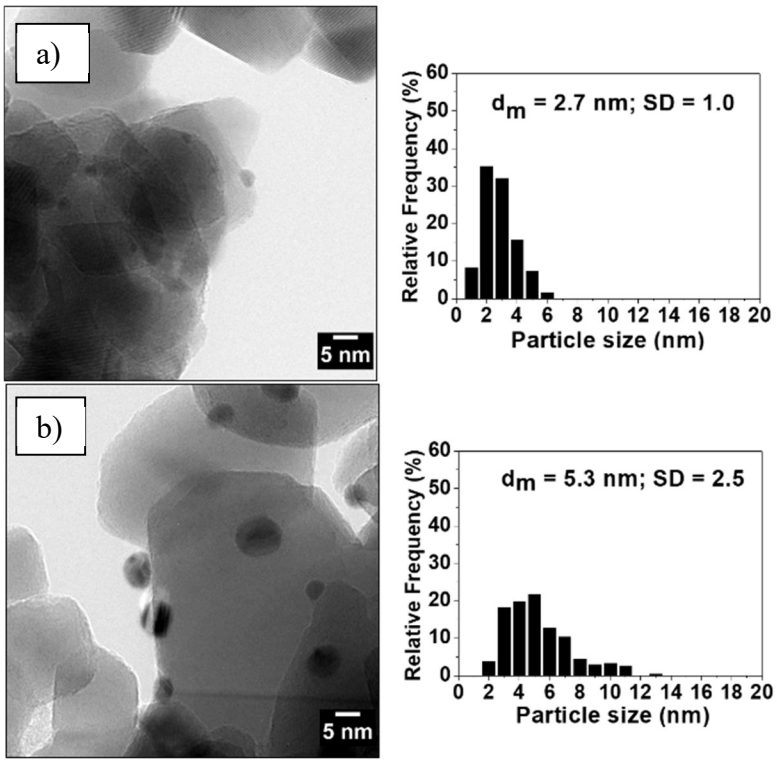

Figure 2-35. Representative HRTEM micrograph (left side) and histogram of particle size (right side) distribution of SOL Au_1Ag_1/TiO_2 as prepared (a) and calcined (b).

UV-Vis

In order to study the surface composition of the nanoparticles, we took advantage of the Localized Surface Plasmon Resonance (LSPR) characteristic of these metals. Gold and Silver nanoparticles, in fact, exhibit a distinct optical feature commonly referred to as LSPR, that is, the collective oscillation of electrons in the conduction band of gold nanoparticles in resonance with a specific wavelength of incident light. LSPR can be measured by UV-Vis spectroscopy.

The monometallic samples were analysed as benchmark comparison to evaluate the bimetallic behaviour.

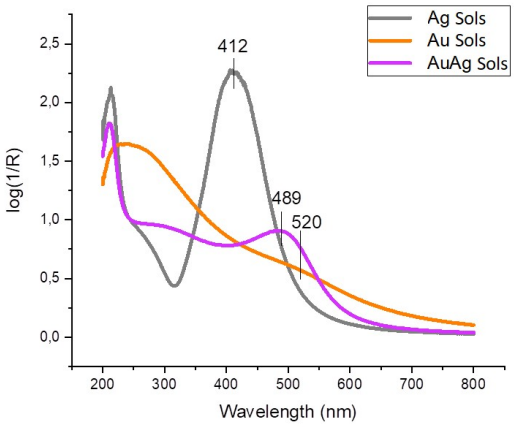

Figure 2-36. UV-Vis of Sols (Nanoparticles suspended in water) showing the mediated AuAg alloying plasmon value (489 nm) between the Au (520 nm) and Ag (412 nm) plasmon values.

Taking in consideration the SOL prepared samples, we firs performed UV-Vis directly on the metal colloid suspended in water (before deposition on support). In this case a transmission mode was exploited. As visible in Figure 3-27, the bimetallic nanoparticles formation is testified by the intermediate value of the AuAg Sols (489 nm) with respect of Ag (412 nm) and Au (520 nm) Sols. This shift normally occurred when the two metals, Au and Ag in this case, are present in alloy form.

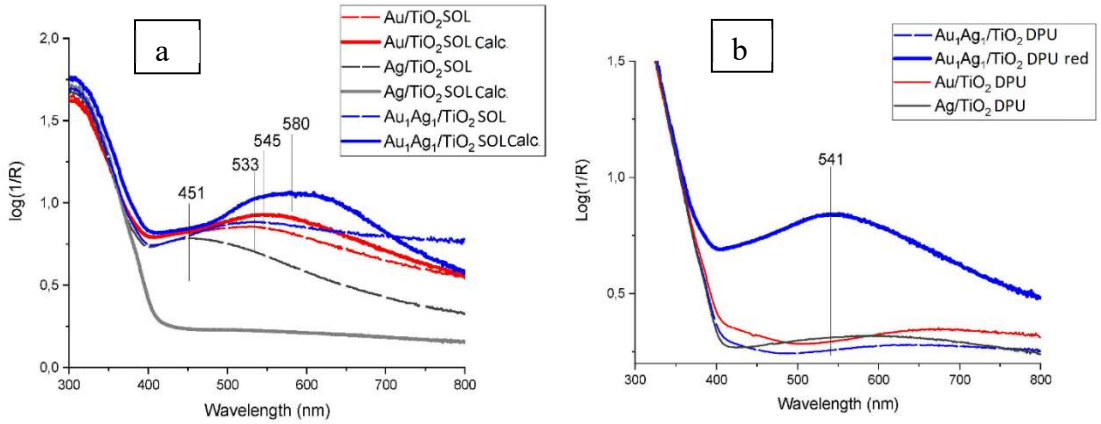

Figure 2-37. DRUV-Vis of Au_1Ag_1/TiO_2 SOL (a) and Au_1Ag_1/TiO_2 DPU(b) before and after calcination. Monometallic Au and Ag are reported as reference.

By observing the spectra of the supported SOL catalysts, as visible in Figure 2-27, all the samples show a LSPR band except for Ag as prepared sample. For these measurements the UV-visible spectra were recorded in diffuse reflectance mode (solid samples).

The benchmark values of the Au and Ag monometallic samples correspond to 451 and 533 nm, respectively. The red shift observed in comparison with the colloidal samples can be addressed to the interaction with the support [131]. The bimetallic as prepared SOL samples appear at about 533 nm as occurred for the monometallic Au sample. Thus, the LSPR band of the as prepared bimetallic, on the contrary of what observed for the

colloid, does not show any blue shift from the monometallic Au signal (533 nm), that should occur towards the LSPR Ag/TiO_2 wavelength (451 nm) [125][132]. We ascribe this behaviour to drying and storing in air the sample. We speculate, in fact, that Ag was oxidised somewhat causing a red shift (as was observed on O_2 contact at room temperature of freshly reduced Ag/TiO_2 [129]) compensating the blue shift resulting from alloying, leading to a value by coincidence corresponding to the Au one.

In calcined state the LSPR generated from SOL Ag disappear after the thermal treatment. This must be due to a total superficial Ag oxidation. This find also a visual confirmation: the sample after calcination results completely decolourised.

On the contrary, the enhanced intensity LSPR band of Au_1Ag_1 SOL and Au SOL were red shifted compared to the as prepared state, even if has occurred in lower extent for Au one. The red shift can be ascribed to the removal of the organic residues from the nanoparticles coupled with an enhanced interaction with the support (as observed following the immobilisation of the colloid). We cannot exclude, for the bimetallic sample, that a partial oxidation of the Ag's surface could also contribute to this shift. In addition, the higher intensity of the signal registered, in comparison with the corresponding as prepared samples, indicates a particle size increase [133]. This latter result is in agreement with the particle size determined by TEM (Figure 2-35).

Taking in consideration the spectra of the DPU samples, on the contrary, the as prepared AuAg and the corresponding monometallic samples show only very weak LSPR signals suggesting the presence of Au and Ag predominantly in their oxidised state. In DPU samples, in fact, Au and Ag are extensively reduced above 80 °C, and the formation of bimetallic nanoparticles was reported to start over 155 °C, as reported by Zanella and co-workers [125]. At temperature higher than 155 °C, in fact, it has been reported how the LSPR associable with the Au value (530 nm), shifts progressively to lower wavelength (515 nm at 300 – 350 °C) towards the Ag (475 nm) value, confirming the formation of bimetallic particles [125]. After the thermal treatment performed for DPU Au_1Ag_1 sample, as expected, plasmonic nanoparticles evolved indicated by LSPR band (541 nm) at somewhat lower wavelength than measured for calcined Au SOL (545 nm) as a result of reduction of Au and Ag and also alloy formation.

XPS

XPS analysis was conducted on the catalysts synthesised (Table 2-8) in order to have complementary information of the catalysts' surface. The bimetallic systems were investigated in as prepared and thermal treated samples to follow the interaction of the two metals, whereas for the monometallic samples, only the thermal threated samples were investigated as comparison.

Table 2-8. XPS analysis of SOL and DPU Au_1Ag_1/TiO_2 samples with respective mean diameters. Comparison between the fresh and calcined[a] catalyst.

Catalyst	Mean diam. (nm)	B.E.* Ag $3d_{5/2}$	B.E.* Au $4f_{7/2}$				AR* Au/Ag	Ag MNN K.E.*	AP*
			$Au^{\delta+}$		Au^0	$Au^{\delta+}/Au^0$			
Au/TiO_2 SOL Calc.	-	-	84.5		82.6	0.21	-	-	-
Ag/TiO_2 SOL Calc.	-	368.8	-		-	-	-	348.2	717.7
Au_1Ag_1/TiO_2 SOL	2.7 ± 1.0	368.7	84.8		-	-	0.63	348.4	719.5
Au_1Ag_1/TiO_2 SOL Calc.	5.3 ± 2.5	367.9	84.8		82.7	0.26	0.34	384.4	718.4
			Au^{3+}	Au^+					
Au_1Ag_1/TiO_2 DPU	No NPs	368.0	87.1	85.0	-	-	3.3	-	-
Au_1Ag_1/TiO_2 DPU red	2.6 ± 1.0	368.2			84.0	-	2.5	-	-

**B.E.= binding energy*
AR = atomic ratio
KE = kinetic energy
AP = Auger parameter

Ag monometallic, as expected and similarly to what occurred for the alumina supported samples, offers after calcination only oxidised species on the nanoparticles surface.

For monometallic Au SOL samples, instead, the results showed that even after the thermal treatment, unlike the samples supported on alumina, Au is not fully reduced and a fraction of $Au^{\delta+}$ is still present ($Au^{\delta+}/Au^0 = 0.21$). This could be partially ascribed to the interaction with TiO_2 or partially to a not sufficiently efficient thermal treatment adopted. It has to be reminded, that the thermal treatment was performed in a milder condition in comparison with the one occurred for the alumina supported samples.

The fresh bimetallic SOL, showed a Ag enrichment at the surface (Au/Ag metal ratio 0.63 instead of 1 as the nominal value). In this case, although, Au is present as $Au^{\delta+}$ state, unlike its ancestor on alumina. This could be again partially ascribed to the interaction with TiO_2 as for the monometallic Au sample. Ag, however, presented an Auger parameter of 719.5 eV, that is comparable with the metallic state in accordance with

Ferraria et al., [102] (as already reported previously: AP= 720.5 eV, 717.8 eV and 718.4 eV for metallic Ag, Ag_2O and AgO).

In the thermal treated bimetallic SOL-derived sample, Ag appeared not totally oxidised as indicated by the AP (718.4 eV), therefore, the beneficial presence of Au for the Ag stability has established as for the alumina supported samples. Au, on the other hand, is still partially present as $Au^{\delta+}$ in almost the same ratio as for the Au calcined SOL samples ($Au^{\delta+}/Au^0$ = 0.26). This could be again ascribed to the metal support interaction. Moreover, the thermal treatment, as expected and already previously observed, lead to a superficial Ag increase (Au/Ag pass from 0.63 of the fresh sample to 0.34).

DPU-derived catalysts in the fresh state showed two peaks for Au ($4f_{7/2}$) at 87.1 and 85.0 eV (Table 2-8). The peak at B.E. 87.1 eV refers to Au^{III}, due to the formation of an Au^{III}-urea complex on TiO_2; the one at 85.0 was attributed to Au^{I}, addressed to the at least partial reduction of part of the Au^{III} species under XPS beam. The binding energy value of Ag ($3d_{5/2}$) at 368.0 eV is a value between those of Ag^0 and Ag^+, ascribed to partially reduced Ag due to the XPS experiments. Is well-know, in fact, how the x-ray beam energy of the XPS could lead to an in-situ reduction on the samples' surface [134, 135]. After in situ reduction, Au is in the metallic form, and we expected that also Ag is completely reduced. The DPU samples presented Au/Ag ratios particularly high with respect to the nominal ones (3.3 in the fresh and 2.5 in the reduced) highlighting Au enrichment at the surface which decreased due to the thermal (reducing) treatment. The particularly high value compared to the nominal one was also addressed to Ag partially segregated as AgCl [125] on titania surface and Au as Au^{III}-urea complex [130] with no interaction between each other. The presence of AgCl is related to the synthesis method adopted: the preparation of AuAg/TiO_2 DPU samples, in fact, occurred by sequential deposition–precipitation (Ag first and then Au). Ag is reduced during the first step and suffers a reoxidation due to the chlorides added during the deposition of Au.

It has already been supposed how the capping agent mediates the nanoparticle interaction with the support. We assumed that the strong interaction between the support and the nanoparticles is responsible to the limited sintering phenomena for the DPU derived samples. On the other hand, the PVA presence, could interfere with this interaction leading to bigger nanoparticles. In view of the XPS results, we speculate that the higher presence of Au at the bimetallic DPU-derived surface nanoparticles, conferring more

stability to the system (as observed with the AuAg supported on alumina), could participate to this phenomena.

CO-DRIFT

Distribution and oxidation state of the metals were further investigated, for the bimetallic systems, by CO-Diffuse Reflectance Fourier Transform Infrared Spectroscopy CO-DRIFT (Figure 2-38-a–b). The CO adsorption bands helped in the interpretation of XPS results. It has to be noted that the intensity of the peaks is not strictly related to the quantity of the species, but more to the strength of the interaction of this latter with the probe molecules. The principal signal expected, thus, are related to the adsorption of the CO to the Au, Au^{+}, Ag^{+} and Ti^{4+} (support signal) species. It is important to point out that CO can be very weakly adsorbed on Ag^{0} surface species, thus this lead to a low signal, in most cases difficult to identify. Thus, the peak at 2055 cm^{-1} corresponds, when detected, to the CO-Ag^{0} [129], while the band at 2160 cm^{-1} refers to CO-Ag^{+} [136]. The band at 2105 cm^{-1} is to refer to CO-Au^{0} species [129, 137]. The peak at 2185 cm^{-1}, was assigned to the CO-Ti^{+4} species [138]. This latter signal is absent in the as prepared samples; in fact, the titania typically exposes preferentially the oxygen on its surface, especially when the catalyst storage is not occurred under inert atmosphere. After the thermal treatment, we speculate that this signal is to be ascribed to weak superficial Lewis acid sites formed by the titania [138].

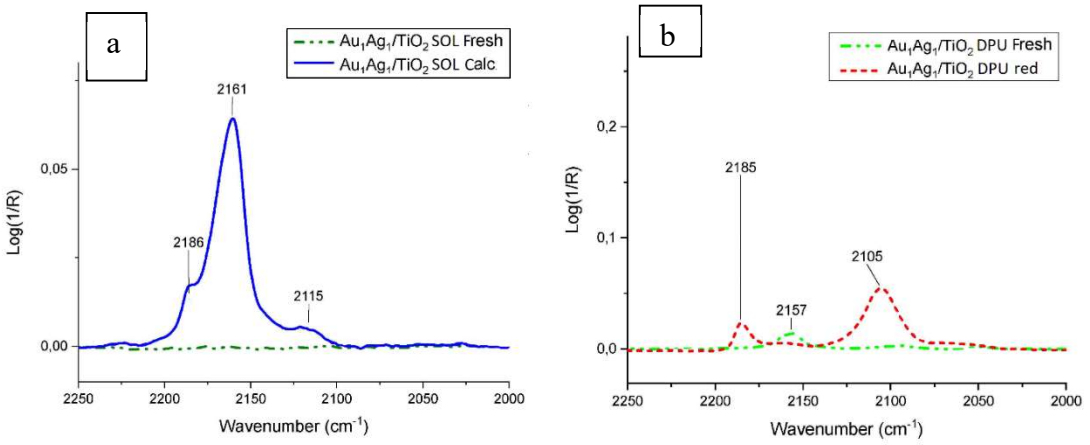

Figure 2-38. DRIFT measurement of CO adsorption at room temperature on Au_1Ag_1/TiO_2 by SOL (a) and DPU (b). Comparison between as prepared (green line), reduced (red line) and calcined (blue line) samples.

In the SOL catalysts (Figure 2-38) we did not observe any signals for the as prepared sample (Figure 2-38-a - green line). We speculate that this is due to the presence, at the

nanoparticles' surface, of PVA and water residues. The presence of these superficial species could further limit the metal-CO interaction: this result, in fact, is consistent with XPS analysis that indicates a situation where the Ag is predominant at the surface, as Ag^0 (Au/Ag atomic ratio 0.63 - Table 2-8) and for this reason suffers from a very weak interaction with the probe molecule.

After calcination, Ag is partially oxidised (AP = 718.4 eV), in fact, a strong peak at 2161 cm^{-1} due to CO adsorbed on Ag^+ appeared (Figure 2-38-a - blue line). The Au (present almost in metallic state, $Au^{\delta+}/Au^0 = 0.26$) seems almost covered by Ag (Au/Ag ratio 0.34), that report a further impoverishment at the nanoparticles' surface after calcination with respect to the original fresh sample. In fact, the Au DRIFT signal it is present only with a low intensity (Figure 2-38-a - 2115 cm^{-1}) and blue-shifted with respect to the Au^0-CO wavelength reference signal (2015 cm-1), suggesting surface Au species with a slightly positive charge after oxidation, that is in line with what has observed for the XPS characterisation ($Au^{\delta+}/Au^0 = 0.26$). The peak at 2185cm^{-1}, instead, was assigned to CO-Ti^{+4} species, as expected following a thermal treatment [139].

Taking in consideration the fresh bimetallic DPU-derived samples (Figure 2-38-b – green line), only a weak signal is present at 2157 cm^{-1} due to the presence of metallic Ag^+. This result is in line with what has hypothesised in the XPS section: Ag is partially present as AgCl and Au as Au^{III}-urea.

The reduced sample (Figure 2-38-b - red line) presented a peak at 2105 cm^{-1} due to the presence of metallic Au. As expected by taking in consideration the XPS results, the amount of Au at the surface is higher than the Ag (Ag/Au = 2.5) and both the metals are in the metallic state. The Ag^0 that should present very weak signal, in this case, is almost totally surmounted by Au.

Characterization of 1%Au_4Ag_1

Analogously to the Au/Ag:1/1 sample, Au_4Ag_1/TiO_2 was fully characterised as prepared, after calcination and after reduction with H_2.

HRTEM

The particle size distribution and, for the thermal treated sample, the composition of the bimetallic particles weres investigated by transmission electron microscopy (TEM, and HAADF-STEM/EDS – reported in Table 2-9). We decided to investigate the thermal treated samples to have a bulk composition of the nanoparticles and therefore confirm the successful alloying.

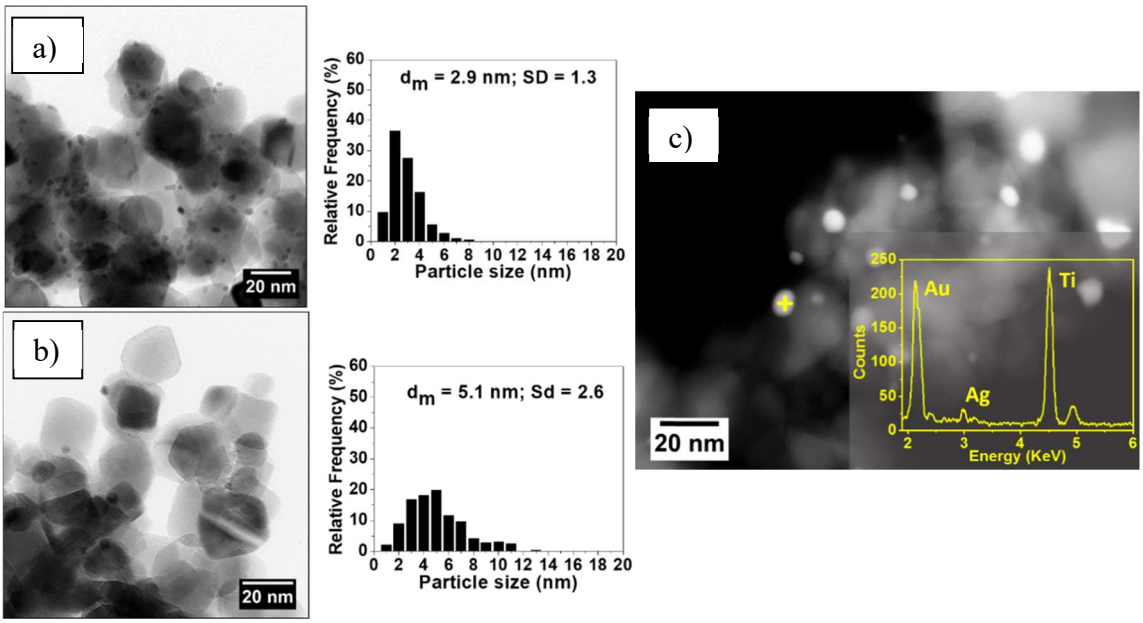

Figure 2-39. Representative HRTEM micrograph (left side) and histogram of particle size (right side) distribution of SOL Au_4Ag_1/TiO_2 as prepared (a) and calcined (b). HAADF-STEM micrograph (c) and EDS spectrum (yellow inset) carried out on a single particle SOL Au_4Ag_1/TiO_2 calcined.

The mean diameters of the bimetallic SOL derived nanoparticles measured by TEM is 2.9 nm for the as prepared sample and 5.1 nm for the thermal treated. Both of the measured values are similar to the ones measured for the Au:Ag/1:1 sample (2.7 and 5.3 nm for as prepared and calcined sample, respectively).

By HAADF-STEM/EDS analysis evaluation, the calcined SOL bimetallic particles (Figure 2-39-c) results with an average Au atomic content of 82.1± 5 % with a Au/Ag molar ratio of 4.6. The average composition of the particles resulted very close to the nominal value.

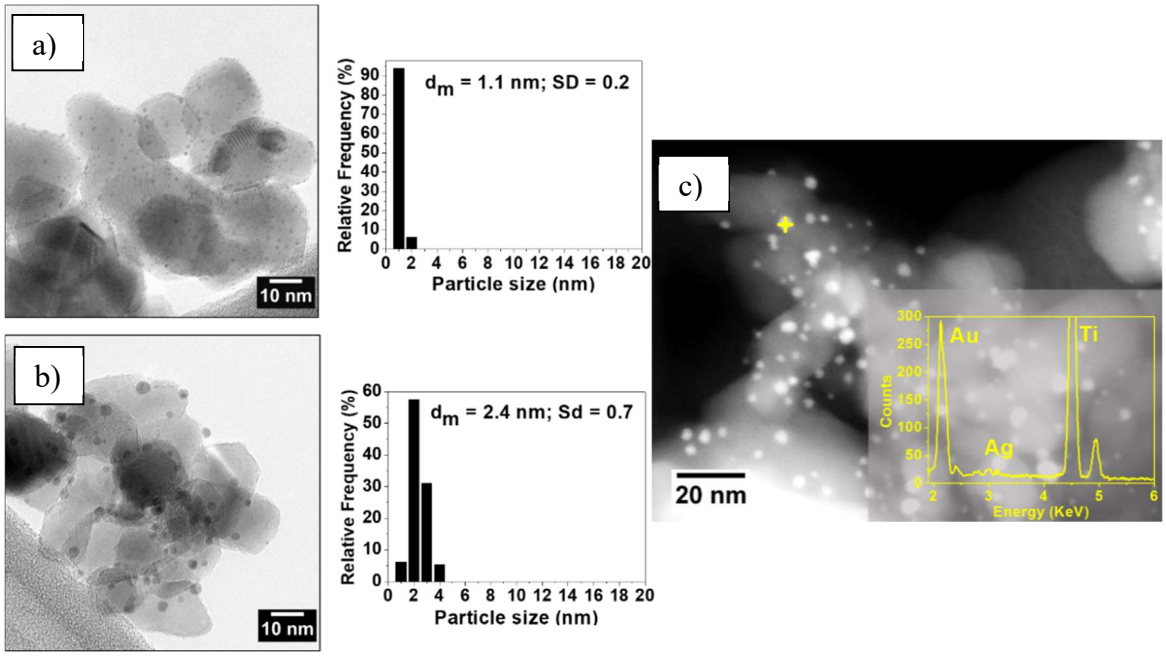

Figure 2-40. Representative HRTEM micrograph (left side) and histogram of particle size (right side) distribution of DPU Au_4Ag_1/TiO_2 as prepared (a) and calcined (b). HAADF-STEM micrograph (c) and EDS spectrum (yellow inset) carried out on a single particle DPU Au_4Ag_1/TiO_2 calcined.

The mean diameters of the bimetallic DPU derived nanoparticles measured by TEM is 1.1 nm for the as prepared sample and 2.4 nm for both the thermal treated ones. The as prepared sample shows a very small particle size, near the instrumental detection limit of the instrument. By HAADF-STEM/EDS analysis, the calcined DPU bimetallic particles (Figure 2-40-c) result with an average Au atomic content of 87.9 ± 5 % with an Au/Ag molar ratio of 7.3. This value in significantly higher than the nominal one, which can be explained, as in the case of 1:1 Au:Ag sample, with a partial segregation of Ag as AgCl. The DPU sample after the thermal treatment is characterised by smaller particle size compared to the SOL ones (dm = 2.4 nm vs 5.11 nm). We speculate, as reported for the Au_1Ag_1/TiO_2 sample, that the support plays a crucial role mediated by the presence of PVA. We assume that the strong interaction between the support and the nanoparticles is

responsible to the limited sintering phenomena for the DPU derived samples. On the other hand, the PVA presence, that as expected leads to small nanoparticles, could interfere with this interaction lading to bigger nanoparticles during the calcination step.

DRUV-Vis

In order to study the surface composition of the nanoparticles, Localized surface plasmon resonance (LSPR) analysis was carried out. The monometallics value were registered as benchmark comparison to evaluate the bimetallic behaviour.

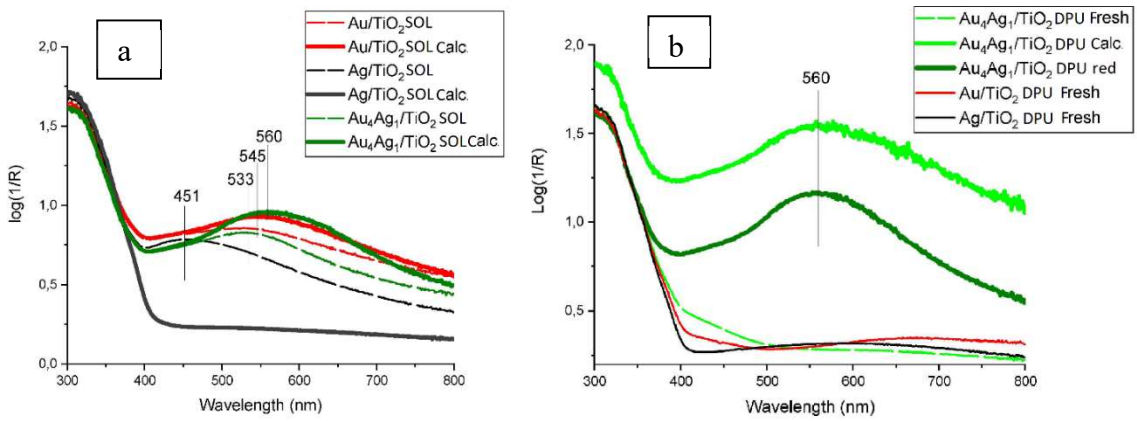

Figure 2-41. UV-Vis of Au_4Ag_1/TiO_2 SOL (a) and Au_4Ag_1/TiO_2 DPU(b) before and after the thermal treatments. Monometallic Au and Ag are reported as reference.

By observing the spectra of the supported SOL catalysts (Figure 2-41–a), all the samples show a LSPR band except for Ag as prepared sample, as for the AuAg 1:1 case. The benchmark values of the Au and Ag monometallic samples correspond to 451 and 533 nm, respectively, as already observed for the Au_1Ag_1/TiO_2 catalyst. We ascribe again this behaviour to drying and storing in air surface the sample. In calcined sample the LSPR generated from SOL Ag disappear after the thermal treatment. This is due to a total superficial Ag oxidation.

On the contrary, similar to what already observed for the 1:1 case, the enhanced intensity of the LSPR peak of Au_4Ag_1 SOL (from 533 to 560 nm) and Au SOL (from 533 to 545 nm) underwent redshift compared to the as prepared catalyst, even if in lower extent for the Au sample. Similar explanation can be proposed as for the 1:1 case: the shift can be ascribed to the removal of the organic residues coupled with an enhanced interaction with the support. We cannot exclude again, for the bimetallic sample, that a partial oxidation of the Ag surface could also contribute to this shift. In addition, the larger intensity of the signal registered indicates a particle size increase [133]. This latter result is in agreement with the particle size determined by TEM (Figure 2-39). On the contrary, the LSPR

generated from SOL Ag disappears after the calcination. This must be due to a total superficial Ag oxidation. The same trend was observed in the 1:1 case.

Taking in consideration the spectra of the DPU samples in Figure 2-41–b, on the contrary, the as prepared Au_4Ag_1 and the corresponding monometallic samples show only very weak LSPR signals suggesting the presence of Au and Ag predominantly in their oxidised state. This trend confirms what was observed for the 1:1 case. On the contrary, a plasmon band appeared after reduction or calcination (560 nm) like in case of the corresponding SOL sample. Similar explanations to this behaviour can be provided, as for the sol bimetallic samples.

XPS

XPS analysis was conducted on the catalysts synthesised (Table 2-9) in order to have complementary information of the catalysts' surface. The bimetallic system where investigated in as prepared and thermal treatment samples to follow the interaction of the two metals.

Table 2-9. XPS analysis of Au_4Ag_1/TiO_2 by sol-immobilization and DPU. Comparison between the catalysts as prepared and the catalysts after calcination and reduction treatments.

Catalyst	Mean diam. (nm)	B.E.* Ag $3d_{5/2}$	B.E.* Au $4f_{7/2}$			AR* Au/Ag	Ag MNN K.E.*	AP*
			Au^{3+}	Au^{+}	Au^{3+}/Au^{+}			
Au_4Ag_1/TiO_2 DPU	1.1 ± 0.2	368.1	87.2	84.8	0.46	9.1	352.9	721.0
			$Au^{\delta+}$	Au^{0}	$Au^{\delta+}/Au^{0}$			
Au_4Ag_1/TiO_2 DPU red	2.4 ± 0.7	366.9	85.4	83.0	0.23	4.2	352.9	719.8
Au_4Ag_1/TiO_2 DPU Calc.	2.4 ± 0.7	367.0	85.4	83.2	0.29	6.4	352.4	719.4
Au_4Ag_1/TiO_2 SOL	2.9 ± 1.3	367.7	86.2	83.9	0.26	3.6	353.0	720.7
Au_4Ag_1/TiO_2 SOL Calc.	5.1 ± 2.6	367.3	86.0	83.4	0.28	4.7	352.8	720.1

**B.E.= binding energy*
AR = atomic ratio
KE = kinetic energy
AP = Auger parameter

The XPS analysis of the bimetallic Au_4Ag_1 revealed a general Au-rich surface (Table 2-9).

In the case of Au_4Ag_1/TiO_2 as prepared by SOL immobilisation, the $Au^{\delta+}/Au^0$ ratio is again 0.26. This value does not show an evident change after calcination (0.28). This result confirms the key role of the support in determining the presence of $Au^{\delta+}$ species. The Au/Ag atomic ratio for the fresh sample is 3.6, similar to the nominal value. This ratio increased to 4.7 after calcination in contrast with what observed with all the thermal treated sample so far. These values are very similar to the one obtained by EDS-TEM analysis (4.6). The APs of Ag indicate in both cases (fresh and calcined) a similar oxidation state which is not sensitive to the treatment.

In the fresh Au_4Ag_1/TiO_2 sample prepared by DPU Au^{III} and Au^{I} form (B.E 87.3 eV and 84.8 eV) as in the case of the 1:1 were detected [130]. The Au^{+3}/Au^{+} ratio evidenced the higher presence of Au^{+} than of Au^{3+} species. The ratio between Au and Ag (9.1) indicates a very high exposure of Au on the nanoparticles surface. This particularly high value compared to the nominal one was also addressed to Ag partially segregated as AgCl [125] on titania surface and Au as Au^{III}-urea complex [130] with no interaction between each other, as already speculated for the 1:1 case. The presence of AgCl is related to the synthesis method adopted and, in the survey XPS spectrum of the as prepared sample, is present a B.E. for metal chloride at ~198.5–199 eV (Cl $p_{3/2}$) that could confirm the presence of AgCl.

Reduction in H_2 at high temperature (550 °C) decreases the Au/Ag ratio to 4.2 (similar to the nominal value), confirming the migration of Ag atoms toward the surface of nanoparticle. Au is not fully reduced and the $Au^{\delta+}/Au^0$ ratio is 0.23. Ag presents an AP decreased with respect to the one of the fresh counterparts. This could indicate a partial oxidation of Ag. We speculate that the fraction of oxidised species, for both Au and Ag, could derive from a strong interaction with the support. Interestingly, the calcination led to the same distribution of species except for the Ag/Au ratio that resulted higher than the one obtained by reduction (6.4 vs 4.2). It is possible that the higher temperature used during the reduction (550 °C), unlike calcination (300 °C), can increase the migration rate of the Ag atoms toward the surface.

Beside the Au exposure differences, in both thermal treatment DPU derived catalysts Ag and Au are present with the same oxidation states. Our opinion is that TiO_2 is able to interact with the metals through the thermal treatment that causes strong metal-support

interaction (SMSI) leading to the same oxidation state distribution regardless the atmosphere exploited for the thermal treatments.

CO-DRIFT

Distribution and oxidation state of the metals were further investigated, for the bimetallic systems, by CO-Diffuse Reflectance Fourier Transform Infrared Spectroscopy CO-DRIFT (Figure 2-42-a and b). The CO adsorption bands helped in the interpretation of XPS results as for the previous 1:1 case.

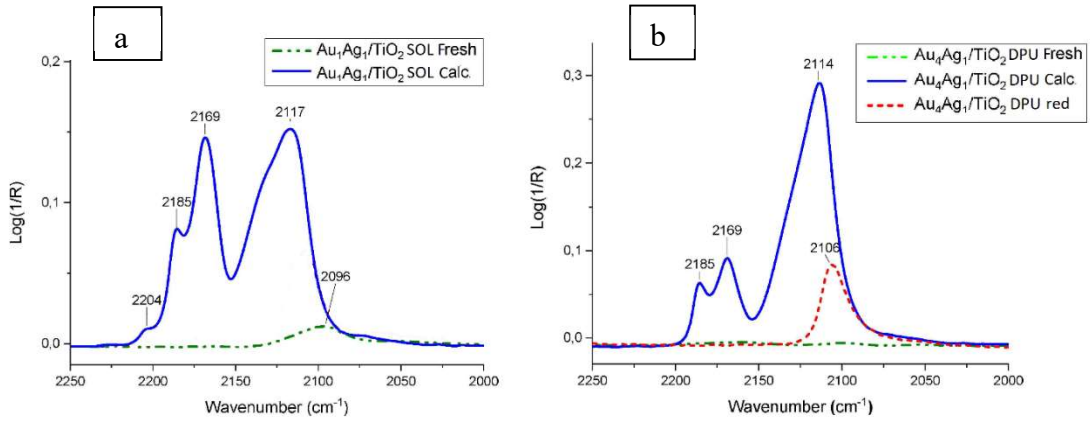

Figure 2-42. DRIFT measurement of CO adsorption at room temperature on Au_4Ag_1/TiO_2 by SOL (a) and DPU (b). Comparison between fresh (green line), reduced (red line) and calcined (blue line) samples.

CO-DRIFT measurements on SOL fresh catalysts (Figure 2-42-a, green line) revealed only a weak peak at 2096 cm^{-1} which can indicate Au in the metallic state but shielded by the protective agent (PVA). In comparison with the 1:1 bimetallic sample, the Au band is visible, probably due to the higher content of Au at the nanoparticles' surface. The peak due to adsorption of CO on Au^0 becomes more important after calcination (2117 cm^{-1} [129, 137]) with a shoulder at 2132 cm^{-1} that can be addressed to the presence of partially oxidised Au [137]. Considering the double contribution of CO adsorbed on Au in different oxidation state, the result is consistent with the $Au^{\delta+}/Au^0$ measured by XPS (0.26). Also in this case, we ascribed the higher intensity of the band with respect to the 1:1 sample, to the higher Au superficial content. Ag^+ is detected for both the fresh and calcined sample with the peak at 2169 cm^{-1} [136]. At 2204 and 2185 cm^{-1} appears a peak and as in the 1:1 case, that can be assigned to the weak Lewis acid sites formation (Ti^{+4}) on the surface of the catalyst [138].

In the case of DPU samples, the CO-DRIFT spectra ((Figure 2-42-b) indicated a situation similar to the SOL catalysts. The fresh DPU catalyst (green line) showed no peaks. After

reduction (red line) the peak correlated to the presence of Au^0 appeared at 2106 cm^{-1} as occurred for its 1:1 counterparts. On the other hand, no signals for Ag were detected. After calcination a clear peak due to the presence of Ag^+ appeared at 2169 cm^{-1}. Considering that the AP obtained by XPS, for the reduced and calcined DPU samples was comparable and indicating the same Ag oxidised species, we ascribe the lack of the Ag^+ peak in the reduced sample to a lower intensity of signals associated with a slightly slower AP and to the less Au content present at the surface of the calcined samples (Table 2-9). Calcination also shifted the peak of Au^0 at 2114 cm^{-1} with the presence, as in the case of SOL, of a shoulder at 2132 cm^{-1}. In agreement with the XPS analyses, the relative ratio between Au and Ag in the DPU samples appeared higher than in the SOL samples. At 2185 cm^{-1} appears the support peak.

2.4.3. *Catalytic tests*

All the catalysts prepared by DPU and by SOL were tested in the selective glycerol oxidation under mild conditions (50 °C, 3 bar of O_2, glycerol/metal ratio of 2000 mol/mol, NaOH/glycerol of 4). The conditions were kept the same as for the alumina-based catalysts in order to allow further comparisons.

Table 2-10. Catalytic results.

Catalyst	**Initial activity[a]**	**Conv. (3h)**	**Selectivity (%)[b]**				
	(h^{-1})	(%)	GA	TA	FA	OxA	GlyA
Au/TiO_2 SOL	245	54	58,9	-	6,6	-	4,0
Au/TiO_2 SOL Calc.	1662	> 99	41.3	12.9	2.7	2.7	10.5
Au/TiO_2 DPU	-	< 1					
Au/TiO_2 DPU red	1679	89	54.9	7.7	10.4	3.0	20.7
Au_4Ag_1/TiO_2 SOL	892	60	67,8	9,6	6,5	4,3	8,3
Au_4Ag_1/TiO_2 SOL Calc.	1616	63	55,6	10,4	10,0	2,1	15,6
Au_4Ag_1/TiO_2 DPU	-	-					
Au_4Ag_1/TiO_2 DPU Calc.	2113	82	54.4	12.3	5.6	2.2	8.8
Au_4Ag_1/TiO_2 DPU red	1524	86	51.3	17.7	2.9	4.0	5.2

[a] Initial activity has been calculated after 15 min calculated as mol converted per mol of metal (h^{-1}).
[b] Selectivity calculated at 30 % of conversion. Reaction conditions: Glycerol 0.3M, Gly/NaOH = 1/4 mol/mol, Gly/metals= 2000 mol/mol, pO_2 = 3atm, T= 50 °C.

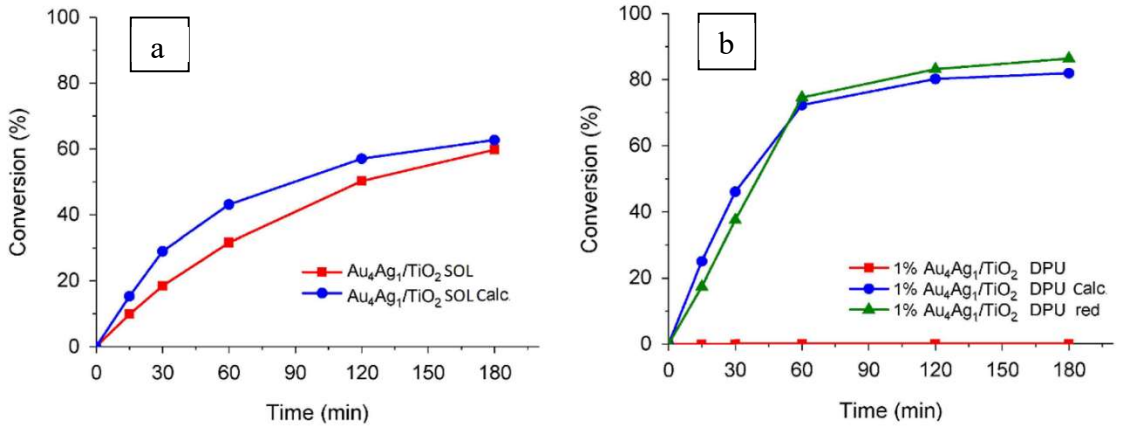

Figure 2-43. (a) Glycerol conversion over time of SOL Au_4Ag_1/TiO_2. Comparison between fresh (red squares) and calcined (blue dots) sample. (b) Glycerol conversion over time of DPU Au_4Ag_1/TiO_2. Comparison between fresh (red squares) and calcined (blue dots) and reduced (green triangles). Reaction conditions: Glycerol 0.3M, Gly/NaOH = 1/4 mol/mol, Gly/metals= 2000 mol/mol, pO_2 = 3atm, T= 50 °C.

All the Au_1Ag_1 bimetallic catalysts did not show any reactivity for both the synthesis methods exploited and for any thermal treatment performed. Also any Ag monometallic samples did not show catalytic activity. This latter result is in agreement with all the Ag catalysts tested so far.

By taking in consideration the fresh SOL-derived samples, the Au/TiO_2 catalyst shows an initial activity of 245 h^{-1}. On the other hand, the Au_4Ag_1/TiO_2 shows an initial activity of 892 h^{-1}. We addressed this remarkable higher activity to the presence of the two metals leading to a synergistic effect.

As synthesised DPU Au and Au_4Ag_1 samples, on the contrary, results inactive. We ascribe this behaviour to the lack of Au^0 on both the catalysts' surfaces.

Taking into consideration the catalytic data of thermal treated samples, instead, we can observe a general beneficial effect for both the synthetic methods.

Starting from the SOL derived samples, the initial activity of the Au/TiO_2 SOL catalyst increases from 245 h^{-1} for the as prepared sample to 1662 h^{-1} for the calcined. We ascribed this behaviour to the loss of PVA, leading to more free metal surface on the catalyst. We speculate that also more reduced Au on the surface could be present at the nanoparticles' surface, contributing to enhance the activity.

The bimetallic sample, starting from an initial activity of 892 h^{-1} (as prepared) and reaching a value of 1616 h^{-1} (calcined), shows again a remarkable higher activity, despite a growth of the particle size (2.9 to 5.1 nm). The two samples show a similar distribution of the oxidised species at the surface ($Au^{\delta+}/Au^0$ = 0.26 and 0.28). We ascribe, thus, the enhance of activity to a beneficial effect of the removal of the protecting agent [98]

coupled with and higher Au superficial content (Au/Ag= 3.6 for fresh and 4.7 for the thermal treated sample).

The DPU samples, after the thermal treatments, showed activity in the conversion of glycerol. The Au monometallic sample shows an initial activity of 1679 h^{-1}, similar to the Au SOL- derived one (1662 h^{-1}). The bimetallic sample shows an enhanced initial activity, compared to the corresponding monometallic catalyst (1679 h^{-1}), with the highest value observed so far (2113 h^{-1}). We ascribe again this behaviour to the synergetic combination of the two metals. The reduced sample, instead, show a value comparable with the monometallic one and significantly less active with respect to the calcined one: 1524 h^{-1}. We address this difference to the lower Au content on the nanoparticles' surface (AuAg = 4.2 for the reduced and 6.4 for the calcined sample).

In light of what observed, considering that 1:1 samples are inactive regardless of the metal distribution (Au rich surface in DPU and Ag rich surface in SOL) and metal oxidation state (reduced or oxidised), we concluded that the activity, and therefore eventual synergistic effects, derived from a delicate balance between the two metals.

From a selectivity point of view, all the bimetallic species behaved similarly except for SOL derived fresh sample, where the protective agent is still present, showing a higher selectivity towards glyceric acid at the expense of tartronic acid (Table 2-10). PVA in fact is known to be able to direct the adsorption-desorption of glycerol favouring the mono-oxidation [45].

2.4.4. *Comparisons*

In this section, the results showed for the fresh bimetallic catalyst supported on titania will be compared with the as prepared supported on alumina.

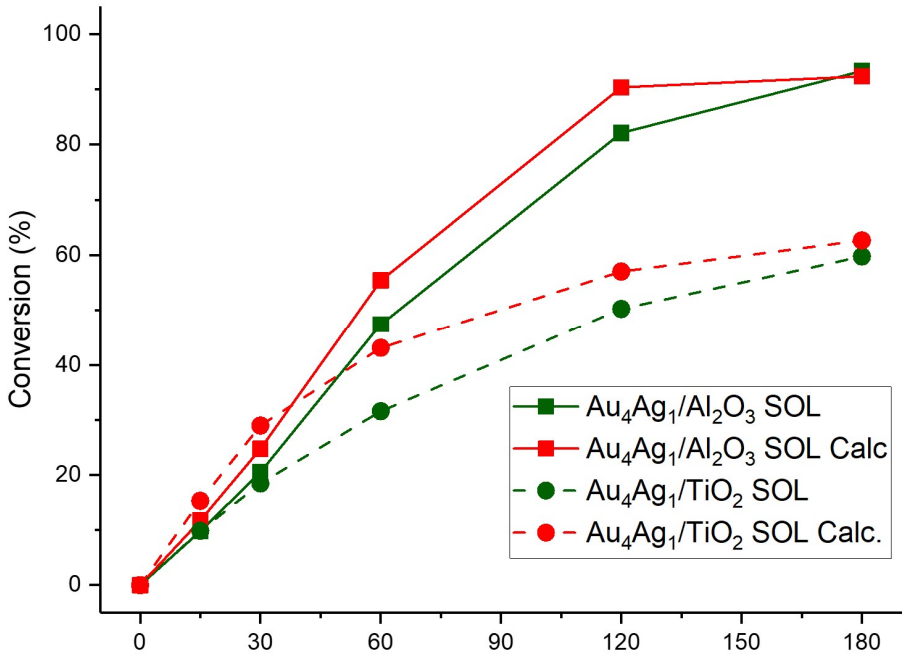

Figure 2-44. Glycerol conversion over time of SOL Au_4Ag_1/TiO_2 and Au_4Ag_1/Al_2O_3. Comparison between fresh (green lines) and calcined (red lines) samples. Reaction conditions: Glycerol 0.3M, Gly/NaOH = 1/4 mol/mol, Gly/metals= 2000 mol/mol, pO_2 = 3atm, T= 50 °C.

The fresh Au_4Ag_1/Al_2O_3, showed a lower initial activity (771 h^{-1}) in comparison with titania supported one (892 h^{-1}); the titania supported sample, on the other hand, showed a slightly deactivation in comparison with the titania one. These differences cannot be ascribed to a particles size effect, indeed the mean nanoparticles diameter is similar (2.4 nm alumina supported – 2.9 nm titania supported sample), neither to the composition of the nanoparticles (both Ag-rich surface). The two samples differ, however, in the oxidative state presented by the superficial atoms of the nanoparticles due to an electronic effect to ascribe to the interaction with the support. Therefore, we ascribe this tendency to a more rapid deactivation due to the presence of Ag^+ on the surface of the titania supported catalyst (alumina supported one presence of only Ag^0). It has been already widely studied the deactivation mechanism of metal catalysts employed in oxidation of alcohols (and aldehydes) with oxygen as oxidising agent [140].

Regarding the thermal treated bimetallics, the Au_4Ag_1/Al_2O_3 showed again a lower initial activity (963 h^{-1}) in comparison with the corresponding Au_4Ag_1/TiO_2 sample (1616 h^{-1}), despite a smaller mean diameter of the nanoparticles (2.8 – 5.1 nm). We ascribe the beneficial effect observed to the SMSI of the titania. The Au_4Ag_1/TiO_2 sample, however, by showing again a lower conversion of 63 % (reached in 3h) in comparison with the Au_4Ag_1/Al_2O_3 sample (> 99 % reached in 2h) seems to suffer more a slightly deactivation.

In this case, again, we ascribe this difference to the presence of Ag^+ on the titania supported system.

It has to be noted that all the titania supported samples present a partially oxidized metal fraction at the surface, unlike the alumina supported ones that show only reduced metals. In conclusion, the SMSI observed with TiO_2, seems to lead to a more active catalysts, but at the same time to a partially oxidation phenomena. We speculate that the presence of the Ag^+ specie at the surface implies a more rapid deactivation of the catalysts. We ascribed this phenomenon to an irreversible adsorption on the catalysts' surface, of the high chelating products of the reaction (i.e. dicarboxylic acid), localised especially on the Ag oxidized species.

To scale by activity the bimetallics species, the DPU techniques lead to the most active bimetallic catalyst (on titania), followed by the SOL (on titania) than the one supported on alumina: first SOL and at finally SMAD derived samples.

The synergetic effects are present for every bimetallic system in comparison with its corresponding monometallics, excepted for the SMAD derived samples that suffer from severe enlargement of the particles dimension after the thermal treatment, making every comparison not reliable.

The SOL derived catalyst supported on alumina, instead, showed more resident systems, that despite a slightly lower initial activity, they are the only systems able to produce tartronic acid, at the expense of the glyceric acid. In conclusion, the Au-rich sol derived systems seem to not suffer, or suffer less, the deactivation phenomena. We suppose that the lack of Ag^+ species on the surface could play a fundamental role in this case.

2.4.5. *Conclusion*

With the aim of studying the ruling factor for developing synergism between Au and Ag in the selective glycerol oxidation, we prepared 1 wt.% $AuAg/TiO_2$ with Au:Ag molar ratio of 1:1 and 4:1 by two different techniques: DPU and SOL immobilisation. Both techniques presented some peculiarities: DPU use a sequential deposition where Ag is deposited on the support first, and then Au is added, whereas SOL immobilisation technique forms the metallic particles in solution (avoiding AgCl precipitation), that are deposited onto the support in a second stage.

The catalysts thus produced highlighted different properties especially for the as prepared materials. In particular, the DPU catalysts showed markedly higher Au/Ag atomic ratio at the surface compared to the SOL catalysts.

Successively, we studied the evolution of the systems by thermal treatment in different atmosphere (H_2 and air). In the case of SOL samples, we observed sintering during calcination with an increase of particle size from 2.9 to 5.1 nm. The particle size of thermally treated DPU samples increased from 1.1 to 2.4 nm. As comparison we performed both the treatments for the Au rich DPU sample as comparison to confirm the equivalent efficiency of the treatments. UV-vis, XPS and CO-DRIFT have been carried out highlighting quite surprising similarities between calcined and reduced samples. In particular, it seems that thermal treatment induced SMSI which become the ruling factor determining the oxidation state of the metal. In fact, despite a different Au/Ag surface ratio, the two thermal treatments performed on the Au_4Ag_1/TiO_2 DPU sample, seem to lead to a comparable and equal efficient systems (similar catalytic behaviour with the same oxidation state).

It has to be reported, how all the active DPU samples have to first undergo a thermal activation treatment. In fact, all the DPU fresh samples, present only oxidized metal species at their surface.

All SOL active samples (except for Au/Ag:1/1), instead, are active in the as prepared form and become even more active after the thermal treatment: the nanoparticles are cleaned by the presence of the PVA and thus more of their surface can take part to the reaction.

Correlating the catalytic behaviour and the characterisation performed on the catalysts, we could conclude that the ratio between Au and Ag is fundamental for developing a synergistic effect. In fact, all the catalysts tested with an initial ratio of 1 :1 resulted inactive, also those thermally treated. In reference to what has just been reported, the composition of the AuAg catalyst that should be adopted for the synthesis is always Au-rich. The presence of larger amount of Au compared to Ag, in fact, allows the Ag to be more stable in the reduced form even in an oxidative environment. The particle size does not appear to influence the activity, at least in the range here investigated (2–5 nm) and especially with the support used. The synergetic effect related to the presence of both metals was established. Moreover, the synergy between Au and Ag could be also mediated by the presence of $Au^{\delta+}$ which can be always formed through the interaction with the support or by Ag presence. In addition, this synergism could vanish where the Ag, especially in its Ag^+ form, could lead to a more rapid deactivation.

2.5. AuPt/Titania

Once explored the advantages of AuAg bimetallic systems in the glycerol oxidation in presence of a base, we looked for a durable and active system that could work also in absence of a base. As already discussed, in recent years, in order to increase the catalytic performance of Au catalysts and combine its resistance to deactivation, metals were combined in bimetallic systems. A typical example of active monometallic systems that usually show deactivation phenomena and, therefore, are combined with Au are Pt and Pd [19, 22]. On the other hand, the crucial limitation of monometallic Au catalysts is the need to work in alkaline condition in order to promote the first step in the glycerol conversion pathway (H-abstraction, oxidative dehydrogenation) [20, 27]. As a consequence of using alkaline conditions, salts of acids are obtained instead of free carboxylic acids, making purification a challenge and limiting their industrial application. Lately, different groups have demonstrated how by alloying Au with Pt it is possible to obtain an effective catalytic system for glycerol oxidation, in terms of activity and selectivity even in the absence of a base [21, 66, 141]

Recently it has been demonstrated how for the AuPt alloyed nanoparticles, TiO_2 (P25) is a valid support leading to a durable and active systems for oxidation of polyols [63, 64]. In view of the above, for the present work, commercial TiO_2 (P25) was used as the selected support for Au_xPt_y bimetallic systems with different Au-Pt ratio (molar ratio: 9-1, 8-2, 6-4, 2-8, 1-9) and the corresponding monometallic Au and Pt catalysts. For this purpose, the catalysts were prepared by sol immobilisation method using polyvinyl alcohol (PVA) as protective agent, following the same experimental procedure employed so far. Then, the catalysts were tested in the liquid-phase glycerol oxidation either in the presence or absence of a base.

2.5.1. *Results and discussion*

Catalyst characterisation

The morphology of the catalysts was investigated by transmission electron microscopy (TEM). The analysis of Au/TiO_2 and Pt/TiO_2 show a metal particle size of 3.5 and 3.6 nm, respectively. The mean particle diameter and the particle distribution of the Au_xPt_y bimetallic systems are reported in Figure 2-45. TEM images revealed a good dispersion of Au_xPt_y nanoparticles on the surface of TiO_2 and a similar mean particle size (2.9–3.3 nm) with a particle size distribution of 1.0–6.0 nm for all the series of bimetallic catalysts. All the catalysts showed a similar and homogeneous particle size distribution on the surface of the support. As for the previous studies, the SOL immobilisation technique allows us to easily compare the systems providing a comparable particle size.

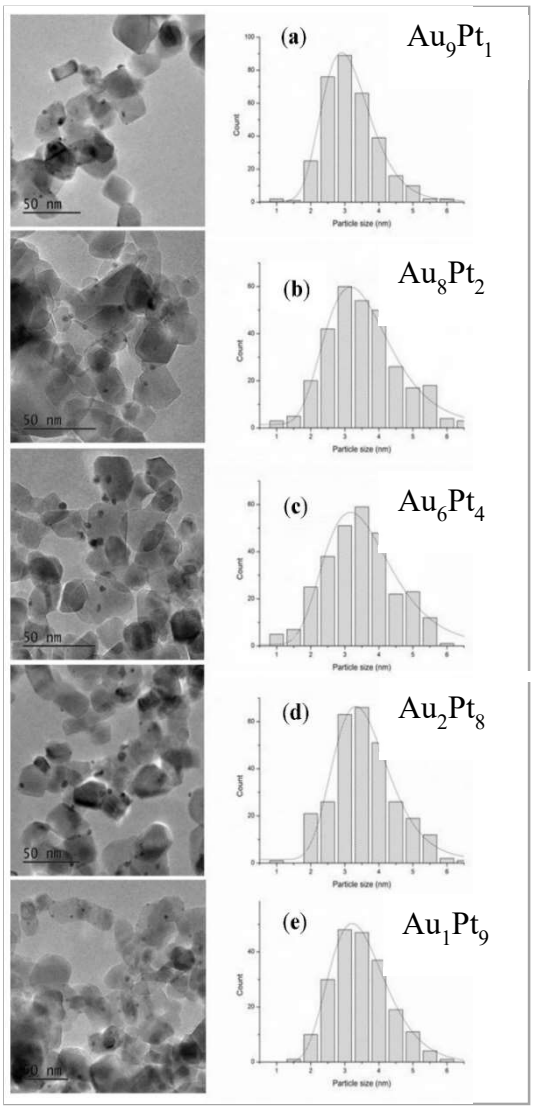

Figure 2-45. High resolution TEM micrographs (left side) and histogram of particle size distribution (right side) of (a) Au_9Pt_1/TiO_2; (b) Au_8Pt_2/TiO_2; (c) Au_6Pt_4/TiO_2; (d) Au_2Pt_8/TiO_2; (e) Au_1Pt_9/TiO_2.

The Energy-Dispersive X-ray Spectroscopy (XEDS) analyses of individual particles confirmed that the majority of the supported nanoparticles were bimetallic (AuPt) for all the samples synthesised. A high-magnification image acquired in High-Angle Annular Dark-Field imaging is a Scanning Transmission Electron Microscope (HAADF STEM) mode coupled with the corresponding XEDS spectrum of a representative AuPt nanoparticle supported on TiO_2 is represented in Figure 2-46. We have also reported a representative EDX elemental map (Figure 2-46) that shows a complete overlap of the two metals confirming the random alloy nature of the AuPt nanoparticle.

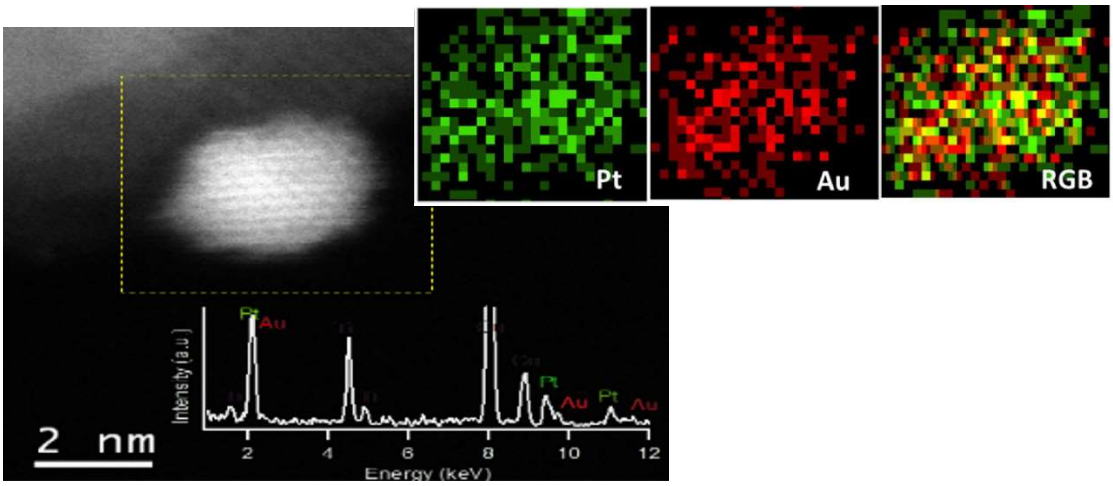

Figure 2-46. HAADF STEM images (inset - EDX spectra) of a representative AuPt/TiO_2 catalyst (Au_6Pt_4) with the corresponding EDX elemental map (Au-L_α and Pt-L_α) showing a complete overlap of the two metals (bimetallic Nanoparticles).

To elucidate the superficial oxidation state of the Au and Pt species, XPS analysis was performed (Table 2-11, Figure 2-47). The oxidation state at the surface of the catalyst was evaluated by analysing the values of binding energy (BE) of the Au $4f_{7/2}$ and Pt $4f_{7/2}$ peaks.

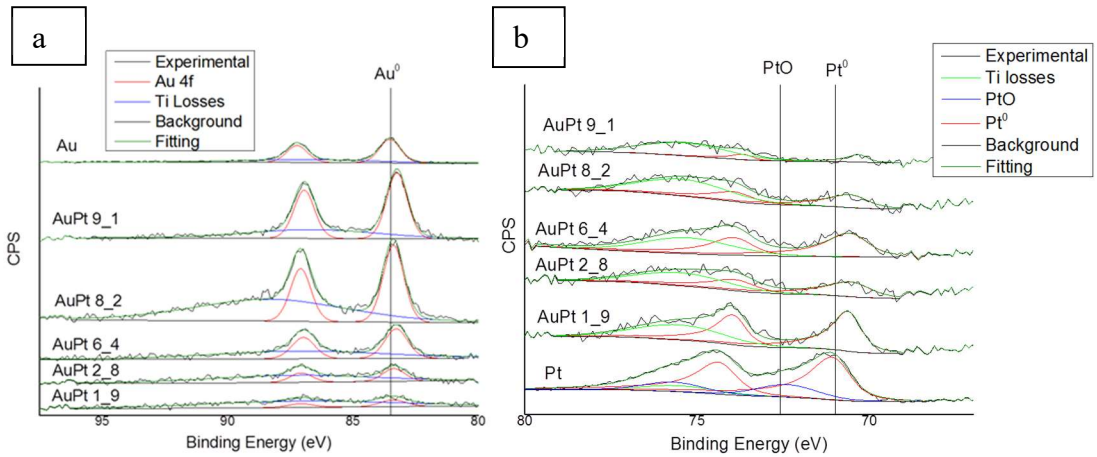

Figure 2-47. Au (a) and Pt (b) XPS Spectra (Binding energy: $Au4f_{7/2}$ and $Pt4f_{7/2}$).

Table 2-11. XPS data. Binding energy of $Au4f_{7/2}$ and $Pt4f_{7/2}$, % abundance of Au and Pt species metal exposure (at %).

Catalyst		Au4f		$Pt4f_{7/2}$		Au-Pt Atomic Ratio			Au at %	Pt at %	Metal at %
		Au^0	Au^+	Pt^0	PtO	Nominal	Measured (ICP)	Surface (XPS)			
1% Au/TiO_2	BE (eV)	83.5	-	-	-	-	-	-	0.40	-	0.40
	%	100	0	-	-						
1% Au_9Pt_1/TiO_2	BE (eV)	83.3	-	70.3	-	9.0	9.3	12.0	0.24	0.02	0.26
	%	100	0	100	0						
1% Au_8Pt_2/TiO_2	BE (eV)	83.4	-	70.5	-	4.0	4.2	3.8	0.19	0.05	0.24
	%	100	0	100	0						
1% Au_6Pt_4/TiO_2	BE (eV)	83.4	-	70.5	-	1.5	1.4	1.9	0.14	0.06	0.20
	%	100	0	100	0						
1% Au_2Pt_8/TiO_2	BE (eV)	83.4	-	70.5	-	0.25	0.3	0.7	0.05	0.07	0.12
	%	100	0	100	0						
1% Au_1Pt_9/TiO_2	BE (eV)	83.4	-	70.6	-	0.1	0.1	0.14	0.02	0.14	0.16
	%	100	0	100	0						
1% Pt/TiO_2	BE (eV)	-	-	71.2	72.4	-	-	-	0.02	0.44	0.46
	%	-	-	77.0	23.0						

** Inductively Coupled Plasma (ICP) Spectroscopy*

The peaks corresponding to the BE of 83.4 ± 0.1 eV are attributed to Au in the metallic state (Au^0, BE = 84.2 eV[142]). Concerning the Pt oxidation states, in the bimetallic samples, the Pt signal presented one single species at 70.4 ± 0.2 eV, corresponding to Pt^0. On the other hand, the monometallic catalyst presented two contributions, the main one at 71.0 eV corresponding to Pt^0 (77.0 %) and a secondary one at 72.4 eV (27.0 %) corresponding to Pt^{II} (PtO). The slight decrease to a lower BE compared to the typical values obtained for the monometallic Au and Pt catalysts (84.0 and 71.4 eV, respectively) can be attributed to the particle size effect [143–145].

Table 2-11 shows that the BE of Pt 4f decreases with an increase of the Au content, respectively 71.2 eV for monometallic Pt/TiO_2, 70.6 eV for Au_1Pt_9/TiO_2, 70.5 eV for Au_2Pt_8/TiO_2, Au_6Pt_4/TiO_2, and Au_8Pt_2/TiO_2 and 70.3 eV for Au_9Pt_1/TiO_2. According to previous reports, this BE shift can be attributed to the interaction between the two metals (Au-Pt) due to the formation of an alloy [146, 147]. The progressive shift towards lower BE of the Pt^0 peak with the enrichment of Au suggests a strong interaction between the two metals. Moreover, the absence of Pt^{II} signal in the bimetallic systems, suggests a strong interaction between Au and Pt which can prevent the partial oxidation of Pt surface and indicates the presence of Au-rich surface nanoparticles, as already observed in the presence of other second metals. The AuPt ratio measured by Inductively Coupled Plasma (ICP) Spectroscopy is in good agreement with the nominal one for almost all the catalysts prepared (Table 2-11). In terms of superficial bimetallic nanoparticles composition, interesting differences were detected by XPS. In the case of Au_9Pt_1/TiO_2, Au_6Pt_4/TiO_2, and Au_1Pt_9/TiO_2 catalysts, the Au/Pt atomic ratio measured by XPS is higher by ~30 % and in the case of Au_2Pt_8/TiO_2 by 133 % than the corresponding bulk Au/Pt atomic ratio, which can indicate surface enrichment of Au atoms in the aforementioned bimetallic nanoparticles (Table 2-11). On the contrary, Au_8Pt_2/TiO_2, the Au/Pt is lower by ~10 % than the corresponding bulk Au/Pt ratio, which can indicate surface segregation of Pt atoms in these nanoparticles.

2.5.2. *Catalytic tests*

The catalytic performance of the prepared catalysts was evaluated in the liquid phase oxidation of glycerol in the presence of a base (NaOH) and in its absence with comparable conditions: glycerol 0.3 M, alcohol/metal: 2000, T = 50 °C, pO_2 = 3 atm, NaOH - 4 eq. NaOH). In comparison with the previous catalytic tests, the metal presence

(alcohol/metal:1000 instead of 2000 as used so far) and the temperature (80 °C instead of 50°C as used so far) were increased in order to better study the activity in the test performed at free pH. The results are summarised in Table 2-12 and 13 and the reaction trends are reported in Figure 2-48, 50 and 53. The whole series of monometallic and bimetallic catalysts showed a lower activity under base-free conditions (initial pH of 4) than in the presence of a strong base (NaOH). Furthermore, any severe deactivation was observed in presence of a base, even for the monometallic Pt catalyst. This trend was expected as the base has the ability to facilitate the initial step of the reaction and the alkoxide (RO^-Me^+) formation [26, 30] and by favouring the desorption of the highly chelating hydroxyacid, thus, decreasing irreversible adsorption on metal active sites and therefore poisoning [148].

In alkaline condition, all bimetallic systems showed an initial activity higher (>3000 h^{-1}) than the corresponding monometallic ones (2657 and 2569 h^{-1} for Au/TiO_2 and Pt/TiO_2, respectively) (Table 2-12 and Figure 2-48). In particular, it can be observed that the best catalytic result was obtained by Au_9Pt_1/TiO_2 (7389 h^{-1}). Decreasing the Au content, the activity progressively decreased, AuPt: 9:1 (7389 h^{-1}) > 8:2 (6845 h^{-1}) > 6:4 (5052 h^{-1}) > 2:8 (3375 h^{-1}) > 1:9 (2569 h^{-1}). Figure 2-49 shows similar reaction profiles for all the catalysts and no evident deactivation phenomena seem to be present, reaching a conversion > 90 % after 2 h. These first results clearly show the presence of a synergistic effect for the bimetallic systems prepared. In addition, the catalytic activity seems proportional to the quantity of Au: the higher the Au content, the higher activity.

To confirm the remarkable resistance of AuPt catalysts against deactivation, stability tests were performed using Au_9Pt_1/TiO_2, the catalyst that showed the highest activity (Table 2-12). Recycling experiments were carried out by filtering and using the catalyst for the next run without any further purification. The catalyst showed similar conversion (approx. 90 %) and selectivity (approx. 65 % toward GA) for six runs (Figure 2-50) confirming the stability and deactivation resistance of the system.

From the selectivity point of view, the reaction proceeds with no significant change in product distribution (Figure 2-51).

On the other hand, the selectivity was strongly influenced by the atomic ratio of Au/Pt; in Table 2-12 the selectivity is reported at iso-conversion. The monometallic Au catalyst showed a selectivity toward glyceric acid of 50 %, with the presence of glycolic acid (24 %) and formic acid (14 %), deriving from the C-C cleavage of glyceric acid, as main

by-products (Table 2-12). Increasing the Pt content, a general decrease in the selectivity towards glyceric acid was observed. In addition, a formation of higher amounts of formic and glycolic acid (Table 2-12) was detected. In the case of Pt monometallic sample, formic acid (40 %) represents the main product.

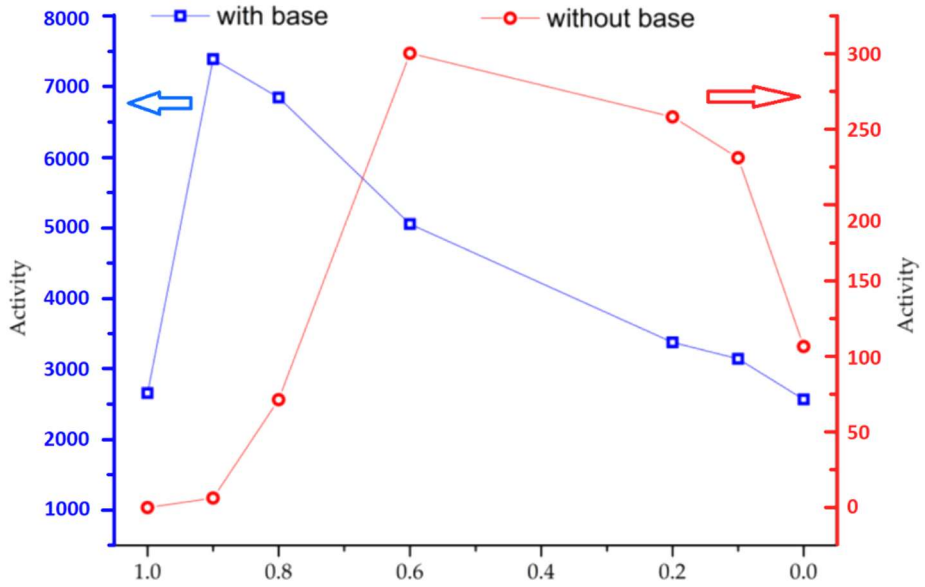

Figure 2-48. Influence of Au-Pt metal ratio on the initial activity (Moles converted/moles of metal x h (0,25 h)) in the glycerol oxidation in presence (blue) and absence (red) of a base. Reaction conditions: Glycerol 0.3M, Gly/NaOH = 1/4 mol/mol (or Base free), Gly/metals= 2000 (or 1000) mol/mol, pO_2 = 3atm, T= 50 (or 80) °C.

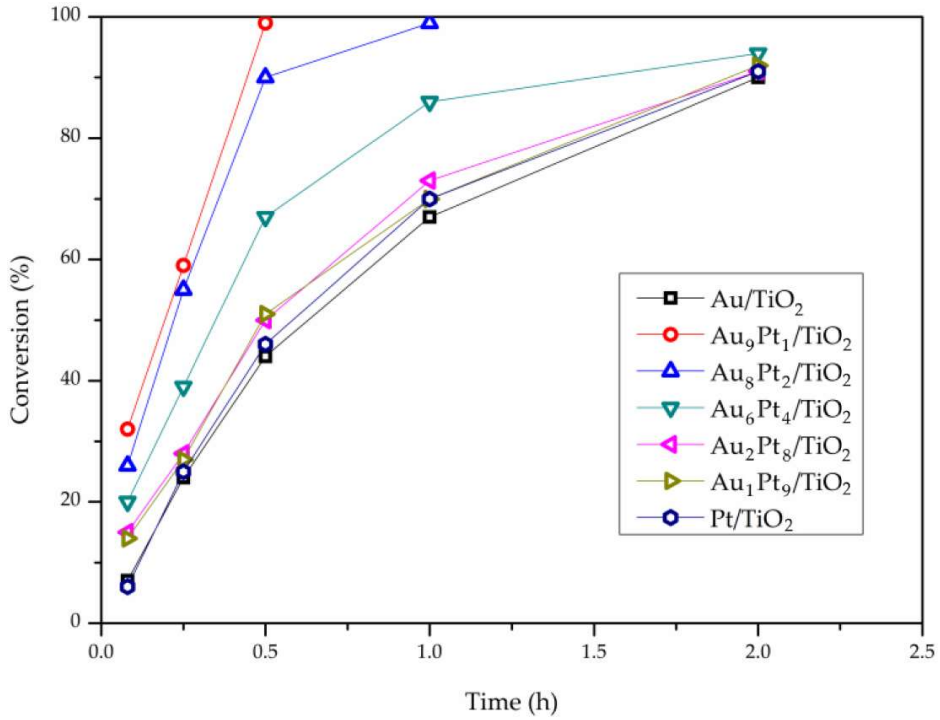

Figure 2-49. Reaction profile of Au-Pt catalyst in the glycerol oxidation in presence of NaOH. Reaction conditions: Glycerol 0.3M, Gly/NaOH = 1/4 mol/mol, Gly/metals= 2000 mol/mol, pO_2 = 3atm, T= 50 °C.

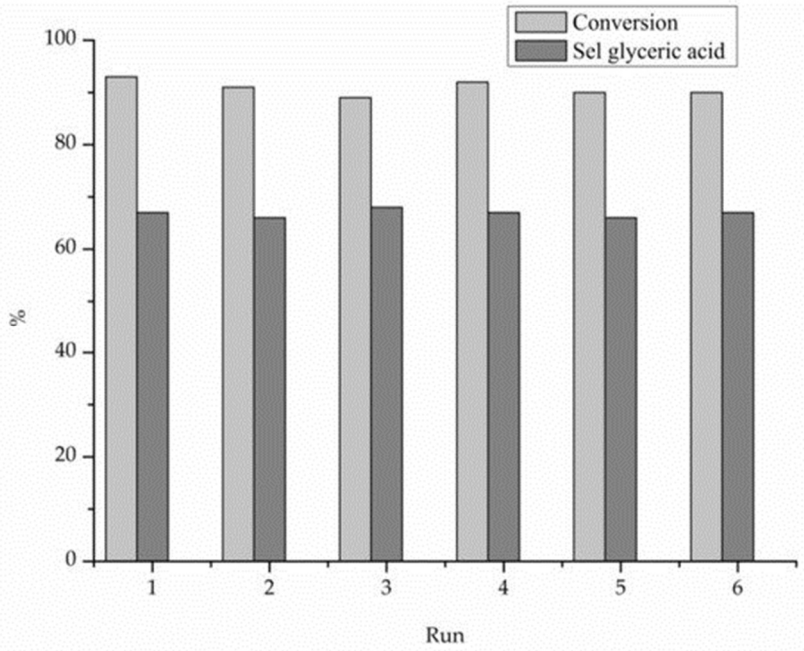

Figure 2-50. Recycle test for Au_9Pt_1/TiO_2 in the glycerol oxidation in presence of NaOH, reaction time 0.5 h. Reaction conditions: Glycerol 0.3M, Gly/NaOH = 1/4 mol/mol, Gly/metals= 2000 mol/mol, pO_2 = 3atm, T= 50 °C.

Table 2-12. Catalytic results for the glycerol oxidation in presence of NaOH[1].

Catalyst	Initial Activity [2]	Selectivity (%) [3]					
		Glyceric Acid	Tartronic Acid	ΣC_3 Products	Formic Acid	Glycolic Acid	Oxalic Acid
Au/TiO_2	2657	50	5	55	14	24	4
Au_9Pt_1/TiO_2	7389	58	7	65	10	23	1
Au_8Pt_2/TiO_2	6845	52	7	59	10	28	1
Au_6Pt_4/TiO_2	5052	42	6	48	29	19	1
Au_2Pt_8/TiO_2	3375	36	8	44	33	20	2
Au_1Pt_9/TiO_2	3142	31	6	37	37	16	4
Pt/TiO_2	2569	28	8	36	40	16	5

[1] Reaction conditions: Glycerol 0.3M, Gly/NaOH = 1/4 mol/mol, Gly/metals= 2000 mol/mol, pO_2 = 3atm, T= 50 °C.
[2] initial activity calculated as: moles converted/moles of metal x h (0,25 h).
[3] Selectivity calculated at 90 % of conversion.

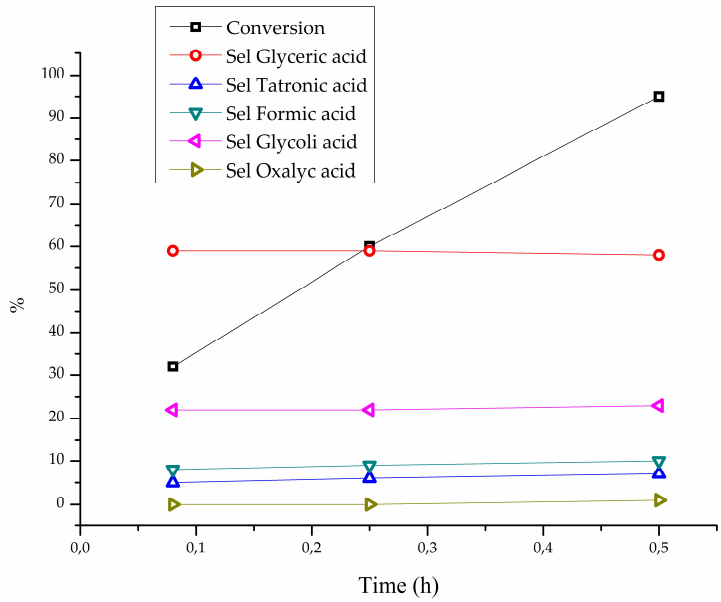

Figure 2-51. Selectivity versus time one stream for Au_9Pt_1/TiO_2 in presence of NaOH. Reaction conditions: Glycerol 0.3M, Gly/NaOH = 1/4 mol/mol, Gly/metals= 2000 mol/mol, pO_2 = 3atm, T= 50 °C.

The same series of catalysts were tested in the absence of base and the results are summarised in Table 2-13 and Figure 2-52. Under base-free conditions, as expected, monometallic Au sample was not active at all, whereas the corresponding monometallic Pt samples showed an activity of 112 h^{-1} (Table 2-13). It is well-known that Au requires the presence of a base to facilitate the first step of the oxidative dehydrogenation, H-abstraction under acid conditions, whereas Pt can carry out this step even under acidic conditions.

For the bimetallic systems, an opposite trend than in the presence of NaOH was observed (Figure 2-52). Indeed, Pt-rich bimetallic systems were more active than Au-rich ones, with Au_6Pt_4/TiO_2 showing the highest catalytic activity, (301 h^{-1}). Au_2Pt_8/TiO_2 and Au_1Pt_9/TiO_2 showed a comparable catalytic activity (263 and 234 h^{-1}, respectively), whereas Au_8Pt_2/TiO_2 and Au_9Pt_1/TiO_2 presented low activity (75 and 7 h^{-1}, respectively). The lower initial activity of Pt-richer catalysts can be explained by the prompt partial oxidation of Pt surface by molecular oxygen as evidenced during the electrocatalytic oxidation of Au- and Pt-based catalysts by Kwon et al. [149]. On the other hand, the low activity shown for the Au-richer samples find an explanation with the high energy barrier that Au have to overcome, in order to perform the first dehydrogenative step. At free pH in fact, as a consequence of a different reaction mechanisms proposed for the oxidative dehydrogenation, it was calculated that the activation of the OH group required a very high activation energy for Au, being lower for Pt [30]. In view of the above, it is

reasonable to conclude that under free pH condition, the presence of high amount of Au (Au-reach samples) is not beneficial, although small amount is necessary to boost the activity and confer resistance to deactivation. In this case the balance is more delicate compared to the alkaline condition, not only the Au amount seems to rule the activity.

Under base-free conditions, the catalyst composition is also influencing the stability (Figure 2-52). Indeed, Pt-rich AuPt catalyst (Au_2Pt_8/TiO_2) and Pt/TiO_2 monometallic deactivated after 2 h of reaction, whereas the other catalysts did not show any deactivation over the 5 hours tested. The deactivation is probably due to surface oxidation and chemical poisoning due to the strong chelating properties of the products deriving from glycerol oxidation (dicarboxylic acids in particular), as already observed in previous experimental studies conducted by Zope and co-authors [150]. The stability of AuPt catalysts was further investigated performing recycling tests using Au_6Pt_4/TiO_2 which showed the highest activity (Table 2-13). The catalyst showed almost constant conversion (approximatively 50 %) and selectivity (approximatively 60 % toward glyceric acid) during the six runs (Figure 2-53). We ascribed this resistance to deactivation to the Au presence.

Table 2-13. Catalytic results for the glycerol oxidation in base free condition[1].

Catalyst	Initial Activity [2]	Selectivity (%) [3]					
		Glyceric Acid	Glycer-aldehyde	ΣC_3 Products	Formic Acid	Glycolic Acid	Oxalic Acid
Au/TiO_2	-	-	-	-	-	-	-
Au_9Pt_1/TiO_2	7	-	-	-	-	-	-
Au_8Pt_2/TiO_2	75	58	9	67	28	1	-
Au_6Pt_4/TiO_2	301	62	10	72	20	5	-
Au_2Pt_8/TiO_2	263	66	12	88	14	6	-
Au_1Pt_9/TiO_2	234	70	13	83	9	5	1
Pt/TiO_2	112	68	15	83	9	3	2

[1] Reaction conditions: Glycerol 0.3M, free pH, Gly/metals= 1000 mol/mol, pO_2 = 3 atm, T= 80 °C.
[2] initial activity calculated as: moles converted/moles of metal x h (0,25 h).
[3] Selectivity calculated at 30% of conversion.

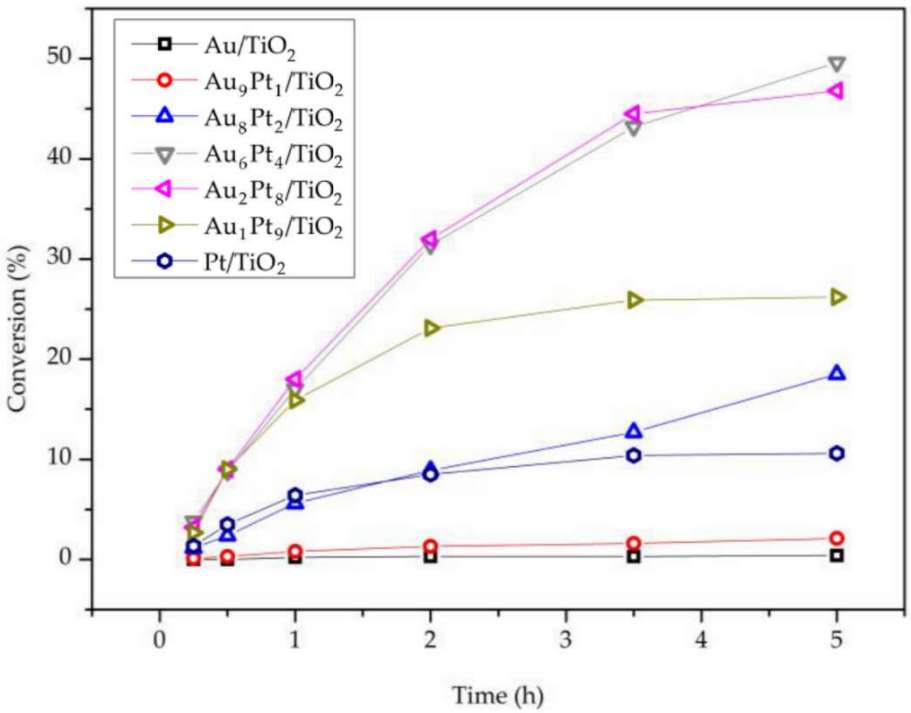

Figure 2-52. Reaction profile of Au-Pt catalyst in the base free glycerol oxidation. Reaction conditions: Glycerol 0.3M, free pH, Gly/metals= 1000 mol/mol, pO_2 = 3atm, T= 80 °C.

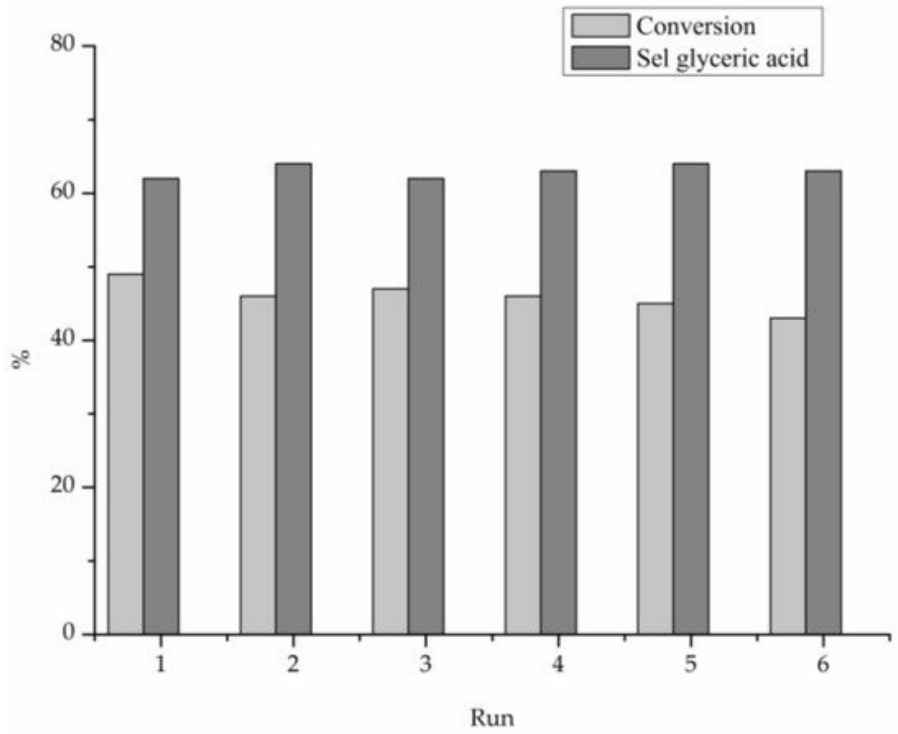

Figure 2-53. Stability test for Au_6Pt_4/TiO_2 in the base free glycerol oxidation, reaction time: 5 h. Reaction conditions: Glycerol 0.3M, free pH, Gly/metals= 1000 mol/mol, pO_2 = 3atm, T= 80 °C.

Considering the selectivity under base-free conditions, glyceric acid was the main product (Table 2-13). Moreover, glyceraldehyde, which rapidly converts to glyceric acid under base conditions, was detected. In general, the selectivity to C_3 products (67–88 %) is higher than using NaOH (42–72 %). Correlating the selectivity to Au:Pt atomic ratio, we observed an opposite trend than in the presence of the base. Indeed, in this case, Pt-rich systems are more selective to glyceric acid (and glyceraldehyde) than Au-rich ones, with a lower formation of C_1 and C_2 products deriving from C-C cleavage.

Summarising what observed in both reaction conditions, an opposite trend was observed according to the pH of the reaction solution. Under base conditions, Au-rich bimetallic catalysts showed higher selectivity to C_3 products than Pt-rich ones, which promote the C-C cleavage and the formation of formic and glycolic acid (Table 2-13).

Considering that it was reported how the formation of glycolic and formic acid can be correlated to the generation of H_2O_2, formed through O_2 reduction by the presence of metal hydride [6, 26], we set up a validation experiment. We determined the amount of H_2O_2 present at the end of the reaction by titration with $KMnO_4$. For these tests, Au_8Pt_2/TiO_2 and Au_2Pt_2/TiO_2 were chosen as representing Au-rich and Pt-rich catalysts. The results showed as under alkaline conditions, 0.05 mmol/L of H_2O_2 were detected using Au_8Pt_2/TiO_2 whereas 0.44 mmol/L were detected using Au_2Pt_8/TiO_2, almost ten times higher amount of H_2O_2. On the other hand, under acidic conditions, the opposite trend was observed; 0.45 mmol/L of H_2O_2 were detected using Au_8Pt_2/TiO_2 whereas 0.080 mmol/L were detected using Au_2Pt_8/TiO_2. These results are consistent with the selectivity data obtained. To better clarify the experimental results, we performed experiments focused on the decomposition of H_2O_2 under the two different conditions. Thus, by following the reactions, we set as alkaline condition a pH of 14 and for the free-base one a pH of 4. The test where conducted at 80 °C. In addition, each test was performed in the absence or in the presence of Au_8Pt_2/TiO_2 and Au_2Pt_8/TiO_2 catalysts.

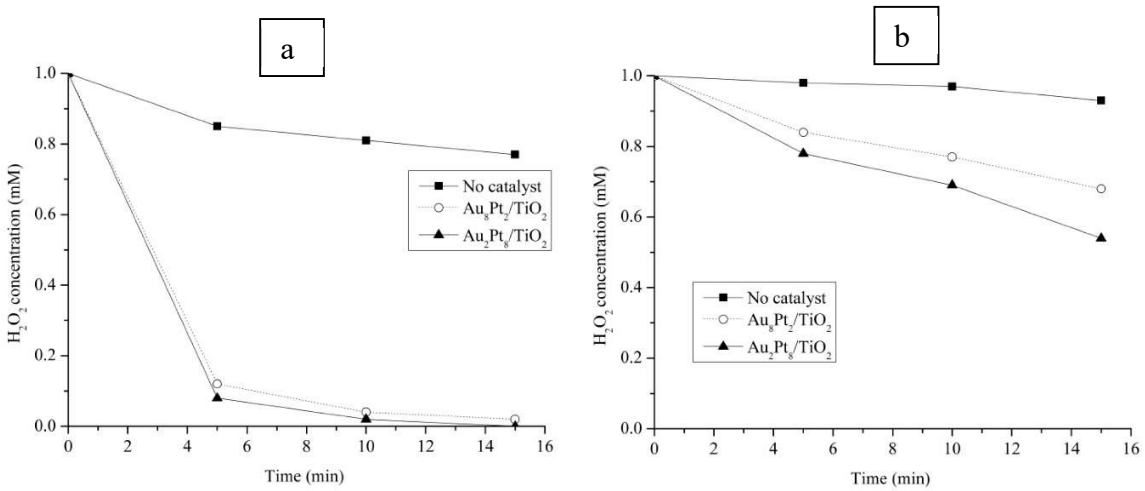

Figure 2-54. H_2O_2 decomposition at (a) 80 °C pH = 14 or (b) 80 °C and pH = 4.

Under basic conditions, the degradation of H_2O_2 proceeded fast and no obvious differences were observed between the two catalysts (Figure 2-54-a). Therefore, under alkaline conditions, Pt-rich catalysts promoted to a higher extent the formation of H_2O_2 compared to Au-rich ones favouring the C-C cleavage, and as a consequence a lower selectivity to C_3 products was observed. On the contrary, under acidic conditions, the decomposition of H_2O_2 is faster on Au_2Pt_8/TiO_2 than on Au_8Pt_2/TiO_2 (Figure 2-54-b), and for this reason, a lower amount of H_2O_2 after reaction was detected and a consequent higher selectivity to glyceric acid was observed for Pt-rich bimetallic systems.

2.5.3. *Conclusions*

We have studied the catalytic performance of supported Au_xPt_y nanoparticles with different atomic compositions for the glycerol oxidation under base and base-free conditions focusing on the influence of the Au:Pt atomic ratio. The catalysts were synthesised using colloidal-preformed nanoparticles via a well-established sol-immobilisation method. By means of this method, we were able to produce comparable catalyst from a particle size and homogeneous distribution. The presence of an AuPt alloy facilitates the increase of the catalytic performance with respect to the Au and Pt monometallic counterparts. This effect was attributed to a synergistic interaction as confirmed by XPS data as well. Furthermore, in presence of a base, the Au content seems to tune the activity: the higher the Au/Pt ratio the more the catalyst was active (Au:Pt - 9:1 more active). In free pH condition, on the contrary, a linear correlation between the metal ratio and the activity was not observed. The most active catalysts under base-free conditions, indeed, was Au_6Pt_4. This result showed the importance of finely tuning the Au:Pt molar ratio depending on the reaction conditions. Moreover, the most active catalysts for both the reaction conditions (Au_6Pt_4/TiO_2), was exploited for recycling test. The results showed, for the sample tested, a reusable system for both the reaction conditions, pointing out the importance of the synergistic effect.

Generally, the activity observed under base-free conditions (initial pH of 4) were considerably lower than in the presence of a strong base (NaOH), as expected. It is well-known, indeed, how the presence of a base favours the first dehydrogenative reaction's step. Furthermore, the inactivity of the monometallic Au catalyst in absence of a base, unlike all the other systems, has confirmed the importance of bimetallic systems and the synergetic effect derived from the combination of the two metals.

Observing the reaction profiles some deactivation phenomena were observed, in particular in the absence of a base and for Pt-rich catalyst; it rapidly deactivated, probably due to surface oxidation and chemical poisoning due to the strong chelating properties of the products deriving from glycerol oxidation (dicarboxylic acids in particular).

In terms of selectivity Au-rich catalyst, under base condition, showed and higher selectivity toward C_3 products (mainly glyceric acid). On the other hand, in base-free condition, C-C cleavage resulted favourite. Pt-rich catalysts showed an opposite trend in comparison with the Au-rich ones. We have ascribed these differences to the concentration and rate of degradation of H_2O_2.

References

1. A. Corma, S. Iborra, A. Velty, A. Corma Canos, S. Iborra, A. Velty (2007) Chemical routes for the transformation of biomass into chemicals. Chem Rev 107(6):2411–2502.
2. A. Rodrigues, J.C. Bordado, R.G. dos Santos, A. Rodrigues, J.C. Bordado, R.G. dos Santos (2017) Upgrading the Glycerol from Biodiesel Production as a Source of Energy Carriers and Chemicals—A Technological Review for Three Chemical Pathways. Energies 10(11):1817.
3. Q. (Sophia) He, J. McNutt, J. Yang (2017) Utilization of the residual glycerol from biodiesel production for renewable energy generation. Renew Sustain Energy Rev 71:63–76.
4. J. Sawin (2017) Renewable energy policy network for the 21st century renewables 2017 global status report. REN21 Secr Paris, Fr :1–302.
5. (2013) OECD-FAO Agricultural Outlook 2013. OECD
6. L. Prati, P. Spontoni, A. Gaiassi (2009) From Renewable to Fine Chemicals Through Selective Oxidation: The Case of Glycerol. Top Catal 52(3):288–296.
7. A. Villa, N. Dimitratos, C.E. Chan-Thaw, C. Hammond, L. Prati, G.J. Hutchings (2015) Glycerol oxidation using gold-containing catalysts. Acc Chem Res 48(5):1403–1412.
8. B. Katryniok, H. Kimura, E. Skrzyńska, J.-S. Girardon, P. Fongarland, M. Capron, R. Ducoulombier, N. Mimura, S. Paul, F. Dumeignil (2011) Selective catalytic oxidation of glycerol: perspectives for high value chemicals. Green Chem 13(8):1960.
9. C.S. Hong, S.Y. Chin, C.K. Cheng, M.M. Sabri, G.K. Chua (2015) Enzymatic Conversion of Glycerol to Glyceric Acid with Immobilised Laccase in Na-Alginate Matrix. Procedia Chem 16:632–639.
10. C. Gätgens, U. Degner, S. Bringer-Meyer, U. Herrmann (2007) Biotransformation of glycerol to dihydroxyacetone by recombinant Gluconobacter oxydans DSM 2343. Appl Microbiol Biotechnol 76(3):553–559.
11. J. Cai, H. Ma, J. Zhang, Z. Du, Y. Huang, J. Gao, J. Xu (2014) Catalytic oxidation of glycerol to tartronic acid over Au/HY catalyst under mild conditions. Cuihua Xuebao/Chinese J Catal 35(10):1653–1660.
12. O.M. Koivistoinen, J. Kuivanen, D. Barth, H. Turkia, J.-P. Pitkänen, M. Penttilä, P. Richard (2013) Glycolic acid production in the engineered yeasts Saccharomyces cerevisiae and Kluyveromyces lactis. Microb Cell Fact 12(1):82.
13. H.A. Emeko, A.O. Olugbogi, E. Betiku (2015) Appraisal of artificial neural network and response surface methodology in modeling and process variable optimization of oxalic acid production from cashew apple juice: A case of surface fermentation. BioResources 10(2):2067–2082.
14. J. Xu, Y. Zhao, H. Xu, H. Zhang, B. Yu, L. Hao, Z. Liu (2014) Selective oxidation of glycerol to formic acid catalyzed by Ru(OH) 4 /r-GO in the presence of FeCl 3. Appl Catal B Environ 154–155:267–273.
15. F. Jérôme, Y. Pouilloux, J. Barrault (2008) Rational Design of Solid Catalysts for the Selective Use of Glycerol as a Natural Organic Building Block. ChemSusChem 1(7):586–613.
16. C.-H. (Clayton) Zhou, J.N. Beltramini, Y.-X. Fan, G.Q. (Max) Lu (2008) Chemoselective catalytic conversion of glycerol as a biorenewable source to valuable commodity chemicals. Chem Soc Rev 37(3):527–549.
17. S. Carrettin, P. McMorn, P. Johnston, K. Griffin, C.J. Kiely, G.J. Hutchings (2003) Oxidation of glycerol using supported Pt, Pd and Au catalysts. Phys Chem Chem Phys 5(6):1329–1336.
18. P. Fordham, M. Besson, P. Gallezot (1995) Selective catalytic oxidation of glyceric acid to tartronic and hydroxypyruvic acids. Appl Catal A Gen 133:79–84.
19. H. Kimura, K. Tsuto, T. Wakisaka, Y. Kazumi, Y. Inaya (1993) Selective oxidation of glycerol on a platinum-bismuth catalyst. Appl Catal A Gen 96(2):217–228.
20. F. Porta, L. Prati (2004) Selective oxidation of glycerol to sodium glycerate with gold-on-carbon catalyst: an insight into reaction selectivity. J Catal 224(2):397–403.
21. A. Villa, G.M. Veith, L. Prati (2010) Selective Oxidation of Glycerol under Acidic Conditions Using Gold Catalysts. Angew Chemie Int Ed 49(26):4499–4502.

22. R. Garcia, M. Besson, P. Gallezot (1995) Chemoselective catalytic oxidation of glycerol with air on platinum metals. Appl Catal A Gen 127(1–2):165–176.
23. Miya H., Matsuda M. (1077) No Title.
24. M. Besson, F. Lahmer, P. Gallezot, P. Fuertes, G. Fleche (1995) Catalytic Oxidation of Glucose on Bismuth-Promoted Palladium Catalysts. J Catal 152(1):116–121.
25. J.C. Béziat, M. Besson, P. Gallezot (1996) Liquid phase oxidation of cyclohexanol to adipic acid with molecular oxygen on metal catalysts. Appl Catal A Gen 135(1):9–13.
26. W.C. Ketchie, Y.-L. Fang, M.S. Wong, M. Murayama, R.J. Davis (2007) Influence of gold particle size on the aqueous-phase oxidation of carbon monoxide and glycerol. J Catal 250(1):94–101.
27. S. Carrettin, P. McMorn, P. Johnston, K. Griffin, G.J. Hutchings (2002) Selective oxidation of glycerol to glyceric acid using a gold catalyst in aqueous sodium hydroxide. Chem Commun 57(7):696–697.
28. S. Carrettin, P. McMorn, P. Johnston, K. Griffin, C.J. Kiely, G.A. Attard, G.J. Hutchings (2004) Oxidation of Glycerol Using Supported Gold Catalysts. Top Catal 27(1–4):131–136.
29. M.S. Ide, R.J. Davis (2014) The important role of hydroxyl on oxidation catalysis by gold nanoparticles. Acc Chem Res 47(3):825–833.
30. B.N. Zope, D.D. Hibbitts, M. Neurock, R.J. Davis (2010) Reactivity of the gold/water interface during selective oxidation catalysis. Science 330(6000):74–78.
31. S.E. Davis, M.S. Ide, R.J. Davis (2013) Selective oxidation of alcohols and aldehydes over supported metal nanoparticles. Green Chem 15(1):17–45.
32. W.C. Ketchie, M. Murayama, R.J. Davis (2007) Promotional effect of hydroxyl on the aqueous phase oxidation of carbon monoxide and glycerol over supported Au catalysts. Top Catal 44(1–2):307–317.
33. S. Cattaneo, M. Stucchi, A. Villa, L. Prati (2019) Gold Catalysts for the Selective Oxidation of Biomass-Derived Products. ChemCatChem 11(1):309–323.
34. N. Dimitratos, A. Villa, C.L. Bianchi, L. Prati, M. Makkee (2006) Gold on titania: Effect of preparation method in the liquid phase oxidation. Appl Catal A Gen 311:185–192.
35. M. Conte, H. Miyamura, S. Kobayashi, V. Chechik (2009) Spin Trapping of Au−H Intermediate in the Alcohol Oxidation by Supported and Unsupported Gold Catalysts. J Am Chem Soc 131(20):7189–7196.
36. D. Wang, A. Villa, D. Su, L. Prati, R. Schlögl (2013) Carbon-Supported Gold Nanocatalysts: Shape Effect in the Selective Glycerol Oxidation. ChemCatChem 5(9):2717–2723.
37. D. Wang, A. Villa, F. Porta, L. Prati, D. Su (2008) Bimetallic Gold/Palladium Catalysts: Correlation between Nanostructure and Synergistic Effects. J Phys Chem C 112(23):8617–8622.
38. S. Demirel-Gülen, M. Lucas, P. Claus (2005) Liquid phase oxidation of glycerol over carbon supported gold catalysts. Catal Today 102–103:166–172.
39. N. Dimitratos, J.A. Lopez-Sanchez, D. Lennon, F. Porta, L. Prati, A. Villa (2006) Effect of particle size on monometallic and bimetallic (Au,Pd)/C on the liquid phase oxidation of glycerol. Catal Letters 108(3–4):147–153.
40. S.M. Rogers, C.R.A. Catlow, C.E. Chan-Thaw, D. Gianolio, E.K. Gibson, A.L. Gould, N. Jian, A.J. Logsdail, R.E. Palmer, L. Prati, N. Dimitratos, A. Villa, P.P. Wells (2015) Tailoring Gold Nanoparticle Characteristics and the Impact on Aqueous-Phase Oxidation of Glycerol. ACS Catal 5(7):4377–4384.
41. G.M. Veith, A.R. Lupini, S.J. Pennycook, A. Villa, L. Prati, N.J. Dudney (2007) Magnetron sputtering of gold nanoparticles onto WO3 and activated carbon. Catal Today 122(3–4):248–253.
42. S. Demirel, K. Lehnert, M. Lucas, P. Claus (2007) Use of renewables for the production of chemicals: Glycerol oxidation over carbon supported gold catalysts. Appl Catal B Environ 70(1–4):637–643.
43. A. Villa, D. Wang, C.E. Chan-Thaw, S. Campisi, G.M. Veith, L. Prati (2016) The confinement effect on the activity of Au NPs in polyol oxidation. Catal Sci Technol 6(3):598–601.
44. A. Villa, D. Wang, D.S. Su, L. Prati (2009) Gold Sols as Catalysts for Glycerol Oxidation: The Role of Stabilizer. ChemCatChem 1(4):510–514.

45. A. Villa, D. Wang, G.M. Veith, F. Vindigni, L. Prati (2013) Sol immobilization technique: a delicate balance between activity, selectivity and stability of gold catalysts. Catal Sci Technol 3(11):3036.
46. J. Akola, H. Häkkinen (2006) Density functional study of gold atoms and clusters on a graphite (0001) surface with defects. Phys Rev B 74(16):165404.
47. E.G. Rodrigues, M.F.R. Pereira, X. Chen, J.J. Delgado, J.J.M. Órfão (2011) Influence of activated carbon surface chemistry on the activity of Au/AC catalysts in glycerol oxidation. J Catal 281(1):119–127.
48. L. Prati, A. Villa, C.E. Chan-Thaw, R. Arrigo, D. Wang, D.S. Su (2011) Gold catalyzed liquid phase oxidation of alcohol: the issue of selectivity. Faraday Discuss 152:353.
49. B.N. Zope, S.E. Davis, R.J. Davis (2012) Influence of Reaction Conditions on Diacid Formation During Au-Catalyzed Oxidation of Glycerol and Hydroxymethylfurfural. Top Catal 55(1–2):24–32.
50. M. Pagliaro, R. Ciriminna, H. Kimura, M. Rossi, C. Della Pina (2007) From Glycerol to Value-Added Products. Angew Chemie Int Ed 46(24):4434–4440.
51. M. Sankar, N. Dimitratos, P.J. Miedziak, P.P. Wells, C.J. Kiely, G.J. Hutchings (2012) Designing bimetallic catalysts for a green and sustainable future. Chem Soc Rev 41(24):8099–8139.
52. D. Wang, A. Villa, F. Porta, D. Su, L. Prati (2006) Single-phase bimetallic system for the selective oxidation of glycerol to glycerate. Chem Commun 162(18):1956.
53. C.L. Bianchi, P. Canton, N. Dimitratos, F. Porta, L. Prati (2005) Selective oxidation of glycerol with oxygen using mono and bimetallic catalysts based on Au, Pd and Pt metals. Catal Today 102–103:203–212.
54. N. Dimitratos, C. Messi, F. Porta, L. Prati, A. Villa (2006) Investigation on the behaviour of Pt(0)/carbon and Pt(0),Au(0)/carbon catalysts employed in the oxidation of glycerol with molecular oxygen in water. J Mol Catal A Chem 256(1–2):21–28.
55. L. Prati, A. Villa, F. Porta, D. Wang, D. Su (2007) Single-phase gold/palladium catalyst: The nature of synergistic effect. Catal Today 122(3–4):386–390.
56. W.C. Ketchie, M. Murayama, R.J. Davis (2007) Selective oxidation of glycerol over carbon-supported AuPd catalysts. J Catal 250(2):264–273.
57. N. Dimitratos, J.A. Lopez-Sanchez, J.M. Anthonykutty, G. Brett, A.F. Carley, R.C. Tiruvalam, A.A. Herzing, C.J. Kiely, D.W. Knight, G.J. Hutchings (2009) Oxidation of glycerol using gold–palladium alloy-supported nanocrystals. Phys Chem Chem Phys 11(25):4952.
58. R.K.P. Purushothaman, J. van Haveren, D.S. van Es, I. Melián-Cabrera, J.D. Meeldijk, H.J. Heeres (2014) An efficient one pot conversion of glycerol to lactic acid using bimetallic gold-platinum catalysts on a nanocrystalline CeO2 support. Appl Catal B Environ 147:92–100.
59. D. Tongsakul, S. Nishimura, K. Ebitani (2013) Platinum/Gold Alloy Nanoparticles-Supported Hydrotalcite Catalyst for Selective Aerobic Oxidation of Polyols in Base-Free Aqueous Solution at Room Temperature. ACS Catal 3(10):2199–2207.
60. G.-Y. Yang, S. Shao, Y.-H. Ke, C.-L. Liu, H.-F. Ren, W.-S. Dong (2015) PtAu alloy nanoparticles supported on thermally expanded graphene oxide as a catalyst for the selective oxidation of glycerol. RSC Adv 5(47):37112–37118.
61. B.S. Sánchez, M.S. Gross, C.A. Querini (2017) Pt catalysts supported on ion exchange resins for selective glycerol oxidation. Effect of Au incorporation. Catal Today 296:35–42.
62. Y. Shen, Y. Li, H. Liu (2015) Base-free aerobic oxidation of glycerol on TiO2-supported bimetallic Au–Pt catalysts. J Energy Chem 24(5):669–673.
63. C.E. Chan-Thaw, L.E. Chinchilla, S. Campisi, G.A. Botton, L. Prati, N. Dimitratos, A. Villa (2015) AuPt Alloy on TiO 2 : A Selective and Durable Catalyst for l -Sorbose Oxidation to 2-Keto-Gulonic Acid. ChemSusChem 8(24):4189–4194.
64. A. Villa, M. Manzoli, F. Vindigni, L.E. Chinchilla, G.A. Botton, L. Prati (2017) Diols Production From Glycerol Over Pt-Based Catalysts: On the Role Played by the Acid Sites of the Support. Catal Letters 147(10):2523–2533.
65. A. Villa, S. Campisi, K.M.H. Mohammed, N. Dimitratos, F. Vindigni, M. Manzoli, W. Jones, M.

Bowker, G.J. Hutchings, L. Prati (2015) Tailoring the selectivity of glycerol oxidation by tuning the acid–base properties of Au catalysts. Catal Sci Technol 5(2):1126–1132.
66. G.L. Brett, Q. He, C. Hammond, P.J. Miedziak, N. Dimitratos, M. Sankar, A. a. Herzing, M. Conte, J.A. Lopez-Sanchez, C.J. Kiely, D.W. Knight, S.H. Taylor, G.J. Hutchings (2011) Selective oxidation of glycerol by highly active bimetallic catalysts at ambient temperature under base-free conditions. Angew Chemie - Int Ed 50(43):10136–10139.
67. E. Auer, A. Freund, J. Pietsch, T. Tacke (1998) Carbons as supports for industrial precious metal catalysts. Appl Catal A Gen 173(2):259–271.
68. A. Villa, C. Campione, L. Prati (2007) Bimetallic gold/palladium catalysts for the selective liquid phase oxidation of glycerol. Catal Letters 115(3–4):133–136.
69. B. Corain, G. Schmid, N. Toshima (2008) Metal nanoclusters in catalysis and materials science : the issue of size control. Elsevier
70. S. Gil, L. Muñoz, L. Sánchez-Silva, A. Romero, J.L. Valverde (2011) Synthesis and characterization of Au supported on carbonaceous material-based catalysts for the selective oxidation of glycerol. Chem Eng J 172(1):418–429.
71. A.M. Venezia, G. Pantaleo, A. Longo, G. Di Carlo, M.P. Casaletto, F.L. Liotta, G. Deganello (2005) Relationship between Structure and CO Oxidation Activity of Ceria-Supported Gold Catalysts. J Phys Chem B 109(7):2821–2827.
72. L. Zhang, C. Zhang, H. He (2009) The role of silver species on Ag/Al2O3 catalysts for the selective catalytic oxidation of ammonia to nitrogen. J Catal 261(1):101–109.
73. M. Akimoto, K. Ichikawa, E. Echigoya (1982) Kinetic and adsorption studies on vapor-phase catalytic oxidation of olefins over silver. J Catal 76(2):333–344.
74. Ç. Güldür, F. Balikçi (2002) Selective carbon monoxide oxidation over Ag-based composite oxides. Int J Hydrogen Energy 27(2):219–224.
75. J. Zhang, Y. Li, Y. Zhang, M. Chen, L. Wang, C. Zhang, H. He (2015) Effect of Support on the Activity of Ag-based Catalysts for Formaldehyde Oxidation. Sci Rep 5(1):12950.
76. J. Shen, W. Shan, Y. Zhang, J. Du, H. Xu, K. Fan, W. Shen, Y. Tang (2006) Gas-phase selective oxidation of alcohols: In situ electrolytic nano-silver/zeolite film/copper grid catalyst. J Catal 237(1):94–101.
77. T. Mitsudome, Y. Mikami, H. Funai, T. Mizugaki, K. Jitsukawa, K. Kaneda (2008) Oxidant-Free Alcohol Dehydrogenation Using a Reusable Hydrotalcite-Supported Silver Nanoparticle Catalyst. Angew Chemie 120(1):144–147.
78. X.E. Verykios, F.P. Stein, R.W. Coughlin (1980) Oxidation of Ethylene over Silver: Adsorption, Kinetics, Catalyst. Catal Rev 22(2):197–234.
79. H. Sperber (1969) Herstellung von Formaldehyd aus Methanol in der BASF. Chemie Ing Tech - CIT 41(17):962–966.
80. M.J. Beier, T.W. Hansen, J.-D. Grunwaldt (2009) Selective liquid-phase oxidation of alcohols catalyzed by a silver-based catalyst promoted by the presence of ceria. J Catal 266(2):320–330.
81. F. Adam, A.E. Ahmed, S.L. Min (2008) Silver modified porous silica from rice husk and its catalytic potential. J Porous Mater 15(4):433–444.
82. P. Nagaraju, M. Balaraju, K. Mohan Reddy, P.S. Sai Prasad, N. Lingaiah (2008) Selective oxidation of allylic alcohols catalyzed by silver exchanged molybdovanado phosphoric acid catalyst in the presence of molecular oxygen. Catal Commun 9(6):1389–1393.
83. L.. Liotta, A.. Venezia, G. Deganello, A. Longo, A. Martorana, Z. Schay, L. Guczi (2001) Liquid phase selective oxidation of benzyl alcohol over Pd–Ag catalysts supported on pumice. Catal Today 66(2–4):271–276.
84. M. Besson, P. Gallezot (2003) Deactivation of metal catalysts in liquid phase organic reactions. Catal Today 81(4):547–559.
85. W. Hou, N.A. Dehm, R.W.J. Scott (2008) Alcohol oxidations in aqueous solutions using Au, Pd, and bimetallic AuPd nanoparticle catalysts. J Catal 253(1):22–27.
86. N. Dimitratos, F. Porta, L. Prati, A. Villa (2005) Synergetic effect of platinum or palladium on gold catalyst in the selective oxidation of D-sorbitol. Catal Letters 99(3–4):181–185.

87. C. Evangelisti, E. Schiavi, L.A. Aronica, A.M. Caporusso, G. Vitulli, L. Bertinetti, G. Martra, A. Balerna, S. Mobilio (2012) Bimetallic Gold–Palladium vapour derived catalysts: The role of structural features on their catalytic activity. J Catal 286:224–236.
88. C. Della Pina, E. Falletta, M. Rossi (2012) Update on selective oxidation using gold. Chem Soc Rev 41(1):350–369.
89. N.K. Chaki, H. Tsunoyama, Y. Negishi, H. Sakurai, T. Tsukuda (2007) Effect of Ag-Doping on the Catalytic Activity of Polymer-Stabilized Au Clusters in Aerobic Oxidation of Alcohol. J Phys Chem C 111(13):4885–4888.
90. X. Huang, X. Wang, X. Wang, X. Wang, M. Tan, W. Ding, X. Lu (2013) P123-stabilized Au–Ag alloy nanoparticles for kinetics of aerobic oxidation of benzyl alcohol in aqueous solution. J Catal 301:217–226.
91. I. Kaskow, P. Decyk, I. Sobczak (2018) The effect of copper and silver on the properties of Au-ZnO catalyst and its activity in glycerol oxidation. Appl Surf Sci 444:197–207.
92. J.F. Gomes, A.C. Garcia, L.H.S. Gasparotto, N.E. de Souza, E.B. Ferreira, C. Pires, G. Tremiliosi-Filho (2014) Influence of silver on the glycerol electro-oxidation over AuAg/C catalysts in alkaline medium: a cyclic voltammetry and in situ FTIR spectroscopy study. Electrochim Acta 144:361–368.
93. Y.-C. Kim, N.-C. Park, J.-S. Shin, S.R. Lee, Y.J. Lee, D.J. Moon (2003) Partial oxidation of ethylene to ethylene oxide over nanosized Ag/α-Al2O3 catalysts. Catal Today 87(1–4):153–162.
94. K. Villani, R. Brosius, J.A. Martens (2005) Catalytic carbon oxidation over Ag/Al2O3. J Catal 236(1):172–175.
95. Y. Wang, J.-M. Zheng, K. Fan, W.-L. Dai (2011) One-pot solvent-free synthesis of sodium benzoate from the oxidation of benzyl alcohol over novel efficient AuAg/TiO2 catalysts. Green Chem 13(7):1644.
96. Y. Guan, N. Zhao, B. Tang, Q. Jia, X. Xu, H. Liu, R.I. Boughton (2013) A stable bimetallic Au–Ag/TiO2 nanopaper for aerobic oxidation of benzyl alcohol. Chem Commun 49(98):11524.
97. B.M. Pagliaro, M. Rossi, M. Pagliaro (2010) Glycerol : Properties and Production. In: Futur. glycerol. pp 1–17
98. S. Campisi, C.E. Chan-Thaw, D. Wang, A. Villa, L. Prati (2016) Metal nanoparticles on carbon based supports: The effect of the protective agent removal. Catal Today 278:91–96.
99. L.A. Aronica, E. Schiavi, C. Evangelisti, A.M. Caporusso, P. Salvadori, G. Vitulli, L. Bertinetti, G. Martra (2009) Solvated gold atoms in the preparation of efficient supported catalysts: Correlation between morphological features and catalytic activity in the hydrosilylation of 1-hexyne. J Catal 266:250–257.
100. L. Prati, A. Villa (2016) Gold catalysis : preparation, characterization, and applications. CRC Press
101. V.K. Kaushik (1991) XPS core level spectra and Auger parameters for some silver compounds. J Electron Spectros Relat Phenomena 56(3):273–277.
102. A.M. Ferraria, A.P. Carapeto, A.M. Botelho do Rego (2012) X-ray photoelectron spectroscopy: Silver salts revisited. Vacuum 86(12):1988–1991.
103. L. Han, Q. Meng, D. Wang, Y. Zhu, J. Wang, X. Du, E.A. Stach, H.L. Xin (2016) Interrogation of bimetallic particle oxidation in three dimensions at the nanoscale. Nat Commun 7:1–9.
104. B.D. Todd, R.M. Lynden-Bell (1993) Surface and bulk properties of metals modelled with Sutton-Chen potentials. Surf Sci 281(1–2):191–206.
105. G.G. Li, F. Bridges, C.H. Booth (1995) X-ray-absorption fine-structure standards: A comparison of experiment and theory. Phys Rev B 52(9):6332–6348.
106. S. Calvin, M.M. Miller, R. Goswami, S.-F. Cheng, S.P. Mulvaney, L.J. Whitman, V.G. Harris (2003) Determination of crystallite size in a magnetic nanocomposite using extended x-ray absorption fine structure. J Appl Phys 94(1):778–783.
107. A.M. Beale, B.M. Weckhuysen (2010) EXAFS as a tool to interrogate the size and shape of mono and bimetallic catalyst nanoparticles. Phys Chem Chem Phys 12(21):5562.
108. A. Balerna, E. Bernieri, P. Picozzi, A. Reale, S. Santucci, E. Burattini, S. Mobilio (1985) Extended x-ray-absorption fine-structure and near-edge-structure studies on evaporated small clusters of Au.

Phys Rev B 31(8):5058–5065.
109. A. Jentys (1999) Estimation of mean size and shape of small metal particles by EXAFS. Phys Chem Chem Phys 1(17):4059–4063.
110. N. Marinkovic, K. Sasaki, R. Adzic (2016) Nanoparticle size evaluation of catalysts by EXAFS: Advantages and limitations. Zast Mater 57(1):101–109.
111. A.I. Frenkel, Q. Wang, S.I. Sanchez, M.W. Small, R.G. Nuzzo (2013) Short range order in bimetallic nanoalloys: An extended X-ray absorption fine structure study. J Chem Phys 138(6):064202.
112. Y.-L. Fang, J.T. Miller, N. Guo, K.N. Heck, P.J.J. Alvarez, M.S. Wong (2011) Structural analysis of palladium-decorated gold nanoparticles as colloidal bimetallic catalysts. Catal Today 160(1):96–102.
113. M.G. Weir, M.R. Knecht, A.I. Frenkel, R.M. Crooks (2010) Structural Analysis of PdAu Dendrimer-Encapsulated Bimetallic Nanoparticles. Langmuir 26(2):1137–1146.
114. H. Deng, Y. Yu, F. Liu, J. Ma, Y. Zhang, H. He (2014) Nature of Ag Species on Ag/γ-Al 2 O 3 : A Combined Experimental and Theoretical Study. ACS Catal 4(8):2776–2784.
115. C.C. Tyson, A. Bzowski, P. Kristof, M. Kuhn, R. Sammynaiken, T.K. Sham (1992) Charge redistribution in Au-Ag alloys from a local perspective. Phys Rev B 45(16):8924–8928.
116. S. Cattaneo, H. Naslhajian, F. Somodi, C. Evangelisti, A. Villa, L. Prati (2018) Ruthenium on Carbonaceous Materials for the Selective Hydrogenation of HMF. Molecules 23(8):2007.
117. J.-L. Shie, Y.-H. Chen, C.-Y. Chang, J.-P. Lin, D.-J. Lee, C.-H. Wu (2002) Thermal Pyrolysis of Poly(vinyl alcohol) and Its Major Products. Energy & Fuels 16(1):109–118.
118. K.J. Klabunde, G.B. Sergeev (2013) Nanochemistry. Elsevier
119. C. Bianchi, F. Porta, L. Prati, M. Rossi (2000) Selective liquid phase oxidation using gold catalysts. Top Catal 13(3):231–236.
120. X. Yang, X. Wang, C. Liang, W. Su, C. Wang, Z. Feng, C. Li, J. Qiu (2008) Aerobic oxidation of alcohols over Au/TiO2: An insight on the promotion effect of water on the catalytic activity of Au/TiO2. Catal Commun 9(13):2278–2281.
121. D.I. Enache, J.K. Edwards, P. Landon, B. Solsona-Espriu, A.F. Carley, A.A. Herzing, M. Watanabe, C.J. Kiely, D.W. Knight, G.J. Hutchings (2006) Solvent-free oxidation of primary alcohols to aldehydes using Au-Pd/TiO2 catalysts. Science 311(5759):362–265.
122. T. Fujitani, I. Nakamura (2011) Mechanism and Active Sites of the Oxidation of CO over Au/TiO2. Angew Chemie Int Ed 50(43):10144–10147.
123. Y. Sugano, Y. Shiraishi, D. Tsukamoto, S. Ichikawa, S. Tanaka, T. Hirai (2013) Supported Au-Cu Bimetallic Alloy Nanoparticles: An Aerobic Oxidation Catalyst with Regenerable Activity by Visible-Light Irradiation. Angew Chemie Int Ed 52(20):5295–5299.
124. Y. Hong, X. Jing, J. Huang, D. Sun, T. Odoom-Wubah, F. Yang, M. Du, Q. Li (2014) Biosynthesized Bimetallic Au–Pd Nanoparticles Supported on TiO $_2$ for Solvent-Free Oxidation of Benzyl Alcohol. ACS Sustain Chem Eng 2(7):1752–1759.
125. A. Sandoval, A. Aguilar, C. Louis, A. Traverse, R. Zanella (2011) Bimetallic Au–Ag/TiO2 catalyst prepared by deposition–precipitation: High activity and stability in CO oxidation. J Catal 281(1):40–49.
126. N. Toshima, T. Yonezawa (1998) Bimetallic nanoparticles—novel materials for chemical and physical applications. New J Chem 22(11):1179–1201.
127. L. Deng, W. Hu, H. Deng, S. Xiao, J. Tang (2011) Au-Ag bimetallic nanoparticles: Surface segregation and atomic-scale structure. J Phys Chem C 115(23):11355–11363.
128. T.J.A. Slater, A. Macedo, S.L.M. Schroeder, M.G. Burke, P. O'Brien, P.H.C. Camargo, S.J. Haigh (2014) Correlating catalytic activity of Ag-Au nanoparticles with 3D compositional variations. Nano Lett 14(4):1921–1926.
129. C. Méthivier, R. Zanella, C. Louis, L. Delannoy, A. Sandoval (2015) Synergetic effect in bimetallic Au–Ag/TiO2 catalysts for CO oxidation: New insights from in situ characterization. Appl Catal A Gen 504:287–294.
130. R. Zanella, L. Delannoy, C. Louis (2005) Mechanism of deposition of gold precursors onto TiO2

during the preparation by cation adsorption and deposition–precipitation with NaOH and urea. Appl Catal A Gen 291(1–2):62–72.
131. Q. Yao, C. Wang, H. Wang, H. Yan, J. Lu (2016) Revisiting the Au Particle Size Effect on TiO_2-Coated Au/TiO_2 Catalysts in CO Oxidation Reaction. J Phys Chem C 120(17):9174–9183.
132. Y.-C. Shi, J.-J. Feng, X.-X. Lin, L. Zhang, J. Yuan, Q.-L. Zhang, A.-J. Wang (2019) One-step hydrothermal synthesis of three-dimensional nitrogen-doped reduced graphene oxide hydrogels anchored PtPd alloyed nanoparticles for ethylene glycol oxidation and hydrogen evolution reactions. Electrochim Acta 293:504–513.
133. F. Bonaccorso, M. Zerbetto, A.C. Ferrari, V. Amendola (2013) Sorting Nanoparticles by Centrifugal Fields in Clean Media. J Phys Chem C 117(25):13217–13229.
134. M. Romeo, K. Bak, J. El Fallah, F. Le Normand, L. Hilaire (1993) XPS Study of the reduction of cerium dioxide. Surf Interface Anal 20(6):508–512.
135. J.M.C. Soares, P. Morrall, A. Crossley, P. Harris, M. Bowker (2003) Catalytic and noncatalytic CO oxidation on Au/TiO2 catalysts. J Catal 219(1):17–24.
136. E. Kukulska-Zając, J. Datka (2008) The IR studies of the interaction of organic molecules with Ag+ ions in zeolites. Microporous Mesoporous Mater 109(1–3):49–57.
137. H. Klimev, K. Fajerwerg, K. Chakarova, L. Delannoy, C. Louis, K. Hadjiivanov (2007) Oxidation of gold metal particles supported on TiO2: an FTIR study by means of low-temperature CO adsorption. J Mater Sci 42(10):3299–3306.
138. M. Kantcheva, M.U. Kucukkal, S. Suzer (2000) Spectroscopic Investigation of Species Arising from CO Chemisorption on Titania-Supported Manganese. J Catal 190(1):144–156.
139. H. Tang, Y. Su, B. Zhang, A.F. Lee, M.A. Isaacs, K. Wilson, L. Li, Y. Ren, J. Huang, M. Haruta, B. Qiao, X. Liu, C. Jin, D. Su, J. Wang, T. Zhang (2017) Classical strong metal–support interactions between gold nanoparticles and titanium dioxide. Sci Adv 3(10):e1700231.
140. R.A. Sheldon, H. van. Bekkum (2001) Fine chemicals through heterogeneous catalysis. Wiley-VCH
141. E.G. Rodrigues, M.F.R. Pereira, X. Chen, J.J. Delgado, J.J.M. Órfão (2013) Selective Oxidation of Glycerol over Platinum-Based Catalysts Supported on Carbon Nanotubes. Ind Eng Chem Res 52(49):17390–17398.
142. J.-W. Park, J.S. Shumaker-Parry (2015) Strong Resistance of Citrate Anions on Metal Nanoparticles to Desorption under Thiol Functionalization. ACS Nano 9(2):1665–1682.
143. A. Zwijnenburg, A. Goossens, W.G. Sloof, M.W.J. Crajé, A.M. Van der Kraan, L.J. De Jongh, M. Makkee, J.A. Moulijn (2002) XPS and Mössbauer characterization of Au/TiO2 propene epoxidation catalysts. J Phys Chem B 106(38):9853–9862.
144. S. Arrii, F. Morfin, A.J. Renouprez, J.L. Rousset (2004) Oxidation of CO on Gold Supported Catalysts Prepared by Laser Vaporization: Direct Evidence of Support Contribution. J Am Chem Soc 126(4):1199–1205.
145. J. Radnik, C. Mohr, P. Claus (2003) On the origin of binding energy shifts of core levels of supported gold nanoparticles and dependence of pretreatment and material synthesis. Phys Chem Chem Phys 5(1):172–177.
146. H.Y. Park, T.Y. Jeon, J.H. Jang, S.J. Yoo, K.H. Choi, N. Jung, Y.H. Chung, M. Ahn, Y.H. Cho, K.S. Lee, Y.E. Sung (2013) Enhancement of oxygen reduction reaction on PtAu nanoparticles via CO induced surface Pt enrichment. Appl Catal B Environ 129:375–381.
147. T.-Y. Yung, T.-Y. Liu, L.-Y. Huang, K.-S. Wang, H.-M. Tzou, P.-T. Chen, C.-Y. Chao, L.-K. Liu (2015) Characterization of Au and Bimetallic PtAu Nanoparticles on PDDA-Graphene Sheets as Electrocatalysts for Formic Acid Oxidation. Nanoscale Res Lett 10(1):365.
148. N. Dimitratos, A. Villa, D. Wang, F. Porta, D. Su, L. Prati (2006) Pd and Pt catalysts modified by alloying with Au in the selective oxidation of alcohols. J Catal 244(1):113–121.
149. Y. Kwon, K.J.P. Schouten, M.T.M. Koper (2011) Mechanism of the Catalytic Oxidation of Glycerol on Polycrystalline Gold and Platinum Electrodes. ChemCatChem 3(7):1176–1185.
150. B.N. Zope, R.J. Davis (2011) Inhibition of gold and platinum catalysts by reactive intermediates produced in the selective oxidation of alcohols in liquid water. Green Chem 13(12):3484.

Chapter 3. Valorisation of 2nd biomass feedstock generation

3.1. Aims and objectives of the chapter

In order to valorise the molecules derived or related to the second generation of biomass, new efficient and durable catalysts need to be designed and optimised. For having an overview on the valorisation of some of the most important molecules derived from the second-generation of biomass feedstock, 5-(hydroxymethyl)furfural and levulinic acid (both cellulose-derived), furfural (from hemicellulose) and lastly the benzyl alcohol (model compound molecule for the building blocks of lignin) transformations were evaluated.

In order to attempt a valuable valorisation of the abovementioned molecules, already exploited systems in the target reactions were evaluated and new modified materials were synthesised on the base of them.

Ru-based catalysts for instance, especially supported on carbonaceous materials, have already highlighted their reactivity toward the target valorisations or more in general for related processes: i.e. Ru/AC showed a fully conversion of levulinic acid with a high selectivity toward the desired γ-Valerolactone and the bare CNFs turned out to be active in the metal-free fructose dehydration to HMF. Ru-based materials were for the reported reason studied in the hydrogenation of 5-(hydroxymethyl)furfural and levulinic acid, two molecules directly derived from cellulose. Different functionalities (oxygen, nitrogen and phosphorus) were introduced onto carbon nanofibers (CNFs). CNFs have shown outstanding features as tenable and valuable support for nanoparticles (or even used as is for cellulose-derived molecules valorisation, opening the door for a future one-pot transformation). Ru nanoparticles supported on CNFs were therefore synthetised in order to promote both the acidic-catalysed and metal-catalysed steps present in the pathways of the target hydrogenations. The aim of this part of the work was therefore to synthesise and characterise these bifunctional catalysts and study how different functionalisations affect the catalytic activity in the aforementioned reactions. The interesting differences to be observed were both in term of selectivity (differences in the reaction pathway) and in activity (differences in conversion rate of the substrate).

On the other hand, Pt-based catalysts were studied in the hydrogenation of furfural: a hemicellulose derived molecule. The choice of platinum was strongly related to our goal: convert in mild reaction conditions (where Pt showed remarkable activity) the substrate into diols, chemicals used in the plastic industry. In order to approach this issue, the

catalysts required two specific active sites: an active metal in the form of nanoparticles that was able to hydrogenate the carbonylic group of the furfural (such as Pt nanoparticles), and acidic sites that could carry on the ring-opening step (such as Brønsted acid sites of niobia). The aim of this part of the work was therefore firstly to synthesise a set of three niobia-based supports with different acidic properties, namely bare niobia and Ti- and W-doped niobia. Pt nanoparticles were then immobilised onto these supports. After thorough characterisation, the catalysts were tested in the aforementioned reaction and the catalytic results correlated with the different acidic properties of the materials. In addition, the choice of using a support that is already active in the xylose dehydration to furfural (niobia), could give us the chance in the future to attempt the direct conversion of sugars into high added-value products.

Finally, different mono- and bi-metallic nanoparticles supported on activated carbon were studied in the oxidation of benzyl alcohol (a model molecule of lignin structure). The metal studied were Pd, Pt, Ru and Cu. The main objective of this latter study was to correlate the different bimetallic structures obtained with differences in the activity and selectivity of the target reaction. In particular, a special attention was payed to AuCu bimetallic nanoparticles, with the aim of studying the effect of relative metal concentration and the importance of the local particles structure and composition and their role on the catalytic properties. To pursuit this purpose, “naked” bimetallic nanoparticles were synthesised by Solvated Metal Atom Dispersion technique (SMAD) and deposited onto activated carbon. The choice of the synthetic technique was dictated to the necessity of having an easily oxidisable Cu surface.

3.2. The importance of cellulose derivatives (LA – HMF)

The production of industrially relevant fine and bulk chemicals from readily available lignocellulosic biomass has become a new trend in catalysis as already discussed in the introduction section [1]. Lignocellulosic biomass is a natural renewable carbon resource composed of lignin, cellulose and hemicellulose, and all together they represent ca. the 75 % of the 170 billion metric tons of the total biomass production per year by photosynthesis [2, 3]. Cellulose, in particular, is a sustainable biomass-derived raw material, made up of D-glucose units linked together by β-1,4 glycosidic bonds [4]. Cellulose can be therefore hydrolysed to glucose, a building block for the production of industrially important chemicals such as levulinic acid (LA) and 5-hydroxymethylfurfural (HMF) as shown in Scheme 3-1 [5].

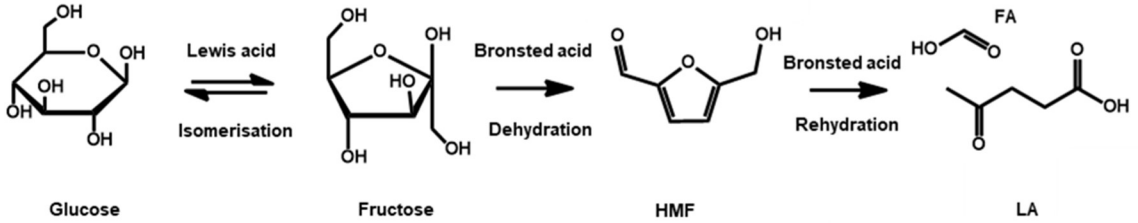

Scheme 3-1. General representation of the formation of levulinic acid from glucose, with 5-hydroxymethylfurfural as intermediate.

Both molecules have attracted much attention in the past several years, as potential renewable feedstocks directly derived from cellulose, for the production of fuels and fine chemicals [6–8].

3.2.1. *HMF hydrogenation*

The conversion of HMF in reducing atmosphere is a much more complicated reaction compared to the LA conversion, and several products can be formed depending on the reaction conditions and catalyst used (Scheme 3-2).

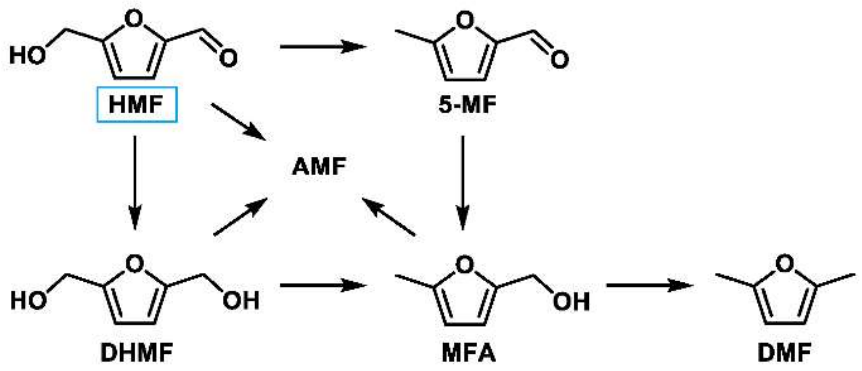

Scheme 3-2. Typical reaction mechanism for the conversion of 5-hydroxymethylfurfural (HMF – blue box) in an alcoholic solvent (Ru catalysed).

In addition to the hydrogenation of the carbonylic group, hydrodeoxygenation reactions can occur with consequent loss of OH groups in the form of water [9]. Aromatic ring hydrogenation and ring opening are reported as well, although they require harsh reaction conditions (high temperature and hydrogen pressure) in order to occur (i.e. levulinic acid, diols and triols [9–11]). Finally, the use of alcoholic solvents can lead to etherification reactions as well.

The conversion of HMF is typically carried out with metal nanoparticles supported on either high surface area metal oxides or carbonaceous materials [12]. Among the plethora of catalysts that show activity towards the aforementioned reactions, Ru nanoparticles supported on carbonaceous materials showed remarkable activity and selectivity [13–18]. Ru, in fact, is considered one of the most effective catalyst in hydrogenation and hydrogenolysis reactions due to its strong ability to interact with O-containing species and promote the hydrodeoxygenation pathway [19, 20].

Several studies have been conducted on the aforementioned catalyst in the last decade. The main products observed were 2,5-dimethylfuran, 2,5-dihydroxymethylfuran and alkoxymethyl furfurals when the reaction was conducted in alcoholic solvents. 2,5-dimethylfuran (DMF), is a well-known potential biofuel with a high research octane number and energy density [21–23], while 2,5-dihydroxymethylfuran (DHMF) can be used in the polymer industry to produce polyethers based polyurethane foams, as a solvent

or as a precursor to the production of other high-value chemicals [24, 25]. The products of etherification of HMF with alcoholic solvents (AMF, alkoxymethyl furfurals), have recently attracted attention due to their potential use as fuel or fuel additives. The formation of ethers from HMF and alcoholic solvents is a well-known and widely reported process, especially as by products in the dehydration process of fructose (or hexose in general) when an alcoholic solvent and an acidic solid catalyst are used [26]. Several patents, for instance, were released in favour of Avantium, who claimed the use of various AMF as potential fuel or fuel additives [27]. Recently, various studies have been published concerning the production of AMF, especially with small molecular weight alcohols (since the reactivity decrease increasing the length of the hydrocarbon chain), obtaining high yields by using various types of solid acid catalysts [15, 28, 29]. Furthermore, the use of an alcoholic solvent in this latter reaction is recommended due to the instability of HMF in water [30].

Other studies are pointing in the appealing direction of synthesise bifunctional Ru catalysts to obtain DMF in one pot and with an high selectivity, using 2-propanol as hydrogen donor (Meerwein-Ponndrof-Verley mechanism) [31]. They observed a synergistic effect derived from the co-presence of reduced and oxidised ruthenium species. It is interesting the provided elucidation of the role of a present portion of RuO_2 on the surface of the catalyst. Pure RuO_2 catalyses the hydrogenation of HMF to 2,5-bis(hydroxymethyl)furan presumably acting as a Lewis acid catalyst. Metallic Ru, on the other hand, catalyses the hydrogenolysis for the production of DMF.

In a recent publication, Ru nanoparticles were supported on activated carbon and carbon nanofibers for the selective production of DMF, DHMF, and AMF [32]. The selectivity to the different products could be tuned simply by changing the type of carbonaceous support; in particular, Ru supported on nanofibers displayed high conversions of HMF into DHMF and AMF with only a small formation of products of hydrogenolysis (DMF) while a high amount of DMF was produced when activated carbon was employed.

Among all the carbon allotropes that are frequently used in catalysis, carbon nanofibers (CNFs) have recently attracted the attention from both academia and industry. CNFs were discovered in 1889, when “hair-like” carbon filaments were reported to grow on metal crucible walls through decomposition of an organic gas at a high temperature [33]. Iijima et al. were the first to characterise in detail such nanostructures, reporting high thermal and electrical conductivity, high mechanical strength, and good chemical resistance[34].

Currently, CNFs are widely used in gas sensors, as polymer additive, in electronic components, as drug delivery systems and as in the present case, as heterogeneous catalysts [35–39].

The incredibly easy tunability of some physiochemical properties, such as a surface area, porosity, and surface chemistry, makes these materials extremely versatile from a catalytic point of view [37, 38]. Depending on the type of functionalisation introduced, the surface acidity/basicity of the support can be modified in order to increase the selectivity towards specific products [40].

In addition, the presence of functionalisation on CNFs proved to enhance the activity and stability of noble metal NPs (Pd and AuPd) in the liquid phase oxidation of benzyl alcohol through an increase in metal-support interaction [41, 42]. The nature of the functionalisation can affect the reaction pathway as well, affecting the selectivity of the system. Pd nanoparticles deposited on pyridine-containing CNFs, in fact, showed higher activity in the same reaction compared to pyrrole/pyridine-containing CNFs due to a higher surface basicity that facilitated the H-abstraction step [43]. Another valuable example derives from O-containing functionalities that proved to be critical in the Pd-catalysed cinnamaldehyde hydrogenation reaction. The presence of oxygen functionalities, in fact, showed to impede the adsorption of the benzene ring on the CNFs surface, which increased the selectivity towards the hydrogenation of the carbonyl group [44–46]. In addition, in a recent report, an efficient procedure for the introduction of functionalities on CNFs was set up and their activity in the metal-free fructose dehydration to HMF was demonstrated [47]. Ruthenium was introduced into the supports by incipient wetness impregnation method.

3.2.2. *LA hydrogenation*

LA, with its two functional active groups (carbonylic and carboxylic groups) can be converted to γ-valerolactone (GVL) and other liquid fuels through hydrogenation reactions [48].

For these reasons GVL has defined as "top 10" biomass platform molecules derivates from carbohydrates [49].

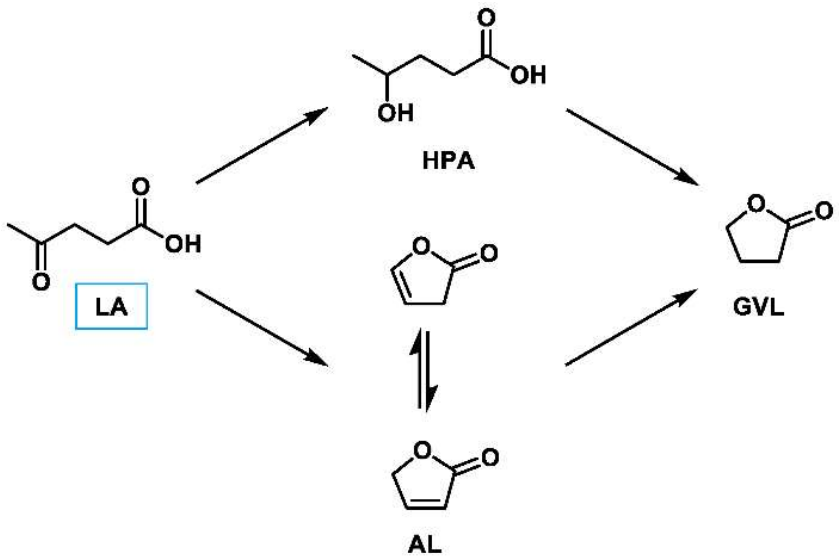

Scheme 3-3. Typical reaction mechanism for the conversion of levulinic acid (LA – blue box) to gamma-valerolactone (GVL) in water media.

This process can occur through either formation of 4-hydroxypentanoic acid (HPA – pathway 1) or angelica lactone (AL – pathway 2) as intermediates as represented in the scheme above (Scheme 3-3) [13, 14].

Pathway 1 leads firstly to a hydrogenation of the ketone group in LA to form 4-hydroxypentanoic acid (HPA – Ru/C catalysed). Subsequently, HPA undergoes acid-catalysed, intramolecular esterification (ring closure) to form the thermodynamically preferred lactone, GVL. Alternatively, pathway 2, angelica lactone (AL) can be formed via endothermic dehydration of LA (acid-catalysed), and they become increasingly prevalent in acidic media and at elevated temperatures. In the presence of Ru/C and under H_2 atmospheres, angelica lactones underwent to a prompt hydrogenate, forming GVL. To date, the relative contributions of each pathway have not been delineated and it is unclear which pathway in are kinetically significant [50].

GVL can be used directly both as additive for biofuels or as solvent; in addiction, it can also be converted into valuable intermediates for the production of biopolymers, fine chemicals or into more refined liquid fuels [51–54]. GVL, due to his high oxygen content,

can be used as additive for fuels, although it usually requires a further valorisation in order to be converted into proper liquid fuel [55]. For example, GVL can be upgraded in 5-nonanol through dehydration and isomerisation in a single step over a USY zeolite catalyst to produce a mixture of branched C_9 alkenes. The branched C_9 alkenes can be than hydrogenated to produce alkanes with appropriate structures and molecular weight for use as fuel [56]. On the other hand, a second approach involves the transformation by ring opening of the GVL to an isomeric mixture of unsaturated pentoic acids, followed by decarboxylation to produce butene isomers. The resulting butene, in gas stream, can be further transformed in C_{8+} alkanes used as fuel for jets (oligomerisation in presence of CO_2 and solid acid catalysts) [57].

Historically, the selective transformation of LA into GVL was started to be studied from the 1930: Schuette and co-workers were the first to attempt this conversion exploiting Pt-based catalyst, achieving a good yield of 87 % (44 h reaction time, 3 bar H_2, 25 °C) [58]. In subsequent years, GVL yield was improved to 94 % by using Raney nickel and copper chromite catalysts (200 bar H_2, 250 °C) [59]. Also other metals (i.e. Cu, Pt and Pd), in addition to Ni, were tested for this valorisation and among all the active systems evaluated, Ru-based catalysts showed the best result [49]. The conversion of LA into GVL was also attempt in supercritical CO_2 media in presence of metal noble catalysts from some research groups: Poliakoff and co-workers, for instance, reported a fully conversion of LA (into GVL) by means of a 5 wt.% Ru/SiO_2 catalyst [60, 61]. Even pure colloidal Ru nanoparticles resulted active for this transformation, both in presence of hydrogen and by means of hydrogenation transfer (from formic acid) [62]. About this latter approach, however, an important obstacle was represented by the recovery of the catalysts [5]. The Ru-based catalysts, thus, leaded to interesting results, especially when the precious metal was supported on carbonaceous materials. AlShaal et al., in fact, reported a 100 % conversion of LA with a 97.5 % of selectivity towards GVL over traditional activated carbon supported ruthenium catalyst (Ru/C) [63]. Other promising studies exploited Ru/C (graphene) as catalysts, leading to a fully conversion of LA into GVL with a selectivity of 99.7 % [49]. Another interesting investigation was conducted by Ren and colleagues: the authors were able to synthesise a very active catalysts, 18 times more active in comparison with the commercial Ru-based catalysts, by supporting Ru nanoparticles on carbon nanofibers, suggestion the requirement of new approaches for the synthesis of novel catalytic systems to be exploited in this reaction [64].

3.2.3. *Catalysts characterisation*

For this work, commercial hollow fishbone pyrolytically stripped nanofibers (CNFs-PS) were used and simply referred as CNFs. The fibers possess a thin chemically vapor deposited (CVD) layer of carbon over a graphitic fishbone core. The pyrolytical stripping step allows to remove any polyaromatic hydrocarbons from the fibers' surface, which leaves a thin surface layer of amorphous carbon. The calculated fibers' average diameter was 80 ± 30 nm with a specific surface area of ca. 50 $m^2 g^{-1}$. This support was then treated as reported in the Chapter 4 (experiential part) in order to introduce different surface functionalisations, such as nitrogen (CNFs-N), oxygen (CNFs-O), and phosphorous (CNFs-P) containing groups.

The three different functionalised supports were fully characterised by X-ray Photoelectron Spectroscopy (XPS) in order to obtain information about the presence and the abundance of the functionalities on the support surface. The analyses were conducted on the 1s orbital of all the three heteroatoms. The peak assignments were made according to previous results [47, 65]. In particular, the atomic ratio between C and the three different functionalities introduced is reported in Table 3-1. On the contrary, the nature of the different functional groups detected, again based on XPS results, has been assigned and reported in Table 3-2.

Table 3-1. Atomic C:N:O:P ratio calculated by XPS analysis of the supports.

Sample	Atomic Ratio % C : N : O : P
CNFs	97 : 0 : 3 : 0
CNFs-N	92 : 4 : 4 : 0
CNFs-O	85 : 0 : 15 : 0
CNFs-P	87 : 0 : 12 : 1

Table 3-2. XPS analysis of the different supports used.

Sample		CNFs-N		CNFs-O		CNFs-P	
		BE (eV)	Atom %	BE (eV)	Atom %	BE (eV)	Atom %
N 1s	Pyridine	398.3	49.3	-		-	
	Pyrrole/PyRidone	400.2	44.1	-		-	
	Quaternary N^+	401.2	3.5	-		-	
	Pyridin Oxide	404.6	3.1	-		-	
O 1s	C=O, P=O, P-O	531.5	43.4	531.3	53.2	531.6	50.1
	C-O, C-O-C, P-O-C	533.6	53.2	533.1	42.4	533.3	44.5
	H_2O	536.2	3.4	534.5	4.4	535.6	5.4
P 2p	C-O-P	-		-		133.7	100
C 1s	sp^2	284.7	73.1	284.6	76.8	284.5	77.4
	sp^3, C-P	286.2	13.4	285.1	13.2	285	14.4
	C-O, C=O	288.1	8.8	288.4	6.8	288.5	5.7
	C=C	291.7	4.8	291.5	3.2	291.1	2.5

Oxygen is always present in all the samples, either as individual functionality or conjugated with other heteroatoms. This was expected since all the supports underwent an oxidative pre-treatment. Pristine CNFs, as expected, showed only small amount of oxygen functionality already present in the commercial support (Table 3-1). The oxidative treatment with HNO_3 dramatically increased the number of oxygen functionality (from 3 % of the CNFs to 15 % of the CNFs-O). The HNO_3, in fact, oxidises the defects in the CNFs structure, i.e. edges of the CNFs cup-like structure. Most of the O-functionalities were present as carbonyl groups (C=O, BE of 531.3 eV), which represents the 53.2% of the total oxygenated species, while the remaining functionalities were composed of single C-O bonds (alcoholic and ether groups, BE of 533.1 eV), representing the 42.4% of the total oxygen content. The remaining 4.4% of oxygen detected in the sample was present as adsorbed H_2O (BE 534.5 eV).

CNFs-N, on the other hand, showed the presence of both N and O functionalities, with a similar relative surface abundance of these two heteroatoms (4 % for both N and O, Table 3-2). The presence of N atoms on the support's surface is an indication of the successful

functionalisation. The N-containing species are predominantly pyridines (49 %, at BE of 398.3 eV) and pyrrole/pyridone groups (44 %, at BE of 400.2 eV). The abundance of pyridone groups was further validated by the high concentration of C=O groups detected in the O 1s spectrum (43.4%, at a BE of 531.5 eV). On the contrary, quaternary N^+ and pyridine oxide N^+- O^- groups were present in a small amount: the results show 3.5 % and 3.1 % of the total nitrogen-content at BE of 401.2 and 404.6 eV respectively. Apart from C=O groups, a high amount of C-O and C-O-C groups were also detected in the CNFs-N sample (53.2% at a BE of 533.6 eV), while the remaining oxygen was present as adsorbed H_2O (3.4% at a BE of 536.2 eV).

Lastly, the CNFs-P support showed only a small presence of P functionalities (1 %) as phosphate groups (C-O-P, at a BE of 133.7 eV). As for the other supports, the O 1s spectrum showed a high amount of both carbonyl and alcoholic/ether groups (50.1% and 44.5% at 531.6 and 533.3 eV, respectively). In this case, however, the two aforementioned peaks overlap with the P=O, P-O, and P-O-C groups characteristic of phosphorylated carbonaceous materials, and possibly alter the results. The remaining 5.4 % of oxygen detected at 535.6 eV, as in the previous cases, is present as adsorbed H_2O.

Regarding the C1s region, the XPS analysis is reported in Table 3-2. Four different components could be identified in a BE range of 284–292 eV and were assigned according to previous results [47]. In particular, the peak at ca. 284 eV corresponded to sp^2 graphitic carbon, the peak at ca. 285–286 eV to sp^3 carbon and C-P bonds and the peak at ca. 288 eV to carbon-oxygen bonds, and the peak at ca. 291 eV to aromatic rings. The relative abundance of the four species did not change significantly. This latter result indicates that the nature of the CNFs structure remains almost unchanged and just in minimal part is affected by the functionalisation processes.

After the introduction of Ru by incipient wetness, and the required activation by reduction in reducing atmosphere (H_2), TEM analyses performed on the four catalysts showed a similar average particle size for all the samples in the range of 1 to 2 nm. A good average particle dispersion was observed in all cases. The corresponding Ru/CNFs images, are reported in Figure 3-1. The similar average particle size allowed us to correlate the different catalytic results to the different surface species presents onto the three different supports, excluding any particle size effect.

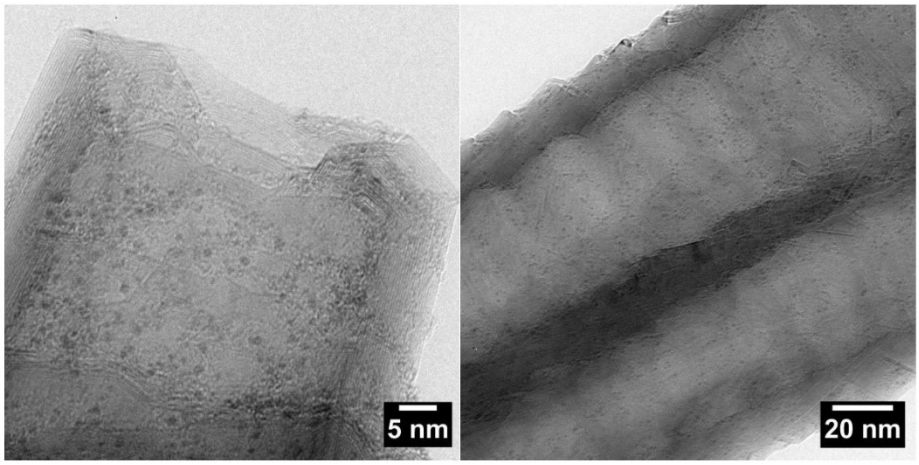

Figure 3-1. Representative TEM micrograph of the Ru/CNFs sample.

3.2.4. *Catalytic results—LA hydrogenation*

The influence of support functionalisation on the catalytic performance was first investigated in the hydrogenation reaction of LA. The reaction conditions chosen were 100 °C and 7 bar of H_2, using water as a solvent (LA concentration of 0.3 mol L^{-1}; Ru:LA molar ratio of 1:1000). Before the reaction, the catalyst was activated in autoclave at 200 °C and 5 bar of H_2 for 1 h, as described in the Chapter 4 (experiential part). As reported in literature, the features of the acid/base sites revealed their importance in tuning the activity of Ru-catalysed hydrogenation of levulinic acid, which demonstrates that, in the presence of strong acidic sites, the conversion increased even though part of the produced GVL was further converted into pentanoic acid [16]. In our case, despite the presence of functionalities of a different nature, the selectivity of the reaction was not affected, with GVL being the only product detected. Although it is impossible to predict the reaction mechanism, based on previous reports we assumed that GVL was formed by the first reduction to HPA followed by a final dehydration step [5, 54]. The impact on the catalytic activity, however, was significant as observable from the results presented in Figure 3-2. The presence of N and O functionalities greatly enhanced the activity, which increased the LA conversion after 3 h from 16 % with bare CNFs to 65 % and 88 % with CNFs-O and CNFs-N, respectively. Since the metal dispersion is comparable in all the catalysts, we tentatively ascribed this effect to the increased hydrophilicity of CNFs-O and CNFs-N with respect to pristine CNFs. The low activity of Ru nanoparticles supported on bare CNFs, has been previously ascribed to the low dispersion of the system in water, due to the high hydrophobicity of the un-functionalised supports [66]. However, considering the lower activity observed in the case of Ru on CNFs-P, we excluded this explanation and ascribed the positive effect of CNFs-O and CNFs-N to the presence of O

and N functionalities. The presence of weak acid sites (carbonyl, alcoholic, and ether groups – XPS data - Table 3-2) on the CNFs-O surface could explain the boost in activity when Ru/CNFs-O was used as a catalyst. The increase in activity in the presence of weak basic N-functionalities, on the other hand, could be attributed to the strong metal-support interaction between the N-containing groups and the anchored metallic Ru nanoparticles. In fact, similar results were obtained with N-doped CNFs in the Pd-catalysed benzyl alcohol oxidation reaction. The enhanced activity was attributed to strong metal-N interactions that prevented agglomeration and thus sintering phenomena of the metal nanoparticles as well as metal leaching [41–43]. With the introduction of P-containing functionalities, we observed only 10 % of LA conversion after 6 h of reaction. This is in contrast with recent results, where an increase in P content resulted in an increase in the conversion rate of the fructose dehydration reaction with metal-free P-functionalised CNFs [47].

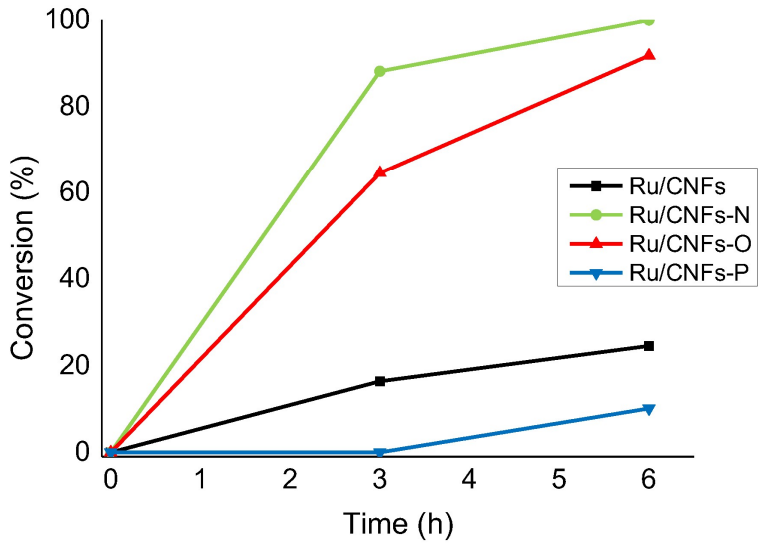

Figure 3-2. Conversion vs. time trends in the LA hydrogenation reaction on the different catalysts tested. All the substrate selectively converted to GVL (selectivity > 99%). Reaction conditions: LA, 0.3 M, substrate/metal = 1000 mol/mol, solvent, 15 mL H_2O, 100 °C, 7 bar H_2.

3.2.5. *Catalytic results—HMF hydrogenation*

The hydrogenation of HMF was performed in 2-butanol as solvent at 150 °C and 20 bar of H_2 (HMF concentration of 0.08 mol L^{-1}, Ru:HMF molar ratio of 1:100). Before the reaction, the catalyst was activated in autoclave at 200 °C and 5 bar of H_2 for 1 h, as described in the Chapter 4 (experiential part). 2-butanol was used since it is one of the most used extraction solvents in the fructose dehydration to HMF [12, 22, 24, 67] and could lead to AMF production, important high added-value products. A graph comparing the activity of the different catalysts is reported in Figure 3-3. The presence of an organic medium in the HMF hydrogenation, annul the negative hydrophobicity effect observed in the LA hydrogenation with Ru/CNFs. In this case, Ru nanoparticles supported on bare CNFs displayed the highest activity among the catalysts studied (86 % of conversion after 1 h). The presence of weak acid sites (CNFs-O) in this case appeared to not have an effect on the catalyst behaviour. Indeed, Ru on CNFs and CNFs-O behaved similarly in terms of activity and selectivity (82 % of conversion after 1 h - Figure 3-3). Apart from LA hydrogenation, the Ru/CNFs-N catalyst showed a detrimental effect in activity (40 % of conversion after 1 h - Figure 3-3). However, most importantly, they catalysed the formation of ethers more efficiently by reacting DHMF and methylfurfuryl alcohol (MFA) with the solvent (Scheme 3-2).

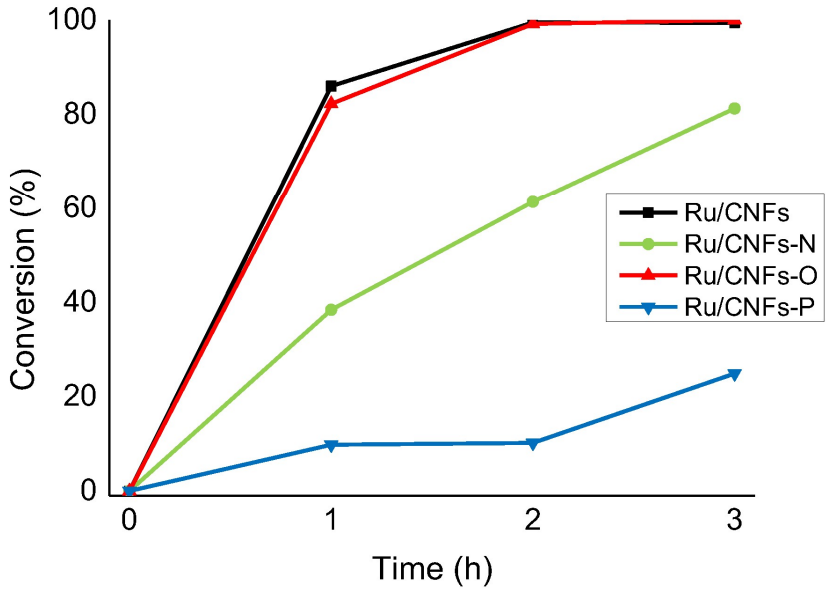

Figure 3-3. Change in activity in the HMF hydrogenation reaction on the different catalysts tested. Reaction conditions: HMF, 0.08 M, substrate/metal = 100 mol/mol, solvent, 15 mL 2-butanol, 150 °C, and 20 bar H_2.

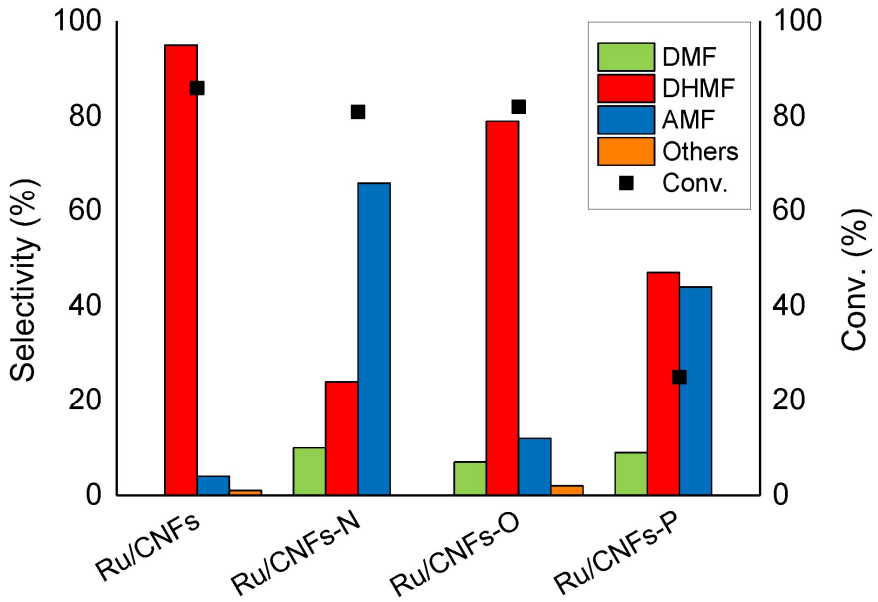

Figure 3-4. Change in selectivity in the HMF hydrogenation reaction on the different catalysts tested. Reaction conditions: HMF, 0.08 M, substrate/metal = 100 mol/mol, solvent, 15 mL 2-butanol, 150 °C, 20 bar H_2, reaction time: Ru/CNFs and Ru/CNFs-O 1 h, Ru/CNFs-N and Ru/CNFs-P 3 h.

Lastly, the Ru/CNFs-P catalysts showed the lowest activity among the catalysts tested (25% of conversion after 3 h -Figure 3-3). Despite the low content of P-functionalities shown (Table 3-1), it appears that the P-groups have a strong negative effect on the catalyst activity in contrast with what was reported for dehydration reactions in water media [47].

Considering more in details the selectivity of this complex reaction, a previous study reported the hydrogenation of HMF in the presence of a CNFs-based catalyst producing a series of products derived from several consecutive and parallel reactions [32]. The selectivity in Figure 3-4 were compared at iso-conversion (80 %, except with Ru/CNFs-P that was compared at ca. 30 % of conversion). The main products observed were DHMF, DMF, and AMF. The latter aforementioned product, is a mixture of ethers derived from the reaction between DHMF or methylfurfuryl alcohol (MFA) with the solvent (Scheme 3-4).

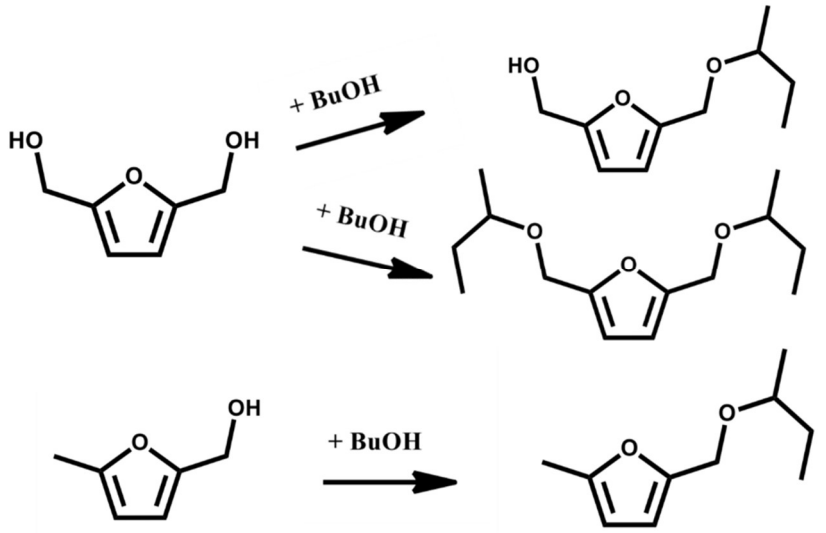

Scheme 3-4. Products of etherification of dihydroxymethylfuran (DHMF – upper part) and furfuryl alcohol (MFA – bottom part) with 2-butanol as solvent.

An interesting very high DHMF selectivity was obtained on Ru nanoparticles supported on un-functionalised CNFs (up to 95 %), with only a small amount of AMF produced. The low functionalisation of CNFs probably inhibits the etherification process that usually requires acid/basic sites to happen [15, 28]. In this case, the hydrogenation reactions prevail on the support catalysed reaction. On the other hand, when N-functionalities were introduced on the CNFs, the selectivity drastically changed towards a high production of AMF (66 %) with only a lower amount of DHMF (24 %). It is not the first time that ethers formation is reported on N-doped carbon-based catalysts. Products of etherification between furfuryl alcohol and the alcoholic solvent were also observed in the hydrogen-transfer reaction of the furfural to furfuryl alcohol [68]. It is interesting to notice that, with Ru/CNFs-N, small amounts of DMF were produced as well (ca. 10 % of selectivity). Comparing the reaction profile of the reactions catalysed by Ru/CNFs and Ru/CNFs-N (Figure 3-5), it is possible to observe that DMF is only produced at a later stage when bare CNFs are used as a support. In particular, once all the substrate is consumed, the DHMF produced starts to convert into AMF and DMF (35 % and 14 % of selectivity after 3 h of a reaction). The DHMF concentration over time, represents the typical consecutive curve trend of an intermediate product, in this case between the substrate and the esterification products (AMF). On the contrary, when N-functionalised fibers were used, both AMF and DMF were produced since the early stage of the reaction (70 % and 11 % of selectivity after 1 h of reaction).

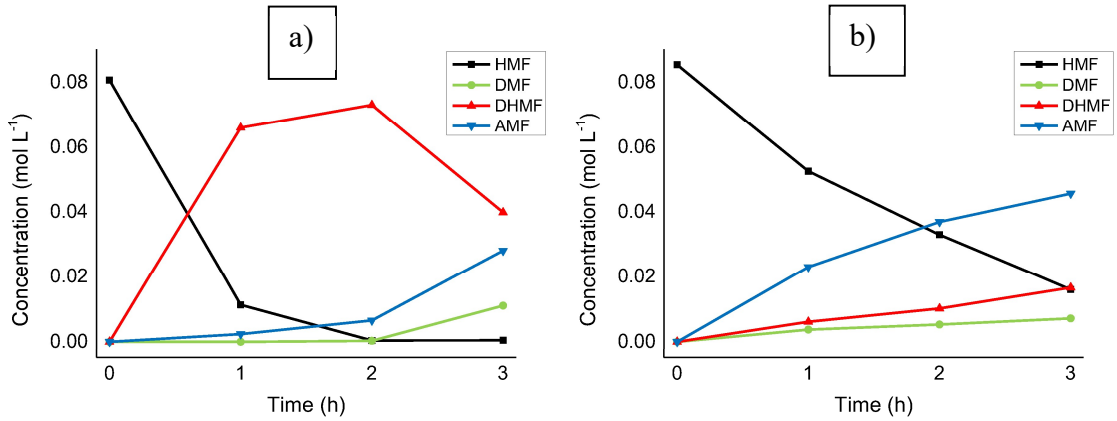

*Figure 3-5. Representation of HMF hydrogenation reaction profile on (**a**) Ru/CNFs and on (**b**) Ru/CNFs-N. Reaction conditions: HMF, 0.08 M, substrate/metal = 100 mol/mol, solvent, 15 mL 2-butanol, 150 °C, 20 bar H_2.*

Similarly to Ru/CNFs, Ru nanoparticles supported on O-functionalised fibers displayed high selectivity towards the production of DHMF (79 % of selectivity after 1 h of reaction). In this case, however, the DHMF produced did not show a tendency to further convert into AMF and DMF even once all the initial HMF was fully converted (Figure 3-5). In fact, the selectivity towards DHMF, did not vary significantly at extended reaction times (from 73 % to 75 % at 2 and 3 h of reaction, respectively); this suggests that DHMF is a stable product in the presence of the Ru/CNFs-O catalyst.

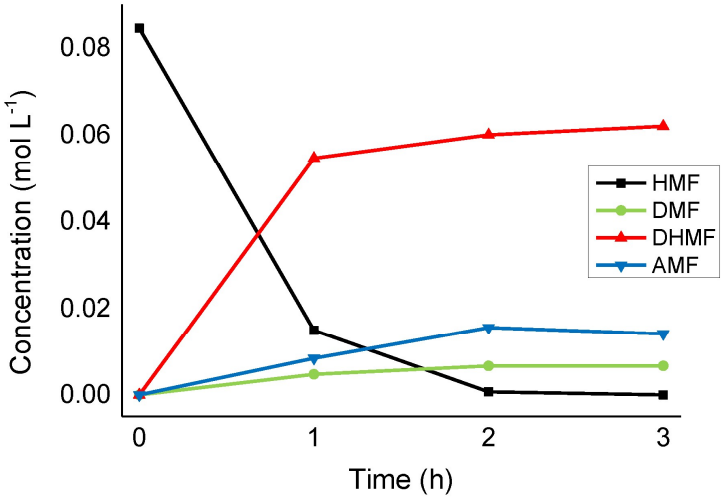

Figure 3-6. HMF hydrogenation reaction profile on Ru/CNFs-O. Reaction conditions: HMF, 0.08 M, substrate/metal = 100 mol/mol, solvent, 15 mL 2-butanol, 150 °C, 20 bar H_2.

Lastly, the Ru/CNFs-P catalyst showed not only the lowest catalytic activity (Figure 3-7) but also poor product selectivity (Figure 3-4), with both DHMF and AMF being produced in a similar amount (47 % and 44 % of selectivity after 3 h of the reaction with ca. 30 % conversion). The products distribution trend is reported in Figure 3-7.

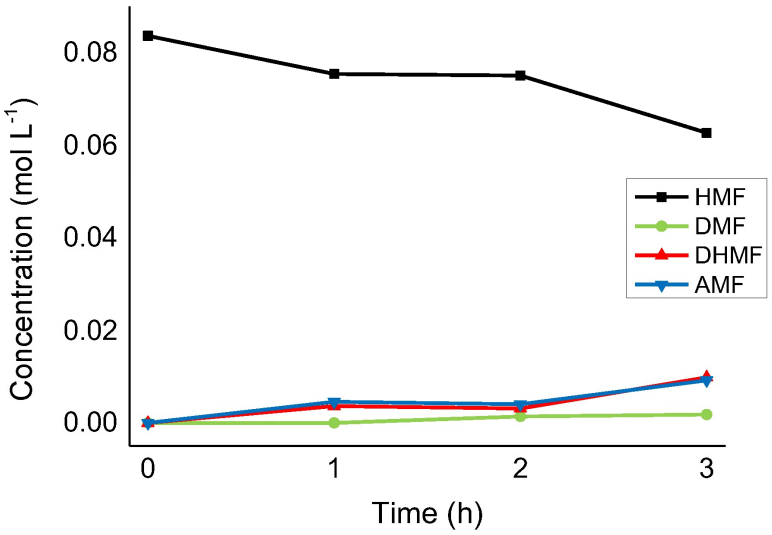

Figure 3-7. HMF hydrogenation reaction profile for Ru/CNFs-P. Reaction conditions: HMF, 0.08 M, substrate/metal = 100 mol/mol, solvent, 15 mL 2-butanol, 150 °C, 20 bar H_2.

3.2.6. *Conclusions*

Carbon nanofibers were functionalised introducing oxygen, nitrogen, and phosphorous-containing groups. These materials were employed as supports for Ru nanoparticles and used in the hydrogenation of HMF and LA. Similar metal dispersion and mean nanoparticles dimension were obtained in all the cases, but the activity of the catalysts differed greatly. This condition allowed us to attribute the differences in catalysis at the different functionalisation. CNFs-N appeared to be the best support for the Ru-catalysed LA hydrogenation in water, with activity even superior to pristine CNFs and CNFs-O. The higher hydrophilicity of the supports (CNFs-N and CNFs-O) did not appear as the only reason for the high activity. We correlated the highest activity also to the strong interaction of N-groups with Ru particles, that could play a crucial role by increasing the metal-support interaction [12,13]. The Ru/CNFs-P, on the contrary, showed a detrimental effect toward the reaction tested.

Regarding the HMF hydrogenation in 2-butanol, Ru on pristine CNFs presented comparable activity/selectivity as Ru on CNF-O, despite a different path showed. On the contrary, Ru/CNF-N and Ru/CNF-P showed a lower activity but also a change in selectivity. In fact, these latter two catalysts enhanced the formation of ethers due to the reaction between DHMF and the methylfurfuryl alcohol (MFA) with the solvent (2-butanol).

3.3. Hemicellulose valorisation (Furfural)

We already fully discussed how during the last decade the depletion of fossil fuel reserves, combined with the environmental crisis, has led scientists to focus their attention on the production of chemicals and fuels in a more sustainable and greener way. In particular, biomass is playing a crucial role, since it is the most attractive carbon feedstock due to its abundancy and low production cost [32, 69–71]. Lignocellulose (non-edible plant-based biomass), is composed of cellulose, hemicelluloses, and lignin. In the previous section we took in consideration the conversion of cellulose derivates, such as levulinic acid e 5-hydroxymethylfurfural. Cellulose, however, is not the only constituent of lignocellulosic biomass; hemicellulose and lignin constitute in fact roughly the 50 % of the overall mass of lignocellulose (30 % and 20 % respectively).

The hydrolysis process of hemicellulose leads to a homogeneous mixture of pentoses and hexoses, such as xylose, arabinose, glucose, mannose and galactose [72–75]. The further dehydration of pentoses generates our target molecule, furfural, a potential chemical platform for the synthesis of several chemicals and biofuels [76, 77]. Furfural can be also produced directly from cascade hydrolysis and dehydration of hemicellulose; in this respect, solid acid catalyst are typically used in biphasic solvent systems in order to promote the process [78, 79].

Depending on the reaction conditions and the catalysts used, the hydrogenation of furfural can proceed in different directions: products of carbonyl hydrogenation, ring hydrogenation, ring opening, etherification, hydrodeoxygenation and decarboxylation have been reported in literature (Scheme 3-5) [80]. The use of such solid acid catalysts has been recently studied in the conversion of furfural into high-added value products [81, 82]. The important presence of acid sites, in fact, can change both the activity and selectivity of the reaction. Bui et al., for example, reported a domino reaction catalysed by zeolites with acid sites for the production of γ-valerolactone, where Lewis sites catalysed the hydrogenation step, while the Brønsted sites catalysed the ring-opening hydration step [83]. Lewis acidity is responsible for acetalisation reactions as well, as reported by Taylor and co-workers which observed considerable amount of furfuraldehyde diethyl/dimethyl acetal during the hydrogenation of furfural to furfuryl alcohol over Pt nanoparticles supported on various metal oxides (γ-Al_2O_3, CeO_2, SiO_2 and ZnO) in alcoholic solvent (either ethanol or methanol) [84]. It is therefore clear that

the reaction pathway can be altered through a careful tuning of the acidic properties of the heterogeneous catalysts used as well as the solvent employed.

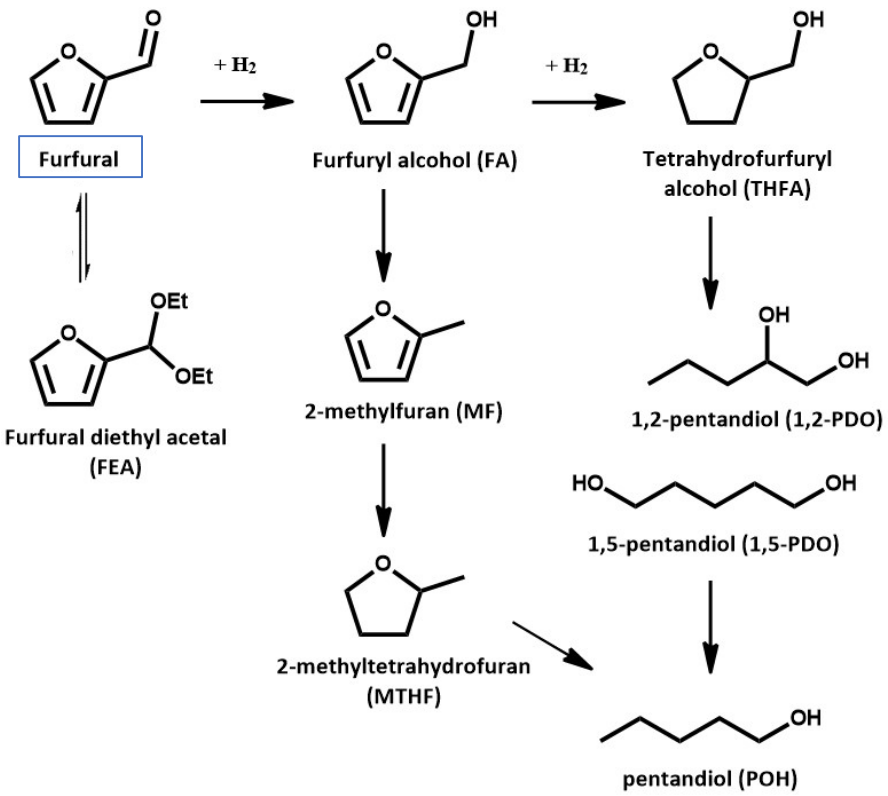

Scheme 3-5. Reaction pathway of the furfural hydrogenation reaction.

As already mentioned, one of the most important solid acid catalysts is niobia (Nb_2O_5, niobium oxide). Niobia is a metal oxide showing NbO_6 octahedra, with a great structural versatility [85, 86]. The presence of Nb=O bonds in the Nb_2O_5 structure, in fact, is associated with Lewis acid sites, while the highly polarised Nb-O bonds could generate surface OH groups in water which function as Brønsted acid sites [86–88]. This intrinsic acidity, combined with air-stability and water-insolubility, makes niobia a suitable catalyst for reactions in aqueous and polar media and therefore a very attractive material for industrial use [89, 90]. Niobia-based catalysts, for the reasons just reported, have been extensively studied for the aforementioned hydrolysis and dehydration of hemicellulose to furfural [81, 90]. However, deactivation phenomena are often reported in these reactions and it is generally attributed to the strong acid nature of the niobia active sites; acid-catalysed formation of solid products such as coke and humin, in fact, can partially cover the active sites and therefore substantially decrease the overall catalytic activity [90–92].

One of the most common method to finely tune the surface acidity of niobia is the addition of a second metal oxide, which can result in the formation of new compounds with different chemical and physical features in comparison with the starting materials. Several techniques can be employed in order to obtain the so-called niobia-based mixed oxides, such as hydrothermal synthesis, sol-gel and co-precipitation techniques [93–98]. Nb_2O_5-MeO_2 (Me = Zr, Ce and Ti) mesoporous mixed oxide were for example prepared by Auroux et al. by evaporation-induced self-assembly and applied in the dehydration of fructose [99]. The synthesised catalysts showed acid properties dependent on the nature of the oxide that was mixed with niobia; moreover, both activity and selectivity showed dependence on the amount of surface strong acid sites.

Another interesting way to finely modulate the surface acidity of niobia is by introducing a second metal into the Nb_2O_5 structure. This procedure is called ion doping and it has been successfully applied in the production of several metal-doped Nb_2O_5. Marzo et al., for example, prepared K, Ba and Nd-doped niobia and tested in the fructose dehydration reaction [91]. The authors showed decreased deactivation phenomena due to the doping of niobia with basic species; these basic species affected only the strong acid sites where humin is formed, while fructose dehydration proceeded with good stability on the lower acidic sites.

The activity and selectivity of niobia-based catalysts can further be improved by deposition of active metal nanoparticles on its surface. These bifunctional catalysts are especially employed in specific reactions, where acid sites provide the active centre for dehydration reactions and the metal nanoparticles provide the catalytic centre for other reactions to occur, such as oxidations or hydrogenations [100]. Moreover, the interaction between the adsorbed metal nanoparticles and the niobia surface can significantly alter the electronic density on the surface of the nanoparticles, leading to a different interaction between the active metal site and the substrates/products [101].

3.3.1. *Catalysts characterisation*

The catalysts synthesised (Nb_2O_5, W-Nb_2O_5 and Ti-Nb_2O_5) were fully characterised in order to understand their physical-chemical properties and be able to correlate the catalysts' features with the catalytic results obtained.

Electronic microscopy (SEM and TEM)

Scanning Electron Microscopy (SEM) coupled with Energy Dispersive X-ray analysis (EDX) was performed on the metal-doped niobia supports (Figure 3-8) in order to calculate the effective loading of the second metal into the niobia structure. The two supports show similar dopant loading very close to the nominal value of 10 atomic % (Table 3-3).

Table 3-3. Dopant loading on the niobia based supports by EDX.

Support	Dopant [at%]
Ti-Nb_2O_5	9.68
W-Nb_2O_5	9.35

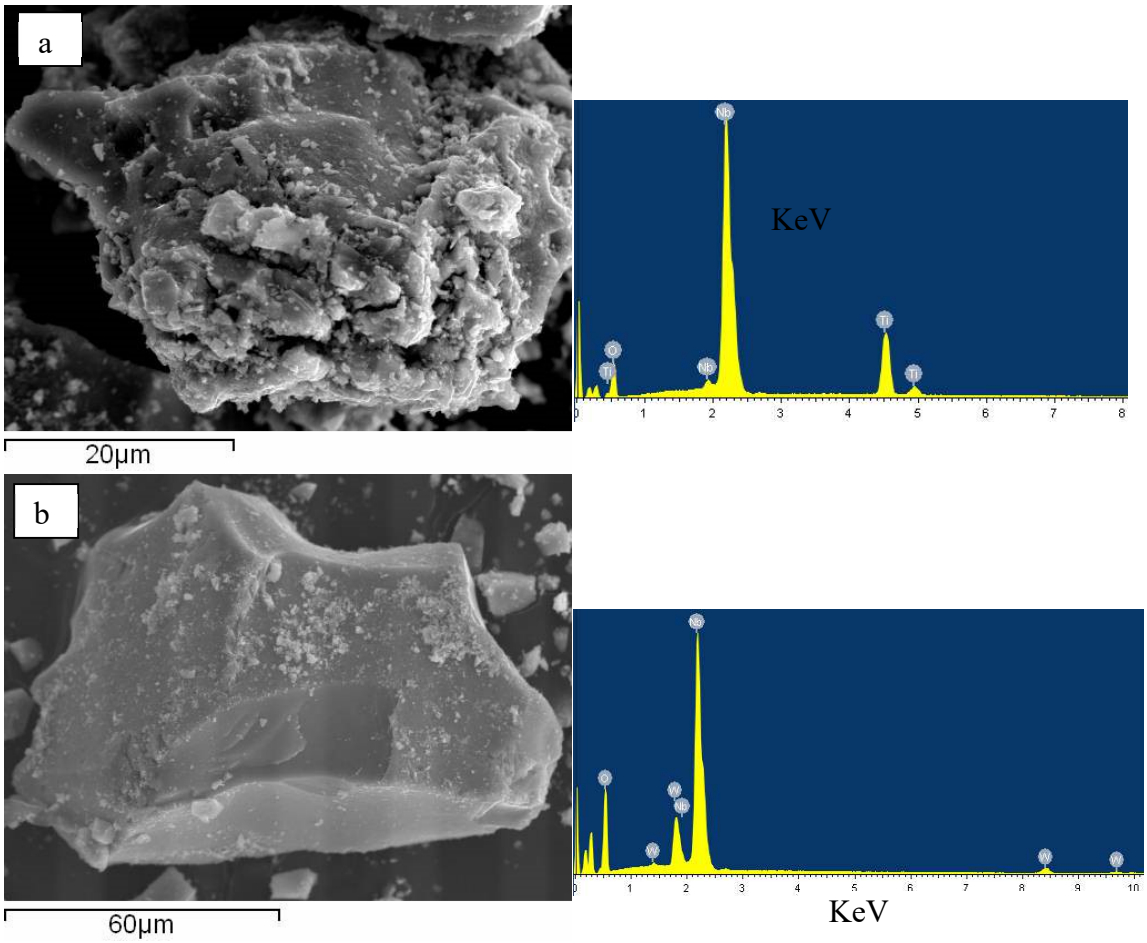

Figure 3-8. Representative SEM images of a) Ti-Nb_2O_5 and b) W-Nb_2O_3 with their corresponding EDX elemental maps (right sides).

Pt was then deposited onto the niobium oxide-based supports by SMA (solvated metal atom) deposition technique following the procedure previously exploited for the catalyst used in the glycerol oxidation (Chapter 2). TEM micrographs collected on the three samples (Figure 3-9) revealed the niobium oxide-based supports densely populated by Pt nanoparticles characterised by a very small particle sizes (S_d=1.1–1.2 nm), regardless of the support used. All the samples prepared showed homogeneous distribution of the nanoparticles on the supports' surface. Once again, the similar particles size allows us to exclude any effect caused by particle size differences.

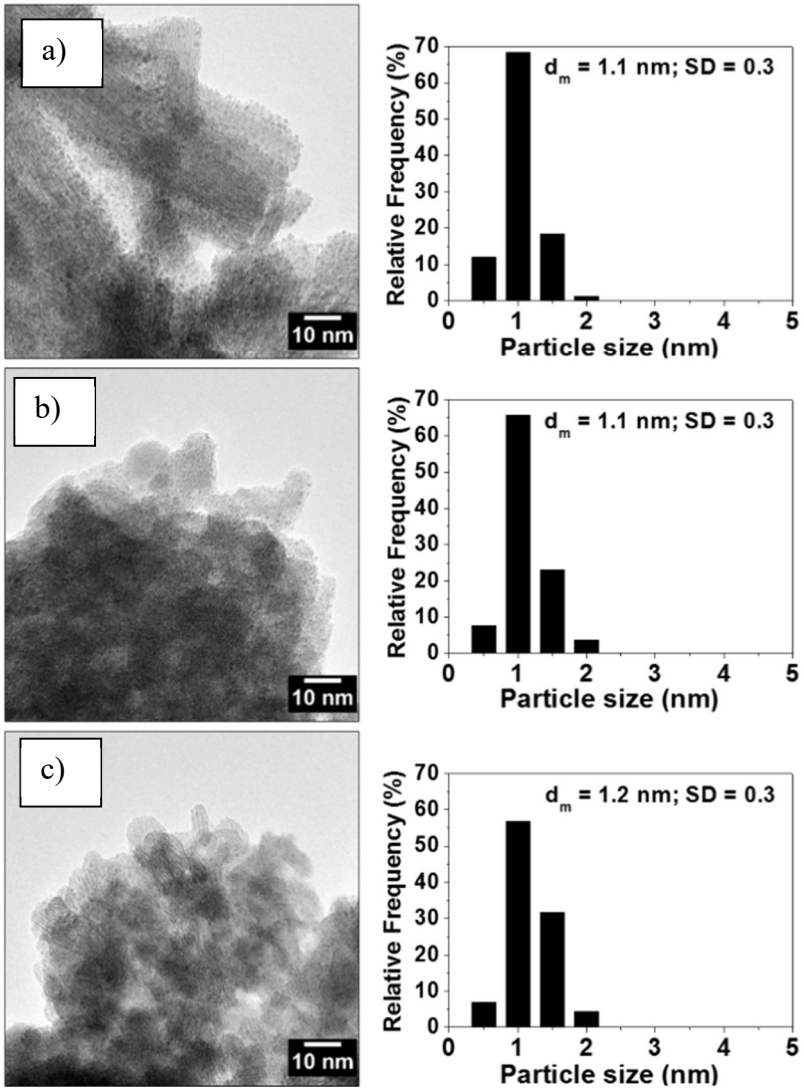

Figure 3-9. Representative TEM micrograph (315000 X) and histogram (right side) of Pt particle size distribution of the Pt/Nb_2O_5 (a), Pt/Ti-Nb_2O_5 (b) and Pt/W-Nb_2O_5 (c) samples.

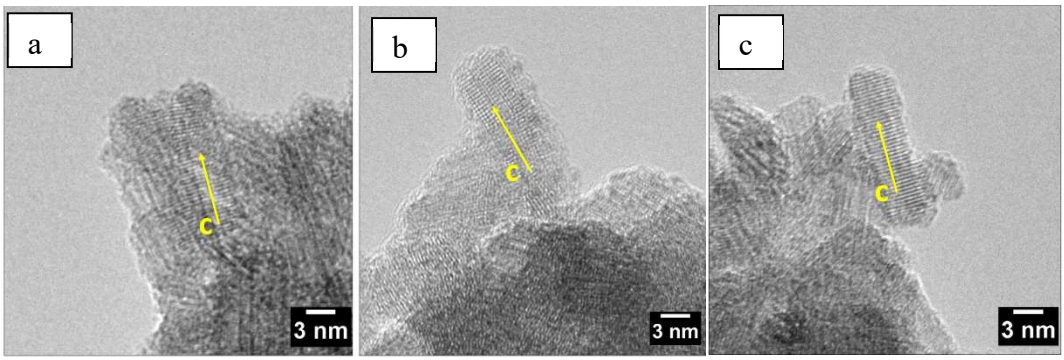

Figure 3-10. Representative TEM micrograph of the (a) Pt/Nb_2O_5, (b) $Pt/Ti\text{-}Nb_2O_5$ and (c) $Pt/W\text{-}Nb_2O_5$. The yellow arrows indicate nano-domains.

High resolution TEM analysis on Pt nanoparticles dispersed on the niobia-based oxides (Figure 3-10) showed the presence of a pseudocrystalline phase of the supports. All of them appeared to be constituted by primary nano-domains, 7 - 20 nm long and 4 - 10 nm in width stacked on each other, mainly along their length, to form agglomerates.

XRD

In order to further investigate the structure of the supports, XRD characterisation was performed. Figure 3-11 depicts XRD patterns of the niobia-based supports. All the materials showed only two well-defined diffraction maxima at 2θ values of ca. 23 and 46 º.

These two signals can be ascribed to 001 and 002 planes in any ReO_3-type related structures, similar to that of perovskite (ABO_3), without the large A cation at the centre of the unit cell: Each rhenium centre is surrounded by an octahedron defined by six oxygen centres [102]. These octahedra share corners to form the 3-dimensional structure., and are assigned to a well-ordered vertex-sharing octahedra along one direction, showing an opposite vertex distance of ca. 3.8 Å. This latter result confirmed what observed by TEM images: the presence of crystalline domains. The rest of the observed signals show a broad profile, indicating the amorphous nature of the *ab*-plane of the structure in all cases.

Accordingly, it becomes difficult to ascribe the distribution of the atoms along *a* and *b* directions to a specific polymorph. Nevertheless, we can estimate the partial substitution of Nb by the dopants by analysing the shifts in 2θ of the abovementioned 001 signal. The *c*-parameter values, calculated from 2θ values of 001 signal by means of Bragg equation, are summarised in Table 3-4. The incorporation of Ti^{4+} into Nb_2O_5 framework led to a decrease in the *c*-parameter, from 3.89 Å to 3.80 Å, which is in line with ionic radius of

Nb^{5+} and Ti^{4+} (0.64 and 0.60 Å, respectively) [103]. On the other hand, when $W^{6+/5+}$ was used as promoter, the *c*-parameter slightly increased up to 3.90 Å (Table 3-4).

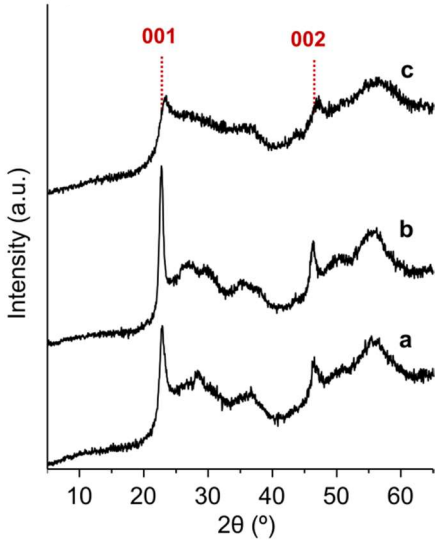

Figure 3-11. XRD patterns of Nb_2O_5-based supports: a) Nb_2O_5; b) W-Nb_2O_5; c) Ti-Nb_2O_5.

When dealing with these pseudocrystalline materials (i.e. with a well-ordered structure just along one crystallographic direction), the demonstration of the partial substitution of Nb by XRD is not so direct. In this sense, the variation of cell parameters can present opposite trends, i.e. the isomorphic substitution in the crystal framework can derive in an increase of the dimensions of the unit cell in some specific directions, while showing decreasing trends in others. This has been observed in the partial substitution of W for Mo in tetragonal tungsten bronze-based materials [104]. According to the XRD results, the direction of elongation of the domains was found to be coincident with the [001] direction, coincident with the *c*-axis of the lattice.

Raman

In order to shed some light on this issue (axis of the elongation of the domains), we analysed the Nb_2O_5-based supports by Raman spectroscopy (Figure 3-12). In this case, the incorporation of $W^{6+/5+}$ or Ti^{4+} within Nb_2O_5 framework should promote variations of the nature of metal-oxygen bonds with respect to the undoped material.

Undoped Nb_2O_5 displayed a broad Raman feature centred at 706 cm^{-1}, that can be assigned to symmetric stretching modes of Nb-O in distorted octahedra (Figure 3-12, spectrum a) [105]. Interestingly, the incorporation of a second element gave rise to frequency shifts to: i) higher frequencies, like in the case of W-containing Nb_2O_5 (719 cm^{-1}) (Figure 3-12, spectra b); ii) lower frequencies, for Ti-containing catalyst

(694 cm^{-1}) (Figure 3-12, spectrum c). The shift can be explained in terms of the specific weight of the dopant elements, i.e. heavier species (like W^{6+}) will shift the band to higher frequencies, while lighter dopants (like Ti^{4+}) would shift the band to lower frequencies. In addition, the doped supports showed broader Raman signals due to a higher disordered degree (as observed in XRD patterns) [106]. In turn, signals corresponding to TiO_2 and WO_3 oxides were always absent in the supports. All these observations suggested either an effective interaction of the dopant species with Nb_2O_5, or the incorporation of the dopants in framework positions.

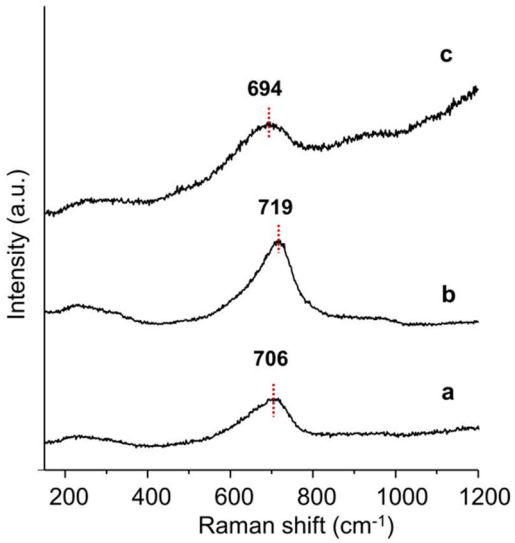

Figure 3-12. Raman Spectra of Nb_2O_5-based supports: a) Nb_2O_5; b) W-Nb_2O_5; c) Ti-Nb_2O_5.

BET

BET analyses were carried out on the pure supports in order to evaluate differences in surface area (Table 3-4). Upon inclusion of W to the niobia lattice, the surface area increased from 95 to 130 m^2 g^{-1} (Nb_2O_5 and W-Nb_2O_5 respectively). On the other hand, the addition of Ti had the opposite effect and the surface area decreased to 35 m^2 g^{-1}.

Table 3-4. Surface area and c-parameter of the different supports used.

Support	Surface Area (m^2 g^{-1})	c-parameter (Å) [a]
Nb_2O_5	95	3.89
W-Nb_2O_5	130	3.90
Ti-Nb_2O_5	35	3.80

[a] *Determined by Bragg equation from XRD patterns, using 2θ values of 001 peak.*

Pyridine FT-IR

In order to better investigate the features of the catalyst's surface, and specifically to evaluate its acidity, adsorption of a basic probe molecules (pyridine, Py) followed by IR analysis was performed. As already reported in literature, the adsorption of the amine gives rise to several bands in the range of 1400-1700 cm^{-1} depending on the type of the interaction between pyridine and catalyst surface. The technique allows distinguishing physisorbed pyridine, Lewis and Brønsted acid sites. Generally, a weak interaction between the catalyst and the probe molecule, resulting from very weak or no acidity (physisorption or hydrogen bonding), gives rise to an adsorption band in the range of 1440–1450 cm^{-1} and at 1580–1600 cm^{-1}. These bands easily decrease with the temperature and over 100 °C physisorbed pyridine can be considered fully desorbed. When pyridine interacts with Lewis acid sites, two main absorption peaks are detected: one centred at ca. 1450 cm^{-1} (ν_{19b} mode) and a second centred at ca. 1610 cm^{-1} (ν_{8a} mode). In the case of Lewis acidity also a small band at 1580 cm^{-1} could be observed. On the other hand, in presence of Brønsted acid sites, a proton transfer occurs to form the pyridinuim ion though the protonation of pyridine. This results in a band at 1550 cm^{-1} (ν_{19b} mode), followed by a band near 1640 cm^{-1} (ν_{8a} mode). Also a band at ca. 1490 cm^{-1} is usually detected, but it was not unambiguously assigned to a specific acid site, being identified as the result of either kind of interactions. Importantly, pyridine on both Lewis and Brønsted sites is resistant to outgassing with bands that could be detected also at high temperature [107–109].

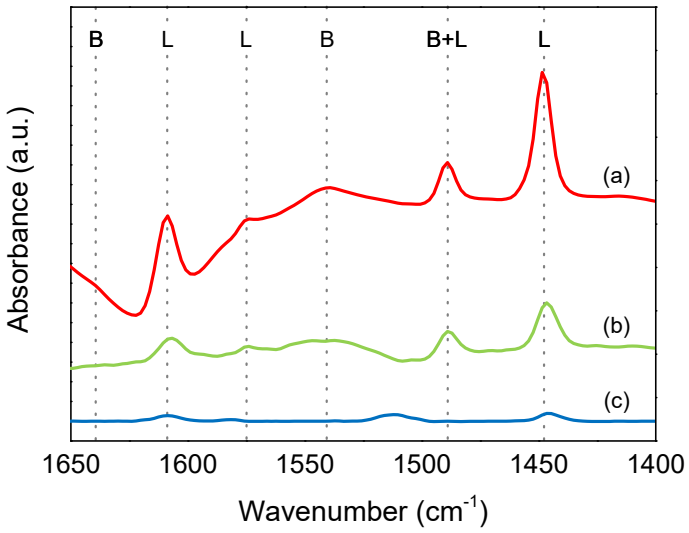

Figure 3-13. FT-IR spectra of pyridine recorded after evacuation at 150 °C (L = Lewis acid site band; B = Brønsted acid sites band) and normalised by the disk weight. (a) Pt/W-Nb_2O_5, (b) Pt/Nb_2O_5 and (c) Pt/Ti-Nb_2O_5.

In Figure 3-13, we reported the FT-IR spectra of pyridine recorded after degassing at 150 °C for the investigated materials. All the catalysts exhibit the bands pattern typical for Lewis acids sites, with the bands at 1448 cm^{-1} and 1609 cm^{-1} (and the small one at 1576 cm^{-1}), whereas Brønsted sites are absent. Nb_2O_5 is well known to feature mainly Lewis acidity, while some structural modifications (e.g. the introduction of phosphate groups) could generate Brønsted sites, although this is not the case [110, 111]. It has to be reported that for the Nb-based materials the Lewis acidity is to be addressed to the unsaturated Nb(V) sites [110, 111]. The bands intensity, however, changes significantly from sample to sample; this indicates a strong difference in terms of concentration of acid sites. For this reason, the quantitative determination of adsorbed pyridine made on the basis of band located at 1448 cm^{-1} according to the procedure reported by Emeis et al. [112], was calculated (Table 3-5). The results show that Pt/Ti-Nb_2O_5 possesses a small acidity compared with the undoped Pt/Nb_2O_5, while the modification with W drastically increases the acid site concentration of the final catalyst. Thus, the introduction of W in the Nb_2O_5 structure enhances the Lewis character of the solid, whereas Ti drastically decreases this feature; Brønsted sites were not detected.

Table 3-5. Concentration of adsorbed pyridine on Lewis site.

Catalyst	$mmol_{Py}/gCAT$
Pt/Nb_2O_5	0.078
Pt/W-Nb_2O_5	0.191
Pt/Ti-Nb_2O_5	0.014

3.3.2. *Catalytic results*

Furfural hydrogenation reactions were carried out in this study at 50 °C and 5 bar of H_2, using ethanol as solvent. Typically, under these mild reaction conditions, furfuryl alcohol (FA) and tetrahydrofurfuryl alcohol (THFA) are reported to be the main products, as a result of the hydrogenation of the carbonyl group and the furan ring (Scheme 3-5).

Figure 3-14 shows the reaction profile of the furfural hydrogenation reaction carried out using Pt/Nb_2O_5 as catalyst. After 15 minutes, almost half of the starting substrate was converted (42 %) and the main products were furfural diethyl acetal (FEA - equilibrium product) and FA (44 and 43 % of selectivity respectively), with low amount of THFA being produced as well (7 %). The presence of the acetal is not surprising, since it is often reported when the reaction is carried out with solid acid catalysts in low-chain alcoholic

solvents (i.e. ethanol). The equilibrium of acetalisation is solely acid catalysed. However, furfural was fully converted after 1 h and both FA and FEA were transformed. The FA reached a maximum after 30 minutes of reaction (52 %) and then decreased, with a consequent increase of THFA (31 % of selectivity after 2 h) whereas FEA decreased over time, with no trace of acetal remained after 2 h. The FEA concentration trend is dictated from the nature of the equilibrium product: as the furfural is consumed the equilibrium moves towards the latter, regenerating the substrate for successive conversions.

Interestingly, products of hydrogenolysis (ring-opening and hydrodeoxygenation) such as 1,2-pentanediol (1,2-PDO), 1,5-pentanediol (1,5-PDO) and 1-pentanol (POH) were present in significant amount in the final reaction mixture. In particular, 1,2-PDO and 1,5-PDO (9 and 13 % of selectivity respectively after 2 h) are generated from the hydrogenolysis of the C-O bond in the THFA ring, while POH (11 % of selectivity after 2 h) can either derive from the hydrodeoxygenation of 1,2-PDO and 1,5-PDO or from the hydrodeoxygenation of THFA and successive hydrogenolysis of the C-O bond. Only small amount of 2-methylfuran (MF) and 2-methyltetrahydrofuran (MTHF) were detected at any point of the reaction (less than 5 % in total) along with other acetalisation products (such as tetrahydrofurfural dietyl acetal and 5-hydroxypentanal diethyl acetal, hereafter identified as “others”).

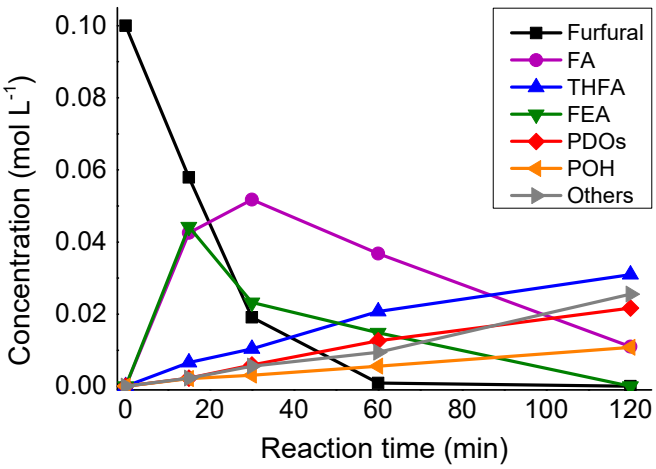

Figure 3-14. Furfural hydrogenation with Pt/Nb_2O_5. Reaction conditions: 10 mL, Furfural 0.1 M, solvent ethanol, substrate/metal = 500 mol/mol, 50 °C, 5 bar H_2.

The influence of the insertion of a second metal into the Nb_2O_5 structure on the catalytic performance was then investigated. $Pt/W\text{-}Nb_2O_5$ and $Pt/Ti\text{-}Nb_2O_5$ were tested in the same reaction conditions as Pt/Nb_2O_5 (50 °C and 5 bar of H_2) and the results are reported in

Figure 3-15. Considering that Pt nanoparticles showed a similar average size (1.0 - 1.5 nm), any difference in catalytic activity and selectivity among the niobia-based materials can be attributed to chemical-physical properties of the various supports. The catalyst that showed the highest activity towards the hydrogenation of furfural was Pt/W-Nb_2O_5, with 88 % of substrate being converted after only 15 minutes. Interestingly, this catalyst was also the one that showed the highest acidity among the series tested, with an acidity value 0.191 $mmol_{py}\ g_{CAT}^{-1}$ compared to 0.078 $mmol_{py}\ g_{CAT}^{-1}$ of Pt/Nb_2O_5 (Table 3-5). BET analysis revealed comparable surface areas, 95 $m^2\ g^{-1}$ and 130 $m^2\ g^{-1}$ respectively for Nb_2O_5 and W-Nb_2O_5 thus excluding any possible effect deriving from different surface areas. At the same time, the catalyst that showed the lowest value of acidity (Pt/Ti-Nb_2O_5, 0.014 $mmol_{py}\ g_{CAT}^{-1}$) resulted the least active of the series, with a conversion of only 23 % reached after 15 min. The difference in terms of initial reaction rate is almost 4 time higher for Pt/W-Nb_2O_5 compared to Pt/Ti-Nb_2O_5 (1,770 h^{-1} versus 470 h^{-1} respectively). It is clear from these results that the acidity has a dramatic effect on the catalytic activity. We cannot exclude the presence of Meerwein-Ponndorf-Verley (MPV) reduction but in this case FA would be present in higher amount using catalyst showing higher Lewis acidity i.e. Pt/W-Nb_2O_5.

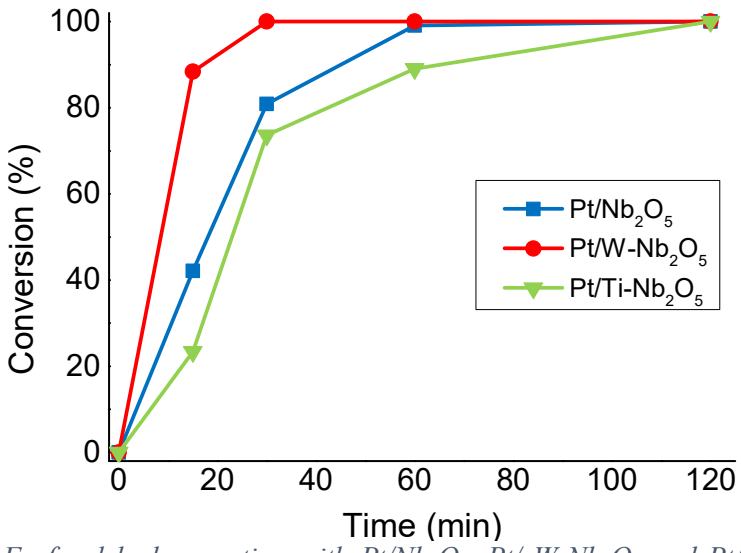

Figure 3-15. Furfural hydrogenation with Pt/Nb_2O_5, Pt/ W-Nb_2O_5 and Pt/Ti-Nb_2O_5. Reaction conditions: 10 mL, Furfural 0.1 M, solvent ethanol, substrate/metal = 500 mol/mol, 50 °C, 5 bar H_2.

Surface acidity affected not only the activity of the catalysts, but also their selectivity although with a lower extent. Comparing the selectivity at iso-conversion (Figure 3-16), in fact, it is possible to notice that the selectivity to FA increased as the acidity decreased

(from 50 % to 61 %, with Pt/W-Nb_2O_5 and Pt/Ti-Nb_2O_5 respectively). At the same time, the selectivity to FEA decreased with low acidity supports from 26 % with Pt/W-Nb_2O_5 to 10 % with Pt/Ti-Nb_2O_5, while the remaining reaction products did not vary significantly.

On the other hand, similar selectivities between Pt/W-Nb_2O_5 and Pt/Nb_2O_5 was observed in respect to the Pt/Ti-Nb_2O_5 one. We can ascribe this behaviour to the different value of acidity: 0.078 and 0.191 for the Pt/W-Nb_2O_5 and Pt/Nb_2O_5 respectively and 0.014 for Pt/Ti-Nb_2O_5.

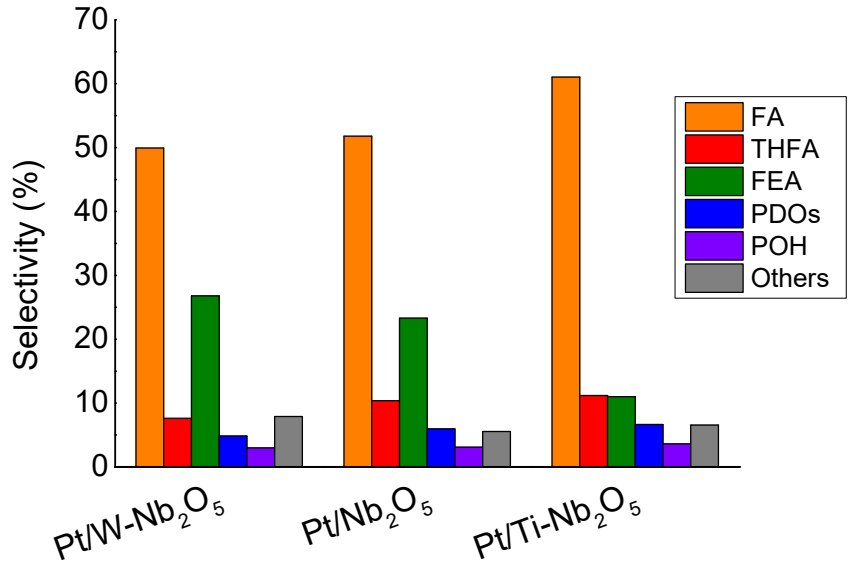

Figure 3-16. Product distribution of furfural hydrogenation calculated at iso-conversion (90 %).

3.3.3. *Conclusions*

Niobia represents an acidic support which can be fruitfully used as supporting material for Pt nanoparticles in furfural hydrogenation, thus creating bifunctional catalyst. We found that acidity is one of the main ruling factors determining the activity in the hydrogenation of furfural, being the Pt on W-modified Nb_2O_5 the most acidic and the most active catalyst. However, the selectivity can also be strongly affected, although to a lesser extent than activity. Indeed, the W-modified niobia which showed the highest Lewis acidity produced the highest selectivity to furan-ethers. Conversely, the Pt on Ti-modified Nb_2O_5, which presents the lowest surface acidity, produces the highest selectivity to furfuryl alcohol derived most probably from Pt catalysed hydrogenation.

3.4. On the Lignin transformations (Benzyl alcohol oxidation)

As already reported and discussed in this section, lignocellulosic biomass is one of the most attractive renewable feedstocks for producing chemicals and fuels. Lignin is a biopolymer that represents roughly 20 % of the lignocellulosic biomass, and it is composed of a series of oxygenated aromatic compounds linked together in long ramified chains [113]. Rational utilization of this resource requires simple, highly efficient and selective catalytic chemical transformations.

We already presented in the previous sections the valorisation of the molecules derived from carbohydrate polymers (cellulose, hemicellulose), the remaining fraction of lignocellulosic biomass. In the current work, we treated a model molecule of lignin: the benzyl alcohol. The main purpose of studying lignin model compounds is to investigate indirectly the reactivity and transformation strategies of molecules derived from the depolymerisation of lignin [113]. Another advantage relates to the simplicity of benzyl alcohol as aromatic substrate and consequently it presents easier analytical challenges relative to the complex lignin models [114]. Moreover, selective oxidation of alcohols to their corresponding carbonyl compounds (especially aldehydes) is one of the important organic transformations as carbonyl compounds are widely used in food, beverages, and pharmaceutical industries, and as precursors in chemical industries [115, 116].

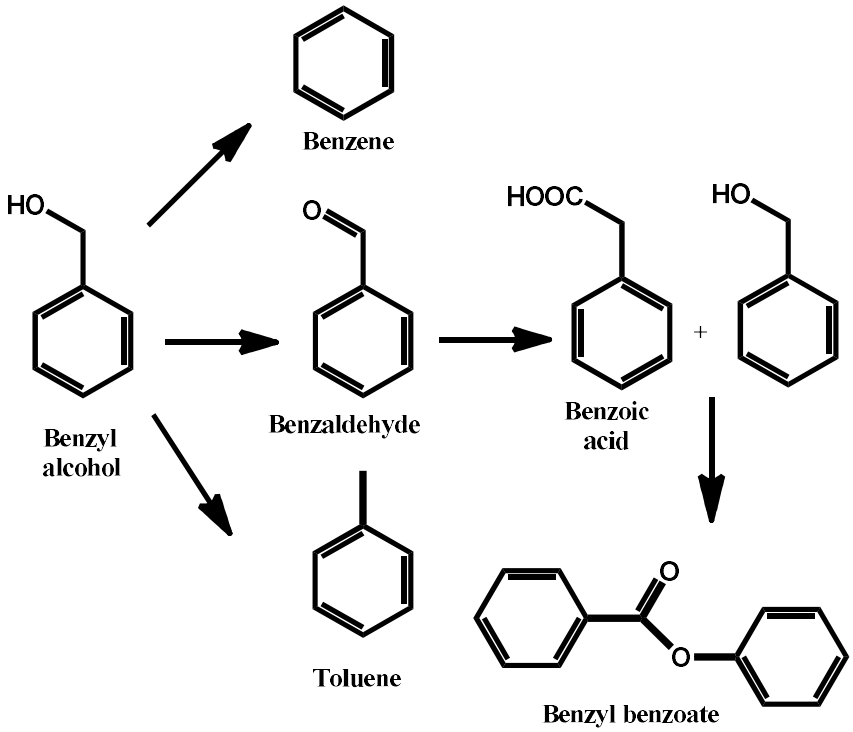

Scheme 3-6.. Pathway of the benzyl alcohol oxidation.

In fact, among the products that the reaction in question could lead (Scheme 3-6), benzaldehyde, the simplest aromatic aldehyde with an active carbonyl group, is widely used in dyestuff, perfumery, and pharmaceutical industries and is also an important organic reaction intermediate [117]. For these reason, the selective oxidation of benzyl alcohol has attracted both academic and industrial interest because of the application of benzaldehyde in perfumery, dyestuff and agro-chemical industries [118–120].

3.4.1. *Gold based systems*

Au based catalysts started to play an important role in the catalysed oxidations since 1980s with the conversion of CO to CO_2 [121–123]. Au use was then extended to other important reactions such as the oxidation of alcohols and aldehydes beside many others (i.e. hydrogenation of aldehydes, epoxidation of propylene and carbon–carbon bond formation) [124, 125, 134, 135, 126–133]. Au catalysts showed peculiar characteristics with respect to other precious metals like Pt or Pd especially in its resistance to O_2-poisoning when molecular oxygen is used as the oxidant and its peculiar selectivity [136–141]. Despite these highly desirable properties, Au catalysts often showed lower activity compared to other catalytic systems that limited their use i.e. the use of basic conditions in alcohol oxidations [142, 143]. Therefore, in the last few years, Au was seen as an ideal modifiers of more active catalysts to promote selectivity and especially durability of the catalytic systems [118]. Bimetallic systems, in fact, often show properties that are the combination of the features of the two constituent metals [118]. It was shown, in fact, that in most cases there is a great enhancement in catalytic properties owing to synergistic effect between the two metals. The kinetics of the reaction, the selectivity toward the desired product and the durability of the catalyst have been shown to be improved upon the use of bimetallic species, where Au is associated to other metals such as Pd, Pt, Ru or Cu [144–146]. The superior performance of bimetallic systems compared to monometallic counterparts has been reported for different chemical reactions, including CO oxidation[13, 144, 145], the selective oxidation of alcohols to aldehydes [144, 145, 147, 148], the direct synthesis of hydrogen peroxide [149], the oxidation of primary C–H bonds [149] and the transformation of biomass to fuel and chemicals [150, 151]. Furthermore, it was shown that the beneficial effect of using Au in the presence of another metal was achieved depending on structure and composition. Bimetallic nanoparticles of Au–Ag [152–157], Au-Pt [158–161], Au–Pd [162–166] and Au–Cu [167, 168] with

hetero-aggregate, core–shell or alloy structures have been studied showing also that in some cases a negative synergistic effect can be revealed [169].

Among the bimetallic systems presented here above, we decided to deeply investigate the AuCu systems. The history of Au-Cu alloy has ancient roots: the two metals, in fact, were largely used for coinage and jewellery since they easily form solid solutions in all proportions and have similar chemistry [170]. Furthermore, Cu is a low-cost transition metal [171] and one of the earth-abundant elements that can also be easily obtained [172]. For these reasons it recently attracted the attention from an industrial point of view as well [173]. Supported Au-Cu nanoparticles as alloy, core-shell or hetero-aggregate structures have also been studied in catalysis, showing in some cases a positive beneficial effect in terms of catalytic performances and stability respect to their monometallic counterparts [168]. AuCu based materials were effectively used for the aerobic oxidation of carbon monoxide [174], oxidation of alcohols to the corresponding aldehydes or ketones [146, 175–177] and propene epoxidation with nitrous oxide [178]. Recently, in order to disclose the essence of the synergistic effect between Au and Cu in oxidation reactions, the structural evolution of supported AuCu alloy nanoparticles, upon their interactions with reactants for aerobic CO oxidation, has been deeply investigated by different research groups [179–181]. X. Liu et al., for instance, have reported in situ studies on SBA-15 supported Au-Cu alloy prepared through consecutive reduction of Au and Cu precursors. They revealed that the active catalyst was composed by Au nanoparticles enriched on the surface by partially or fully oxidised CuO_x tiny patches, which boosted the CO/O_2 activation [174, 182]. Similar results were obtained by J.C. Bauer et al. with SiO_2-supported Au-Cu catalysts synthesised by adding Cu acetate precursor to support Au nanoparticles. The formation of Au-CuO_x heterostructures significantly improved the CO oxidation reaction, whereas the reduction led to a AuCu alloy formation which showed negligible catalytic activity[183]. Finally, J. Yin et al. studied the CO oxidation on carbon-supported $Au_{51}Cu_{49}$ catalysts prepared by impregnation method. The superficial oxygenated Cu species resulted able to activate oxygen affording a significantly increase of the catalytic activity. In contrast, the catalyst deactivates upon treatment under strong oxidative conditions due to the formation of an Au_{core} enclosed in a thick CuO_{shell} structure, thus totally blocking the Au active sites [173]. Despite experimental and theoretical efforts, the control of the Cu surface segregation (i.e. the thickness of CuO on surface) in AuCu alloy nanoparticles during the catalytic

oxidation and the consequent catalyst performance is still a challenge. As a matter of facts, the degree of phase segregation is strongly influenced by the catalytic conditions and oxidative/reductive pre-treatments, the substrates-metals interaction, the particles metal ratio as well as the synthetic approach.

3.4.2. *Catalysts characterisation*

To approach the oxidation of benzyl alcohol, bimetallic (with respectively monometallic samples) systems have prepared by SOL-immobilization techniques over a commercial activated carbon (Camel X40S). The SOL-immobilization synthetic technique, as already shown, is able to assure a good control over the size distribution of the metal nanoparticles. All the bimetallic samples were prepared with a nominal Au:Met ratio of 6:4, apart from Au-Cu systems (Au:Cu=8:2), where we decided to slightly enhance the Au content with the intent of compensate the non-noble metal nature of the dopant (more prone to give oxidation).

All the bimetallic systems will be compared with the corresponding monometallics (Au monometallic catalyst will be used as benchmark for all the systems).

The bimetallic catalysts synthesised were characterised by HR-TEM (high resolution transmission electron microscopy) in order to disclose the structure that can derive from the different dopant metal exploited.

Electronic microscopy (TEM)

The average particles diameter of all the catalysts is reported in Table 3-6.

Table 3-6. Statistical median and standard deviation of particle size analysis.

Catalyst	Statistical median (nm)	Standard deviation (nm)
Au/C	3.3	0.6
Pd/C	2.9	0.8
Au_6Pd_4/C	3.4	1.0
Pt/C	3.1	1.2
Au_6Pt_4/C	3.2	0.8
Ru/C	2.1	0.3
Au_6Ru_4/C	3.8	0.6
Cu/C	1.5	0.2
Au_4Cu_1/C	2.1	0.5

Au, Pd and AuPd nanoparticles showed a similar particle size and standard deviation (3.3 ± 0.6 nm, 2.9 ± 0.8 nm and 3.4 ± 1.0 nm for Au, Pd and AuPd respectively). In addition, the AuPd particle morphology was studied by High Resolution TEM analysis. The micrographs revealed that most of the particles are multiply twinned in the form of decahedra or truncated decahedra (Figure 3-17-a). The uniform lattice spacing of 2.30 Å is in between the Pd (111) plane (2.25 Å) and the Au (111) plane (2.35 Å), confirming the presence of an alloy. Energy-dispersive X-ray spectroscopy (EDX) spectra were acquired on more than 50 bimetallic particles of different sizes. Figure 3-17-b shows a representative spectrum. The Au/Pd ratio is consistent from particle to particle and with an average molar ratio of 6.3 to 3.7, similar to the nominal one (6:4), indicating that almost all of the particles were present in a bimetallic form. The strong Cu signal is caused by the Cu grid used for TEM analysis.

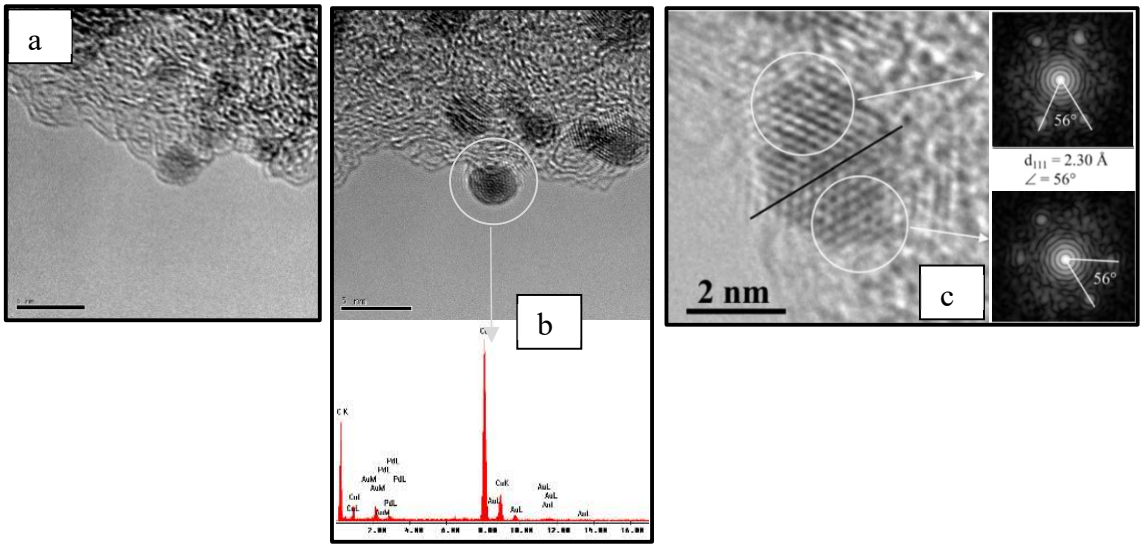

Figure 3-17. a) Representative TEM image of Pd/C. b) Representative HRTEM image (upper side) of a AuPd/C particle with a EDX representative spectrum (bottom side) taken from an individual single particle. c) HRTEM of a AuPd/C particle showing the fast Fourier transformations (right side)

For the second set of catalysts prepared, again both monometallic Au and Pt and bimetallic AuPt catalysts showed similar particle size (3.3 ± 0.6 nm, 3.1 ± 1.2 nm and 3.2 ± 0.8 nm for Au, Pt and AuPt respectively). In addition, the AuPt particle morphology was investigated also in this case. The uniform lattice spacing of 2.29 Å between the Pt (111) plane (2.26 Å) and the Au (111) plane (2.35 Å), confirmed the alloying state (Figure 3-18-b). EDX spectra were acquired from single particles on more than 50 particles of different sizes. Figure 3-18 shows a representative spectrum. The ratios of Pt to Au is similar for all the examined single particles, with an average molar ratio comparable to

the nominal one (6:4), even the measurement can be affected by some uncertainness due to the partial overlapping of Au and Pt signals. The Cu signal is again to ascribe to the use of Cu grid for TEM analysis.

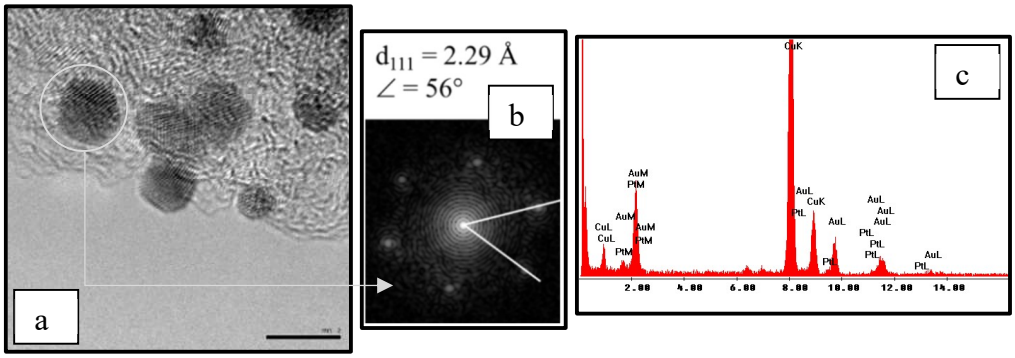

Figure 3-18. a) Representative HRTEM image of a AuPt/C particle with corresponding b) fast Fourier transformations and c) EDX representative spectrum taken from an individual single particle.

Monometallic Ru nanoparticles showed a smaller average particle size (Figure 3-19-a) compared to Au, Pd and Pt catalysts (~3 nm - Table 3-6). However, alloying Ru to Au generated larger particles (3.3 ± 0.6 nm, 2.1 ± 0.3 nm and 3.8 ± 0.6 nm for Au, Ru and AuRu respectively) (Table 3-6, Figure 3-19). STEM-EDX analysis show that Au and Ru are present as bimetallic particles; Ru clusters were also observed in the monometallic catalyst (Figure 3-19-b). Moreover, a combination of HAADF STEM equipped with EDX indicated the presence of an Au_{core}-Ru_{shell} structure with Ru cluster decorating the surface of Au particles (Figure 3-19-c).

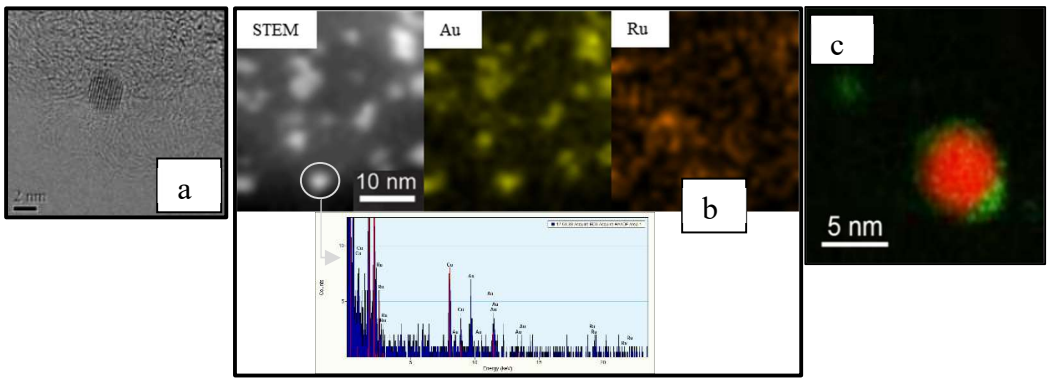

Figure 3-19. a) Representative HRTEM image of Ru/C, b) STEM-EDX representative image with respectively EDX map and c) HAADF STEM-EDX mapping of Au_6Ru_4/C.

In this particular case, given the non-noble nature of Cu (Cu can be easily oxidised even at room temperature) [184], we decide to use a slightly higher Au content with a Au/Cu molar ratio of 4/1 (in comparison with the other ratios Au/Met – 6/4), as mentioned before. The catalysts synthesised were investigated by transmission electron microscopy (TEM). Cu/C and Au_4Cu_1/C (Figure 3-20-a) showed an average particle size of 1.5 and

2.1 nm respectively (Table 3-6). STEM-EDX analysis showed that Au and Cu are present as bimetallic particles, with a calculated Au:Cu molar ratio of 2.5/1, lower than the nominal one (4:1) suggesting that part of Au is present also as segregated pure Au nanoparticles. The bimetallic nanoparticles are therefore Cu-rich with respect to the nominal value.

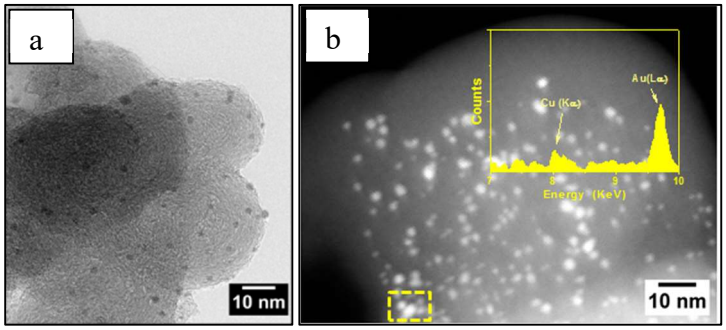

Figure 3-20. a) Representative TEM overview of Au_4Cu_1/C and correspond b) STEM images with relative EDX spectrum of the selected particle as example (yellow inset).

3.4.3. *Catalytic results*

The activity of all the sets of catalysts prepared was evaluated in the oxidation of benzyl alcohol (0.3 M, metal/substrate 1/500, 4 bar O_2, 120 °C, cyclohexane as solvent). The results are reported in Figure 3-21.

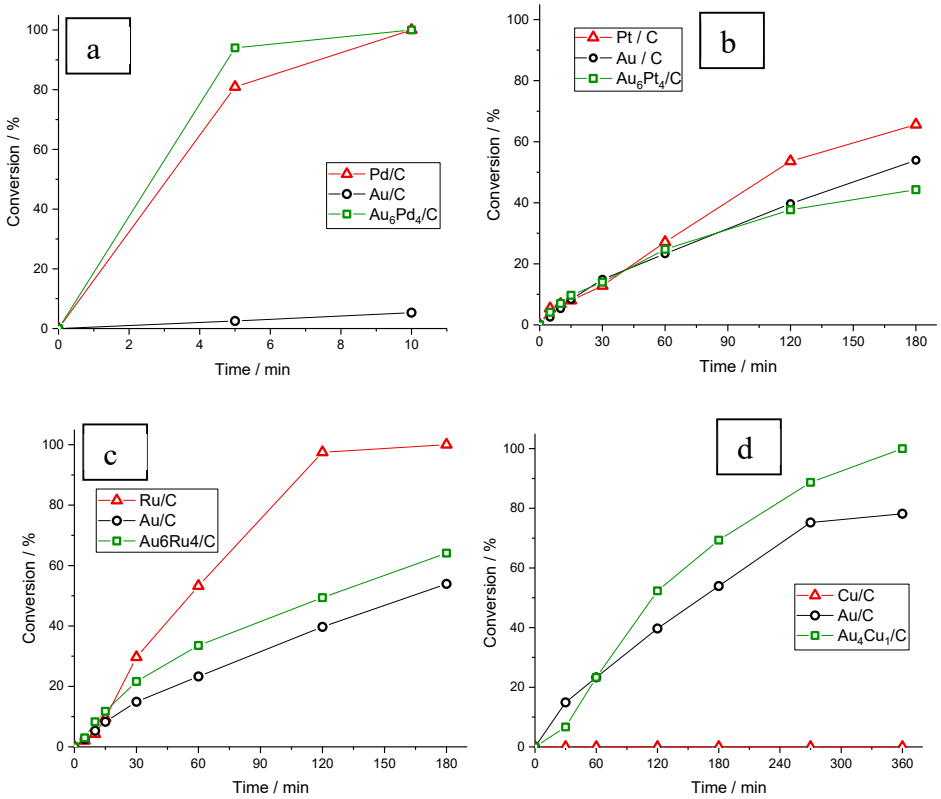

Figure 3-21. Reaction profile of a) Au/C, Pd/C and Au_6Pd_4/C, b) Au/C, Pt/C and Au_6Pt_4/C, c) Au/C, Ru/C and Au_6Ru_4/C and d) Au/C, Cu/C and Au_4Cu_1/C in the benzyl alcohol oxidation. Reaction conditions: Benzyl alcohol 0.3 M, metal/substrate 1/500, 4 bar O_2, 120 °C, cyclohexane as solvent.

Starting from an initial assessment of the reactivity, the AuPd catalysts resulted the most active catalysts (94 % conversion after 5 min), followed by its corresponding Pd monometallic counterpart (81 % conversion after 1 min). Under these reaction conditions and for the reaction time taken in consideration, Au did not show any appreciable activity in comparison with Pd and AuPd systems (Figure 3-21-a). Furthermore the synergistic effect present for this set of catalysts is evident, with a conversion value of 81 and 94 % (after 5 min) for Pd and AuPd respectively. On the other hand, the bimetallic AuPt catalyst showed an opposite trend compared to AuPd, despite the presence also in this case of an alloyed structure. After 3 h of reaction, in fact, the conversion of the bimetallic AuPt is lower than the monometallic counterparts (65 % and 54 % for Pt and Au, respectively). In addition, we can observe from the reaction profiles how the bimetallic seems to suffer from deactivation (evident after 2 h) with respect to corresponding monometallic ones. This means that there is only a slight (and negative for this reaction) interaction between Au and Pt. The best result achieved with these sets of catalysts was 66 % of conversion observed after 3 h for the monometallic Pt.

Similarly to the previous case, monometallic Ru showed the highest conversion in benzyl alcohol oxidation (53 % after 1h) compared to Au (23 % after 1h) but also to AuRu (33 % after 1h) as reported in Figure 3-21-c. In this latter case we evaluated that the expected conversion would be roughly 35 %, at 1 h of reaction, considering two separate contribution of the metals would be slightly higher as the one obtained with the bimetallic (reaction time 1 h: $\%con._{Au}/10 \cdot 6 + \%con._{Ru}/10 \cdot 4$). Therefore, we concluded that there is a slightly negative interaction between the two metals for the reaction studied.

Lastly, AuCu bimetallic system, despite the Cu-enrichment observed by means of TEM in the bimetallic nanoparticles, showed a strong positive synergistic effect (complete conversion after 6 h, Figure 3-21-d); Cu/C, in fact, showed negligible activity and Au a conversion of 78 % after 6 h. This is a unique example, among the catalysts tested, where the second metals added to Au is completely inactive when not alloyed but shows remarkable activity when combined with Au. Furthermore, what resulted more appealing, is the not-noble nature of the dopant metal.

From a selectively point of view, for all the catalysts tested, the target substrate was converted with full selectivity to benzaldehyde.

3.4.4. *On the Gold-Copper systems*

Among the bimetallic systems prepared and tested in the benzyl alcohol oxidation (previous section), we decided to deeply investigates the AuCu systems. The synergistic effect promoted by the combination of gold with a not-noble metal (copper) resulted very appealing, thus we decided to investigate the composition effect changing the AuCu ratio. The synthesis of AuCu bimetallic nanoparticles by SMAD method led to Au and Cu metals in the zero valent state (working in inert-gas environment) stabilised by a weak-coordinative solvent (acetone) without the presence of additional ligands. Indeed, the SMAD approach has been recently proposed as an effective way for the preparation of supported bimetallic nanoparticles with a high control on their size/composition, avoiding the use of any surfactant or capping agent [185, 186]. The Au_xCu_y nanoparticles deposition onto the support takes place by a simple impregnation at room temperature (25 °C). Contrary to classic colloidal impregnation, high temperature post-process calcinations (to remove the ligands) which can induce structural and morphological modifications of the nanoparticles are not required. Controlling the co-evaporation rate of Au and Cu metals, we prepared three Au_xCu_y nanoparticles supported on activated carbon with different Au/Cu molar ratios (Table 3-7). We decided to evaluate two Au-rich and one Cu-rich systems given the lack of activity previously shown by Cu samples. For comparison purpose, we also synthesised the corresponding carbon-supported Au and Cu monometallic systems. All the catalysts were prepared with 1 wt.% on carbon of total metal loading. The choice of carbonaceous support (Vulcan) was dictated by the experience acquired in the previous chapter (section 2.3), were Vulcan as carbonaceous support among others led to the smallest nanoparticles SMAD derived with the lowest standard deviation.

3.4.5. *Catalysts characterisation*

TEM

The particle size distribution and dispersion of the metallic particles of both mono and bimetallic catalysts was investigated by transmission electron microscopy (TEM). A summary of particle size and size distribution for all the catalysts synthesised is presented in Table 3-7, along with the experimental metal loading measured by inductively coupled plasma- atomic emission spectroscopy (ICP-AES).

Table 3-7. AuCu molar ratio (ICP-AES) and particle size (TEM) of the different Au_xCu_y/C samples.

Sample	**Molar ratio**		**Weight % on Carbon**		**Average Size (nm)**
	Au	Cu	Au	Cu	
Au/C	1	0	1.0	0	2.5
$Au_{13}Cu_1$/C	13	1	0.98	0.02	3.5
Au_4Cu_1/C	4	1	0.93	0.07	4.5
Au_1Cu_{17}/C	1	17	0.15	0.85	3.5
Cu/C	0	1	0	1.0	2.9

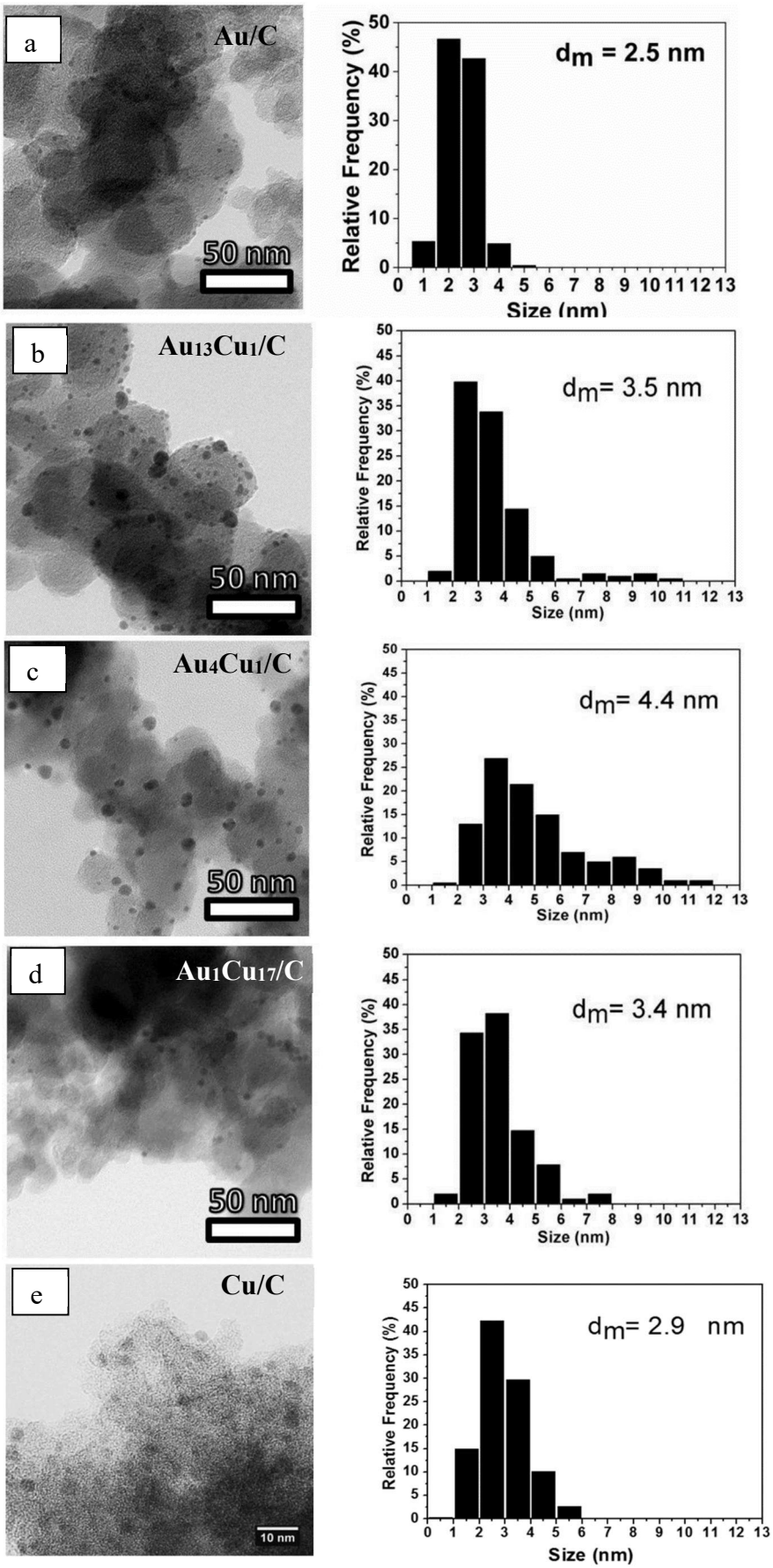

Figure 3-22. Representative TEM micrographs (left side) and related size distributions (right side) for a) Au/C, b) $Au_{13}Cu_1/C$, c) Au_4Cu_1/C, d) Au_1Cu_{17}/C and e) Cu/C.

All the samples show a homogeneous and comparable distribution on the support. For the monometallic catalysts, the analysis revealed a similar nanoparticles dimension with a mean particle size of 2.5 nm and 2.9 nm for Au/C and Cu/C, respectively (Figure 3-22-a and e). In both samples, their sizes lie in a quite narrow range (1 to 5 nm). Moving to the AuCu bimetallic catalysts (Figure 3-22-b,c,d), the mean values of the size distributions are slightly shifted to bigger values than the ones found for monometallic systems (see Table 3-7). The nanoparticles sizes appeared meanly distributed in the 1 to 6 nm range even if in all the three samples also a minor population of larger particles (ranging from 7 to 12 nm) were detected. In details, for the Au_4Cu_1/C sample we observed a higher number of larger nanoparticles (less than 15 %) than that observed for the $Au_{13}Cu_1/C$ and Au_1Cu_{17}/C samples (less than 5%). We speculated that the co-presence of the two metals influenced the metal nucleation and thus, the growth processes.

In order to have a deep insight into the nature of the nanoparticles by their structural features, high resolution transmission electronic microscope (HR-TEM), scanning TEM coupled with electron energy loss spectroscopy (STEM-EELS) and x-ray fine structure spectroscopy (XAFS) were used to deeply investigated the bimetallic samples.

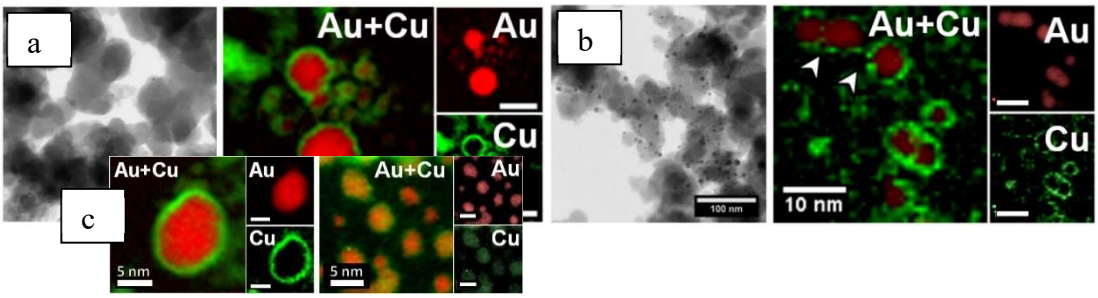

Figure 3-23. Representative TEM micrographs (left side) and STEM-EELS maps (right side) for a) Au_1Cu_{17}/C (with a mapping of nanoparticles different in dimensions -c) and b) Au_4Cu_1/C (Au@2239.0-2477.0eV – Cu@ 953.0-1202.0eV).

The Cu-rich sample (Au_1Cu_{17}/C) showed two different discrete systems: CuO_x nanoparticles and Au-CuO_x core-shell structures (Figure 3-23-a). It is worth point out that SMAD initially led to reduced metal nanoparticles; the CuO_x species were formed after the exposure at air. This result was ascribed to the tendency of small Cu nanoparticles to be oxidised even at room temperature when exposed to air [187]. As estimated by TEM analysis performed on the supported sample (Figure 3-22- d), both Au-CuO_x and CuO_x nanoparticles provided a metal size distribution centered around 3.4 nm (ranging from 2 to 6 nm). STEM-EELS maps clearly revealed that Au atoms tend to aggregate leading to Au-core nanoparticles fully surrounded by a thin Cu enriched shell ranging from less than

1 nm to 3 nm depending on the whole particle size. Indeed, the Cu shell appeared thicker for the oversize nanoparticles (Figure 3-23 – c left) although it is still clearly visible also all throughout the particle size range (Figure 3-23 – c right). Moreover, for the bigger nanoparticles the segregation of the two metals appeared more marked.

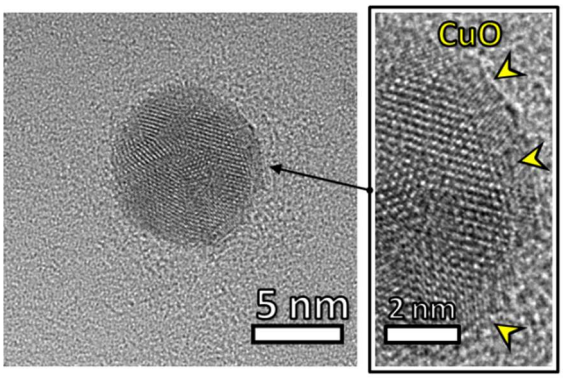

Figure 3-24. Representative HR-TEM-micrograph for Au_4Cu_1/C sample: on the right, the arrows highlighted the CuO (023) shell.

Moving to the Au_4Cu_1/C sample, TEM analysis highlighted nanoparticles characterised by a size diameter of 4.4 nm (ranging from 2 to 9 nm, Figure 3-22-c). Analogously to the previous sample, the copper is present on the nanoparticles surface leading to Au_{core}-CuO_x $_{shell}$ where CuO_x partially covered the Au enriched cores. HR-TEM analysis confirms the presence of a discontinued Cu-enriched outer shell and the crystal planes detected could be ascribed to the (023) CuO planes (Figure 3-24).

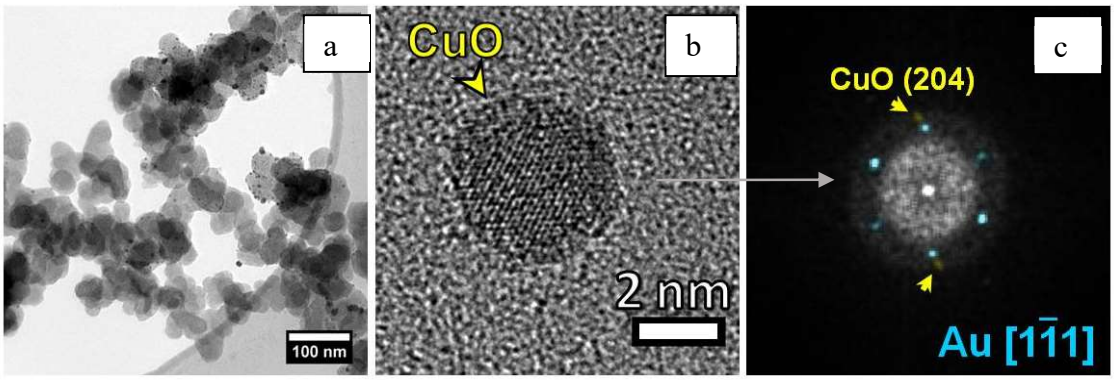

Figure 3-25. Representative TEM (a) and HR-TEM (b) micrographs for sample $Au_{13}Cu_1$/C. (c) The Fast Fourier Transform (FFT) of micrograph shows the Au NP aligned along zone axis [1-11] (brighter azure dots) and a reflex indexed as CuO (204).

Finally, STEM-EELS mapping mode performed on the $Au_{13}Cu_1$ sample (containing only the 0.02 Cu wt.%) was not able to reveal the fine structure of the nanoparticles. However, by means of HR-TEM the presence of isolated CuO crystallites onto the Au nanoparticles surface (Figure 3-25) were detected. For this sample, a mean size diameter calculated by TEM of 3.5 nm was detected (Figure 3-22 - b).

XAFS

X-ray absorption fine structure (XAFS) measurements and data analysis were performed on the Cu K edge and on the Au L_3 to define the Cu oxide phase and to confirm the presence of a Au-core and Cu(II) like shell structure.

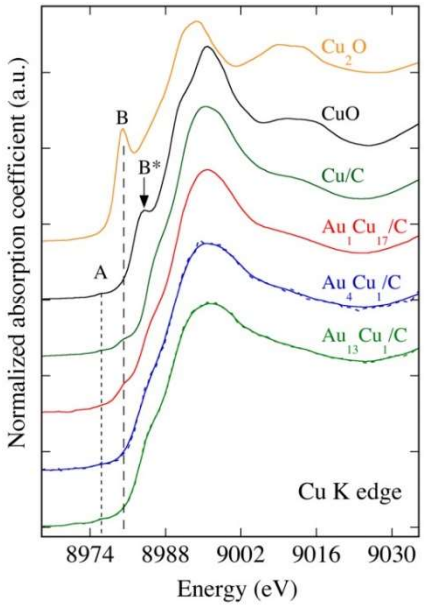

Figure 3-26. XANES spectra of the catalysts and of the Cu_2O and CuO reference samples. For the bimetallic Au_4Cu_1/C and $Au_{13}Cu_1/C$ catalysts the full lines represent the smoothed experimental data

In Figure 3-26 the XANES spectra of all the catalysts (Cu/C and Au_xCu_y/C) and of al the references (Cu_2O and CuO) was reported. The relevant similarities between the XANES spectra of the CuO reference sample and all catalysts profile show that Cu atoms in these samples are all in a Cu(II) phase confirming what found with STEM-EELS analysis.

The weak peak A, present in CuO and in the bimetallic and monometallic samples, is typical of Cu(II) compounds. While Cu(I) compounds have no holes in the 3d orbitals, Cu(II) ones, being in a d^9 configuration, have this the weak pre-edge absorption peak A, corresponding to a 1s ➔ 3d dipole forbidden but quadrupole allowed transition [187]. This weak peak can be considered as a signature of the presence of divalent copper. Another important characteristic of Cu(II) compounds is the higher energy value of the X-ray absorption edge compared to the one of Cu(I) compounds. This is clearly visible taking into account that the positions of the B* peak (Figure 3-26) of CuO reference sample (and of the corresponding shoulders present in the XANES spectra of the bimetallic and monometallic samples) that is present at a higher energy value compared to the B peak in Cu_2O. Of the three AuCu bimetallic catalysts, the one with the higher

amount of Cu (Au_1Cu_{17}/C), showed in the near edge region (Figure 3-26) the presence of a shoulder that was already observed for other bimetallic systems (AuCu and PdCu catalysts [183, 186, 188]) at comparable energy to the one of the B peak in Cu_2O. This shoulder with a lower intensity, is also visible in the pre-edge region of the Cu/C sample. The 'B' absorption peak is normally assigned to the electric dipole-allowed 1s → 4p transition, characteristic of Cu(I) ($3d^{10}$) samples like Cu_2O having no holes in the 3d orbitals. The shoulders present in these two catalysts, could indicate the presence of a small contribution coming from Cu(II) reduction. This latter supposed contribute, had not found any correspondence in the EXAFS data analysis that does not reveal the presence of O nearest neighbours at a distance comparable to the one of Cu(I) oxide compounds (R = 1.85 Å)[187].

Since the intensity of this shoulder is higher in the bimetallic sample than in the monometallic one, the increase of its intensity could be related to a small Cu-Au contribution that give a charge transfer from Au to Cu [188]. Since the crystallographic structure of Cu(II) and Cu (I) compounds is quite different [187], if we take into account the CuO and the Cu_2O reference samples we know that in Cu(II) compounds like CuO, copper is four-fold coordinated to O with a mean first shell coordination distance of about 1.95 Å while in Cu (I) compounds like Cu_2O, copper atoms have as nearest neighbors two O atoms at a distance of about 1.85 Å.

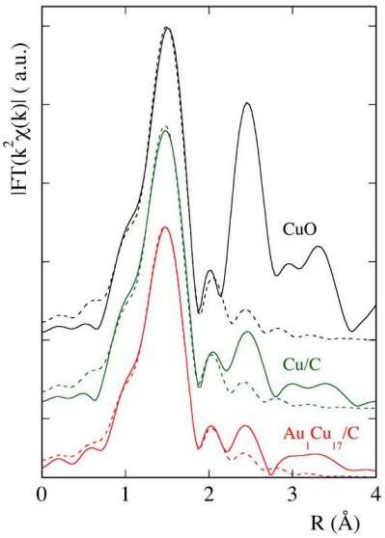

Figure 3-27. Fourier transforms of the experimental (full lines) and theoretical (dashed lines) EXAFS spectra of the Au_1Cu_{17}/C bimetallic sample compared to the one of monometallic Cu/C and of the CuO reference sample (Δk = (2.5 – 11.4) $Å^{-1}$).

As clearly visible in Figure 3-27, the Fourier Transform spectra of the EXAFS data of the monometallic Cu (N1 = 3.8, R1=1.937 Å) and of the bimetallic Au_1Cu_{17}/C (N1= 3.6, R1=

1.934 Å) samples are very similar and the position of their peaks corresponding to their first coordination shells are nearly that of the CuO reference sample (N1=4, R1=1.95 Å). The small contraction of the Cu–O distance in the Cu/C sample compared to the value of the CuO bulk distance can be ascribed to size effects given by the small dimensions of the nanoparticles [189, 190].

Due to very low amount of Cu in the other two bimetallic samples and to signal/noise ratio of the EXAFS data, the fitting procedure was limited to the first coordination shell with N and R values fixed to what found for the Au_1Cu_{17}/C sample due to the short usable k range ($\Delta k = (2.5 - 7)$ Å^{-1}).

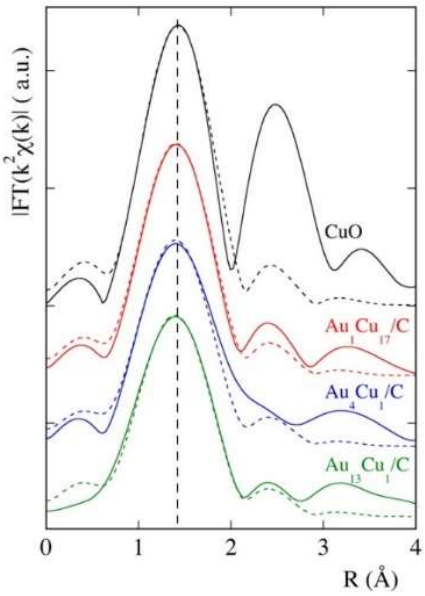

Figure 3-28. Fourier transforms of the experimental (full lines) and theoretical (dashed lines) EXAFS spectra of the AuCu bimetallic samples compared to the one of CuO reference sample ($\Delta k = (2.5 - 7)$ Å^{-1}).

As shown in Figure 3-28 the first coordination shells of the bimetallic sample are practically all at a same position that is very similar to the one of the CuO reference. Due to the short usable EXAFS data range it was not possible to investigate the presence of a possible presence of a second Cu-Au coordination shell in the samples with lower Cu amount.

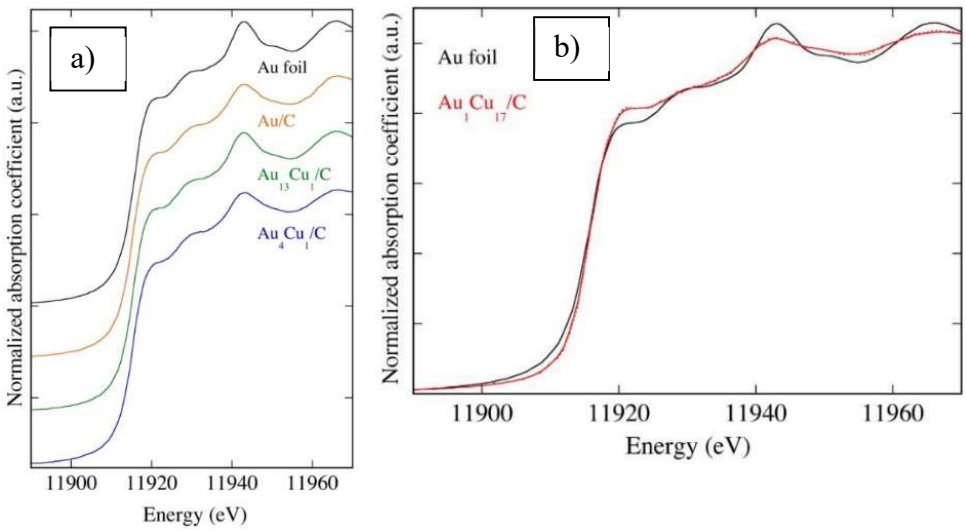

Figure 3-29. XANES spectra of a) the monometallic Au/C, $Au_{13}Cu_1$/C, Au_4Cu_1/C and b) Au_1Cu_{17}/C bimetallic catalysts compared to the one of the Au foil reference sample.

As clearly visible in Figure 3-29-a, the feature of white line (fist peak), centred at about 11920 eV in XANES spectra shows a slightly lower intensity in the bimetallic systems when compared to the Au reference sample.

In bulk Au, the presence of this white line was ascribed to the s-p-d atomic level hybridisation that gives a partial depletion of the filled $5d^{10}$ orbitals. The small Au nanoparticle size reduces this hybridisation, leading to an increase of the 5d occupancy and therefore a reduction of the intensity of white line [185, 191].

Concerning the sample with the highest Cu content (Figure 3-29-b), an increase of the intensity of the white line with respect of the Cu foil is visible. Because this increase is related to the presence of d-holes, the charge transfer from Au to Cu was confirmed (as already evidenced in the Cu K-edge data).

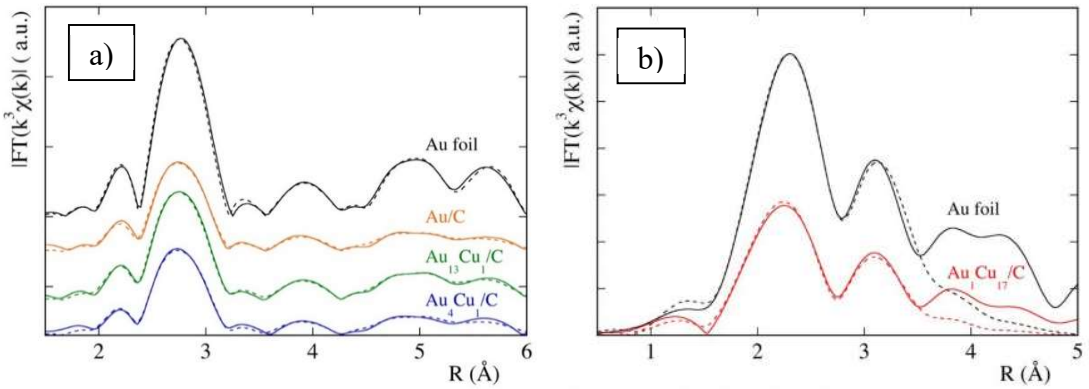

Figure 3-30. Fourier transforms of the experimental (full lines) and theoretical (dashed lines) EXAFS spectra of the a) Au/C, $Au_{13}Cu_1$/C, Au_4Cu_1/C and b) Au_1Cu_{17}/C catalysts compared to the Au foil reference sample (k range a = (2.5 – 14.5) $Å^{-1}$ b= (Δk = (2.5 – 8.0) $Å^{-1}$).

As shown in Figure 3-30-a, the EXAFS data of the catalysts with the higher Au amount were fitted using an FCC structure and including multiple scattering contributions to fit also the higher coordination shells. Due to the signal to noise ratio of the EXAFS data and having k_{max} = 8.0 $Å^{-1}$ (Figure 3-30-b), the fitting procedure was limited to the first coordination shell for the Au_1Cu_{17}/C sample.

For the two samples with the higher Au amount, the EXAFS data analysis can confirm the presence of Au cores and, not finding any Au/Cu contribution, that Cu could be confined in the outer shell around the Au-rich cores (as observed by HR-TEM analysis). In the case of the Au_1Cu_{17}/C sample, EXAFS data analysis gives a contracted Au/Au first shell distance and a low coordination number (N1 = 8, R1 = 2.83 Å; N1 bulk = 12, R1 bulk = 2.872 Å) showing the presence of smaller Au cores (Figure 3-30-b). The only effect of the Cu presence is given by the charge transfer from Au to Cu as shown in Figure 3-29-b. As detected by the STEM−EELS analysis, probably only a small part of the Cu atoms interacts with the surface atoms of these small Au cores while the biggest amount contributes to the formation of pure Cu(II) phase nanoparticles, taking into account the EXAFS data analysis at the Cu K edge.

3.4.6. *Catalytic activity*

The activity of the catalysts was evaluated in the oxidation of benzyl alcohol (benzyl alcohol 0.15 M, cyclohexane as solvent, alcohol/metal = 500/1 mol/mol, 120 °C, pO_2 = 4 bar). Table 3-8 reports the activity (moles of reactant converted per hour per mol of metal) and the selectivity calculated at 70 % of conversion. It can be observed that only the Au/C, $Au_{13}Cu_1/C$ and Au_4Cu_1/C are active under these reaction conditions, whereas Cu/C and Au_1Cu_{17}/C, did not show any activity. The best catalytic result was obtained using the Au-rich catalysts, 399 h^{-1} and 327 h^{-1} with Au_4Cu_1/C and $Au_{13}Cu_1/C$ respectively.

Table 3-8. Catalytic results.

Catalyst [a]	Activity [b] (h^{-1})	Conversion (%) after 6h	Selectivity to benzaldehyde [c]
Au/C	164	74	98
$Au_{13}Cu_1/C$	327	99	96
Au_4Cu_1/C	399	97	95
Au_1Cu_{17}/C	0	0	-
Cu/C	0	0	-

[a] *Reaction conditions: benzyl alcohol 0.15M, alcohol/metal = 500/1 mol/mol, 120 °C, pO_2 = 4 bar, cyclohexane as solvent.*
[b] *Moles of reactant converted per hour per mol of metal calculated after 30 min of reaction.*
[c] *Selectivity calculated at 70% conversion.*

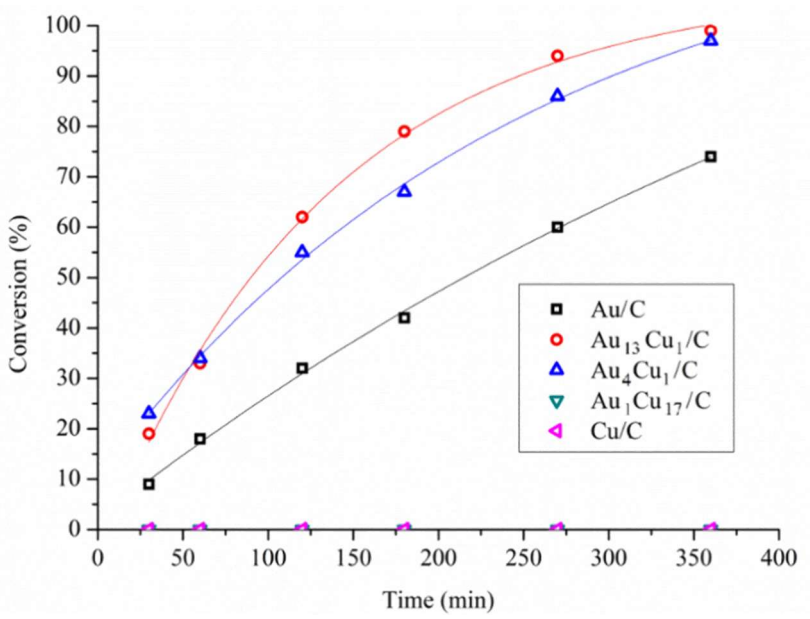

Figure 3-31. Conversion vs time for Au, $Au_{13}Cu_1$, Au_4Cu_1, Au_1Cu_{17} and Cu, catalysts. Reaction conditions: benzyl alcohol 0.15M, alcohol/metal = 500/1 mol/mol, 120 °C, pO_2 = 4 bar, cyclohexane as solvent.

Figure 3-31 shows a similar reaction profile for Au/C, $Au_{13}Cu_1$/C and Au_4Cu_1/C with no evident catalyst deactivation. In the case of the $Au_{13}Cu_1$/C and Au_4Cu_1/C catalysts, almost full conversion was obtained after 6 h while monometallic Au/C reached 74% of conversion. Finally, the catalysts showed similar selectivity regardless of their different structural features, leading to high benzaldehyde yields (selectivity 95−98 %, Table 3-8). In the case of Au-rich catalysts, a small amount of benzoic acid (1−3 %) was also detected. A particle size effect on the catalytic performances of the Au/Cu bimetallic catalysts can be excluded based on the results reported above. The data match with the beneficial synergetic effect caused by the copresence of Au and segregated CuO at the nanoparticles surface, as observed for the gas-phase CO oxidation reaction [173, 182]. It was demonstrated, in fact, that CO reacts with O_2 to produce CO_2 only when adsorbed on Au sites, whereas Cu species activate O_2 [182]. In particular, when CuO_x partially covers the Au-rich core nanoparticles, such as for Au_4Cu_1/C and $Au_{13}Cu_1$/C, the reaction can occur at the Au/CuO interface. Otherwise, in the presence of a thick layer of CuO_x, Au sites are not available and the reaction cannot proceed [182]. The enhanced performances of the hybrid Au/CuO bimetallic catalysts can be also ascribed to the oxygen "spillover" effect previously mentioned also for other intermetallic precious metal/metal oxide composites, even if observed for different catalytic reactions [192, 193].

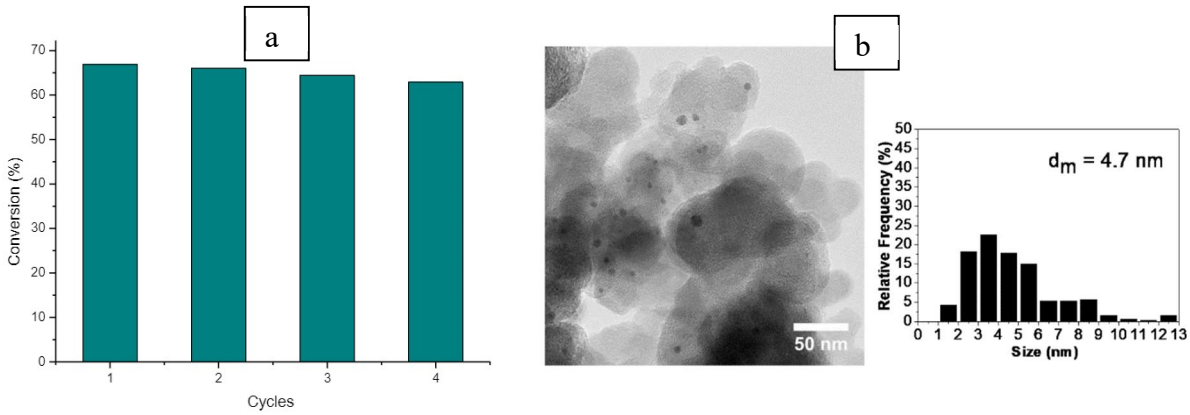

Figure 3-32. a) Stability tests running in 4 reaction cycles of Au_4Cu_1/C (reaction time 2h). b) Representative TEM micrograph and related size distribution for Au_4Cu_1/C after 4 catalytic cycles.

We also investigated the life-time of Au_4Cu_1/C, the sample that showed the highest initial activity value (399 h^{-1}) at the same condition reported for catalytic tests (reaction time 2h). The results are reported in Figure 3-32. The sample showed stability over 4 runs. The small decrease in terms of activity observed can be addressed to an unavoidable loss of catalysts during the recovery of the catalyst obtained by filtration. TEM investigation of the used catalyst was also performed. The results show only a slight increase of the mean size of the nanoparticles (from 4.4 to 4.7 nm) confirming the stability of the system.

3.4.7. *Conclusions*

In this section, we studied the behaviour of bimetallic AuMet/C catalysts prepared by SOL immobilisation technique (Met= Pd, Pt, Ru and Cu). We obtained similar metal dispersion which made possible to exclude the particle size effect but, depending on the second metal, led to different nanoparticles structure. In the case of Pd and Pt as second added metal, alloyed structures were revealed. On the other hand, in the case of Ru as second added metal, a core-shell structure was observed. For all this three dopant metals, the theoretical atomic proportion (Au:Met/6:4) was maintained. When Cu was added as the second metal, on the contrary, an enriched composition in Cu was found. All the catalysts were tested in benzyl alcohol oxidation and only in the case of Pd and Cu a beneficial synergistic effect between the two metals was shown. The AuPd catalyst, in particular, showed the highest activity (full conversion after 5 min), while the AuCu catalyst showed a synergetic effect despite Cu being the only non-noble metal used and the only metal that showed no activity in the reaction tested.

We decide then to investigate the composition effect changing the AuCu ratio. We synthesised for this purpose, by SMAD method, a batch of AuCu bimetallic nanoparticles

supported on carbon with different Au/Cu ratios and similar size distributions (with corresponding monometallics). We observe through HR-TEM, STEM-EELS maps and EXAFS measurements the formation of Au_{core}-CuO_{shell} heterostructures. The catalytic behaviour of the bimetallic catalysts was evaluated for selective benzyl alcohol oxidation in order to explore the effect of the CuO structures on the Au-driven catalytic activity. The highest increase in the catalytic activity with respect to monometallic Au sample was observed with the Au_4Cu_1/C catalyst (399 vs. 164 h^{-1}) where the segregated CuO phase partially covers the nanoparticles surface. This highly active sample resulted stable even after 4 recycling runs. Surprisingly, the catalytic activity was maintained very high (237 h^{-1}) also for the $Au_{13}Cu_1$/C catalyst even if it contains very low Cu loading (Cu 0.02 wt.%, Au 0.98 wt.%). On the other hand, when the CuO shell wrapped completely the Au core (high Cu loading – Au_1Cu_{17}/C) the reaction was completely inhibited. We addressed the O_2 activation to Cu species, and we speculated that the reaction occurred at the Au/CuO interface (over the Au atoms). When the external copper oxide shell was thick enough, the activity of the sample was therefore inhibited. Thus, we concluded that the beneficial synergistic effect of Au-CuO core-shell heterostructures linked to the degree of core coverage which is in turn related to the Au/Cu metal ratio.

References

1. F. Yang, J. Fu, J. Mo, X. Lu (2013) Synergy of Lewis and Brønsted Acids on Catalytic Hydrothermal Decomposition of Hexose to Levulinic Acid. Energy & Fuels 27(11):6973–6978.
2. X. Qi, M. Watanabe, T.M. Aida, R.L. Smith (2012) Synergistic conversion of glucose into 5-hydroxymethylfurfural in ionic liquid-water mixtures. Bioresour Technol 109:224–228.
3. G. Jäger, J. Büchs (2012) Biocatalytic conversion of lignocellulose to platform chemicals. Biotechnol J 7(9):1122–1136.
4. J. Fu, X. Xu, X. Lu, X. Lu (2016) Hydrothermal Decomposition of Carbohydrates to Levulinic Acid with Catalysis by Ionic Liquids. Ind Eng Chem Res 55(42):11044–11051.
5. Z.-P. Yan, L. Lin, S. Liu (2009) Synthesis of γ-Valerolactone by Hydrogenation of Biomass-derived Levulinic Acid over Ru/C Catalyst. Energy & Fuels 23(8):3853–3858.
6. C. Fang, Y. Liu, W. Wu, H. Li, Z. Wang, W. Zhao, T. Yang, S. Yang (2019) One Pot Cascade Conversion of Bio-Based Furfural to Levulinic Acid with Cu-Doped Niobium Phosphate Catalysts. Waste and Biomass Valorization 10(5):1141–1150.
7. K. Gupta, R.K. Rai, S.K. Singh (2018) Metal Catalysts for the Efficient Transformation of Biomass-derived HMF and Furfural to Value Added Chemicals. ChemCatChem 10(11):2326–2349.
8. M. Besson, P. Gallezot, C. Pinel (2014) Conversion of Biomass into Chemicals over Metal Catalysts. Chem Rev 114(3):1827–1870.
9. S. Lima, D. Chadwick, K. Hellgardt (2017) Towards sustainable hydrogenation of 5-(hydroxymethyl)furfural: a two-stage continuous process in aqueous media over RANEY® catalysts. RSC Adv 7(50):31401–31407.
10. X. Tang, J. Wei, N. Ding, Y. Sun, X. Zeng, L. Hu, S. Liu, T. Lei, L. Lin (2017) Chemoselective hydrogenation of biomass derived 5-hydroxymethylfurfural to diols: Key intermediates for sustainable chemicals, materials and fuels. Renew Sustain Energy Rev 77:287–296.
11. M.J. Climent, A. Corma, S. Iborra (2014) Conversion of biomass platform molecules into fuel additives and liquid hydrocarbon fuels. Green Chem 16(2):516–547.
12. A.A. Rosatella, S.P. Simeonov, R.F.M. Frade, C.A.M. Afonso (2011) 5-Hydroxymethylfurfural (HMF) as a building block platform: Biological properties, synthesis and synthetic applications. Green Chem 13(4):754.
13. A. Villa, C.E. Chan-Thaw, S. Campisi, C.L. Bianchi, D. Wang, P.G. Kotula, C. Kübel, L. Prati (2015) AuRu/AC as an effective catalyst for hydrogenation reactions. Phys Chem Chem Phys 17(42):28171–28176.
14. A. Villa, M. Schiavoni, C.E. Chan-Thaw, P.F. Fulvio, R.T. Mayes, S. Dai, K.L. More, G.M. Veith, L. Prati (2015) Acid-Functionalized Mesoporous Carbon: An Efficient Support for Ruthenium-Catalyzed γ-Valerolactone Production. ChemSusChem 8(15):2520–2528.
15. J. Jae, E. Mahmoud, R.F. Lobo, D.G. Vlachos (2014) Cascade of Liquid-Phase Catalytic Transfer Hydrogenation and Etherification of 5-Hydroxymethylfurfural to Potential Biodiesel Components over Lewis Acid Zeolites. ChemCatChem 6(2):508–513.
16. W. Luo, U. Deka, A.M. Beale, E.R.H. Van Eck, P.C.A. Bruijnincx, B.M. Weckhuysen (2013) Ruthenium-catalyzed hydrogenation of levulinic acid: Influence of the support and solvent on catalyst selectivity and stability. J Catal 301:175–186.
17. A.S. Piskun, J.E. de Haan, E. Wilbers, H.H. van de Bovenkamp, Z. Tang, H.J. Heeres (2016) Hydrogenation of Levulinic Acid to γ-Valerolactone in Water Using Millimeter Sized Supported Ru Catalysts in a Packed Bed Reactor. ACS Sustain Chem Eng 4(6):2939–2950.
18. L. Hu, X. Tang, J. Xu, Z. Wu, L. Lin, S. Liu (2014) Selective Transformation of 5-Hydroxymethylfurfural into the Liquid Fuel 2,5-Dimethylfuran over Carbon-Supported Ruthenium. Ind Eng Chem Res 53(8):3056–3064.
19. F. Jalid, T.S. Khan, F.Q. Mir, M.A. Haider (2017) Understanding trends in hydrodeoxygenation reactivity of metal and bimetallic alloy catalysts from ethanol reaction on stepped surface. J Catal 353:265–273.
20. A. Bjelić, M. Grilc, M. Huš, B. Likozar (2019) Hydrogenation and hydrodeoxygenation of aromatic

lignin monomers over Cu/C, Ni/C, Pd/C, Pt/C, Rh/C and Ru/C catalysts: Mechanisms, reaction micro-kinetic modelling and quantitative structure-activity relationships. Chem Eng J 359:305–320.

21. C. Wang, H. Xu, R. Daniel, A. Ghafourian, J.M. Herreros, S. Shuai, X. Ma (2013) Combustion characteristics and emissions of 2-methylfuran compared to 2,5-dimethylfuran, gasoline and ethanol in a DISI engine. Fuel 103:200–211.
22. Y. Román-Leshkov, C.J. Barrett, Z.Y. Liu, J.A. Dumesic (2007) Production of dimethylfuran for liquid fuels from biomass-derived carbohydrates. Nature 447(7147):982–985.
23. J. Jae, W. Zheng, R.F. Lobo, D.G. Vlachos (2013) Production of Dimethylfuran from Hydroxymethylfurfural through Catalytic Transfer Hydrogenation with Ruthenium Supported on Carbon. ChemSusChem 6(7):1158–1162.
24. J.N. Chheda, G.W. Huber, J.A. Dumesic (2007) Liquid-Phase Catalytic Processing of Biomass-Derived Oxygenated Hydrocarbons to Fuels and Chemicals. Angew Chemie Int Ed 46(38):7164–7183.
25. S. Dutta, S. De, B. Saha (2012) A Brief Summary of the Synthesis of Polyester Building-Block Chemicals and Biofuels from 5-Hydroxymethylfurfural. Chempluschem 77(4):259–272.
26. M. Bicker, D. Kaiser, L. Ott, H. Vogel (2005) Dehydration of d-fructose to hydroxymethylfurfural in sub- and supercritical fluids. J Supercrit Fluids 36(2):118–126.
27. G. Gerardus Johannes Maria, M. Leo Ernest, D.S.D. Ana Sofia Vagueiro, D. Frits, P. Jindra (2008) Hydroxymethylfurfural ethers and esters prepared in ionic liquids.
28. J. Luo, J. Yu, R.J. Gorte, E. Mahmoud, D.G. Vlachos, M.A. Smith (2014) The effect of oxide acidity on HMF etherification. Catal Sci Technol 4(9):3074–3081.
29. M. Mascal, E.B. Nikitin (2008) Direct, high-yield conversion of cellulose into biofuel. Angew Chemie - Int Ed 47(41):7924–7926.
30. B. Girisuta, L.P.B.M. Janssen, H.J. Heeres (2006) A kinetic study on the decomposition of 5-hydroxymethylfurfural into levulinic acid. Green Chem 8(8):701.
31. J. Jae, W. Zheng, A.M. Karim, W. Guo, R.F. Lobo, D.G. Vlachos (2014) The Role of Ru and RuO_2 in the Catalytic Transfer Hydrogenation of 5-Hydroxymethylfurfural for the Production of 2,5-Dimethylfuran. ChemCatChem 6(3):848–856.
32. S. Cattaneo, H. Naslhajian, F. Somodi, C. Evangelisti, A. Villa, L. Prati (2018) Ruthenium on Carbonaceous Materials for the Selective Hydrogenation of HMF. Molecules 23(8):2007.
33. T.A. Edison (1892) Manufacture of carbon filaments.
34. S. Iijima (1991) Helical microtubules of graphitic carbon. Nature 354(6348):56–58.
35. L. Feng, N. Xie, J. Zhong, L. Feng, N. Xie, J. Zhong (2014) Carbon Nanofibers and Their Composites: A Review of Synthesizing, Properties and Applications. Materials (Basel) 7(5):3919–3945.
36. K.P. De Jong, J.W. Geus (2000) Carbon Nanofibers: Catalytic Synthesis and Applications. Catal Rev - Sci Eng 42(4):481–510.
37. N.M. de A. Coelho, J.L.B. Furtado, C. Pham-Huu, R. Vieira (2008) Carbon nanofibers: a versatile catalytic support. Mater Res 11(3):353–357.
38. P. Serp, M. Corrias, P. Kalck (2003) Carbon nanotubes and nanofibers in catalysis. Appl Catal A Gen 253(2):337–358.
39. M.H. Al-Saleh, U. Sundararaj (2011) Review of the mechanical properties of carbon nanofiber/polymer composites. Compos Part A Appl Sci Manuf 42(12):2126–2142.
40. J.-P. Tessonnier, D. Rosenthal, T.W. Hansen, C. Hess, M.E. Schuster, R. Blume, F. Girgsdies, N. Pfänder, O. Timpe, D.S. Su, R. Schlögl (2009) Analysis of the structure and chemical properties of some commercial carbon nanostructures. Carbon N Y 47(7):1779–1798.
41. L. Prati, A. Villa, C.E. Chan-Thaw, R. Arrigo, D. Wang, D.S. Su (2011) Gold catalyzed liquid phase oxidation of alcohol: the issue of selectivity. Faraday Discuss 152:353.
42. A. Villa, D. Wang, P. Spontoni, R. Arrigo, D. Su, L. Prati (2010) Nitrogen functionalized carbon nanostructures supported Pd and Au–Pd NPs as catalyst for alcohols oxidation. Catal Today 157(1–4):89–93.

43. C.E. Chan-Thaw, A. Villa, G.M. Veith, L. Prati (2015) Identifying the Role of N-Heteroatom Location in the Activity of Metal Catalysts for Alcohol Oxidation. ChemCatChem 7(8):1338–1346.
44. M.L. Toebes, F.F. Prinsloo, J.H. Bitter, A.J. van Dillen, K.P. de Jong (2003) Influence of oxygen-containing surface groups on the activity and selectivity of carbon nanofiber-supported ruthenium catalysts in the hydrogenation of cinnamaldehyde. J Catal 214(1):78–87.
45. M.L. Toebes, Y. Zhang, J. Hájek, T. Alexander Nijhuis, J.H. Bitter, A. Jos van Dillen, D.Y. Murzin, D.C. Koningsberger, K.P. de Jong (2004) Support effects in the hydrogenation of cinnamaldehyde over carbon nanofiber-supported platinum catalysts: characterization and catalysis. J Catal 226(1):215–225.
46. A.J. Plomp, H. Vuori, A.O.I. Krause, K.P. de Jong, J.H. Bitter (2008) Particle size effects for carbon nanofiber supported platinum and ruthenium catalysts for the selective hydrogenation of cinnamaldehyde. Appl Catal A Gen 351(1):9–15.
47. S. Campisi, F. Sanchez Trujillo, D. Motta, T. Davies, N. Dimitratos, A. Villa (2018) Controlling the Incorporation of Phosphorus Functionalities on Carbon Nanofibers: Effects on the Catalytic Performance of Fructose Dehydration. C 4(1):9.
48. C. Chang, X. Ma, P. Cen (2006) Kinetics of Levulinic Acid Formation from Glucose Decomposition at High Temperature. Chinese J Chem Eng 14(5):708–712.
49. C. Xiao, T.-W. Goh, Z. Qi, S. Goes, K. Brashler, C. Perez, W. Huang (2016) Conversion of Levulinic Acid to γ-Valerolactone over Few-Layer Graphene-Supported Ruthenium Catalysts. ACS Catal 6(2):593–599.
50. O.A. Abdelrahman, A. Heyden, J.Q. Bond (2014) Analysis of Kinetics and Reaction Pathways in the Aqueous-Phase Hydrogenation of Levulinic Acid To Form γ-Valerolactone over Ru/C. ACS Catal 4(4):1171–1181.
51. D.M. Alonso, S.G. Wettstein, J.A. Dumesic (2013) Gamma-valerolactone, a sustainable platform molecule derived from lignocellulosic biomass. Green Chem 15(3):584.
52. I.T. Horváth, H. Mehdi, V. Fábos, L. Boda, L.T. Mika (2008) γ-Valerolactone—a sustainable liquid for energy and carbon-based chemicals. Green Chem 10(2):238–242.
53. J.Q. Bond, D.M. Alonso, D. Wang, R.M. West, J.A. Dumesic (2010) Integrated catalytic conversion of γ-valerolactone to liquid alkenes for transportation fuels. Science 327(5969):1110–1114.
54. W.R.H. Wright, R. Palkovits (2012) Development of Heterogeneous Catalysts for the Conversion of Levulinic Acid to γ-Valerolactone. ChemSusChem 5(9):1657–1667.
55. Z. Zhang (2016) Synthesis of γ-Valerolactone from Carbohydrates and its Applications. ChemSusChem 9(2):156–171.
56. J.C. Serrano-Ruiz, D.J. Braden, R.M. West, J.A. Dumesic (2010) Conversion of cellulose to hydrocarbon fuels by progressive removal of oxygen. Appl Catal B Environ 100(1–2):184–189.
57. X. Tang, X. Zeng, Z. Li, L. Hu, Y. Sun, S. Liu, T. Lei, L. Lin (2014) Production of γ-valerolactone from lignocellulosic biomass for sustainable fuels and chemicals supply. Renew Sustain Energy Rev 40:608–620.
58. H.A. Schuette, R.W. Thomas (1930) Normal valerolactone. III. Its preparation by the catalytic reduction of levulinic acid with hydrogen in the presence of platinum oxide. J Am Chem Soc 52(7):3010–3012.
59. B. V Robert Christian, H.D. Brown, R.M. Hixon (1947) Derivatives of -Valerolactone, 1,4-Pentanediol and l,4-Di-(β-cyanoethoxy)-pentane.
60. L.E. Manzer, K.W. Hutchenson (2004) Catalytic intramolecular cyclocondensation production of gamma-valerolactone from levulinic acid in supercritical media.
61. R.A. Bourne, J.G. Stevens, J. Ke, M. Poliakoff (2007) Maximising opportunities in supercritical chemistry: the continuous conversion of levulinic acid to γ-valerolactone in CO2. Chem Commun 28(44):4632–4634.
62. D.R. Jones, S. Iqbal, P.J. Miedziak, D.J. Morgan, J.K. Edwards, Q. He, G.J. Hutchings (2018) Selective Hydrogenation of Levulinic Acid Using Ru/C Catalysts Prepared by Sol-Immobilisation. Top Catal 61(9–11):833–843.

63. M.G. Al-Shaal, W.R.H. Wright, R. Palkovits (2012) Exploring the ruthenium catalysed synthesis of γ-valerolactone in alcohols and utilisation of mild solvent-free reaction conditions. Green Chem 14(5):1260.
64. W. Ren, X. Pan, G. Wang, W. Cheng, Y. Liu (2016) Dodecylated lignin-: G -PLA for effective toughening of PLA. Green Chem 18(18):5008–5014.
65. L. He, F. Weniger, H. Neumann, M. Beller (2016) Synthesis, Characterization, and Application of Metal Nanoparticles Supported on Nitrogen-Doped Carbon: Catalysis beyond Electrochemistry. Angew Chemie Int Ed 55(41):12582–12594.
66. X. Xu, Y. Li, Y. Gong, P. Zhang, H. Li, Y. Wang (2012) Synthesis of Palladium Nanoparticles Supported on Mesoporous N-Doped Carbon and Their Catalytic Ability for Biofuel Upgrade. J Am Chem Soc 134(41):16987–16990.
67. R.-J. van Putten, J.C. van der Waal, E. de Jong, C.B. Rasrendra, H.J. Heeres, J.G. de Vries (2013) Hydroxymethylfurfural, A Versatile Platform Chemical Made from Renewable Resources. Chem Rev 113(3):1499–1597.
68. J. Li, J. Liu, H. Zhou, Y. Fu (2016) Catalytic Transfer Hydrogenation of Furfural to Furfuryl Alcohol over Nitrogen-Doped Carbon-Supported Iron Catalysts. ChemSusChem 9(11):1339–1347.
69. J.B. Binder, R.T. Raines (2009) Simple Chemical Transformation of Lignocellulosic Biomass into Furans for Fuels and Chemicals. J Am Chem Soc 131(9):1879–1985.
70. Q. Cao, X. Guo, J. Guan, X. Mu, D. Zhang (2011) A process for efficient conversion of fructose into 5-hydroxymethylfurfural in ammonium salts. Appl Catal A Gen 403(1–2):98–103.
71. J.C. Serrano-Ruiz, J.A. Dumesic (2012) Catalytic Production of Liquid Hydrocarbon Transportation Fuels. In: Catal. Altern. Energy Gener. Springer New York, New York, NY, pp 29–56
72. S.-T. Yang (2007) Bioprocessing - from biotechnology to biorefinery. In: Bioprocess. Value-Added Prod. from Renew. Resour. pp 1–24
73. R. Ormsby, J.R. Kastner, J. Miller (2012) Hemicellulose hydrolysis using solid acid catalysts generated from biochar. Catal Today 190(1):89–97.
74. B.P. Lavarack, G.J. Griffin, D. Rodman (2002) The acid hydrolysis of sugarcane bagasse hemicellulose to produce xylose, arabinose, glucose and other products. Biomass and Bioenergy 23(5):367–380.
75. P.D. Carà, M. Pagliaro, A. Elmekawy, D.R. Brown, P. Verschuren, N.R. Shiju, G. Rothenberg (2013) Hemicellulose hydrolysis catalysed by solid acids. Catal Sci Technol 3(8):2057–2061.
76. R. O'Neill, M.N. Ahmad, L. Vanoye, F. Aiouache (2009) Kinetics of Aqueous Phase Dehydration of Xylose into Furfural Catalyzed by ZSM-5 Zeolite. Ind Eng Chem Res 48(9):4300–4306.
77. R. Weingarten, J. Cho, W.C. Conner, Jr., G.W. Huber (2010) Kinetics of furfural production by dehydration of xylose in a biphasic reactor with microwave heating. Green Chem 12(8):1423–1429.
78. H. Gómez Bernal, L. Bernazzani, A.M. Raspolli Galletti (2014) Furfural from corn stover hemicelluloses. A mineral acid-free approach. Green Chem 16(8):3734–3740.
79. F. Delbecq, Y. Wang, A. Muralidhara, K. El Ouardi, G. Marlair, C. Len (2018) Hydrolysis of Hemicellulose and Derivatives—A Review of Recent Advances in the Production of Furfural. Front Chem 6:1–29.
80. Á. O'Driscoll, J.J. Leahy, T. Curtin (2017) The influence of metal selection on catalyst activity for the liquid phase hydrogenation of furfural to furfuryl alcohol. Catal Today 279:194–201.
81. R. Mariscal, P. Maireles-Torres, M. Ojeda, I. Sádaba, M. López Granados (2016) Furfural: A renewable and versatile platform molecule for the synthesis of chemicals and fuels. Energy Environ Sci 9(4):1144–1189.
82. K. Yan, G. Wu, T. Lafleur, C. Jarvis (2014) Production, properties and catalytic hydrogenation of furfural to fuel additives and value-added chemicals. Renew Sustain Energy Rev 38:663–676.
83. L. Bui, H. Luo, W.R. Gunther, Y. Román-Leshkov (2013) Domino Reaction Catalyzed by Zeolites with Brønsted and Lewis Acid Sites for the Production of γ-Valerolactone from Furfural. Angew Chemie Int Ed 52(31):8022–8025.
84. M.J. Taylor, L.J. Durndell, M.A. Isaacs, C.M.A. Parlett, K. Wilson, A.F. Lee, G. Kyriakou (2016)

Highly selective hydrogenation of furfural over supported Pt nanoparticles under mild conditions. Appl Catal B Environ 180:580–585.
85. B. Arpini, A. Andrade Bartolomeu, C. Andrade, L. da Silva-Filho, V. Lacerda (2015) Recent Advances in Using Niobium Compounds as Catalysts in Organic Chemistry. Curr Org Synth 12(5):570–583.
86. S.M. Maurer, E.I. Ko (1992) Structural and acidic characterization of niobia aerogels. J Catal 135(1):125–134.
87. J.-M. Jehng, I.E. Wachs (1990) The molecular structures and reactivity of supported niobium oxide catalysts. Catal Today 8(1):37–55.
88. J.M. Jehng, I.E. Wachs (1991) Molecular structures of supported niobium oxide catalysts under in situ conditions. J Phys Chem 95(19):7373–7379.
89. P. Carniti, A. Gervasini, M. Marzo (2010) Silica-niobia oxides as viable acid catalysts in water: Effective vs. intrinsic acidity. Catal Today 152(1–4):42–47.
90. N.K. Gupta, A. Fukuoka, K. Nakajima (2017) Amorphous Nb 2 O 5 as a Selective and Reusable Catalyst for Furfural Production from Xylose in Biphasic Water and Toluene. ACS Catal 7(4):2430–2436.
91. M. Marzo, A. Gervasini, P. Carniti (2012) Improving stability of Nb 2O 5 catalyst in fructose dehydration reaction in water solvent by ion-doping. Catal Today 192(1):89–95.
92. P. Carniti, A. Gervasini, S. Biella, A. Auroux (2006) Niobic acid and niobium phosphate as highly acidic viable catalysts in aqueous medium: Fructose dehydration reaction. Catal Today 118(3-4 SPEC. ISS.):373–378.
93. K. Omata, S. Izumi, T. Murayama, W. Ueda (2013) Hydrothermal synthesis of W–Nb complex metal oxides and their application to catalytic dehydration of glycerol to acrolein. Catal Today 201:7–11.
94. C. García-Sancho, J.A. Cecilia, A. Moreno-Ruiz, J.M. Mérida-Robles, J. Santamaría-González, R. Moreno-Tost, P. Maireles-Torres (2015) Influence of the niobium supported species on the catalytic dehydration of glycerol to acrolein. Appl Catal B Environ 179:139–149.
95. Â. Silva, K. Wilson, A.F. Lee, V.C. dos Santos, A.C. Cons Bacilla, K.M. Mantovani, S. Nakagaki (2017) Nb2O5/SBA-15 catalyzed propanoic acid esterification. Appl Catal B Environ 205:498–504.
96. F.B. Noronha, D.A.G. Aranda, A.P. Ordine, M. Schmal (2000) The promoting effect of Nb2 addition to Pd/Al2O3 catalysts on propane oxidation. Catal Today 57(3–4):275–282.
97. M.J.C. Molina, M.L. Granados, A. Gervasini, P. Carniti (2015) Exploitment of niobium oxide effective acidity for xylose dehydration to furfural. Catal Today 254:90–98.
98. D. Stošić, S. Bennici, V. Rakić, A. Auroux (2012) CeO 2 -Nb 2 O 5 mixed oxide catalysts: Preparation, characterization and catalytic activity in fructose dehydration reaction. Catal Today 192(1):160–168.
99. D. Stošić, S. Bennici, V. Pavlović, V. Rakić, A. Auroux (2014) Tuning the acidity of niobia: Characterization and catalytic activity of Nb 2 O 5 -MeO 2 (Me = Ti, Zr, Ce) mesoporous mixed oxides. Mater Chem Phys 146(3):337–345.
100. H. Li, Z. Fang, R.L. Smith, S. Yang (2016) Efficient valorization of biomass to biofuels with bifunctional solid catalytic materials. Prog Energy Combust Sci 55:98–194.
101. B. Coq (2000) Metal-Support Interaction In Catalysis. In: Russo N, Salahub DR (eds) Met. Interact. Chem. Phys. Biol. Springer Netherlands, Dordrecht, pp 49–71
102. N.N. (Norman N. Greenwood, A. (Alan) Earnshaw (1997) Chemistry of the elements. Butterworth-Heinemann
103. R.D. Shannon (1976) Revised Effective Ionic Radii and Systematic Studies of Interatomie Distances in Halides and Chaleogenides. Acta Cryst 32(5):751–767.
104. P. Botella, B. Solsona, J.M. López Nieto, P. Concepción, J.L. Jordá, M.T. Doménech-Carbó (2010) Mo–W-containing tetragonal tungsten bronzes through isomorphic substitution of molybdenum by tungsten. Catal Today 158(1):162–169.
105. J.M. Jehng, I.E. Wachs (1991) Structural chemistry and Raman spectra of niobium oxides. Chem

Mater 3(1):100–107.
106. Y. Zu, P. Yang, J. Wang, X. Liu, J. Ren, G. Lu, Y. Wang (2014) Efficient production of the liquid fuel 2,5-dimethylfuran from 5-hydroxymethylfurfural over Ru/Co3O4 catalyst. Appl Catal B Environ 146:244–248.
107. N. Scotti, M. Dangate, A. Gervasini, C. Evangelisti, N. Ravasio, F. Zaccheria (2014) Unraveling the Role of Low Coordination Sites in a Cu Metal Nanoparticle: A Step toward the Selective Synthesis of Second Generation Biofuels. ACS Catal 4(8):2818–2826.
108. G. Crépeau, V. Montouillout, A. Vimont, L. Mariey, T. Cseri, F. Maugé (2006) Nature, Structure and Strength of the Acidic Sites of Amorphous Silica Alumina: An IR and NMR Study. J Phys Chem B 110(31):15172–15185.
109. C. Ravindra Reddy, G. Nagendrappa, B.S. Jai Prakash (2007) Surface acidity study of Mn+-montmorillonite clay catalysts by FT-IR spectroscopy: Correlation with esterification activity. Catal Commun 8(3):241–246.
110. A. Gervasini, P. Carniti, F. Bossola, C. Imparato, P. Pernice, N.J. Clayden, A. Aronne (2018) New Nb-P-Si ternary oxide materials and their use in heterogeneous acid catalysis. Mol Catal 458:280–286.
111. P. Carniti, A. Gervasini, F. Bossola, V. Dal Santo (2016) Cooperative action of Brønsted and Lewis acid sites of niobium phosphate catalysts for cellobiose conversion in water. Appl Catal B Environ 193:93–102.
112. C.A. Emeis (1993) Determination of Integrated Molar Extinction Coefficients for Infrared Absorption Bands of Pyridine Adsorbed on Solid Acid Catalysts. J Catal 141(2):347–354.
113. M.P. Pandey, C.S. Kim (2011) Lignin Depolymerization and Conversion: A Review of Thermochemical Methods. Chem Eng Technol 34(1):29–41.
114. J.C. Colmenares, W. Ouyang, M. Ojeda, E. Kuna, O. Chernyayeva, D. Lisovytskiy, S. De, R. Luque, A.M. Balu (2016) Mild ultrasound-assisted synthesis of TiO2 supported on magnetic nanocomposites for selective photo-oxidation of benzyl alcohol. Appl Catal B Environ 183:107–112.
115. A. Maldotti, A. Molinari, R. Amadelli (2002) Photocatalysis with Organized Systems for the Oxofunctionalization of Hydrocarbons by O 2. Chem Rev 102(10):3811–3836.
116. X. Lang, W. Ma, C. Chen, H. Ji, J. Zhao (2014) Selective Aerobic Oxidation Mediated by TiO 2 Photocatalysis. Acc Chem Res 47(2):355–363.
117. C. Zheng, G. He, X. Xiao, M. Lu, H. Zhong, X. Zuo, J. Nan (2017) Selective photocatalytic oxidation of benzyl alcohol into benzaldehyde with high selectivity and conversion ratio over Bi4O5Br2 nanoflakes under blue LED irradiation. Appl Catal B Environ 205:201–210.
118. T. Mallat, A. Baiker (2004) Oxidation of alcohols with molecular oxygen on solid catalysts. Chem Rev 104(6):3037–3058.
119. M. Besson, P. Gallezot (2000) Selective oxidation of alcohols and aldehydes on metal catalysts. Catal Today 57(1–2):127–141.
120. A. Savara, C.E. Chan-Thaw, J.E. Sutton, D. Wang, L. Prati, A. Villa (2017) Molecular Origin of the Selectivity Differences between Palladium and Gold-Palladium in Benzyl Alcohol Oxidation: Different Oxygen Adsorption Properties. ChemCatChem 9(2):253–257.
121. G.J. Hutchings (1985) Vapor phase hydrochlorination of acetylene: Correlation of catalytic activity of supported metal chloride catalysts. J Catal 96(1):292–295.
122. M. Haruta, N. Yamada, T. Kobayashi, S. Iijima (1989) Gold catalysts prepared by coprecipitation for low-temperature oxidation of hydrogen and of carbon monoxide. J Catal 115(2):301–309.
123. M. Haruta, T. Kobayashi, H. Sano, N. Yamada (1987) Novel Gold Catalysts for the Oxidation of Carbon Monoxide at a Temperature far Below 0 °C. Chem Lett 16(2):405–408.
124. A.S.K. Hashmi, G.J. Hutchings (2006) Gold Catalysis. Angew Chemie Int Ed 45(47):7896–7936.
125. A.S.K. Hashmi (2007) Gold-Catalyzed Organic Reactions Gold-Catalyzed Organic Reactions. Chem Rev 107:3180–3211.
126. M.C.M. Daniel, D. Astruc (2004) Gold Nanoparticles: Assembly, Supramolecular Chemistry, Quantum-Size Related Properties and Applications toward Biology, Catalysis and

Nanotechnology. Chem Rev 104:293–346.
127. B.K. Min, C.M. Friend (2007) Heterogeneous Gold-Based Catalysis for Green Chemistry: Low-Temperature CO Oxidation and Propene Oxidation. Chem Rev 107(6):2709–2724.
128. C. Della Pina, E. Falletta, L. Prati, M. Rossi (2008) Selective oxidation using gold. Chem Soc Rev 37(9):2077–2095.
129. A. Corma, H. Garcia (2008) Supported gold nanoparticles as catalysts for organic reactions. Chem Soc Rev 37(9):2096–2126.
130. J.C. Fierro-Gonzalez, B.C. Gates (2008) Catalysis by gold dispersed on supports: the importance of cationic gold. Chem Soc Rev 37(9):2127–2134.
131. M. Chen, D.W. Goodman (2008) Catalytically active gold on ordered titania supports. Chem Soc Rev 37(9):1860–1870.
132. Z. Li, C. Brouwer, C. He (2008) Gold-Catalyzed Organic Transformations. Chem Rev 108(8):3239–3265.
133. Y. Zhang, X. Cui, F. Shi, Y. Deng (2012) Nano-Gold Catalysis in Fine Chemical Synthesis. Chem Rev 112(4):2467–2505.
134. G.C. Bond, C. Louis, D.T. Thompson (2007) Catalysis by Gold. Imperial College Press, London
135. M. Sankar, N. Dimitratos, P.J. Miedziak, P.P. Wells, C.J. Kiely, G.J. Hutchings (2012) Designing bimetallic catalysts for a green and sustainable future. Chem Soc Rev 41(24):8099–8139.
136. S. Carrettin, P. McMorn, P. Johnston, K. Griffin, G.J. Hutchings (2002) Selective oxidation of glycerol to glyceric acid using a gold catalyst in aqueous sodium hydroxide. Chem Commun 57(7):696–697.
137. S. Demirel-Gülen, M. Lucas, P. Claus (2005) Liquid phase oxidation of glycerol over carbon supported gold catalysts. Catal Today 102–103:166–172.
138. A. Abad, C. Almela, A. Corma, H. García (2006) Efficient chemoselective alcohol oxidation using oxygen as oxidant. Superior performance of gold over palladium catalysts. Tetrahedron 62(28):6666–6672.
139. C.L. Bianchi, P. Canton, N. Dimitratos, F. Porta, L. Prati (2005) Selective oxidation of glycerol with oxygen using mono and bimetallic catalysts based on Au, Pd and Pt metals. Catal Today 102–103:203–212.
140. N. Dimitratos, F. Porta, L. Prati, A. Villa (2005) Synergetic effect of platinum or palladium on gold catalyst in the selective oxidation of D-sorbitol. Catal Letters 99(3–4):181–185.
141. L. Prati, M. Rossi (1998) Gold on carbon as a new catalyst for selective liquid phase oxidation of diols. J Catal 176(2):552–560.
142. S. Carrettin, P. McMorn, P. Johnston, K. Griffin, C.J. Kiely, G.J. Hutchings (2003) Oxidation of glycerol using supported Pt, Pd and Au catalysts. Phys Chem Chem Phys 5(6):1329–1336.
143. F. Porta, L. Prati (2004) Selective oxidation of glycerol to sodium glycerate with gold-on-carbon catalyst: an insight into reaction selectivity. J Catal 224(2):397–403.
144. N. Dimitratos, J.A. Lopez-Sanchez, G.J. Hutchings (2012) Selective liquid phase oxidation with supported metal nanoparticles. Chem Sci 3(1):20–44.
145. S.E. Davis, M.S. Ide, R.J. Davis (2013) Selective oxidation of alcohols and aldehydes over supported metal nanoparticles. Green Chem 15(1):17–45.
146. C. Della Pina, E. Falletta, M. Rossi (2008) Highly selective oxidation of benzyl alcohol to benzaldehyde catalyzed by bimetallic gold-copper catalyst. J Catal 260(2):384–386.
147. N. Dimitratos, A. Villa, D. Wang, F. Porta, D. Su, L. Prati (2006) Pd and Pt catalysts modified by alloying with Au in the selective oxidation of alcohols. J Catal 244(1):113–121.
148. D.I. Enache, J.K. Edwards, P. Landon, B. Solsona-Espriu, A.F. Carley, A.A. Herzing, M. Watanabe, C.J. Kiely, D.W. Knight, G.J. Hutchings (2006) Solvent-free oxidation of primary alcohols to aldehydes using Au-Pd/TiO2 catalysts. Science 311(5759):362–265.
149. J.K. Edwards, S.J. Freakley, A.F. Carley, C.J. Kiely, G.J. Hutchings (2014) Strategies for designing supported gold-palladium bimetallic catalysts for the direct synthesis of hydrogen peroxide. Acc Chem Res 47(3):845–854.
150. D.M. Alonso, S.G. Wettstein, J.A. Dumesic (2012) Bimetallic catalysts for upgrading of biomass

to fuels and chemicals. Chem Soc Rev 41(24):8075–8098.
151. H. Zhang, N. Toshima (2013) Glucoseoxidation using Au-containing bimetallic and trimetallic nanoparticles. Catal Sci Technol 3(2):268–278.
152. H. Zhu, L. Bao, S.M. Mahurin, G.A. Baker, E.W. Hagaman, S. Dai (2008) Seeded growth of robust SERS-active 2D Au@Ag nanoparticulate films. J Mater Chem 18(10):1079–1081.
153. C. Wang, H. Yin, R. Chan, S. Peng, S. Dai, S. Sun (2009) One-pot synthesis of oleylamine coated AuAg alloy NPs and their catalysis for CO oxidation. Chem Mater 21(3):433–435.
154. M. Tominaga, T. Shimazoe, M. Nagashima, H. Kusuda, A. Kubo, Y. Kuwahara, I. Taniguchi (2006) Electrocatalytic oxidation of glucose at gold-silver alloy, silver and gold nanoparticles in an alkaline solution. J Electroanal Chem 590(1):37–46.
155. J.H. Liu, A.Q. Wang, Y.S. Chi, H.P. Lin, C.Y. Mou (2005) Synergistic effect in an Au-Ag alloy nanocatalyst: CO oxidation. J Phys Chem B 109(1):40–43.
156. M. Kim, K.Y. Lee, G.H. Jeong, J. Jang, S.W. Han (2007) Fabrication of Au–Ag Alloy Nanoprisms with Enhanced Catalytic Activity. Chem Lett 36(11):1350–1351.
157. N.K. Chaki, H. Tsunoyama, Y. Negishi, H. Sakurai, T. Tsukuda (2007) Effect of Ag-Doping on the Catalytic Activity of Polymer-Stabilized Au Clusters in Aerobic Oxidation of Alcohol. J Phys Chem C 111(13):4885–4888.
158. S. Zhou, G.S. Jackson, B. Eichhorn (2007) AuPt alloy nanoparticles for CO-tolerant hydrogen activation: Architectural effects in Au-Pt bimetallic nanocatalysts. Adv Funct Mater 17(16):3099–3104.
159. S. Zhou, K. McIlwrath, G. Jackson, B. Eichhorn (2006) Enhanced CO tolerance for hydrogen activation in Au-Pt dendritic heteroaggregate nanostructures. J Am Chem Soc 128(6):1780–1781.
160. S. Mandal, A.B. Mandale, M. Sastry (2004) Keggin ion-mediated synthesis of aqueous phase-pure Au@Pd and Au@Pt core-shell nanoparticles. J Mater Chem 14(19):2868–2871.
161. H. Lang, S. Maldonado, K.J. Stevenson, B.D. Chandler (2004) Synthesis and Characterization of Dendrimer Templated Supported Bimetallic Pt−Au Nanoparticles. J Am Chem Soc 126(40):12949–12956.
162. D. Wang, A. Villa, F. Porta, L. Prati, D. Su (2008) Bimetallic Gold/Palladium Catalysts: Correlation between Nanostructure and Synergistic Effects. J Phys Chem C 112(23):8617–8622.
163. M.O. Nutt, J.B. Hughes, M.S. Wong (2005) Designing Pd-on-Au Bimetallic Nanoparticle Catalysts for Trichloroethene Hydrodechlorination. Environ Sci Technol 39(5):1346–1353.
164. M.O. Nutt, K.N. Heck, P. Alvarez, M.S. Wong (2006) Improved Pd-on-Au bimetallic nanoparticle catalysts for aqueous-phase trichloroethene hydrodechlorination. Appl Catal B Environ 69(1–2):115–125.
165. F. Ksar, L. Ramos, B. Keita, L. Nadjo, P. Beaunier, H. Remita (2009) Bimetallic palladium-gold nanostructures: application in ethanol oxidation. Chem Mater 21(15):3677–3683.
166. D.A. Cadenhead, N.G. Masse (1966) The microcatalytic hydrogenation of benzene over groups VIII and Ib metals and alloys. J Phys Chem 70(11):3558–3566.
167. M. Tominaga, Y. Taema, I. Taniguchi (2008) Electrocatalytic glucose oxidation at bimetallic gold–copper nanoparticle-modified carbon electrodes in alkaline solution. J Electroanal Chem 624(1–2):1–8.
168. C.L. Bracey, P.R. Ellis, G.J. Hutchings (2009) Application of copper–gold alloys in catalysis: current status and future perspectives. Chem Soc Rev 38(8):2231.
169. D. Halliche, R. Bouarab, O. Cherifi, M.M. Bettahar (1996) Carbon dioxide reforming of methane on modified Ni/α-A12O3 catalysts. Catal Today 29(1–4):373–377.
170. P.P. Fedorov, S.N. Volkov (2016) Au–Cu Phase Diagram. Russ J Inorg Chem 61(6):772–775.
171. X. Du, S. Luo, H. Du, M. Tang, X. Huang, P.K. Shen (2016) Monodisperse and self-assembled Pt-Cu nanoparticles as an efficient electrocatalyst for the methanol oxidation reaction. J Mater Chem A 4(5):1579–1585.
172. Z.L. Zhao, L.Y. Zhang, S.J. Bao, C.M. Li (2015) One-pot synthesis of small and uniform Au@PtCu core–alloy shell nanoparticles as an efficient electrocatalyst for direct methanol fuel cells. Appl Catal B Environ 174–175:361–366.

173. J. Yin, S. Shan, L. Yang, D. Mott, O. Malis, V. Petkov, F. Cai, M. Shan Ng, J. Luo, B.H. Chen, M. Engelhard, C.J. Zhong (2012) Gold-copper nanoparticles: Nanostructural evolution and bifunctional catalytic sites. Chem Mater 24(24):4662–4674.
174. X. Liu, A. Wang, X. Wang, C.-Y. Mou, T. Zhang (2008) Au–Cu Alloy nanoparticles confined in SBA-15 as a highly efficient catalyst for CO oxidation. Chem Commun (27):3187.
175. Y. Sugano, Y. Shiraishi, D. Tsukamoto, S. Ichikawa, S. Tanaka, T. Hirai (2013) Supported Au-Cu Bimetallic Alloy Nanoparticles: An Aerobic Oxidation Catalyst with Regenerable Activity by Visible-Light Irradiation. Angew Chemie Int Ed 52(20):5295–5299.
176. Q. Jia, D. Zhao, B. Tang, N. Zhao, H. Li, Y. Sang, N. Bao, X. Zhang, X. Xu, H. Liu (2014) Synergistic catalysis of Au–Cu/TiO 2 -NB nanopaper in aerobic oxidation of benzyl alcohol. J Mater Chem A 2(38):16292–16298.
177. W. Li, A. Wang, X. Liu, T. Zhang (2012) Silica-supported Au–Cu alloy nanoparticles as an efficient catalyst for selective oxidation of alcohols. Appl Catal A Gen 433–434:146–151.
178. J. Llorca, M. Domínguez, C. Ledesma, R.J. Chimentão, F. Medina, J. Sueiras, I. Angurell, M. Seco, O. Rossell (2008) Propene epoxidation over TiO2-supported Au-Cu alloy catalysts prepared from thiol-capped nanoparticles. J Catal 258(1):187–198.
179. P. Destro, T.M. Kokumai, A. Scarpellini, L. Pasquale, L. Manna, M. Colombo, D. Zanchet (2018) The Crucial Role of the Support in the Transformations of Bimetallic Nanoparticles and Catalytic Performance. ACS Catal 8(2):1031–1037.
180. W. Zhan, J. Wang, H. Wang, J. Zhang, X. Liu, P. Zhang, M. Chi, Y. Guo, Y. Guo, G. Lu, S. Sun, S. Dai, H. Zhu (2017) Crystal Structural Effect of AuCu Alloy Nanoparticles on Catalytic CO Oxidation. J Am Chem Soc 139(26):8846–8854.
181. P. Destro, S. Marras, L. Manna, M. Colombo, D. Zanchet (2017) AuCu alloy nanoparticles supported on SiO2: Impact of redox pretreatments in the catalyst performance in CO oxidation. Catal Today 282:105–110.
182. X. Liu, A. Wang, L. Li, T. Zhang, C.-Y. Mou, J.-F. Lee (2011) Structural changes of Au–Cu bimetallic catalysts in CO oxidation: In situ XRD, EPR, XANES, and FT-IR characterizations. J Catal 278(2):288–296.
183. J.C. Bauer, D. Mullins, M. Li, Z. Wu, E.A. Payzant, S.H. Overbury, S. Dai (2011) Synthesis of silica supported AuCu nanoparticle catalysts and the effects of pretreatment conditions for the CO oxidation reaction. Phys Chem Chem Phys 13(7):2571.
184. G.H. Chan, J. Zhao, E.M. Hicks, G.C. Schatz, R.P. Van Duyne (2007) Plasmonic Properties of Copper Nanoparticles Fabricated by Nanosphere Lithography. Nano Lett 7(7):1947–1952.
185. C. Evangelisti, E. Schiavi, L.A. Aronica, A.M. Caporusso, G. Vitulli, L. Bertinetti, G. Martra, A. Balerna, S. Mobilio (2012) Bimetallic Gold–Palladium vapour derived catalysts: The role of structural features on their catalytic activity. J Catal 286:224–236.
186. C. Evangelisti, A. Balerna, R. Psaro, G. Fusini, A. Carpita, M. Benfatto (2017) Characterization of a Poly-4-Vinylpyridine-Supported CuPd Bimetallic Catalyst for Sonogashira Coupling Reactions. ChemPhysChem 18(14):1921–1928.
187. A. Balerna, C. Evangelisti, C. Tiozzo (2017) XAFS structural characterization of Cu vapour derived catalysts supported on poly-4-vinylpyridine and carbon. X-Ray Spectrom 46(2):82–87.
188. S.W.T. Price, J.D. Speed, P. Kannan, A.E. Russell (2011) Exploring the First Steps in Core–Shell Electrocatalyst Preparation: In Situ Characterization of the Underpotential Deposition of Cu on Supported Au Nanoparticles. J Am Chem Soc 133(48):19448–19458.
189. A. Sharma, M. Varshney, J. Park, T.-K. Ha, K.-H. Chae, H.-J. Shin (2015) XANES, EXAFS and photocatalytic investigations on copper oxide nanoparticles and nanocomposites. RSC Adv 5(28):21762–21771.
190. T. Comaschi, A. Balerna, S. Mobilio (2008) Temperature dependence of the structural parameters of gold nanoparticles investigated with EXAFS. Phys Rev B 77(7):075432.
191. A. Balerna, E. Bernieri, P. Picozzi, A. Reale, S. Santucci, E. Burattini, S. Mobilio (1985) Extended x-ray-absorption fine-structure and near-edge-structure studies on evaporated small clusters of Au. Phys Rev B 31(8):5058–5065.

192. B. Sun, X. Feng, Y. Yao, Q. Su, W. Ji, C.-T. Au (2013) Substantial Pretreatment Effect on CO Oxidation over Controllably Synthesized Au/FeO_x Hollow Nanostructures via Hybrid Au/β-FeOOH@SiO_2. ACS Catal 3(12):3099–3105.
193. S. Hu, G. Goenaga, C. Melton, T.A. Zawodzinski, D. Mukherjee (2016) PtCo/CoOx nanocomposites: Bifunctional electrocatalysts for oxygen reduction and evolution reactions synthesized via tandem laser ablation synthesis in solution-galvanic replacement reactions. Appl Catal B Environ 182:286–296.

Chapter 4. Experimental section

4.1. Materials

All the amount expressed in grams have been determined using an analytical balance Gibertini E42 (weighing capacity: 100 g; detection limit: 0,0001 g). Deionised water (Milli-Q purified) was used for all the experiments. The specification of all the materials exploited will be provided during the discussion of the procedures for the sake of clarity.

4.2. Support preparation

4.2.1. *Carbon nanofibers functionalisation*

Commercial carbon nanofibers (CNFs) were used for the study as is (CNFs PR24-PS, from Applied Science Inc.) or opportunely functionalised.

CNFs-O – The oxygen-containing CNFs were obtained by treating the pristine support with HNO_3 according to the following procedure, also reported schematically in Figure 4-1. A suspension of CNFs in concentrated HNO_3 (20 g of CNFs per litre of HNO_3 65 wt.%) was kept at 100 °C for 2 h under continuous stirring. The CNFs were then recovered, filtered, rinsed with distilled water until the washing water reached the neutrality and dried overnight at 80 °C in oven.

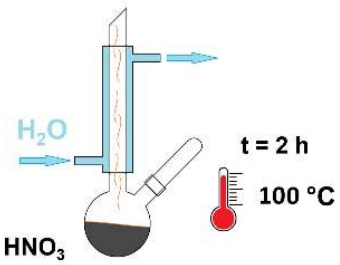

Figure 4-1. Schematic representation of the preparation of a CNFs-O support.

CNFs-N – Nitrogen-containing CNFs were obtained from the pre-oxidised CNFs (CNFs-O) by an additional thermal treatment (10 g for each batch) with $NH_{3(v)}$ at 600 °C for 4 h. A schematic representation of the procedure is reported in Figure 4-2.

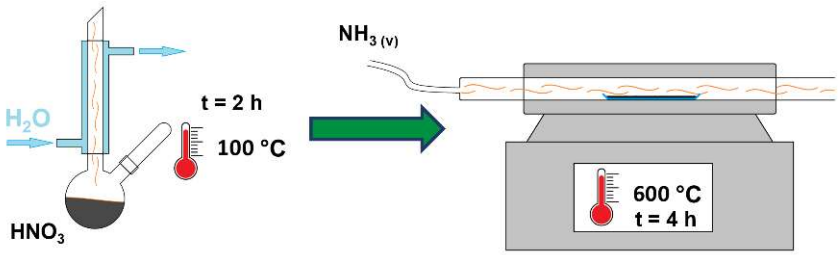

Figure 4-2. Schematic representation of the preparation of a CNFs-N support.

CNFs-P – For the phosphorous functionalisation, 2 g of the pristine CNFs sample were suspended in 250 mL of a HNO_3-H_3PO_4 (1:1 vol/vol mixture) under stirring and heated at 150 °C (2 h). A schematic representation of the treatment is reported in Figure 4-3.
The functionalised carbon samples were then recovered, thoroughly washed with distilled water until the washing water reached the neutrality and dried at 80 °C overnight.

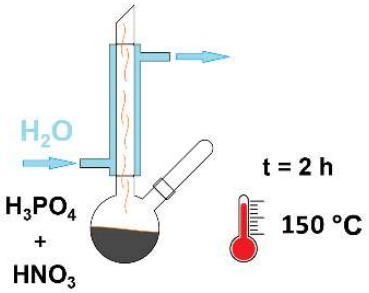

Figure 4-3. Schematic representation of the preparation of a CNFs-P support.

4.2.2. *Niobium oxide*

Niobium oxide (Nb_2O_5) and doped-niobium oxide supports (W-Nb_2O_5 and Ti-Nb_2O_5) were prepared by hydrothermal synthesis. The molar ratio between niobia and the dopant was Nb:Met = 9:1 for both the modified niobium-based materials. All the following procedures are referred to the synthesis of approximatively 3 g of support. A schematic representation of the synthesis is reported in Figure 4-4.
For a standard synthesis of niobia, 11.5 g of ammonium niobium oxalate (purity 99.5 %, from abcr-GmbH) were solubilised in 24 mL of water (MilliQ) under stirring at 80 °C for 10 minutes. The mixture was then poured in an autoclave, sealed, and kept at 175 °C for 48 hours. The solid so obtained was filtered, washed with 0.5 L of deionised water and dried for 16 hours at 100 °C. Subsequentially the material was thermally treated at 550 °C for 2 hours (heating rate 3 °C/min) under nitrogen flow (N_2 flow 30 mL/min).
For the tungsten-doped niobium oxide 10.04 g of niobium oxalate were dissolved in 19.00 g of water (MilliQ) under stirring at 80 °C for 10 minutes. At the same time, 0.59 g of ammonium metatungstate hydrate (purity 99.99 %, from Sigma-Aldrich) were dissolved in 5 mL of water (MilliQ) under stirring for 10 minutes at 80 °C. The solution containing the dopant metal precursor were then added dropwise to the niobium oxalate solution (under stirring at 80 °C) and kept stirred for an additional 10 minutes at 80 °C. The resulting mixture was then poured in an autoclave, sealed and kept at 175 °C for 48 hours. The solid so obtained was filtered, washed with 0.5 L of deionized water and dried for 16 hours at 100 °C. Subsequentially the material was thermally treated at 550 °C for 2 hours (heating rate 3 °C/min) under nitrogen flow (N_2 flow, 30 mL/min).

The tungsten-doped niobium was prepared starting from the dissolution of 10.04 g of niobium oxalate in 19.00 g of water (MilliQ) under stirring for 10 min at 80 °C. Meanwhile, a solution prepared from 0.66 g of titanium(IV)oxysulfate-sulphuric acid hydrate (purity 99.99 %, from Sigma-Aldrich) dissolved in 5 mL of water (MilliQ) was prepared and kept under stirring at 80 °C for 10 minutes. The solution containing the dopant metal precursor was then added dropwise to the niobium oxalate solution (under stirring at 80°C) and kept stirred for an additional 10 minutes at 80 °C. The resulting mixture was then poured in an autoclave, sealed and kept at 175 °C for 48 hours. Finally, the material was thermally treated for 2 hours at 550 °C with a heating rate of 3 °C/min under an inert flow of nitrogen (30 mL/min).

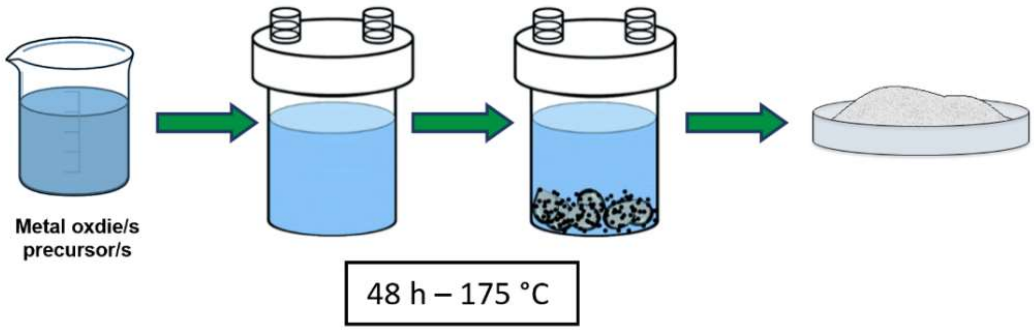

Figure 4-4. Schematic representation of the preparation by hydrothermal synthesis of niobia and doped niobia.

4.3. Catalyst preparation

4.3.1. *SOL synthesis*

Au/C

A freshly aqueous solutions of metal precursor ([Met^{n+}] = 5×10^{-4} M), polyvinyl alcohol (PVA, 1 wt.%) and $NaBH_4$ (0.1 M, purity > 96%, from Fluka) were separately prepared. The Au metal precursor ($HAuCl_4 \cdot 3H_2O$, purity ≥ 99.9%, from Sigma-Aldrich) and protecting agent (PVA M_W = 9,000–10,000, 80 % hydrolysed, from Sigma-Aldrich) were initially added in 100 mL of water (MilliQ) (Au/PVA 1:0.5, weight/weight). After 5 min, the reducing agent $NaBH_4$ (Au/$NaBH_4$ 1:4 mol/mol) solution was promptly added to the pale yellow solution under vigorous magnetic stirring. An excess of the $NaBH_4$ is used to guarantee a complete reduction of the gold precursor. After the insertion of the reducing agent, a ruby-red Au^0 sol was immediately formed. Within a few minutes from sol generation, the support was added to the colloid (acidified at pH 2 by sulfuric acid) under vigorous stirring. The procedure is schematically summarised in Figure 4-5. The selected carbons were all commercially available and were X40S activated carbon from Camel, VulcanXC72R and Norit Carbon GSX from Cabot. Further features of the selected carbons are reported in the section 2.3. The amount of support was calculated to obtain 1 g of catalysts with a final metal loading of 1 wt.%. The catalysts were finally filtered, washed several times with milliQ water (≈ 300 mL to remove the excess of PVA from the catalyst's surface) and then dried overnight at 80 °C in oven. The metal loading was verified by Inductively Coupled Plasma - Optical Emission Spectrometry (ICP-OES) technique.

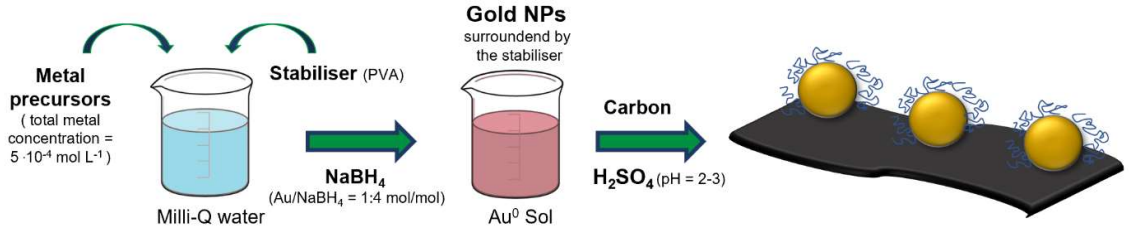

Figure 4-5. Representative scheme of a SOL- immobilisation synthesis techniques (Au/Carbon).

Au/Al_2O_3, Ag/Al_2O_3 and Au_4Ag_1/Al_2O_3

Stock aqueous solutions of metal precursor ($[Met^{n+}] = 6 \times 10^{-3}$ M), PVA (0.2 wt.%) and $NaBH_4$ (0.025 M) were freshly prepared. Alumina (Al_2O_3 Degussa, Aluminium oxide, SA: 100 $m^2\ g^{-1}$) was selected as the support. In SOL preparation the bimetallic AuAg sol or the corresponding monometallic Au and Ag sols were firstly prepared by reduction of the precursors by $NaBH_4$ in aqueous solution in the presence of polyvinyl alcohol (PVA, MW = 9000–10,000, 80 % hydrolysed, from Aldrich) as stabilising agent, and then adsorbed on alumina support as for the previous preparative procedure.

Specifically, to prepare 1 g of monometallic catalyst with a final loading of 1.8 wt.% and 2 wt.% for Au and Ag, respectively, the monometallic (Au or Ag) sol was generated from a mixture of 8 mL of 6.0×10^{-3} M of metal precursor solution ($HAuCl_4$ purity > 99.0 %, from Aldrich or 15 mL $AgNO_3$ purity >99.0 %, from Aldrich), 25.0 mL 0.2 wt.% PVA solution in 600 mL of MilliQ water. The reducing step was performed by addition of 0.025 M $NaBH_4$ (purity > 96 %, from Fluka) solution (Met/$NaBH_4$ 1:8 mol/mol). Appropriate amount of Sols and alumina was mixed and stirred at room temperature for about two hours to allow a complete adsorption of metal nanoparticles on the substrate. When the supernatant solution was colourless, it was then filtered and washed by water (approximately 300 mL). The catalysts so obtained were then dried overnight at 80 °C in oven.

The bimetallic Sol of Au/Ag = 4/1 atomic ratio was prepared by consecutive reduction of the $AgNO_3$ and $HAuCl_4 \cdot 3H_2O$ to avoid the AgCl precipitation. The calculation was made to obtain 2.5 g of catalyst. A mixture of 7.5 mL 6.0×10^{-3} M $AgNO_3$ and 30.0 mL 0.2 wt.% PVA solution diluted in 600 mL MilliQ water was stirred and cooled in an icy water bath, then 15 mL of freshly prepared $NaBH_4$ solution (0.025 M) was added. The sudden appearance of yellow colour indicated the reduction of silver. After 30 min of stirring a mixture of 30 mL 6.0×10^{-3} M $HAuCl_4$, 15.0 mL 0.2 wt.% PVA solution was added to the suspension. Then 60 mL of a freshly prepared $NaBH_4$ solution (0.025 M) were immediately added to the mixture. After the addition of the sodium borohydride a brown colour appeared at once highlighting the prompt reduction of the gold precursor. The catalyst was then recovered by filtration and washed with approximately 300 mL of water, before being dried overnight at 80 °C in oven. The real amount of metal was determined by ICP-OES. A general scheme of the bimetallic synthesis is reported in Figure 4-6.

According to these procedures Au/Al_2O_3, Ag/Al_2O_3 and Au_4Ag_1/Al_2O_3 supported catalyst with a nominal weight percentage of 1.8, 2.0, and 3.2 were respectively obtained.

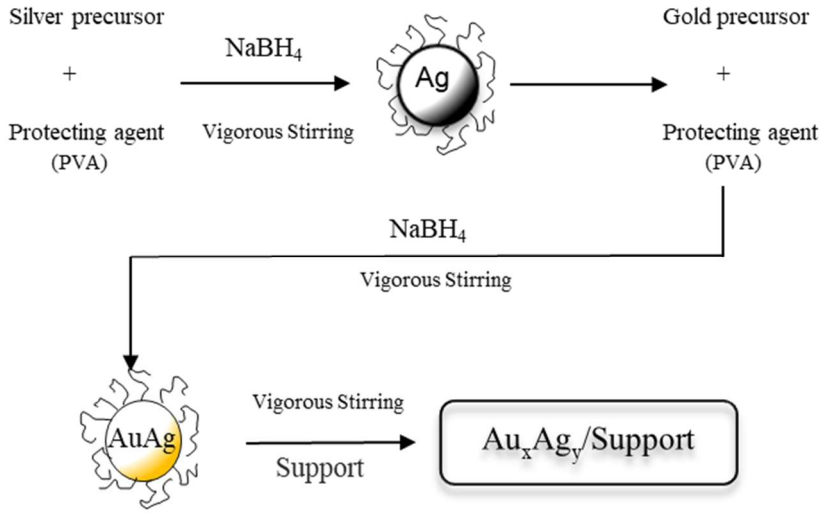

Figure 4-6. Representative scheme of a subsequent deposition of Ag and Au NPs by SOL-immobilisation technique (Au_xAg_y/Support)

Au/TiO_2, Ag/TiO_2, Au_1Ag_1/TiO_2 and Au_4Ag_1/TiO_2

The catalysts were prepared by SOL immobilisation procedure, consisting in a reduction step of the metal precursors by $NaBH_4$ in aqueous solution in the presence of polyvinyl alcohol (PVA) as stabilising agent and a deposition step, where the support was added to the colloidal solution, containing preformed metal nanoparticles. Titania (Titanium oxide, TiO_2, SA: 45 m^2 g^{-1}, 70 % anatase and 30 % rutile, purity > 99.5 %, from Aldrich) was selected as the support.

The monometallic Au (or Ag) sols were synthetised starting from a mixture of 20.8 mL of a 6.0×10^{-3} M $HAuCl_4$ solution (or 18.8 mL 6.0×10^{-3} M $AgNO_3$ solution), 22.5 mL 0.2 wt.% PVA solution in 300 mL of MilliQ water. The reducing step was performed by addition of 37.5 mL of 0.025 M $NaBH_4$ freshly prepared solution. Appropriate amounts of the Sol and alumina were mixed and stirred at room temperature for about two hours to allow a complete immobilisation of metal nanoparticles on the support. When the supernatant solution was colourless, the suspension was then filtered and washed by water (approximately 300 mL). The solid catalysts so obtained were then dried overnight at 80 °C in oven. Following this procedure, 1 wt.% Au/TiO_2 and 1 wt.% Ag/TiO_2 supported catalyst were respectively prepared.

Bimetallic AuAg Sols were prepared by consecutive reduction of the $AgNO_3$ and successively of $HAuCl_4$ (in two separate steps to avoid the AgCl precipitation), with an

Au/Ag molar ratio equal to 1:1 and 4: 1, respectively. Firstly, a mixed $AgNO_3$ and PVA solution (0.2 wt.%, Met/PVA 1:0.5, w/w) in MilliQ water was prepared and then a freshly prepared 0.025 M $NaBH_4$ solution was added (under vigorous stirring). The appearance of a yellow colour confirmed the reduction of Ag^+ ions. The solution was stirred for 30 minutes, then a proper amount of $HAuCl_4$ mixed with PVA solution (0.2 wt.%, Met/PVA = 1:0.5 w/w) was added. Further addition of $NaBH_4$ solution (0.025 M, Met/$NaBH_4$ 1:4 mol/mol) has been done under vigorous stirring. The solution colour quickly changed to brown. Subsequentially, the appropriate amount of Sol and TiO_2 were mixed to provide 1 wt.% of metal loading. The adsorption of nanoparticles was favoured by addition of proper amount of p-phenylenediamine solution (PDDA solution: 0.08 wt.%). The suspension was stirred at room temperature for 2 h, in order to allow the complete adsorption of the metal nanoparticles on the support surface indicated by the complete decolouration of the supernatant. The obtained powder was separated by filtration, washed with water (approximately 300 mL) and dried at 80°C overnight in the oven. Finally, the real loading was verified by ICP-OES.

Au/TiO_2, Pt/TiO_2 and Au_xPt_y/TiO_2

The catalysts were prepared according to the sol immobilisation procedure, extensively described above.

For the monometallic 1% wt. Au/TiO_2, 0.051 mmol of $NaAuCl_4 \cdot 2H_2O$ (purity 99.99 %, from Aldrich) and PVA (1 wt.%) solution (Au/PVA = 1/0.5 w/w) were added to 100 mL of MilliQ water. After 5 min, a freshly prepared solution of $NaBH_4$ (0.1 M) (Au/$NaBH_4$ = 1/4 mol/mol) was added to the yellow solution under vigorous magnetic stirring. Within a few minutes of Sol generation, the colloid was immobilized by adding the support under vigorous stirring. The amount of support was calculated as having a total final metal loading of 1 wt.%. After 2 h, the slurry solution was filtered (transparent solution confirmed both the complete adsorption of the nanoparticles and the complete reduction of all the metal precursor) and washed thoroughly with approximately 300 mL of water and dried overnight at 80 °C in the oven.

Monometallic Pt/TiO_2 was prepared starting from 0.051 mmol of K_2PtCl_4 (purity >99.99 %, from Aldrich) and PVA (1 wt.%) solutions (Pt/PVA = 1/0.5 w/w), added to 100 mL of H_2O (MilliQ). After 5 min, H_2 was bubbled (50 mL/min) under atmospheric pressure and room temperature for 2 h. The colloid was immobilized by adding the support under

vigorous stirring. The amount of support was calculated as having a total final metal loading of 1 wt.%. After 2 h the slurry solution was filtered and the catalyst was washed thoroughly with distilled water (approximately 300 mL) and dried overnight at 80 °C in the oven.

For the bimetallic preparative, a general scheme is reported in Figure 4-7. and the procedure for the preparation of Au_6Pt_4/TiO_2 catalyst is reported as example. $NaAuCl_4 \cdot 2H_2O$ (0.031 mmol) was dissolved in 60 mL of H_2O and a PVA (1 wt.%) solution was added (Au/PVA = 1/0.5 w/w) under stirring. After 3 minutes, to the yellow solution a fresh solution of 0.1 M $NaBH_4$ (Au/$NaBH_4$ = 1:4 mol/mol) was added under vigorous magnetic stirring. Within a few minutes of Sol generation, the gold Sol was immobilized by adding the support under vigorous stirring. The amount of support was calculated as having a gold loading of 0.60 wt.%. After 2 h, the slurry solution was filtered and the catalyst washed thoroughly with distilled water (approximately 300 mL). The recovered supported Au material was then re-dispersed in 40 mL of water (it will be used as support for the sequential Pt immobilisation) in presence of K_2PtCl_4 (0.021 mmol) and PVA solution (Pt/PVA = 1:0.5 w/w). H_2 was bubbled (50 mL/min) under atmospheric pressure at room temperature for 2 h. The slurry solution was then filtered and the catalyst washed thoroughly with distilled water (approximately 300 mL) before being dried overnight at 80 °C. The total metal loading was 1 wt.%. The final loading was verified by ICP-OES for all the samples. Using the same procedure and varying the ratio between Au and Pt, the following catalysts were prepared: Au_9Pt_1/TiO_2, Au_8Pt_2/TiO_2, Au_6Pt_4/TiO_2, Au_2Pt_8/TiO_2, Au_1Pt_9/TiO_2.

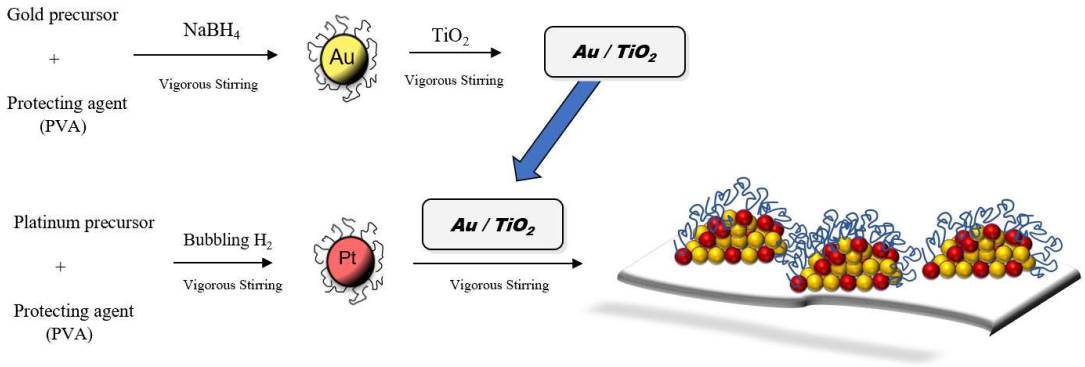

Figure 4-7. Representative scheme of a subsequent deposition by SOL- immobilisation technique (Au_xPt_y/TiO_2).

Monometallic Au, Pd Pt and Cu catalysts

$NaAuCl_4 \cdot 2H_2O$ (0.051 mmol, purity 99.99 %, from Aldrich), $Na_2PdCl_4 \cdot 2H_2O$ (0.094 mmol, purity 99.99 %, from Aldrich), K_2PtCl_4 (0.051 mmol, purity 99.99 %, from Aldrich) or $RuCl_3$ (0.099 mmol, purity 99.99 %, from Aldrich) salt and freshly prepared 1 wt.% PVA (polyvinyl alcohol, MW = 9,000–10,000, 80 % hydrolysed, from Aldrich) solution was added to 100 mL of H_2O (metal/PVA = 1/0.5 w/w), respectively. After 3 min, $NaBH_4$ (purity > 96 %, from Fluka) 0.1 M solution ($Au/NaBH_4$ = 1/4 mol/mol and $Met/NaBH_4$ = 1/8 for Pt, Pd and Ru) was added to the solution under vigorous magnetic stirring. Within a few minutes from the Sol generation, the suspension was acidified at pH 2 by sulphuric acid and the support was then added always under vigorous stirring. The support is an activated carbon (AC) obtained from Camel (X40S, surface area 1100 $m^2\ g^{-1}$, pore volume 1.5 mL g^{-1}). The catalyst was subsequentially filtered and washed with distilled water (approximately 300mL). Finally, the samples were dried overnight at 80 °C in oven. The amount of the support was calculated to obtain a final metal loading of 1 wt.% for all the catalysts prepared.

For the monometallic Cu, similarly to the previous monometallics preparative, the copper Sol was produced from the mixture of 11.3 mL of 20 mM of $Cu(NO_3)_2$ solution and 45 mL of 0.2 wt.% PVA (polyvinyl alcohol, MW = 9,000–10,000, 80 % hydrolysed, from Aldrich) solution (in 600 mL of water) through the further addition of 75 mL of the reducing agent ($NaBH_4$ solution, 0.025 M , purity > 96 %, from Fluka). An appropriate amount of carbon was added to the solution under stirring to obtain a final metal loading of 1 wt.%. The support is an activated carbon (AC) obtained from Camel (X40S, surface area 1100 $m^2\ g^{-1}$, pore volume 1.5 mL g^{-1}). The catalyst was then filtered and washed with approximately 300 mL of distilled water. The sample was finally dried overnight at 80 °C in oven. The metal loading was verified by ICP-OES.

Au–based catalysts (Au-Pd, Au-Pt, Au-Ru and Au-Cu)

$NaAuCl_4 \cdot 2H_2O$ (0.037 mmol) was dissolved in 70 mL of H_2O and PVA (1 % w/w, polyvinyl alcohol, MW = 9,000–10,000, 80 % hydrolysed, from Aldrich) was added (Au/PVA = 1/0.5 w/w). After 3 min $NaBH_4$ (purity > 96 %, from Fluka) 0.1 M solution ($Au/NaBH_4$ = 1/4 mol/mol) was added under vigorous magnetic stirring. The amount of support was calculated as having a gold loading of 0.73 wt.% for AuPd and AuRu, 0.60 wt.% for AuPt to respect the molar ratio desiderated. The support is an activated carbon

(AC) obtained from Camel (X40S, surface area 1100 $m^2\ g^{-1}$, pore volume 1.5 mL g^{-1}). After 2 h of stirring the slurry solution was filtered and the catalyst washed with approximately 300mL of distilled water. The Au/C samples prepared was then re-dispersed in 70 mL of water for the subsequent immobilisation. Na_2PdCl_4, K_2PtCl_4 and $RuCl_3$ (0.024 mmol) with PVA (1 % wt.) solution (Met/PVA = 1/0.5 w/w) were added. The reduction of the all the metal precursors occurred under H_2 bubbling (50 mL/min) under atmospheric pressure at room temperature for 2 hours. The slurry solutions so obtained were filtered and the catalysts were washed with approximately 300 mL of distilled water. The samples were then dried overnight at 80 °C in oven. All the three bimetallic catalysts were prepared with a molar ration of Au : Met = 6 : 4. The total metal loading was 1 % wt. for all the samples prepared.

For the preparation of bimetallic AuCu/C, a mixture of 35.4 mL 5.12 mM $HAuCl_4$ solution, 2.5 mL 20 mM of $Cu(NO_3)_2$ solution and 45 mL of 0.2 wt.% PVA solution (polyvinyl alcohol, MW = 9,000–10,000, 80 % hydrolysed, from Aldrich) was added to 600 mL of water (MilliQ) and the mixture was stirred and cooled in an icy water bath. Successively, 75 mL of freshly prepared solution 0.025 M of $NaBH_4$ (purity > 96 %, from Fluka) was added and the mixture was left under vigorous stirring for 2 hours. An appropriate amount of carbon was the added under stirring. The support is an activated carbon (AC) obtained from Camel (X40S, surface area 1100 $m^2\ g^{-1}$, pore volume 1.5 mL g^{-1}). The catalyst was finally filtered and washed with approximately 300 mL of distilled water. The catalyst has prepared with a molar ration of Au:Cu = 8:2.The sample was finally dried overnight at 80 °C in oven. The amount of the support exploited was calculated to obtain a final metal loading of 2.6 wt.%. The final loading was verified by ICP-OES.

4.3.2. *SMAD synthesis*

Au/C

Gold beads (1–6 mm, purity 99.999 %, from Aldrich) and acetone (from Merk purified by conventional methods, distilled and stored under argon) were used in this synthetic route. The co-condensation of gold and acetone vapours occurred in a static metal vapor synthesis (MVS) reactor as already described in the introduction chapter (Chapter 1). Au vapours generated at 10^{-5} mbar by resistive heating of alumina-coated tungsten crucibles (filled with 120 mg of Au beads, 1–6 mm, purity 99.999 %, from Aldrich) were co-condensed simultaneously with acetone (100 mL) onto the frozen walls of the glass reactor maintained at liquid nitrogen temperature (-196 °C) for 1 h. The reactor chamber was then heated to the melting point of the solid matrix (approximately – 95 °C) and the resulting Au solvated metal atoms (SMA) solution (approximately 95.0 mL) was kept under argon atmosphere in a Schlenk tube (- 40 °C). Au SMAs are red-purple in colour and stable at room temperature. The precise metal lading of the final solution is calculated by ICP-OES analysis after a proper digestion of the sample (hot mixture of nitric acid and hydrochloric acid, 1:3, heated by microwave). This latter step is necessary to calculate the proper amount of suspension (withdrew by a glass pipette from the Schlenk tube) and support to be exploited in order to reach the desired final metal loading (1 % in this case). The Au calculated content in the suspension was 0.86 mg/mL. Subsequentially, 45 mL of the [Au]/acetone SMA (0.39 mmol, 77.4 mg of Au) was added to a suspension of alumina (3.9 g) in acetone (50 mL) under vigorous stirring (at RT). After a variable amount of time (depends on the adsorption rate proper of every support) the black solid is recovered and the solvent removed under vacuum. The solid was then washed with 50 mL of n-pentane for three times and subsequentially carefully removed under vacuum and modest warming (approximately 60 °C). This last step allows a compete removal of the solvent: n-pentane is exploited because it is a very volatile solvent. Au/C catalysts with 1 wt.% of total metal loading were finally obtained. A general scheme of a monometallic Au/C SMAD synthesis is reported in Figure 4-8.

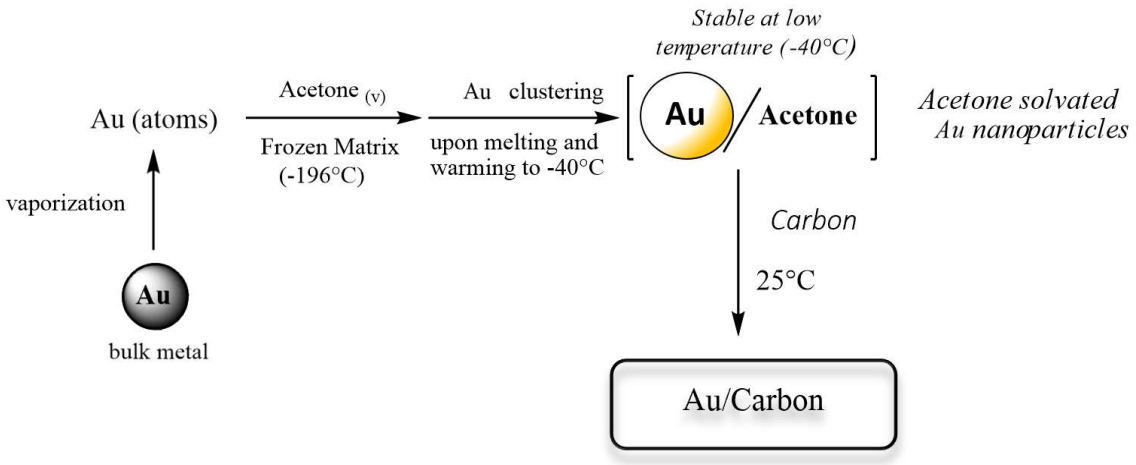

Figure 4-8. General scheme of a monometallic SMAD synthesis (Au/Carbon)

Au/Al_2O_3, Ag/Al_2O_3 and Au_4Ag_1/Al_2O_3

Both the monometallic Au and Ag catalysts were prepared by co-condensation of Au (120 mg, beads or alternatively Ag, 110 mg wire) vapours with acetone (100 mL, from Merck distilled and stored under argon) vapours. The co-condensation of gold (or silver) and acetone vapours was carried out in a static reactor in the same procedure above reported (Au/C preparation). The resulting Au (or Ag) solvated metal atoms (SMA) solution (total volume produced = 95 mL) containing 0.8 mg/mL Au (and 0.65 mg/mL, Ag) measured by ICP-OES analysis, was adsorbed on alumina support (3.8 g, 2 wt.% for Au, or 6.2 g, 1 wt.% for Ag), following the previously described route (Au/C).

For the preparation of the bimetallic AuAg catalysts, on the other side, Au and Ag vapours generated at 10^{-5} mbar by resistive heating of two different alumina-coated tungsten crucibles (filled with 120 mg of Au beads, 1–6 mm, 99.999 % purity and 20 mg of Ag wire, diam. 2.0 mm, > 99.99 % purity, both from Aldrich) were co-condensed simultaneously with acetone (100 mL) onto the frozen walls of the glass reactor maintained at liquid nitrogen temperature (- 196 °C) for 1 h. The reactor chamber was heated to the melting point of the solid matrix (approximately - 95 °C) and the resulting Au-Ag solvated metal atoms (SMA) solution (95.0 mL) was kept under argon atmosphere in a Schlenk tube (- 40°C). The Au and Ag content, calculated by means of the ICP-OES analysis, was 0.88 mg/mL of Au and 0.12 mg/mL of Ag, corresponding to the desired Au/Ag molar ratio = 4.0.

Subsequentially, 90 mL of the [Au-Ag]/acetone SMA (0.40 mmol, 79.2 mg of Au and 0.10 mmol, 10.8 mg of Ag) was added to a suspension of alumina (2.8 g) in acetone (50 mL) under vigorous stirring. The mixture was stirred for 12 h at room temperature.

Au-Ag bimetallic nanoparticles were quantitatively deposited on the support, the colourless solution was removed under vacuum. The resulted light-brown solid was washed with n-pentane (3 times with 50 mL) and dried under reduced pressure and slightly warming (approximately 60 °C). Au-Ag bimetallic catalysts (Au_4Ag_1/Al_2O_3 SMAD) with a 3.2 wt.% total metal loading finally were obtained. A schematic representation of the bimetallic synthesis procedure is reported in Figure 4-9.

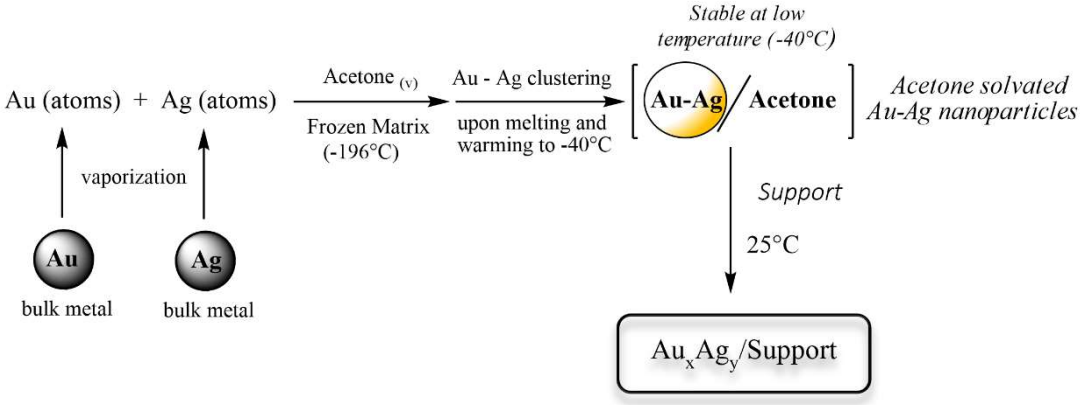

Figure 4-9. General scheme of a bimetallic SMAD synthesis (Au_xAg_y/Support).

Pt/Nb_2O_5 and Modified Niobia

A tungsten wire, whose surface had covered by approximately 103.0 mg of electrodeposited platinum (reduction from metal powder precursor) was firstly prepared. The platinum vapours generated by resistive heating of the tungsten coated wire under vacuum (10^{-5} mbar) were co-condensed with mesitylene (100 mL, 98 % purity, from Aldrich) in a glass reactor at – 196 °C. In this case was exploited a different solvent (from acetone) that, thanks to its aromatic rings, is capable to well stabilise the geminal nanoparticles and lead to smaller particles (range ≈ 1-1.5 nm). The reactor chamber was heated to the melting point of the solid matrix and the resulting brown solution (95 mL) was kept under argon atmosphere in a Schlenk tube at - 40 °C. The Pt-content of the obtained Pt solvated metal atoms (SMA) was determined by ICP-OES (0.8 mg/mL). The Pt/mesitylene SMA (2.5 mL of Pt/mesitylene, 2 mg Pt) was added to a dispersion of the support (200 mg) in mesitylene (5 mL) under vigorous stirring. Afterwards the solvent was removed by vacuum and the so-obtained solids Pt/Nb_2O_5, Pt/W-Nb_2O_5, Pt/Ti-Nb_2O_5 were washed with 50 mL of *n*-pentane (99 % purity, from Aldrich) 3 times and dried under reduced pressure and modest warming (≈ 60 °C). All the so-obtained samples contained 1.0 wt.% of Pt.

Au/C, Cu/C and Au_xCu_y/C

For the bimetallic preparative, the preparation of Au_4Cu_1/C is reported as an example. As in a typical synthesis, gold and copper vapours generated by resistive heating of two alumina-coated tungsten crucibles, filled with approximately 100 mg and 8 mg of gold (beads, 1 - 6 mm, purity 99.999 %, from Aldrich) and copper (powder, purity 99.999 %, from Aldrich), respectively, were co-condensed at liquid nitrogen temperature with acetone (100 mL) in the glass reactor chamber of the MVS reactor (for 1 hour). The reactor chamber was warmed to the melting point of the solid matrix (approximately -95°C), and the resulting purple-brown solution (95 mL) was siphoned at a low temperature into a Schlenk tube and kept in a refrigerator at -20°C. The Au and the Cu-contents of the AuCu-solvated metal atoms (SMA) solution were 0.52 mg/mL and 0.042 mg/mL for Au and Cu (Au/Cu molar ratio = 4:1), respectively, as determined by ICP-OES analysis. AuCu nanoparticles were then quantitatively deposited onto Vulcan XC-72 carbon by adding 90 mL of the AuCu-SMA solution to a suspension of the support (5.1 g) in acetone (50 mL) under vigorous stirring at 25°C for 12 h. Subsequentially the solution separated from the solid was then washed with 50 mL of n-pentane for 3 times. The drying final step occurred under reduced pressure and modest warming (≈ 60 °C). The preparations of the carbon supported AuCu catalysts containing different Au/Cu molar ratios (13:1 and 1:17) were carried out by the same procedure by varying the amount of copper powder used.

The monometallic was prepared with the same strategies and rather than have a co-evaporation of the two metals, copper and gold were employed one at a time in two different synthesis.

4.3.3. *Deposition-Precipitation synthesis*

Au/TiO_2, Ag/TiO_2, Au_1Ag_1/TiO_2 and Au_4Ag_1/TiO_2

Titania (TiO_2, Titanium oxide, SA: 45 m^2 g^{-1}, 70 % anatase and 30 % rutile, purity >99.5 %, from Aldrich) was selected as support. Commercial $HAuCl_4 \cdot 3H_2O$ and $AgNO_3$ (purity >99.99 %, both from Aldrich) were used as gold and silver precursors. The preparation of 1 wt.% Au/TiO_2 sample was performed by deposition–precipitation with urea (DPU) in the absence of light. The gold precursor, $HAuCl_4$ (4.2×10^{-3} M), and the urea (0.42 M) were dissolved in 50 mL of distilled water (MilliQ); the initial pH of the solution was 2.4. Then, 1 g of titania was added to the solution. Thereafter, the suspension temperature was increased to 80 °C (pH increases) and kept constant for 16 h under stirring.

The preparation of 1 wt.% Ag/TiO_2 was performed by deposition–precipitation with NaOH (DPNaOH). For some reasons, not yet elucidated, Ag could not be deposited on the support by DPU (attempted to have a comparable way of synthesis). 1 g of TiO_2 was added to 54 mL of an aqueous solution containing $AgNO_3$ (4.2×10^{-3} M). The solution was heated to 80 °C. The initial pH was ≈ 3, subsequentially it was adjusted to 9 by a dropwise addition of NaOH (0.5 M), promoting AgOH precipitation on the surface of the support. The suspension was vigorously stirred for 2 h at 80 °C.

For the preparation of the bimetallic AuAg catalysts, Ag was first deposited by deposition-precipitation with NaOH (DPNaOH) followed by the deposition of Au by DPU. 1 g of the support (TiO_2) was added to the aqueous solution of $AgNO_3$ and heated at 80°C. The pH was adjusted to 9 by dropwise addition of NaOH (0.5 M), in order to promote the precipitation of AgOH on the support. The suspension was kept under stirring for 2 h at 80°C. Gold was then deposited by DPU method after recover and dry the Ag/TiO_2 under vacuum at 80°C for 2 h (used ad support for the second deposition). The amount of the metal precursors were opportunely calculated on the base of the ratio desiderated (Au:Ag=4:1 or Au:Ag=1:1). The final metal loading (Ag + Au) was 1 wt.% for all the samples prepared. After the deposition–precipitation procedure, all samples were centrifuged, washed with water four times, centrifuged again, and dried under vacuum for 2 h at 80 °C. The real amount of metal was checked by means of ICP-OES. A schematic representation of the bimetallic DP synthesis is reported in Figure 4-10.

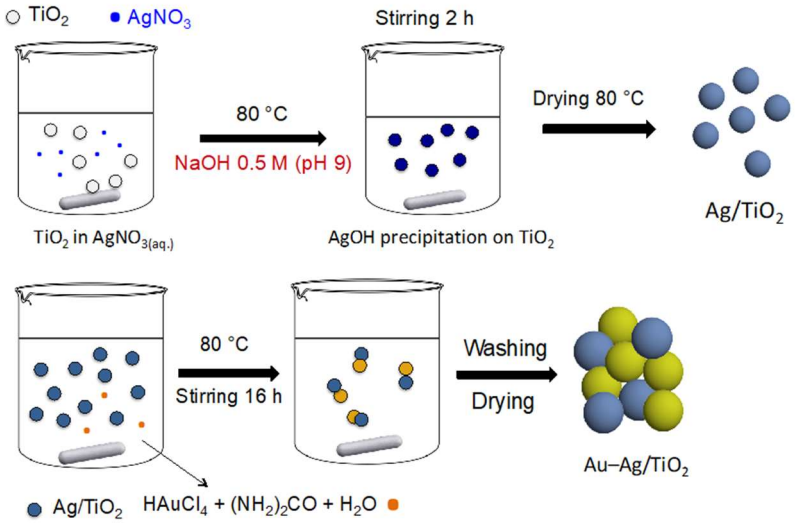

Figure 4-10. Representative scheme of bimetallic synthesis by DPU (Au_xAg_y/TiO_2).

4.3.4. *Incipient wetness impregnation*

Ru/CNFs

The catalysts were prepared by incipient wetness impregnation method using an aqueous solution of the metal precursor ($RuCl_3 \cdot xH_2O$, purity 99.98 %, from Aldrich). The appropriate amount of Ru precursor was dissolved in a proper volume of deionised water (MilliQ) in order to obtain a final volume that corresponded to the specific pore volume of the support. For each support (CNFs, CNFs-O, CNFs-N and CNFs-P), pore volume was previously carefully measured by gradual addition of 100 µL of deionised water (MilliQ) to a 1 g sample of CNFs until the complete impregnation was reached (*Table 4-1*). For the catalyst preparation, the ruthenium solution was added to a weighed amount of support placed into a glass cylinder and manually stirred through a glass rod until the sample homogeneity was reached. The black slurry was finally dried in an oven at 80 °C for 16 h. A general representation of the synthesis procedure is reported in Figure 4-11. Before use, the catalyst was activated as reported in the following section (activation procedure).

Table 4-1. Specific support pore volume.

Support	Pore Volume (mL/g)
CNFs	11.0
CNFs-N	7.2
CNFs-O	5.1
CNFs-P	8.3

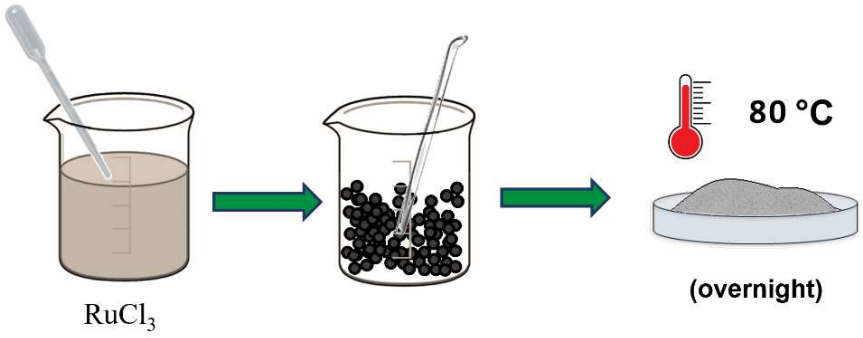

Figure 4-11. Representative scheme of an incipient wetness impregnation synthesis techniques (Ru/CNFs).

4.3.5. *Post-synthesis treatments and activations procedure*

Calcination

The calcination step was performed in a tubular furnace, with a heating rate of 5 °C/min until reaching the desired temperature (400 °C or 300 °C) and kept for 30 minutes (or 1 h) in static air. The cooling down step to reach the RT has not been performed under a controlled rate. In the case of catalysts prepared by sol immobilisation, the calcination allowed to remove the protecting agent and then to study its influence by comparison with uncalcined samples. Samples prepared according to the other procedures (i.e. SMAD), underwent the same thermal treatment for comparison purpose. More details are reported in the appropriate section (section 2.4).

Activation procedure

All the DP and incipient wetness-derived catalysts, required a thermal reductive treatment in order to produce the metal nanoparticles from the metallic precursors deposited on the support surfaces.

The standard procedure for the activation of the DP samples consists in a reductive treatment performed in a tubular furnace at 550 °C under H_2 flux for 1 hour. The heating (rate 2°C/min) and cooling down steps (to RT) occurred under N_2 flow.

The CNFs, impregnated with the Ru salt precursor, were activated by means of a reductive activation step: 200 °C, 5 bar of H_2 for 1 h. The reductive treatments were performed *in situ*, in the reaction autoclave (before adding the reaction mixture), considering the tendency of ruthenium to be re-oxidised if exposed to air [1].

4.4. Catalytic tests

4.4.1. *Glycerol reactions*

Reactions were all carried out in a glass reactor (30 mL) provided with an electronically controlled magnetic stirrer (≈ 1250 rpm to guarantee a kinetic regime) and connected to a large cylinder (99.99 % pure, from SIAD, 40 L of capacity) containing dioxygen. The reaction occurred under pressure (3 bar provided by a Pressure regulator) and the dioxygen uptake of the consumed gas was controlled by the use of a mass flow controller (Readout&Control Electronics 0154 mass flow controller). Typically, 0.31 g of glycerol was dissolved in 10 mL of water and mixed with the catalyst powder (final concentration of glycerol: 0.3 M, glycerol/metal = 2000 $mol \cdot mol^{-1}$ or 1000 $mol \cdot mol^{-1}$). Where indicated, 4 equivalents of NaOH were added (0.48 g). The pressurized reactor was thermostated at the appropriate temperature (50 °C or 80 °C), by dunking in an oil-bath heated by Heidolph MR 3002 hot plate (maximum stirring rate: 1400 rpm; thermal power: 600W; maximum temperature: 300°C; dimension: 240 x 155 x 120 mm) with thermal control (Heidolph EKT 3001 thermocouple, -50 °C ÷ 300 °C). Once the required temperature (50 or 80 °C) was reached, the gas supply was switched to oxygen and the monitoring of the reaction started. The reaction was considered initiated when stirring was activated. Glycerol (86–89 wt.% solution), glyceric acid and all the intermediates used in the catalytic tests were from Aldrich. Deionised water (Milli-Q purified) was used as the solvent for all the experiments.

4.4.2. *Levulinic acid hydrogenation reactions*

The Levulinic Acid (LA) hydrogenation reactions were carried out in a 100 mL stainless steel autoclave. The catalytic test was carried out in a glass inlet inserted in an Heidolph MR 3002 hot plate for simultaneous heating and stirring (maximum stirring rate: 1400 rpm; thermal power: 600W; maximum temperature: 300 °C; dimension: 240 x 155 x 120 mm) equipped with thermal control (Heidolph EKT 3001 thermocouple, -50 ÷ 300 °C).
In a typical experiment, 15 mL of a 0.3 mol/L aqueous solution of LA (purity 99 %, from Aldrich) and an appropriate amount of catalyst (Met:LA molar ratio of 1:1000) were placed into the glass inlet along with a magnetic stirrer. The system was flushed and pressurised for 3 times with 3 bar of N_2 in order to remove any residual oxygen in the atmosphere and then pressurised with 7 bar of H_2. The reaction system was then heated at the desired temperature (100 °C) and the solution stirred at a constant rate of 1250 rpm

(kinetic regime). Samplings were carried out by stopping the stirring and quenching of the reaction in an ice bath. The withdrawn samples of (approximately 300 μL) were centrifuged in order to separate the catalyst and 200 μL of the supernatant solution were diluted into 5 mL of a 1 wt.% solution of H_3PO_4. The diluted solution was then injected into an HPLC system for product analysis.

4.4.3. *Hydroxymethylfurfural hydrogenation reactions*

The 5-hydroxymethylfurfural (HMF) hydrogenation reactions were carried out in a 100 mL stainless steel autoclave (reactor) equipped with a mechanical stirrer and a thermocouple (4843 Controller, autoclave and controller from Parr Instrument Company). In a typical experiment, 0.1550 g of HMF (purity 99 %, from Aldrich) were dissolved in 15 mL of 2-butanol (purity 99 %, from Aldrich). The solution was placed into a glass inlet with the appropriate amount of activated catalyst (Met:HMF molar ratio of 1:100). The system was then sealed and purged with N_2 (3 bar for 3 times) and then the reactor was pressurized with H_2, to the desired pressure (20 bar). The autoclave was heated up to 150 °C and the solution was stirred at 1000 rpm (kinetic regime). Samplings were carried out by stopping the stirring and quenching of the reaction in an ice bath. The samples of the reaction solution (approximately 500 μL) was withdrawn and centrifuged in order to separate the catalyst from the solution. 200 μL of the supernatant solution were then diluted with a solution of an external standard (dodecanol, purity > 98 %, from Aldrich) for GC measurements. Product quantification was carried out through a GC-FID. Product identification was carried out with a GC-MS and the resulting fragmentation peaks were compared with standards present in the software database.

4.4.4. *Furfural hydrogenation reactions*

Furfural hydrogenation reactions were carried out in a 100 mL stainless steel autoclave equipped with a glass inlet. Heating was provided by an Heidolph MR 3002 hot plate (maximum stirring rate: 1400 rpm; thermal power: 600W; maximum temperature: 300°C; dimension: 240 x 155 x 120 mm) equipped with thermal control (Heidolph EKT 3001 thermocouple, -50 °C ÷ 300 °C).

In a typical experiment, 10 mL of a 0.1 M solution of furfural (purity 99 %, from Aldrich) in ethanol (purity 99.8 %, from Aldrich) and an appropriate amount of catalyst (Furfural:Met molar ratio of 1:500) were placed into the glass inlet along with a magnetic stirrer. The autoclave was sealed and flushed and pressurised several times (3 times with

3 bar) with N_2 in order to remove any residual oxygen in the atmosphere and then pressurized with 7 bar of H_2. The autoclave was then heated up to the desired temperature (50 °C) and the reaction mixture stirred at a constant stirring rate of 1250 rpm (kinetic regime). Samplings were carried out by stopping the stirring and quenching of the reaction under cold water. Approximately 500 µL of reaction mixture were withdrawn and centrifuged in order to separate the catalyst. 200 µL of the supernatant solution were then diluted with a solution of an external standard (dodecanol, purity 98 %, from Aldrich) for GC measurement. Product quantification was carried out through a GC-FID. Product analysis was carried out with a GC-MS and the resulting fragmentation peaks were compared with standards present in the software database.

4.4.5. *Benzyl alcohol oxidation*

The benzyl alcohol reactions were carried out in a 100 mL stainless steel autoclave equipped with a mechanical stirrer and a thermocouple (4843 Controller, autoclave and controller from Parr Instrument Company). The experiments were carried out using 10 mL of a solution of 0.3 M (or 0.15 M) of benzyl alcohol (cyclohexane as solvent, substrate/metal = 500 mol/mol, 120 °C, pO_2 = 4 bar). The autoclave was sealed and flushed several times with O_2 in order to remove any residual air in the atmosphere and pressurized at 4 bar. The autoclave was then heated up to the desired temperature (120 °C) and the reaction mixture stirred at a constant rate of 1250 rpm (kinetic regime). The progress of the reaction was monitored by periodic removal of samples from the reactor. Samplings were carried out by stopping the stirring and quenching of the reaction in an ice bath. A sample of the reaction solution (approximately 500 µL) was withdrawn and centrifuged in order to separate the catalyst from the solution. 200 µL of the supernatant solution were then diluted with a solution of an external standard (dodecanol, purity > 98 %, from Aldrich,) for GC measurement. Product quantification was carried out through a GC-FID. Product analysis was carried out with a GC-MS and the resulting fragmentation peaks were compared with standards present in the software database.

4.4.6. *Recycling tests*

Each run was carried out under the same conditions of the reference experiments. At the end of each run, the catalysts were separated from the reaction mixture by centrifugation or by simple filtration and then re-used without any further treatment. For all the tests performed a recovery > 98 % of the catalysts was obtained.

4.5. Product analysis

4.5.1. *High performance liquid chromatography (HPLC)*

The progress of the reaction and the distribution of products have been controlled by High Pressure Liquid Chromatography (HPLC) analyses for the aqueous reaction mixtures. Samples were withdrawn periodically (after 15', 30', 60' and so on from the start of reaction) and analysed by HPLC Agilent 1220 LC system equipped with an Alltech OA-10308 column (300 mm × 7.8 mm, thermostated at 50 °C and an integrated UV detector (λ = 210 nm) and an online refractive index (RI) detector (Agilent 1260 infinity). 1wt.% H_3PO_4 solution was used as eluent. As already reported, 200 μL of solution (homogeneous sample proper centrifuged to remove the catalyst) have taken with a micropipette and diluted to 5 mL with the eluent (1 % H_3PO_4 solution). This dilution ratio was selected to achieve an optimal concentration of the injected sample so that it results within the linearity range and the detection limits of the analytical method. The degrees of uncertainty for this type of instrument is typically ± 5 %. Finally, 40 μL of the prepared solution has been injected in the column and analysed under a flow of 0.400 mL/min. The identification of the products was performed on the basis of retention times by comparison with the standard compounds. The quantification has performed by peaks integration through Chem. Station for LC Systems software (Rev. B.04.03), using calibration curve method (plotting of the recorded signals versus concentrations).

For each compound, at least four standard solutions were prepared at different and known analyte concentrations. These solutions were injected and the so obtained peak area was determined. For each standard concentration, analyses were replicated three or more times.

Calibration curves were obtained by plotting the measured areas as a function of standard concentrations.

A line of best fit (regression line) is used to join the points of the curve obtained. All the calibration curves show an accuracy (evaluated based on the R^2 factor) of $R^2 > 99.0$ %.

$$A = \boldsymbol{R_f} \cdot C + i$$

The regression coefficient R^2, calculated by means of the residuals (error) of each data point, represents a statistical measure and provides an information about the quality of the straight-line fitting with the experimental data. The intercept of the regression equation indicates the systematic errors. The slope (R_f) of the line represents the response factor. This latter is related with the concentration and the area of peaks. The response factors of both UV detector and refraction index has considered where possible (wavelength of UV detector = 210 nm, specific to be adsorbed from carbonyl groups). This calibration strategy is applicable thanks to the loop which is equipped the HPLC that guarantee a precise and reproducible injection of 10 μL in the column for each analysis. The concentration range should always cover the concentration of the analysed solution. From the concentration data it was possible to estimate glycerol conversion and product selectivity at different time. Conversion and selectivity were calculated on a carbon atom basis, i.e. considering the number of carbon atoms contained in the molecule.

4.5.2. *Gas chromatography (GC)*

Product quantification was carried out through a GC equipped with a non-polar column (ThermoScientific, TRACE 1300 equipped with a non-polar column: Agilent HP-5 column, 60 m, ø 0.32 mm, 1 μm film thickness) and a Flame ionization detector (FID). The experimental conditions were schematically reported in Figure 4-12.

Quantification of the reaction products, as already reported, was performed by the internal standard method, using dodecanol as the internal standard. Constant volumes (200 μL) of reaction mixture and dodecanol solution were mixed for the preparation of all the samples. The same amount of the internal standard was also included in the calibration standards. For each compound a calibration curve has drawn by reporting in a graph the ratio of the peak area of the analyte to the peak area of the internal standard as a function of the ratio of analyte concentration to internal standard concentration. The experimental points obtained have been interpolated by a regression line. The slope of the line indicates the response factor (R_f), which is then used in the analyses for determining the concentration of the substrates and products as reported in the following equation:

$$(A_x/A_{std}) = R \cdot (C_x/C_{std}) \text{ and therefore } C_x=(A_x/A_{std}) \cdot (C_{std}/R_f)$$

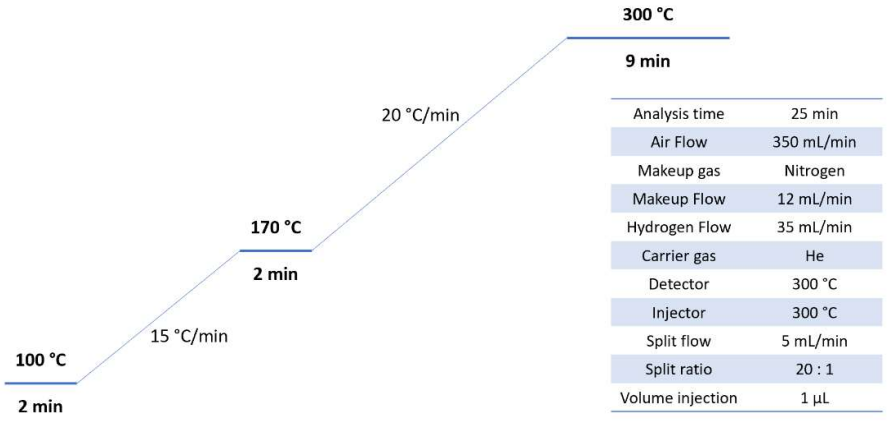

Analysis time	25 min
Air Flow	350 mL/min
Makeup gas	Nitrogen
Makeup Flow	12 mL/min
Hydrogen Flow	35 mL/min
Carrier gas	He
Detector	300 °C
Injector	300 °C
Split flow	5 mL/min
Split ratio	20 : 1
Volume injection	1 µL

Figure 4-12. Experimental conditions for Gas Chromatographic analysis.

The regression coefficient R^2, calculated by means of the residuals (error) of each data point, that provides an information about the quality of the straight-line fitting with the experimental data, for each calibration was > 0.99.

On the other hand, product identification was carried out with a Gas chromatography–mass spectrometry (GC-MS, Thermo Scientific, Waltham, MA, USA, ISQ QD equipped with an Agilent VF-5ms column) and the resulting fragmentation peaks were compared with standards present in the software database.

4.5.3. *Calculation of conversion, selectivity and activity*

The substrate conversion percentage was calculated as the ratio between converted mols (initial moles - residual moles of the substrate) and the initial concentration:

$$\%\ conv = converted\ mols\ /\ initial\ mol \times 100$$

The selectivities (expressed as percentage) towards each product were calculated as the ratio between the mols of the examined product and the converted mols (of the substrate):

$$\%\ sel = product\ mols\ /\ converted\ mols \times 100$$

Initial activity (IA) or *turnover frequency* (TOF or alternatively the TON, turn over number) are commonly used to compare the activity of the catalysts. These factors represent another simple and applicative concept of the number of catalyse cycles (n) that occur in the active sites per unit of time (with fixed reaction conditions and for a specific reaction temperature, pressure, concentration, reactant ratio, extent of reaction, catalyst quantities have to be constant in every experiment to assure fixed reaction conditions.

The initial activity is often calculated with the first catalytic data available (15' or 30'). The activity was calculated as follow:

$$\text{Activity} = (conversion\ initial\ substrate\ mols)\ /\ (metal\ mols \cdot time\ (h))$$

4.6. Characterization techniques

4.6.1. *Inductively Coupled Plasma - Optical Emission Spectrometry (ICP-OES)*

The metal contents were verified by ICP analysis of the reaction mixtures (for leaching evaluation), Sol solutions and solution's filtrates or alternatively directly on catalysts after the acid digestion of the solid samples (for metal loading determination). The analyses were performed by ICP-OES (ICAP6300 Duo purchased from Thermo Fisher Scientific) with an external calibration methodology. Where necessary microwave digestion of the samples (approximately 5 mg sample) in 3 mL of aqua regia and subsequentially dilution with highly deionized water (Milli-Q) to a final weight of 20 g was performed.

4.6.2. *X-ray Powder Diffraction (XRD)*

Powder X-ray diffraction patterns were collected in a PANalytical X´pert PRO diffractometer with an X´Celerator detector, using a monochromatic Cu $K\alpha_1$ as X-rays source. Diffractograms were recorded with the detector arranged in a Bragg-Brentano geometry.

4.6.3. *Diffuse Reflectance Infrared Fourier Transform Spectroscopy (DRIFTS)*

Where required the top surface of the samples was probed by CO adsorption at room temperature monitored by DRIFTS. Spectra were collected by a Nicolet iS50 infrared spectrometer equipped with an MCT detector, a Specac DRIFT accessory and a Specac environmental chamber with a ZnSe window. Multiple scans (64) were collected with a resolution of 4 cm^{-1}. CO adsorption was measured under a 1 % CO/Ar flow after 5 minutes on as prepared or variously pre-treated samples. The analysis performed just before CO addition were used as background. The spectra were presented as log(1/R), where R was the reflectance (CO gas spectrum was subtracted). The as prepared samples were measured after 10 min under Ar flow in the DRIFT cell, the ex situ prepared ones after a short (5 min) refreshing in situ pre-treatment at the same conditions. Longer *in-situ* pre-treatments were performed where necessary. The *in-situ* calcinations or reducing pre-treatments were performed under synthetic air or 5 % H_2/Ar flow with 10 °C/min heating rate and after a given isothermal period with cooling down to room temperature in air and Ar flow, respectively.

In order to evaluate the acidity of the samples, where necessary, FTIR studies by pyridine adsorption and desorption were performed. A spectrophotometer (FTS-60) equipped with a mid-IR MCT detector (BioRad) was exploited for all the experiments. Before the

analysis, the sample (disk of 10−20 mg) was dehydrated at 75 °C for 40 min under vacuum, then a blank spectrum was collected before probe molecule adsorptions. Subsequentially, pyridine (purity 99.8 %, from Aldrich) adsorption was carried out at room temperature and the following desorption steps were run for 30 minutes at various temperatures (from room temperature up to 250 °C). All spectra were recorder at room temperature. The determination of the amount of adsorbed pyridine ($mmol_{Py}/g_{cat}$) was performed according to the procedure reported by Emeis [2] on the spectra registered at 150 °C.

4.6.4. *Diffuse Reflectance UV-vis (DRUV-Vis) Spectroscopy*

UV-visible spectra of fresh and the pre-treated supported catalysts were recorded in the range 200-2600 nm by an Agilent Cary 60 spectrometer equipped with an DRA accessory in diffuse reflectance to measure the localized surface plasmon resonance (LSPR) of metallic nanoparticles.

4.6.5. *Raman Spectroscopy*

Raman spectra were recorded in an inVia Renishaw spectrometer equipped with a Renishaw HPNIR laser and an Olympus microscope. The measurements were carried out at an exciting wavelength of 514 nm and an approximate power on the sample of 15 mW.

4.6.6. *Transmission Electron Microscopy (TEM)*

Morphology and microstructures of the catalysts were characterized by transmission electron microscopy (TEM). Before the analysis, the samples were finely smashed in an agate mortar (to homogenise the sample), suspended in isopropanol and sonicated for approximately 10 minutes. Subsequentially, the suspension was dropped onto a holey carbon-coated copper grid (300 mesh) and the solvent was evaporated under a delicate air compressed flow (Mo TEM grids were used for Cu samples). Electron micrographs were carried out using a ZEISS LIBRA200FE microscope equipped with a 200 kV FEG source in the Z-contrast mode in which the brightness depended on the thickness and, approximately, the square of the atomic number. Particle sizes were determined by using ImageJ software to process the STEM images. X-ray spectra (Energy Dispersive X-ray Spectroscopy, EDS-Oxford INCA Energy TEM 200) and elemental maps were collected in HAADF-STEM (high angular annular dark field scanning transmission electron microscopy) mode. Histograms of the particle size distribution were obtained by counting at least 300 particles onto the TEM micrographs; the mean particle diameter (d_m) was

calculated by using the formula $dm=\Sigma d_i n_i / \Sigma n_i$ where n_i was the number of particles of diameter d_i. Crystallographic data were processed by CrystBox Software [3]. Alternatively, in the case of Au_xCu_y systems (with the corresponding monometallic SMAs) the catalysts were analysed with Cs-aberration-corrected TEM. Samples were prepared dropping the SMA solution prepared (same strategy above mentioned) onto supported ultra-thin film grids. Analysis were performed after complete solvent evaporation. HRTEM micrographs were collected by a Cs-image-corrected JEOL ARM200F, HRSTEM. STEM-EELS (scanning transmission electron microscope equipped with electron energy loss spectroscopy) maps were collected by a Cs-Probe-corrected JEOL ARM200F equipped with a Gatan GIF Quantum ERS energy filter. Energy filtered maps were collected at energy loss 2239.0-2477.0eV for gold and 953.0-1202.0eV for copper.

The morphology and microstructures of other samples (i.e. Ru/C and AuRu/C SOL-derived catalysts), were characterized using a FEI Titan 80-300 electron microscope with a conventional EDX detector as well as in a probe aberration corrected Titan 80-200 with an in column Super-X EDX detector. The microscopes were operated at an accelerating voltage of 300 kV in the image corrected Titan and 200 kV in the probe corrected Titan. Spectrum imaging with probe corrected STEM and a Super-X EDX detector offered high spatial resolution and the opportunity to resolve the components by using multivariate analysis before inducing significant changes of the structures during electron beam irradiation.

4.6.7. *X-ray Photoelectron Spectroscopy (XPS)*

By means of X-ray photoelectron spectroscopy (XPS) the surface composition and oxidation state of the metals were investigated using a KRATOS XSAM 800 XPS machine equipped with an atmospheric reaction chamber. All the XPS lines acquired of O 1s, C 1s, N 1s, P 2p, Au 4f, Ag 3d, Pt 4f, Al 2p and Ti 2p regions were recorded applying Al K_α Characteristic X-ray line, 40 eV pass energy and FAT mode. Where necessary the Auger parameter (AP) (i.e. for silver) was calculated as the sum of the kinetic energy of Ag $M_5N_{45}N_{45}$ Auger lines and the binding energy (i.e. of Ag $3d_{5/2}$ peak). The instrument is equipped with an atmospheric pre-treatment chamber directly connected to the UHV chamber with a load lock gate. This latter allows treatments of samples avoiding any contact with air or source of contaminations. The accuracy of the binding energies (BE) can be estimated to be ± 0.2 eV. A curve fitting procedure of the experimental spectra

was performed. References for charge compensation were Al 2p binding energy at 74.4 eV and Ti $2p_{3/2}$ binding energy at 458,6 eV. In the case of the CNFs, thanks to charge neutralization of the sample (combination of energy electrons and argon ions), the measure gave a C(1s) binding energy of 284.8 eV. Charge referenced to adventitious C1s, C-C peak at 284.8 eV [4]. All data were analysed using CasaXPS (v2.3.17 PR1.1).

4.6.8. *BET measurements*

N_2-adsorption experiments were carried out in a Micromeritics ASAP 2000 instrument. All the samples were initially degassed under vacuum at 400 °C. Specific surface areas were determined from N_2 adsorption isotherms by means of Brunauer–Emmett–Teller (BET) model.

4.6.9. *Test for hydrogen peroxide detection and degradation*

A solution of H_2O_2 (15 mL, concentration 1 mM) was stirred at the appropriate temperature under N_2 atmosphere. The pH of the solution was adjusted by adding H_2SO_4 0.1 M (pH 4) or NaOH 1 M (pH > 14) solutions. The amount of the catalyst added was approximatively the same exploited in the reaction (glycerol oxidation). Hydrogen peroxide was quantified by sampling and by a subsequentially permanganate titration. Samples of 5 mL of the filtered reacting solution was titrated with a 0.01 N $KMnO_4$ solution at constant pH of 7.5 ± 0.1 (by adding concentrated H_2SO_4). The detection limit of H_2O_2 was 0.01 mM.

4.6.10. *X-ray Absorption Fine Structure (XAFS) spectroscopy*

The local atomic structure of the monometallic Au/Al_2O_3 and Au/C and bimetallic $AuAg/Al_2O_3$ and Au_xCu_y/C catalysts was investigated by XAFS spectroscopy at the Au L_3 absorption edge and at the Ag K edge. Measurements were performed at the LISA beamline [5] of the European Synchrotron Radiation Facility (ESRF-Grenoble, France). The XAFS spectra of the catalysts at the Au L_3 edge and of the reference samples (Au, Ag and Cu foils and Ag_2O, CuO and Cu_2O oxide) at both edges were taken in transmission mode while measurements of the catalysts were performed in fluorescence mode using a 13-element high purity germanium (Ge) solid state detector. In transmission mode the absorption coefficient was calculated as $\mu(E) = ln(I_0/I_T)$ while in fluorescence mode as $\mu(E) = I_F/I_0$. All X-ray absorption spectra were collected at liquid nitrogen temperature (LNT) in order to reduce the thermal effects. The measured catalytic samples were prepared pressing into pellets their fine powders together with boron-nitride (invisible at

the synchrotron radiations). The powder amounts were calculated to achieve appropriate edge jumps [6]. Reference samples at both edges were used to calibrate the energy scales, to align the absorption spectra and to evaluate S_0^2 values [7]. In the data analysis both the near edge region (XANES) and the extended x-ray absorption fine structure (EXAFS) were considered. EXAFS data, usually indicated as $\chi(k)$ where k is the photoelectron wave vector [7], were extracted using the ATHENA program [8] and the least-square parameter fitting was performed using the ARTEMIS program [8] both implemented in the IFEFFIT package [9]. The fitting procedure was used to determine the coordination numbers (N), the interatomic distances (R) and Debye-Waller factors (σ^2) of the coordination shells around the absorbing Au, Ag and Cu atoms. In the fitting procedure of the reference samples and of many catalysts at the Au L_3 edge single and multiple-scattering contributions, calculated by the FEFF6 software package [10], were used. At the Ag K and Cu K edge, only single scattering contributions were included for the bimetallic catalysts. In all the cases an estimation of the accuracy of the obtained structural parameters, compatible with data quality and range [11] used was achieved.

References

1. A. Galal, H.K. Hassan, N.F. Atta, A.M. Abdel-Mageed, T. Jacob (2019) Synthesis, structural and morphological characterizations of nano-Ru-based perovskites/RGO composites. Sci Rep 9(1):7948.
2. C.A. Emeis (1993) Determination of Integrated Molar Extinction Coefficients for Infrared Absorption Bands of Pyridine Adsorbed on Solid Acid Catalysts. J Catal 141(2):347–354.
3. M. Klinger (2017) More features, more tools, more CrysTBox. J Appl Crystallogr 50:1226–1234.
4. XPS Interpretation of Carbon. https://xpssimplified.com/elements/carbon.php. Accessed 29 Oct 2019
5. F. d'Acapito, A. Trapananti, A. Puri (2016) LISA: the Italian CRG beamline for x-ray Absorption Spectroscopy at ESRF. J Phys Conf Ser 712:012021.
6. P. a Lee, P.H. Citrin, P. Eisenberger, B.M. Kincaid (1981) Extended x-ray absorption fine structure—its strengths and limitations as a structural tool. Rev Mod Phys 53(4):769–806.
7. C. Evangelisti, E. Schiavi, L.A. Aronica, A.M. Caporusso, G. Vitulli, L. Bertinetti, G. Martra, A. Balerna, S. Mobilio (2012) Bimetallic Gold–Palladium vapour derived catalysts: The role of structural features on their catalytic activity. J Catal 286:224–236.
8. B. Ravel, M. Newville (2005) ATHENA , ARTEMIS , HEPHAESTUS : data analysis for X-ray absorption spectroscopy using IFEFFIT. J Synchrotron Radiat 12(4):537–541.
9. M. Newville (2001) IFEFFIT : interactive XAFS analysis and FEFF fitting. J Synchrotron Radiat 8(2):322–324.
10. S.I. Zabinsky, J.J. Rehr, A. Ankudinov, R.C. Albers, M.J. Eller (1995) Multiple-scattering calculations of x-ray-absorption spectra. Phys Rev B 52(4):2995–3009.
11. G.G. Li, F. Bridges, C.H. Booth (1995) X-ray-absorption fine-structure standards: A comparison of experiment and theory. Phys Rev B 52(9):6332–6348.

General conclusions

This thesis' project was dedicated on the design, synthesis and study of new and tuneable heterogeneous catalysts to be exploited in emerging, eco-friendly and sustainable processes. The valorisation of biomass derived molecules, indeed, nowadays represents one of the most important challenges that have to be overcome in order to replace the exploiting of petrochemical resources to produce commodity chemicals and fuels with renewable ones. The latter could contribute to loosen the grip of pollution and global warming.

In order to achieve this goal, a clear disclosure of the correlation between the structure of the catalysts and the catalytic performances was performed. This latter was possible following a knowledge-based approach shaped around the following pillars:

- Approach the target reaction by acquiring a deep theoretical knowledge
- Control of the catalytic systems' characteristics during their synthesis
- Collecting significant experimental results
- Perform precise and appropriate characterisations
- Critically correlate the fine structure of the catalysts with their corresponding catalytic behaviours

For the valorisation of glycerol (by-product of biodiesel production – 1st generation of biomass feedstock) following the aforementioned pillars, several gold-based systems, were prepared, tested and fully characterized. In the oxidations performed under alkaline conditions (needed for gold and to push the reaction's kinetic), monometallic Au, Ag and bimetallic AuAg catalysts were synthesised with SOL and SMAD techniques. Then DPU derived systems were introduced in the comparison. The SOL derived catalysts have the peculiarity to present protected nanoparticles (by a polymer exploited in the synthesis), and can offer a valid comparison with naked nanoparticles (derived from the other synthetic techniques adopted) to clarify the role of the capping agent. The SOL-derived materials, indeed, showed advantages such as controlled metal particle size regardless the type of support used (crucial to exclude the particle size effect from the discussion) and improved resistance to deactivation in comparison with the other synthetic routes. On the other side, since this first valorisation performed by Au on different carbonaceous supports systems (Au/C), the supports have confirmed their key and active role in the catalysis. For instance, the catalyst supported on the carbon Vulcan has showed an

enhanced initial activity favoured by the high graphitisation degree carbon exploited in comparison with two other activate carbons. For bimetallic AuAg/TiO_2, on the other side, strong metal support interaction (SMSI) induced by thermal treatments appeared to be the ruling factor in determining the oxidation state of the metals. This latter has subsequently shown to affect the catalytic activities, and to stabilise the nanoparticle size during the thermal treatments. These catalysts, indeed, showed and enhanced initial activity in comparison with the alumina supported ones (AuAg/Al_2O_3), but a faster deactivation due to the presence of Ag^+ species at the nanoparticles' surface. The as mentioned oxidation state, furthermore, showed to be strongly influenced also by the nanoparticles composition: i.e. the silver in bimetallic Au-rich AuAg systems, showed more resistance towards the overoxidation. The stability is conferred by the beneficial presence of the gold and the bimetallic systems led also to synergistic effects with a consequent remarkable enhanced catalytic activity. Gold, however, has to be present in high amount relative to the silver to observe the beneficial effects aforementioned. It has also been demonstrated, in one of the last set of experiments, how the AuPt nanoparticles supported on titania offered a valid system to perform the glycerol oxidation also in the absence of a base (eliminating the need of a final treatment to obtain the desired acidic products from their salts). The platinum confers activity in bimetallic catalysts toward the first dehydrogenative step, inhibited in the case of Au monometallic catalyst. The mutual ratio of the two metals, on the other side, deeply influences the reactivity of the catalytic systems. For instance, the highest initial activity in alkaline and free pH condition was obtained with a 9:1:/Au:Pt and 6:4/Au:Pt molar ratio, respectively. Gold, once more, have confirmed its key role in bimetallic resistance to deactivation that also shown synergistic effects.

Beside all the aspects treated so far, we were able to synthetize active catalysts fot the glycerol oxidation, with a high selectivity toward the appealing glyceric acid product. We were also able for some systems, to tune the selectivity toward more C-C cleavage products (with smaller nanoparticles) or to the tartronic acid, obtained from a subsequentially oxidation of the tartronic acid (with the most active catalysts).

Through the valorisation of the 2nd generation of biomass related substrates, on the other hand, other important general considerations can be reported. It should be recalled that the exploited molecules, derived from the progenitor cellulose, hemicellulose and lignin: the three main components of a plant. By studying the valorisation of cellulose derived

molecules (hydrogenation of levulinic acid, LA, and 5-hydroxymethylfurfural, HMF) performed on ruthenium nanoparticles supported on CNFs and functionalised CNFs (CNFs-P, CNFs-O and CNFs-N), the importance of support modification was highlighted. Thanks to the high monodispersity of the Ru nanoparticles (prepared by incipient wet impregnation), indeed, we were able to investigate and properly isolate the effect of the tailor-made supports. For instance, the Ru/CNFs-N showed the highest catalytic activity among the set of catalysts tested for the levulinic acid hydrogenation, due to a strong interaction between the Ru nanoparticles and the support. All the catalysts showed a selectivity >99% toward *y*-valerolactone (GVL). On the other side, exploring the HMF valorisation, Ru/CNF-N and Ru/CNF-P showed a detrimental effect but also a change in selectivity. However, these two catalytic systems enhanced the formation of ethers: products of the reaction between intermediate reaction products (dihydroxymethylfuran, DHMF, and methylfurfuryl alcohol, MFA) and the solvent (2-butanol). This result pointed out once again the influence of the support on the catalytic activities and on the reaction paths.

Guided by a similar aim, analogous considerations could also be done for the valorisation of one of the most appealing hemicellulose derived molecules: the furfural. Platinum supported on niobia were the catalyst's family designed for this reaction. Niobia, was hydrothermally prepared as pure metal oxide or doped with either W or Ti (W-Nb_2O_5 and Ti-Nb_2O_5) to tune the acidity of the system. The latter, turned out to be the key factor for the catalytic behaviour in the furfural hydrogenation by influencing both the activity and selectivity. The highest was the acid site concentration the greater was the catalytic activity showed. In parallel also the selectivity was addressed, driven by the acidity, toward the acetalization product (combination of furfural and ethanol, the solvent) at the expense of furfuryl alcohol (however always the main product). This latter study highlighted once again the active role of the supports in catalysis.

Lastly, the catalytic systems prepared to perform the benzyl alcohol oxidation (model compound containing linkages that resemble those found in lignin), remarked again the value of bimetallic systems and in particular of gold as modifier. AuM/C materials (M=Pd, Pt, Ru and Cu), indeed, deeply changed the catalytic behaviours of the final catalyst depending on their composition. Detrimental effect was observed in the case of AuPt and AuPd. On the contrary, AuRu (with the highest activity showed) and AuCu (only case of a bimetallic system with one not noble metal) showed synergistic catalytic

affects. The composition of the catalysts, furthermore, can profoundly influence also the features of the bimetallic nanoparticles: alloyed, core-shell and segregated systems were observed depending on the second metal used. The appealing AuCu bimetallic system, furthermore, were deeply investigated. This bimetallic systems showed a marked synergetic effect even when the copper is present in low amount (Au:Cu/13:1 molar ratio). Further investigation disclosed also the presence and the role of two catalytic elements: copper oxide was the responsible of the activation of oxygen, while gold, on the other side, was responsible of the oxidation of the substrate. For this reason, we speculate that the reaction took part at Au-CuO interface. From this latter study, in conclusion, it appeared also clearly how the nanoparticles' structure play a fundamental role in ruling a reaction; the composition effect, on the other side, pointed out the importance of having a good knowledge and control of the synthetic routes. To conclude, for all the catalysts exploited in the benzyl alcohol oxidation, we were able to fully address the selectivity toward the desired and industrial appealing product: benzaldehyde. In the end, this type of catalysts, designed for the valorisation of biomasses, could soon represent an enormous asset for the development of biorefineries: the eco-friendly alternative to the current environmental not sustainable oil refineries to produce commodity chemicals and fuels.

List of figures

List of tables

List of schemes

List of publications

1. **Furfural hydrogenation on modified niobia**

Jouve A., Cattaneo S., Delgado-Munoz D., Scotti N., Evangelisti C., Lopez-Nieto J. M., Prati L.
Appl. Sci. 2019, 9(11): 2287

2. **Gold-silver catalysts: ruling factors for establishing synergism**

Prati L., Stucchi M., Jouve A., Villa A., Gergely G., Németh M., Evangelisti C., Zanella R.
ChemCatChem 2019, 11: 4043 – 4053

3. **Carbon-supported hybrid Au-CuO bimetallic nanoparticles for selective benzyl alcohol oxidation**

Marelli M., Jouve A.; Villa A., Psaro R., Balerna A., Prati L., Evangelisti C.
J. Phys. Chem. C, 2019, 123 (5): 2864–2871

4. **CNF-functionalisation as versatile tool for tuning activity in cellulose-derived product hydrogenation**

Jouve A., Cattaneo S., Stucchi M., Capelli S., Villa A., Evangelisti C., Prati L.
Molecules, 2019, 24(2): 316.

5. **Gold-Silver catalysts: effect of catalyst structure on the selectivity of glycerol oxidation**

Jouve A., Nagyc G., Somodic F., Tiozzo C., Villa A., Balerna A., Beck A., Evangelisti C., Prati L.
Journal of Catalysis, 2018, 368: 324-335

6. **Spectroscopic insights leading to a better understanding of site-isolation in heterogeneous nanocatalysts**

Manzoli M., Jouve A., Gill A. M., Cravotto G., Raja R.
Journal of Materials Chemistry A (2018), 6(29): 14410-14419

7. **Carbon-Supported Au nanoparticles: catalytic activity ruled out by carbon support**

Jouve A., Stucchi M., Barlocco I., Evangelisti C., Somodic F., Villa A., Prati L.
Topics in Catalysis, 2018, 61(18-19): 1928-1938.

8. **Gold as a modifier of metal nanoparticles: effect on structure and catalysis**

Prati L., Villa A., Jouve A., Beck A., Evangelisti C., Savara A.
Faraday Discuss., 2018, 208: 395-407.

9. **Exploring the effect of Au/Pt ratio on glycerol oxidation in presence and absence of a base**

Villa A., Jouve A., Sanchez Trujillo F. J., Motta D., Prati L., Dimitratos N.
Catalysts 2018, 8(2): 54.

10. **Production of biofuels and chemicals with bifunctional catalysts**

(Chapter 7) of "Production and upgrading of γ-valerolactone with bifunctional catalytic processes"
Prati L., Villa A., Jouve A.
Edited by Prof. Zhen Fang, Prof. Richard L. Smith Jr., and Dr. Hu Li